
Theoretical stellar atmosphere models for cool stars

Zazralt Magic



München 2014

Theoretical stellar atmosphere models for cool stars

Zazralt Magic

Dissertation
an der Fakultät für Physik
der Ludwig–Maximilians–Universität
München

vorgelegt von
Zazralt Magic
aus Ulaanbaatar, Mongolei

München, den 8. Januar 2014

Erstgutachter: Priv.-Doz. Dr. Achim Weiss
Zweitgutachter: Priv.-Doz. Dr. Joachim Puls
Tag der mündlichen Prüfung: 14. Mai 2014

Contents

Zusammenfassung	xv
Summary	xvii
Preface	xix
1 Introduction	1
1.1 Motivation	1
1.2 Radiation-hydrodynamics of stellar convection	5
1.2.1 Hydrodynamic equations	5
1.2.2 Radiative transfer	8
2 Methods	11
2.1 Multi-dimensional atmosphere modeling	11
2.1.1 Details on the numerics	11
2.1.2 Geometrical properties	12
2.1.3 Equation of state	13
2.1.4 Opacity	14
2.1.5 Radiative transfer	14
2.2 STAGGER-grid models	17
2.2.1 Stellar Parameters	17
2.2.2 Scaling and relaxing 3D models	17
2.2.3 Scaling the initial models	18
2.2.4 Selection of the opacity bins	20
2.3 Temporal and horizontal averages	21
2.3.1 Basic averaging procedure	23
2.3.2 Interpolation to the new reference depth scale	24
2.3.3 Extrapolation at the top	25
2.4 The STAGGER-grid 1D atmospheres	26
2.4.1 Basic equations	26
2.4.2 Numerical methods	27
3 STAGGER-grid	29
3.1 Global properties	29
3.1.1 Stellar parameters	29
3.1.2 Constant entropy of the adiabatic convection zone	30
3.1.3 Entropy jump	34
3.1.4 Large-amplitude fluctuations	35
3.1.5 Emergent intensity	37
3.1.6 Granule size	40
3.2 Mean $\langle 3D \rangle$ atmosphere	43
3.2.1 Temperature stratification	45
3.2.2 Velocity field	51

3.2.3	Turbulent pressure	56
3.2.4	Total pressure and density	57
3.2.5	Electron number density	58
3.2.6	Entropy	58
3.2.7	Superadiabatic temperature gradient	60
3.2.8	Transport of energy	61
3.3	Comparison of the $\langle 3D \rangle$ with 1D models	64
3.3.1	1D models	64
3.3.2	MARCS and ATLAS models	65
3.4	Comparison of the averaging methods	66
3.4.1	Temperature	66
3.4.2	Density	68
3.4.3	Electron number density	69
3.4.4	Vertical velocity	69
3.5	Statistical properties	71
3.5.1	Contrast	71
3.5.2	Upflows and downflows	73
3.5.3	Histograms	74
3.6	Reversed granulation	76
3.7	Hydrostatic equilibrium	78
3.8	Deviations from the EOS	79
4	Stellar granulation	81
4.1	Granule recognition	81
4.2	Granule properties	83
4.2.1	Diameter of granules	84
4.2.2	Intensity distribution of granules	85
4.2.3	Temperature and density of granules	87
4.2.4	Velocity of granules	88
4.2.5	Geometrical properties	88
4.3	Fractal dimension	90
4.4	Optical surface	93
4.4.1	Corrugation of the optical surface	93
4.4.2	Surface velocity correlations	94
4.5	Topology of granulation	96
5	Spectral line formation	101
5.1	Multi-dimensional line formation calculations	102
5.2	Two components of the line profile	104
5.3	Spectral line formation: $\langle 3D \rangle$ and 3D LTE calculations	106
5.3.1	Comparison of $\langle 3D \rangle$ and 3D line formation	106
5.3.2	Cautionary remarks	111
5.3.3	Comparison with 1D models	111
5.4	Fe line shapes, shifts and asymmetries	113
5.4.1	Line shape	113
5.4.2	Line strength	114
5.4.3	Line width and depth	115
5.4.4	Line shift	116
5.4.5	Line asymmetry	119
5.4.6	Conditions at the height of line formation	122

6	Limb Darkening	125
6.1	Deriving the limb darkening	126
6.2	The resulting limb darkening predictions	130
6.3	Transit light curves	133
6.4	Comparison with results from 1D models	136
7	STAGGER-grid and 1D models	139
7.1	Mixing Length from 1D atmosphere models	140
7.1.1	Matching the adiabatic entropy value	141
7.1.2	Matching the entropy jump	141
7.1.3	Additional MLT parameters	143
7.2	Mixing Length from 1D envelope models	145
7.2.1	Matching the adiabatic entropy	146
7.2.2	Comparison with 2D calibrations	147
7.2.3	Impact on stellar evolutionary tracks	148
7.2.4	Comparison with observations	148
7.3	$T(\tau)$ relations	149
7.4	Velocity correlation length	151
7.5	Mass mixing length	153
8	Conclusions	157
A	Functional fits	161
B	Tables	165
	Acknowledgment	176
	Curriculum vitae	177

List of Figures

1.1	Temperature stratification of the Sun.	2
1.2	Comparison of solar granulation pattern with a numerical simulation.	3
1.3	The solid angle $d\vec{\Omega}$ in spherical polar coordinates.	8
2.1	Eulerian mesh of the solar simulation.	12
2.2	Solar abundances by AGS09.	13
2.3	Equation of state with isocontours of pressure and Rosseland opacity.	14
2.4	Overview of the targeted STAGGER-grid parameters.	16
2.5	The non-equidistant spacing, Δz , of the vertical depth scale.	19
2.6	The selected opacity bins for the solar simulation and a single opacity bin.	20
2.7	Comparison of the radiative heating and cooling.	21
2.8	Temperature stratifications for three different reference depth scale.	24
2.9	Double-extrapolation of a truncated 3D stratification.	25
3.1	Overview of the constant entropy value of the adiabatic convection zone s_{bot}	31
3.2	Lines of constant entropy of the adiabat s_{bot} in the Kiel diagram.	32
3.3	Comparison of the constant entropy of the adiabat s_{bot} and Δs with 2D results.	33
3.4	Overview of the entropy jump Δs	33
3.5	Scaling of entropy jump Δs with the adiabatic value s_{bot}	35
3.6	Overview of maximum contrast for T , ρ and s	36
3.7	Overview of the emergent (bolometric) intensity for a selection of stars.	38
3.8	Temporally averaged histograms of the (bolometric) intensity.	39
3.9	Overview of the (bolometric) intensity contrast ΔI_{rms}	40
3.10	Overview of the temporally averaged 2D spatial powerspectrum of the intensity.	41
3.11	Overview of the granule diameter d_{gran}	41
3.12	Comparison of the granule diameter d_{gran} with the pressure scale height.	42
3.13	Filling factor of the up- and downflows.	43
3.14	Overview of the solar mean $\langle 3D \rangle$ stratification for different variables.	44
3.15	Temperature stratification.	45
3.16	Variation of temperature stratification with stellar parameter.	47
3.17	Overview of the maximum temperature gradient ∇_{peak} and Rosseland opacity κ_{Ross}	48
3.18	The mean internal energy against mean density illustrating the EOS.	50
3.19	The vertical rms-velocity, $v_{z,\text{rms}}$	52
3.20	Overview of the entropy jump, vertical velocity and density.	53
3.21	Comparison of the entropy jump Δs , ρ_{peak} vs. maximal vertical rms-velocity $v_{z,\text{rms}}^{\text{peak}}$	54
3.22	Vorticity $ \vec{\omega} $	55
3.23	Fraction of turbulent pressure to total pressure, $p_{\text{turb}}/p_{\text{tot}}$	56
3.24	Total pressure p_{tot}	57
3.25	Density ρ	58
3.26	Local electron number density n_{el}	59
3.27	Mean entropy s	59
3.28	Superadiabatic gradient ∇_{sad}	60

3.29	Normalized energy fluxes F/F_{tot}	62
3.30	Normalized cooling and heating rates $q_{\text{rad}}^{\text{norm}}$	64
3.31	Comparison of the temperature stratification for the $\langle 3\text{D} \rangle$ and the 1D models.	65
3.32	Comparison of the temperature stratification for the $\langle 3\text{D} \rangle$ and the 1D MARCS models.	66
3.33	Relative differences in the temperature for different averages.	67
3.34	Relative differences in density for different averages.	68
3.35	Comparison of mean electron number density n_{el} for different averages.	70
3.36	Comparison of vertical rms-velocity for different averages.	70
3.37	Temperature and density contrast.	71
3.38	Difference in temperature and density between averages in up- and downflows.	73
3.39	Temporal averaged histogram of the temperature and density.	74
3.40	Histograms of the temperature and density taken at $\langle \log \tau_{\text{Ross}} \rangle = -4.0$	75
3.41	Temperature-contours for solar and metal-poor TO simulation.	77
3.42	Deviations from the hydrostatic equilibrium.	78
3.43	Deviations between mean pressure and opacity, and derived from the EOS.	79
4.1	Emergent (bolometric) intensity map showing the granule recognition algorithm.	82
4.2	Histogram of the solar granules sizes and the area contribution function.	83
4.3	Histograms of granule sizes for different stellar parameters.	85
4.4	Mean intensity of the granules for different stellar parameters.	86
4.5	Intensity contrast of the granules for different stellar parameters.	86
4.6	Mean normalized temperature of the granules for different stellar parameters.	87
4.7	Mean normalized density of the granules for different stellar parameters.	88
4.8	Mean rms vertical velocity of the granules for different stellar parameters.	89
4.9	Geometrical shape factors for the solar granules.	89
4.10	Area perimeter histogram with the solar fractal dimensions.	91
4.11	Overview of the fractal dimensions for different stellar parameters.	92
4.12	Corrugated optical surfaces including the vertical velocity for selected simulations.	93
4.13	Overview of the corrugation of the optical surface.	94
4.14	Velocity correlation with T, ρ and δI at the optical surface.	95
4.15	Temperature and density fluctuations of the Sun depicting solar granules.	97
4.16	Comparison of the temperature excess with the bolometric intensity of the solar simulation.	98
4.17	The vorticity of the Sun illustrating the turbulent downdrafts.	99
4.18	Transsonic and supersonic Mach numbers located in the turbulent downdrafts.	100
5.1	Different Fe I lines at 5000\AA and curve-of-growth.	103
5.2	Single Fe I line divided in up- and downflows.	104
5.3	Overview of full 3D and two-stream models for Fe I and Fe II lines.	105
5.4	Overview of the $\langle 3\text{D} \rangle - 3\text{D}$ line formation differences for solar metallicity.	107
5.5	Overview of the $\langle 3\text{D} \rangle - 3\text{D}$ line formation differences for sub-solar metallicity.	108
5.6	Overview of the mean difference $\Delta \log \epsilon$	109
5.7	Overview of the relative difference in the continuum intensity.	110
5.8	Overview of Fe I and Fe II lines with different stellar parameters.	112
5.9	Overview of line strength W_λ for Fe I and Fe II line.	114
5.10	Overview of relative difference between full 3D and $\langle 3\text{D} \rangle$ line strength.	115
5.11	Overview of line width and depth.	116
5.12	Overview of line shift and maximal bisector.	117
5.13	Overview of line shift with line strength for the Fe I and Fe II lines.	118
5.14	Overview of bisectors for the Fe I and Fe II lines.	120
5.15	Overview of bisectors.	121
5.16	Comparison between maximal bisector and maximal vertical rms-velocity.	122
5.17	Correlation of velocity and temperature.	123
5.18	Overview of rms-temperature and rms-velocity.	124

6.1	Overview of emergent intensity at 500nm for different μ angles.	127
6.2	Synthetic full 3D spectral energy distributions.	128
6.3	Solar limb darkening.	130
6.4	Overview of limb darkening for different stellar parameters.	131
6.5	Synthetic stellar disks with increasing T_{eff}	131
6.6	Overview of the four parameters for the non-linear limb darkening law.	132
6.7	Overview of the coefficient for the linear limb darkening law.	134
6.8	Transit light curves.	135
6.9	Differences in the transit light curves between 3D and 1D predictions.	135
6.10	Overview of maximal differences in the limb darkening.	137
7.1	Illustration of the calibration of the mixing length with the 1D atmosphere code.	141
7.2	Overview of the mixing length calibrated with s_{bot}	142
7.3	Overview of the mixing length calibrated with Δs	142
7.4	Comparison of the mixing length with inverse of Δs	143
7.5	Variation of the additional MLT parameters.	144
7.6	Illustration of the calibration of the mixing length with ASTEC.	145
7.7	Overview of the mixing length from ASTEC.	146
7.8	Comparison of mixing length with 2D calibration.	147
7.9	Estimated variation of the mixing length for stellar evolutionary tracks.	148
7.10	Comparison of mixing length with inferred values from observations.	149
7.11	Overview of $T(\tau)$ -relations.	150
7.12	Overview of $T(\tau)$ -relations at the optical surface.	150
7.13	Vertical two-point correlation function of the vertical velocity for the solar simulation.	151
7.14	Vertical two-point correlation function of the vertical velocity for different stellar parameters.	152
7.15	Overview of mean vertical correlation length of the vertical velocity.	153
7.16	The mass mixing length and the gradients of the density and vertical velocity.	155
7.17	Overview of the mass mixing length.	156
7.18	Correlation of α_{MML} with the inverse entropy jump Δs	156

List of Tables

6.1	Accuracy of limb darkening fits.	129
A.1	Coefficients of linear functional fits.	162
A.2	Coefficients of exponential and parabolic functional fits.	162
A.3	Coefficients of hyperbolic functional fits.	163
B.1	List of global properties.	166
B.2	The line list for the Fe I and Fe II lines.	167
B.3	Line strength, width, depth, shift, extrema of bisector for the solar simulation.	168
B.4	Limb darkening coefficients derived from 3D RHD models in the Kepler filter.	169

Zusammenfassung

In kühlen Sternen wie der Sonne wird die nuklear erzeugte Energie aus dem Inneren an die Oberfläche transportiert. Diese kann dann in den freien Weltraum entfliehen, und so können wir das Sternenlicht letztlich beobachten. Die theoretische Modellierung des photosphärischen Übergangsbereiches – vom konvektiven zum radiativen Energietransport – ist aufgrund der inhärenten dreidimensionalen (3D) Natur der Konvektion und der komplexen, nicht-linearen und nicht-lokalen Interaktionen des Strahlungsfelds mit dem stellaren Plasma sehr anspruchsvoll. Theoretische Atmosphärenmodelle stellen die fundamentale Basis für die Untersuchung von Sternen dar, daher sind Astronomen für ihr Verständnis der Sterne auf diese letztlich angewiesen. Die üblicherweise verwendeten eindimensionalen (1D) Atmosphärenmodelle beinhalten verschiedene Vereinfachungen. Insbesondere wird die Konvektion für gewöhnlich mit der Mischungswegtheorie berechnet, trotz ihrer wohlbekanntem Fehler, da derzeit keine deutlich besseren Alternativen vorhanden sind. Der einzige Ausweg, um dieses Problem zu überwinden ist, die zeitabhängigen, dreidimensionalen, hydrodynamischen Gleichungen, welche mit einem realistischen Strahlungstransport gekoppelt sind, zu lösen. Aufgrund der in den vergangenen Jahrzehnten rasch gestiegenen Rechenleistung wurden bedeutende Fortschritte mit Simulationen für 3D Strahlungshydrodynamik (RHD) von Atmosphären erzielt. Diese Modelle sind außerordentlich leistungsfähig, und besitzen eine enorme Vorhersagekraft, wie präzise Vergleiche mit Sonnenbeobachtungen wiederholt beweisen konnten.

Ausgestattet mit diesen ausgereiften Methoden möchte ich als Ziel meiner Dissertation die drei folgenden Fragen näher untersuchen: Was sind die Eigenschaften der Atmosphären von kühlen Sternen? Welche Unterschiede sind zwischen den 1D und 3D Modellen vorhanden? Wie verändern sich die Vorhersagen für die Sternstrukturen und Spektrallinien? Um mich dieser Aufgabenstellung systematisch anzunehmen, habe ich das STAGGER-Gitter berechnet. Das STAGGER-Gitter ist ein umfangreiches Gitter aus 3D RHD Atmosphärenmodellen von kühlen Sternen, welches einen großen stellaren Parameterbereich abdeckt. In der vorliegenden Dissertation beschreibe ich die Methoden, welche angewendet wurden, um die vielen Atmosphärenmodelle zu berechnen. Zudem werden die allgemeinen Eigenschaften der resultierenden 3D Modelle, auch deren zeitliche und räumliche Mittelwerte detailliert dargestellt und diskutiert. Die Unterschiede zwischen den 1D und 3D Schichtungen, sowie die Details der stellaren Granulation (die Manifestation der Konvektion unterhalb der Sternoberfläche) werden ebenfalls umfangreich erläutert und beschrieben. Des Weiteren habe ich folgende Anwendungen für die 3D Atmosphärenmodelle untersucht: Berechnung theoretischer Spektrallinien, wichtig für die Bestimmung von Sternparametern, Spektroskopie und Häufigkeiten-Analyse; die sogenannte Randverdunkelung, notwendig für die Analyse interferometrischer Beobachtungen und Suche nach extrasolaren Planeten; und die Kalibrierung der Mischungsweglänge, womit 1D-Sternmodelle verbessert werden können.

Die Qualität der hochauflösenden Beobachtungen hat inzwischen die der theoretischen 1D Atmosphärenmodelle aufgrund der technischen Entwicklungen in den vergangenen Jahren überschritten. Daher hat sich der Bedarf an besseren Simulationen für Atmosphärenmodelle erhöht. Durch die Bereitstellung eines umfangreichen Gitters aus 3D RHD Atmosphärenmodellen wurde dazu ein erheblicher Beitrag geleistet. Damit werden wir den Anforderungen an die Theorie für die derzeitigen und zukünftigen Beobachtungen gerecht werden, und können somit zu einem besseren Verständnis der kühlen Sterne beitragen.

Summary

In cool stars, like the Sun, energy from the inside is transported to its surface by convection, which then can escape into space as radiation that we can observe. Modeling this photospheric transition region – from convective to radiative energy transport – is notoriously challenging due to the inherent three-dimensional (3D) nature of convection itself and the complex non-linear and non-local interaction of the radiation field with the stellar plasma. Astronomers rely on theoretical atmosphere models, which provide the fundamental basis to study and understand stars. The commonly employed one-dimensional (1D) atmosphere models make use of several simplifications, in particular, convection is usually treated with the mixing-length theory (MLT), despite its well-known wrongness simply due to the lack of a considerably improved alternative. Therefore, the only appropriate approach to overcome this issue, is to solve the time-dependent, 3D, hydrodynamic equations coupled with the realistic treatment of radiative transfer. Due to the soaring computational power in the recent decades, significant progress has been established with the advent of 3D radiative hydrodynamic (RHD) atmosphere simulations. Nowadays, these perform exceedingly well and offer exceptional predictive potential as detailed comparisons with the Sun have repeatedly revealed.

Equipped with this matured, powerful tool, I want to address the following three main questions as the aim of my thesis: What are the atmospheric properties of cool stars besides the Sun? Which differences are given between 1D and 3D models? How do the application-based predictions change? To attend to this matter in a systematical approach, I have computed the STAGGER-grid, a comprehensive grid of 3D RHD model atmospheres of cool stars covering a wide range in stellar parameters. In this thesis I describe the methods I have applied for the computation of the grid models, and the general properties of the 3D models, as well as their temporal and spatial averages are presented and discussed in detail. Also, the differences between 1D and 3D stratifications are determined, and the details of stellar granulation, the manifestation of subsurface convection, is extensively depicted. Furthermore, I investigated with the STAGGER-grid several applications for 3D atmosphere simulations including: spectral line profiles, important for stellar parameter determination, stellar spectroscopy and abundance analysis; limb darkening, necessary for interferometry and extrasolar planet search; and the calibration of the mixing length, which will improve stellar evolution models.

The cumulative technical developments of high-resolution observations in the recent years have surpassed the standards of theoretical 1D atmosphere models, thereby, it has given rise to the enhanced demand of improved atmosphere simulations. By providing a comprehensive grid of 3D RHD atmosphere models to the astronomical community, a major contribution has been achieved to live up to the current and future high-precision observations, which ultimately will lead to a better understanding of cool stars.

Preface

The presented dissertation is segmented into eight chapters, with the first one being the introductory one, while the final chapter (Chapter 8) contains the conclusions to all findings. The content of three chapters originate partly from the two published publications Magic et al. (2013a,b), and has been supplemented with additional illustrations, discussions and sections. Both publications have been written by the author primarily by himself, however, the guidance provided by Martin Asplund at all times and the initial practical introduction by Remo Collet are to be emphasized. Also, the helpful consultation by Aake Nordlund on the Section on the energy fluxes in the first paper is also noteworthy. Otherwise, the remaining co-authors provided only minor support for the completion of the subsequently presented STAGGER-grid project results. Furthermore, I want to remark that four chapters contain material that has been prepared for four additional publications.

In Chapter 1, I introduce the subject of stellar atmospheres of cool stars by elucidating its development in the past and its current status. Subsequently, the theoretical background is covered with a brief discussion of the equations for hydrodynamic and radiative transfer. Then, in Chapter 2 I present all the methods I have applied for the computation of the large grid of 3D atmosphere models – the STAGGER-grid – that comprises of ~ 220 grid models ranging in effective temperature, T_{eff} , from 4000 to 7000 K in steps of 500 K, in surface gravity, $\log g$, from 1.5 to 5.0 in steps of 0.5 dex, and metallicity, $[\text{Fe}/\text{H}]$, from -4.0 to $+0.5$ in steps of 0.5 and 1.0 dex. In order to generate the STAGGER-grid models in a consistent fashion, I have developed a comprehensive set of routines, which automatizes all the necessary intermediate steps that involves in the computation of new 3D atmosphere simulations with the STAGGER-code including realistic input physics for the equation of state (EOS) and for continuous and line opacities. Despite all automatization, the still laborious computations of all grid models were performed by myself, in particular, these necessitated the executing, monitoring and checking of the individual jobs. Moreover, I have also developed an extensive set of routines (during my work a total of ~ 70000 lines of code were written) for the detailed analysis of the vast data set that includes the calculation of the temporal and spatial averages of various statistical properties, which are presented and discussed in Chapter 3. Various interesting scaling relations between different global properties are pointed out, between which I want to accentuate our finding on the enhancement of the intensity contrast and the reversed granulation in metal-poor simulations for the first time. Furthermore, the mean stratifications are discussed in great detail and compared with classical 1D MLT models, in order to quantitatively reveal their discrepancies. We find that metal-poor stars are most affected, and their temperature stratifications can be mismatched by up to ~ 1000 K. This is followed by the comparison of the different averaging procedures and the discussion of additional statistical properties, such as the contrast, histogram and the averages separated in up- and downflows. I have also performed (by myself) a detailed analysis of stellar granulation in Chapter 4 by applying a granule recognition algorithm to the emergent intensity map, a method that has been developed and applied by solar observers. For the detected granules I derived extensive details, like granule diameter, intensity, temperature and density distribution, also vertical velocity and geometrical properties. I would like to highlight my findings on the dual fractal dimensions, since these challenge the findings by some observational studies.

Besides the analysis of the STAGGER-grid itself, I have also covered solitarily three important applications for 3D RHD simulations. In Chapter 5 I have performed spectral line formation calculations for various iron lines. The line profiles resulting from 1D models and mean 3D stratifications based on the different averaging procedures were compared with the full 3D computations, and we found the interesting outcome that the averages on layers of column mass density leads to better mean representations than averages determined on layers of constant optical depth. We find that using mean 3D models would signif-

icantly improve the spectroscopical analysis of metal-poor stars, since the 1D models show here the largest deviations. The effects of a realistic velocity field and the inhomogeneities arising from the convective motions on the spectral line profiles were studied with iron line shifts and asymmetries. Furthermore, in Chapter 6 I utilized full 3D synthetic energy flux computations performed by Andrea Chiavassa to derive limb darkening and transit light curve predictions for the parameterization of exoplanets. In Chapter 7 I calibrated the mixing length with both 1D models for atmospheres and envelopes from 3D simulations, which will be useful for improving stellar structure computations. I derived also the vertical correlation length of the vertical velocity and the mass mixing length, and their values are qualitatively comparable to the mixing length. Here, I want to highlight my derivation of the mass mixing length from the hydrodynamic mean field equations, which has been achieved for the first-time. Furthermore, I found the mixing length and the mass mixing length scales with the inverse of the entropy jump.

The STAGGER-grid states a significant contribution to the development of stellar atmosphere modeling due to the almost similar large extent in stellar atmospheric parameter space that conventional 1D models had one or two decades ago. Furthermore, the complete grid will be made publicly available for stellar astronomical community, so that in the future, the limitations of 1D models can be exceeded. The 3D atmosphere models will lead to improvements in various astronomical applications that will follow in the coming years, including stellar parameter determination, stellar spectroscopy and abundance analysis, asteroseismology, calibration of stellar evolution models, interferometry, and extrasolar planet search. Finally, the detailed, comprehensive analysis of the STAGGER-grid models states a spadework for the future, since due to a better understanding of the subsurface convection in cool stars novel theoretical models might be developed as a result, which ultimately could substitute the MLT models that are currently still widely used.

Chapter 1

Introduction

1.1 Motivation

The primary source of information for stellar objects is the light they emit, which carries information about the physical conditions at its origin. However, in order to interpret the information correctly, one first needs either theoretical or semi-empirical models of the atmospheric layers at the surface of stars from where the stellar radiation escapes. Therefore, models of stellar atmospheres are essential for much of contemporary astronomy.

In the case of late-type stars, the theoretical modeling of stellar atmospheres is complicated by the presence of convective motions and turbulent flows as well as of magnetic fields in their envelopes (see review by Nordlund et al., 2009, and references therein). In particular, convection can significantly affect both the atmospheric stratification and emergent spectral energy distribution in these stars. Hence, in order to correctly represent the temperature stratifications in the outer layers of stars, from where the stellar light escapes, it is vital to accurately account for the interaction between radiative and convective energy transport at the optical surface .

The first realistic grids of line-blanketed atmosphere models for late-type stars appeared with the publication of MARCS (Gustafsson et al., 1975, 2008) and ATLAS models (Kurucz, 1979; Castelli & Kurucz, 2004). Subsequently, other one-dimensional (1D) atmosphere codes, e.g., PHOENIX (Hauschildt et al., 1999) and MAFAGS (Grupp, 2004), were developed to model the atmospheres of stars. In general, these theoretical 1D atmosphere models assume hydrostatic equilibrium, flux constancy, and local thermodynamic equilibrium (LTE). For the modeling of convective energy transport, they commonly employ the mixing-length theory (MLT, see Böhm-Vitense, 1958), which is characterized by several free parameters, the most commonly known being the mixing-length l_m , or equivalently, the parameter $\alpha_{\text{MLT}} = l_m/H_P$. Alternatively, some relatives thereof are available, such as the full turbulence spectrum (FTS) theory by Canuto & Mazzitelli (1991), which itself also has a free parameter. The values of these free parameters are not known from first principles and need to be calibrated based on observations or simulations. The mixing-length theory has in total four free parameters (see Böhm-Vitense, 1958; Henyey et al., 1965; Mihalas, 1970). These free parameters can be calibrated based on their effect on synthetic spectra, but usually only α_{MLT} is calibrated based on the reproduction of selected lines (Fuhrmann et al., 1993; Barklem et al., 2002; Smalley et al., 2002). Moreover, the free mixing length is calibrated in stellar evolutionary calculations by matching the observed luminosity and radius of the Sun at its current age (e.g. Magic et al., 2010). To construct simple yet realistic 1D models of convection is rather difficult, in particular, convective overshooting beyond the classical Schwarzschild instability criterion is normally not considered in 1D atmospheric modeling. Attempts have been made at including its effects in 1D model atmospheres albeit with only limited success (Castelli et al., 1997).

The first numerical 1D model stellar atmosphere codes usually assumed a plane-parallel geometry for the atmospheric stratification. This was later improved upon by changing to a spherical symmetry, leading to lower temperatures in the upper layers, in particular, for giant stars, due to the dilution of the radiation field with increasing radial distance, which can cover a significant fraction of the stellar radius at low

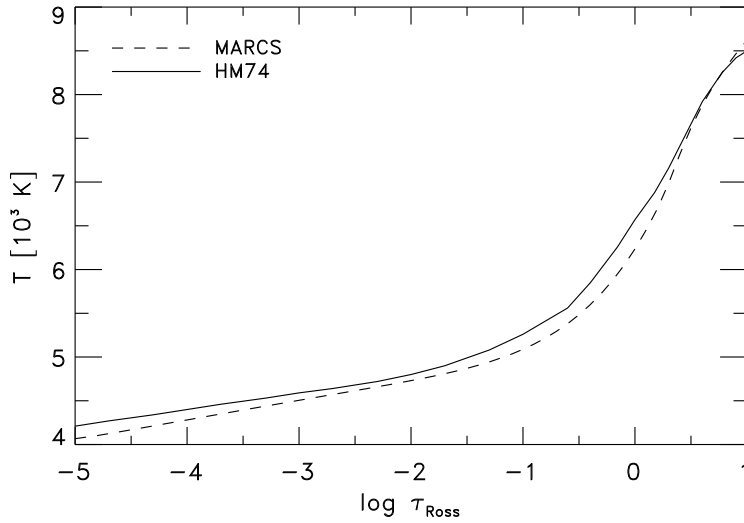


Figure 1.1: Temperature vs. optical depth of the Sun inferred semi-empirically by Holweger & Mueller (1974), and the 1D model prediction by the MARCS code.

$\log g$ (see Gustafsson et al., 2008). Initially line blanketing was included by means of opacity distribution functions (ODFs, Gustafsson et al., 1975) with a few hundred ODFs covering the entire spectrum, eventually replaced by opacity sampling (OS) including thousands of wavelength points (Johnson & Krupp, 1976). Nowadays, thousands of ODFs or hundreds of thousands of OS wavelengths are used. Despite such high resolution in wavelength, the computational costs for 1D atmosphere models are currently quite small, at least for LTE models. Large, homogeneous grids of atmospheres with up to $\sim 10^5$ models exist (Gustafsson et al., 2008; Cassisi et al., 2004; Hauschildt et al., 1999), covering a wide range of stellar atmosphere parameters.

Even though the 1D atmosphere models are based on numerous simplifications, they have demonstrated high predictive capabilities owing to major improvements in the atomic and molecular data (e.g., line lists by Kurucz (1993) or VALD by Piskunov et al. (1995)). Also, the continuum opacity sources and the EOS have undergone similar developments. Thanks to these, 1D atmosphere models are in many respects very successful in comparisons with observations and are widely applied in astronomy today.

Another approach, almost exclusively used for solar atmosphere modeling, is the use of semi-empirical models. In these models, the temperature stratification is inferred from observations (e.g., from lines forming at different heights or continuum center-to-limb variations). Often-used semi-empirical 1D solar atmosphere models are the Holweger & Mueller (1974), VAL3C (Vernazza et al., 1976), Maltby et al. (1986) and MISS (Allende Prieto et al., 2001) models. A similar approach can be used to integrate spatially resolved observations and thus infer the three-dimensional (3D) atmosphere structures using inversion techniques (Ruiz Cobo & del Toro Iniesta, 1992; Socas-Navarro, 2011). Semi-empirical modeling is rarely attempted for other stars, although exceptions exist (e.g. Allende Prieto et al., 2000). In Fig. 1.1 we show the semi-empirical temperature stratification derived by Holweger & Mueller (1974), and for comparison the solar 1D MARCS model (Gustafsson et al., 2008).

Constructing more realistic models requires one to go beyond the 1D framework and model convection without relying on MLT. Stellar convection is an inherently 3D, time-dependent, non-local, and turbulent phenomenon. Therefore, one cannot expect 1D models to reproduce all observed properties accurately, even with access to free parameters to tweak. The next natural step is to abandon some of these crude simplifications by constructing realistic 3D atmosphere models of solar convection. Early hydrodynamic simulations (Nordlund, 1982; Nordlund & Dravins, 1990; Steffen et al., 1989) revealed that stellar surface convection operates in a distinctly different fashion from the MLT picture. Instead of the homogeneous convective elements, they displayed highly asymmetrical motions with slow broad steady upflows interspersed with fast narrow turbulent downdrafts, sometimes even supersonic (e.g., Stein & Nordlund 1998, hereafter SN98; Asplund et al. 2000a; Nordlund et al. 2009; Carlsson et al. 2004; Ludwig et al. 1999). The advent of 3D simulations, which are constructed from first principles, has enabled astronomers to predict

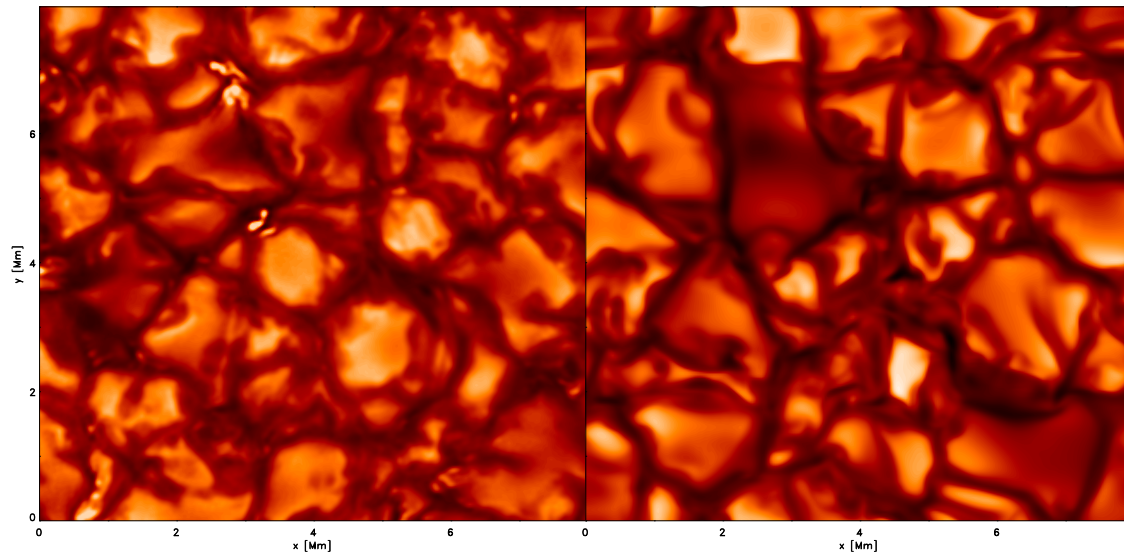


Figure 1.2: Granulation pattern in the emergent intensity of the Sun, observed with the Swedish Solar Telescope (left; resolution is 25 km) and the numerical simulation (right).

various observables such as solar granulation properties and spectral line profiles astonishingly well. More recent solar 3D simulations are remarkably good at reproducing the observed center-to-limb variation (e.g. Pereira et al., 2009a; Asplund et al., 2009; Ludwig, 2006). In Fig. 1.2, we show a comparison between the observed¹ and theoretical solar granulation pattern in the emergent intensity map, which are hardly distinguishable.

3D atmosphere models are by design free from the adjustable parameters of MLT and other parameters such as micro- and macro-turbulence that have hampered stellar spectroscopy for many decades. Instead, in 3D simulations, convection emerges naturally, by solving the time-dependent hydrodynamic equations for mass-, momentum- and energy-conservation, coupled with the 3D radiative transfer equation in order to account correctly for the interaction between the radiation field and the plasma. Also, the non-thermal macroscopic velocity fields associated with convective motions are rendered realistically, and various natural kinetic consequences such as overshooting and excitation of waves emerge from the simulations, without the need for further ad hoc modeling or additional free parameters. The inhomogeneities in the convective motions arise spontaneously and self-organize naturally to form a distinct flow pattern that exhibits the characteristic granulation at the surface. Furthermore, additional spectral observables such as limb-darkening and detailed spectral line shapes, including asymmetries and shifts, are also modeled unprecedentedly accurately with 3D models for the Sun (Nordlund et al., 2009; Pereira et al., 2009b).

For metal-poor late-type stars, it has been shown (Asplund et al., 1999b; Collet et al., 2006, 2007) that the assumption of pure radiative equilibrium in the convectively stable photospheric layers of classical hydrostatic models is generally insufficient. In particular, in the upper photosphere, the thermal balance is instead primarily regulated by radiative heating due to spectral line re-absorption of the continuum-radiation from below above granules and adiabatic cooling due to the expansion of upflowing gas above the intergranular lane. While the adiabatic cooling due expansion is less important in metal-rich stars, in metal-poor stars, the balance between heating by radiation and cooling by mechanical expansion of the gas occurs at lower temperatures because of the weakness and scarcity of spectral lines at low metallicities. By contrast, 1D MLT models have no velocity fields outside their convection zones, and are therefore in pure radiative equilibrium. The temperature stratification there is therefore regulated solely by radiative heating and cooling, thus neglecting altogether the adiabatic cooling component. This results in an overestimation of the temperatures by up to $\sim 1000\text{K}$ in 1D models at very low metallicities, which can potentially lead to severe systematic errors in abundance determinations based on 1D models (see Asplund et al., 1999b;

¹Taken from <http://www.solarphysics.kva.se/gallery/images/2010/>.

Asplund & García Pérez, 2001; Ludwig et al., 2010; Collet et al., 2009; González Hernández et al., 2010). These shortcomings of 1D models are manifested as inconsistencies in the analysis of observed spectra, such as abundance trends with excitation potential of the lines (e.g., analysis of NH lines in the very metal-poor star HE1327-2326, by Frebel et al. (2008)) and discrepant abundances between atomic and molecular lines involving the same elements (e.g. Nissen et al., 2002). For further discussion, we refer to a review of possible impacts of 3D models on stellar abundance analysis by Asplund et al. (2005).

Additionally, there are discrepancies between observations and predictions from 1D models of the solar structure in the context of helioseismology, which point to mistakes in the outer layers of theoretical 1D stellar-structure models, and which are usually referred to as *surface effects* (Rosenthal et al., 1999). With classical 1D stellar structures, higher frequency p-modes of the Sun are systematically shifted due to discrepancies at the upper turning points of the modes, which occur in the superadiabatic peak at the top of the convection envelope. Rosenthal et al. (1999) found better agreement of stellar structures with helioseismic observations, when including the mean stratification of solar 3D models at the top, since the turbulent pressure, usually neglected in 1D models, extends the resonant cavity. Also, it was found that with 3D solar models the predicted p-mode excitation rates are much closer to helioseismic observations (Nordlund & Stein, 2001; Stein & Nordlund, 2001). Ludwig et al. (2009b) compared the power spectra of the photometric micro-variability induced by granulation and found good agreement between the theoretical predictions of 3D solar models and observations with SOHO.

With the comparison of visibility amplitude and phase predictions from 3D simulations with interferometric observations, stellar radii have been derived for a number of red giants (Chiavassa et al., 2010, 2012). The determined stellar radii are slightly larger than estimated with the use of 1D models, which has an impact on the zero point of the effective temperature scale derived by interferometry. Furthermore, Chiavassa et al. (2012) showed that for interferometric techniques a detailed knowledge of the granulation pattern of planet-hosting stars is crucial for the detection and characterization of exoplanets.

Several 3D magnetohydrodynamics codes with realistic treatment of radiative transfer have been developed and applied to the modeling of stellar surface convection. Here, we make use of the STAGGER-code, which is developed specifically to run efficiently on the massively parallel machines available today (Nordlund & Galsgaard 1995²; Kritsuk et al. 2011). The BIFROST-code is an Oslo derivative of the STAGGER-code (Gudiksen et al., 2011), tailored for simulations of the solar photosphere and chromosphere, and therefore including true scattering (Hayek et al., 2010). Other widely used codes are CO⁵BOLD (Freytag et al., 2012), MURAM (Vögler et al., 2005) and ANTARES (Muthsam et al., 2010), which have been independently developed in the last decades. These codes perform similarly a box-in-a-star setup, and the differences can be pointed out mostly in the details of the numerics, such as numerical diffusion and interpolation schemes. Beeck et al. (2012) compared solar models from three of the above 3D stellar atmosphere codes (STAGGER, CO⁵BOLD and MURAM), and showed that the models are overall very similar, despite the distinct numerical approaches. Most of the available 3D stellar convection codes are now highly parallelized, which when coupled with the computational power available today makes it feasible to construct grids of 3D convection simulations within a reasonable time-scale. Grids of 2D and 3D atmosphere models already exist (Ludwig et al., 1999, 2009a; Trampedach, 2007; Trampedach et al., 2013; ?). Clearly, the age of 3D atmosphere modeling has arrived, partly driven by the rising demand created by improved high-resolution spectroscopic and asteroseismic observations.

It is advantageous to reduce the relatively large amount of data from the full 3D atmospheric models to temporally and spatially averaged (hereafter ⟨3D⟩) representations. However, this reduction comes at the expense of physical self-consistency (see Atroshchenko & Gadun, 1994). Nonetheless, in this way one can deal with more manageable atmospheric data structures compared to the otherwise enormous amount of information associated with the full 3D models. These mean ⟨3D⟩ stratifications are usually compared with classical 1D hydrostatic atmosphere models. Nordlund & Stein (2001) point out that the large-amplitude fluctuations in the superadiabatic region³ (SAR) leads to deviations from the hydrostatic equilibrium. Furthermore, the 3D data sets incorporate quantities emerging from the hydrodynamics and associated with convection itself, such as, self-consistent velocity fields and turbulent pressure, for which

²http://www.astro.ku.dk/~kg/Papers/MHD_code.ps.gz

³The SAR can be approximately located with the superadiabatic gradient, e.g., with $\vec{\nabla}_{\text{sad}} > 0.1 \max [\vec{\nabla}_{\text{sad}}]$ one obtains typically a range of $-0.5 \lesssim \log \tau_{\text{Ross}} \lesssim 4.0$.

there are no physically consistent counterparts in the case of 1D hydrostatic models.

The definition of the $\langle 3D \rangle$ stratifications is neither unambiguous nor unique, but depends largely on the choice of reference depth scale. When dealing with the analysis of the atmospheric layers above the optical surface, monochromatic or Rosseland optical depth scales are usually considered the appropriate choice since these are the natural reference depth scales that are used to describe radiative transfer processes in the photosphere. On the other hand, the optical depth loses its usefulness somewhat in the very deep optically thick layers below the optical surface, since here the mean free path of photons becomes very short and the radiative transfer insignificant. Therefore, other reference scales are best suited to describing the main properties of the stellar stratification. Also, the bimodal and highly asymmetric distribution of bulk upflows and of downflows in the convective zone complicates the definition of a meaningful unique average value, particularly near the surface, at the transition between convectively unstable and stable regions.

Uitenbroek & Criscuoli (2011) investigated the application of $\langle 3D \rangle$ models to spectral line formation. They computed and compared continuum and atomic line intensities and their respective CLV from $\langle 3D \rangle$ and 3D models. They conclude that a mean $\langle 3D \rangle$ stratification is insufficient to represent the full 3D atmosphere model in the light of spectral analysis. As reasons for the latter they list the non-linearity of the Planck function, formation of molecules, and the asymmetry of convective motions.

Despite the enormous success and the *ab-initio* nature of 3D atmosphere modeling, as last we want to mention the weaknesses. In order to keep the computation costs reasonable, the radiative transfer is usually simplified with the opacity binning method, which may influence the outcome. Also, the numerical resolutions of these so called large-eddy simulations are not resolving the microscopic viscous dissipation length scales, hence, the need to introduce numerical diffusion. However, these do not affect the main properties of the macroscopic flows and of the physical stratification. Also, we minimize the diffusion coefficients once under the constraint of numerical stability, and then apply them for all the simulations. These issues can be solved, and the easiest rectification will be enhancement of the numerical resolution, in particular, for giants. Accounting for non-LTE effects and magnetic fields is extremely expensive for 3D simulations, therefore, these are usually neglected.

1.2 Radiation-hydrodynamics of stellar convection

In order to understand stellar atmospheres, we need to establish the fundamental physics of the energy transport, which is giving rise to the actual thermodynamical stratification in the subsurface layers of stars. Two intrinsically distinct regimes for the transport of energy can be pointed out at the boundaries of late-type stars: one being the convective energy flux below the optical surface, where the hydrodynamic equations are governing the physics, and other one being the radiative energy flux above the photosphere, which is described by the radiative transfer equation. To numerically determine the thin superadiabatic photospheric transition region at the top of the convection is challenging due to the non-linear, non-local interactions between radiation and matter leading to large-amplitude fluctuations. Therefore, one has to consider the equations of radiation-hydrodynamics, which we will discuss in the following Section.

1.2.1 Hydrodynamic equations

The hydrodynamic equations – known as the Euler equations – are the conservation laws of mass (Eq. 1.5), momentum (Eq. 1.2) and energy (Eq. 1.3). In the case of the numerical modeling of stellar atmospheres we express them as

$$\partial_t \rho = -\vec{\nabla} \cdot (\rho \vec{v}), \quad (1.1)$$

$$\partial_t \rho \vec{v} = -\vec{\nabla} \cdot (\rho \vec{v} \otimes \vec{v} + \underline{\underline{\tau}}) - \vec{\nabla} p_{\text{th}} + \rho \vec{g}, \quad (1.2)$$

$$\partial_t e = -\vec{\nabla} \cdot (e \vec{v}) - p_{\text{th}} \vec{\nabla} \cdot \vec{v} + q_{\text{rad}} + q_{\text{visc}}. \quad (1.3)$$

Here ρ denotes the density, e the internal energy per unit volume⁴, \vec{v} the velocity field, \vec{g} the gravitational acceleration, p_{th} the thermodynamic pressure, q_{rad} the radiative cooling and heating rate, and q_{visc} the viscous dissipation rate.

⁴In the following, we will indicate the internal energy per unit mass with $\varepsilon = e/\rho$.

The passive transport (advection) for any given scalar field, $\psi(\vec{x}, t)$, in a velocity field \vec{v} can be evaluated with the advection equation

$$\partial_t \psi + \vec{\nabla} \cdot (\psi \vec{v}) = 0, \quad (1.4)$$

which is a nonlinear hyperbolic differential equation of the first order with its general solution being wave functions of the form

$$\psi(\vec{x}, t) = \psi_0(\vec{x} - \vec{v}t).$$

The scalar field ψ can be any conserved, extensive quantity, e.g., advection of enthalpy (heat), and the fluids motions are described with the velocity vector field, \vec{v} . The advection equation is equivalent to the more fundamental Gauss's theorem (divergence theorem)

$$\int_V \partial_t \psi dV = \oint_S \vec{\nabla} \cdot f dS,$$

which states that the temporal change of ψ in the volume V is equal to the flux, f , through its enclosed surface $S = \partial V$ in the infinitesimal limit. In other words, the scalar fields follows its conservation law. Then, by considering the conservation of mass-, momentum-, and energy-density one yields the standard Euler equations. Furthermore, the differential forms in Eqs. 1.2 and 1.3 are derived from the standard Euler equations by subtracting the velocity times the mass conservation (Eq. 1.5) from the momentum equation (Eq. 1.2), and subtracting the velocity times the momentum equation from the energy equation (1.3). The (classical) fluid dynamics are described by a coupled system of five⁵ non-linear hyperbolic partial differential equations of the first order, which determine the source and sink terms that give rise to the temporal variations in density, momentum and internal energy. Due to their so-called conservation form, their physical origins can be then identified conveniently.

In the quasi-stationary state, the time derivatives of a given variable X vanishes in the hydrodynamic equations, $\partial_t X = 0$. Furthermore, applying the temporal and spatial averaging operator, denoted by $\langle \dots \rangle$, gives us the mean field hydrodynamic equations, where the only remaining spatial dependence is the vertical one, $X(z)$, and the divergence terms thus reduce to vertical derivatives, i.e., $\vec{\nabla} \cdot \langle X \rangle = \partial_z \langle X \rangle$.

For stellar surface convection we consider compressible fluids to properly account for the highly stratified layers in stellar atmospheres (for incompressible fluids is $\vec{\nabla} \cdot \rho = 0$). The mass conservation, also referred as continuity equation (Eq. 1.5), determines the expansion or compression of the advected stellar plasma. When one considers the stationary continuity equation (anelastic approximation, $\partial_t \rho = 0$), then the right hand side of Eq. 1.5 can be written as

$$v_z \partial_z \ln \rho \approx -\partial_x v_x - \partial_y v_y - \partial_z v_z, \quad (1.5)$$

which states that for an ascending (descending) fluid parcel, the decrease (increase) of the density $\ln \rho$ is balanced by lateral and vertical expansion (compression), which results in an acceleration (deceleration). The main expansion or compression will take place in the horizontal direction, and the horizontal density gradients can be neglected, since the atmosphere is vertically stratified.

The momentum equations, also referred as the Navier Stokes equations, are the equations of motions, therefore, the hydrodynamic equivalent to the Newton's second law of motion. The first term in the right hand side of the i th component of Eq. 1.2 contains the divergence of the dyadic (tensor) product⁶ from the velocity field, $\partial_j (\rho v_j v_i)$. The second one is the viscous stress tensor

$$\tau_{ij} = \eta_j \rho \partial_j v_i \quad (1.6)$$

with η_j the viscosity and $\partial_j v_i$ the strain tensor, and τ_{ij} amounts the diffusion of the velocity field. One can also express the viscous stress tensor with

$$s_{ij} = \frac{1}{2} (\partial_j v_i + \partial_i v_j)$$

⁵Two scalar (Eqs. 1.5 and 1.3) and three vector equations (Eq. 1.2).

⁶Here we make use of the Einstein summation convention.

being the symmetric part of the strain tensor. The other ones being the gradient of the thermal pressure and the external force being the gravitational downward acceleration due to buoyancy; and $\vec{g} = -\vec{\nabla}\Phi$ with the gravitational potential Φ . The gravitational acceleration contains only the vertical direction, and at the vicinity of the stellar surface, one can assume it being constant with depth. Furthermore, the buoyancy force is acting only the density fluctuations, i.e. $f_b = \rho' g_z$. The over-dense regions will experience a negative buoyancy force, thereby pulling the heat depleted cool gas downwards, while the under-dense ones will gain positive buoyant acceleration. The buoyancy term is mediating the convective motions, therefore, this term is essential for the occurrence of convection.

The stationary mean field equation for the momentum takes

$$0 = -\left\langle \vec{\nabla} \cdot (\rho \vec{v}\vec{v} + \underline{\underline{\tau}}) \right\rangle - \left\langle \vec{\nabla} p_{\text{th}} \right\rangle + \langle \rho, \vec{g} \rangle, \quad (1.7)$$

and the first (inertial) term reduces to turbulent pressure $p_{\text{turb}} = \rho v_z^2$; we therefore obtain $\left\langle \vec{\nabla} \cdot (\rho \vec{v}\vec{v}) \right\rangle = \partial_z \langle p_{\text{turb}} \rangle$. The divergence of the viscous stress tensor, $\vec{\nabla} \cdot \underline{\underline{\tau}}$, vanishes on average. The last two terms yield $\partial_z \langle p_{\text{th}} \rangle$ and $\langle \rho g \rangle$, and we retrieve the equation for hydrodynamic equilibrium with

$$\partial_z (\langle p_{\text{turb}} \rangle + \langle p_{\text{th}} \rangle) = -\langle \rho \rangle g, \quad (1.8)$$

which is identical to the equation for hydrostatic equilibrium. The latter states how much mass weight a certain pressure stratification can support against its directed downwards gravitational force. We remark that the hydrodynamic equilibrium is only fulfilled on the temporal average.

The kinetic energy equation can be derived by taking the scalar product of the velocity with the momentum equation (Eq. 1.2), i.e.

$$\partial_t e_{\text{kin}} = -\vec{\nabla} \cdot (e_{\text{kin}} \vec{v} + \underline{\underline{\tau}} \cdot \vec{v}) - \vec{v} \cdot (\vec{\nabla} p_{\text{th}}) + \rho \vec{v} \cdot \vec{g}.$$

Then one can obtain that the variation of the kinetic energy, $e_{\text{kin}} = \rho \vec{v}^2$, is given by the divergence of the kinetic energy flux, the viscous dissipation, the work performed by the thermodynamic pressure gradient force and the work by the gravity force. The latter is also referred as the buoyancy work, however, only the fluctuations of the density and vertical velocity are contributing, i.e. $W_b = \rho' v_z g_z$. Also, we can see now that the buoyancy force is entering the energy balance through the kinetic energy equation.

The (internal) energy equation (Eq. 1.3) contains the divergence of the internal energy flux, $\vec{\nabla} \cdot (e\vec{v})$. Furthermore, the second term, $p_{\text{th}} \vec{\nabla} \cdot \vec{v}$, determines the adiabatic heating (cooling) due to compression (expansion) of the stellar plasma, and is the $p dV$ -work. The third term is the cooling and heating rates due to radiative losses, which we discuss closer in Sec. 1.2.2. Another channel for internal energy losses or yields is the viscous dissipation rate

$$q_{\text{visc}} = \tau_{ij} \partial_j v_i. \quad (1.9)$$

The total energy is defined with $e_{\text{tot}} = e + \vec{v}^2/2$ and by adding the kinetic energy to the internal energy equation (Eq. 1.3) we retrieve the total energy equation with

$$\partial_t e_{\text{tot}} = -\vec{\nabla} \cdot \left(e + p_{\text{th}} + \rho \vec{u}^2/2 + \underline{\underline{\tau}} \right) \vec{v} + q_{\text{rad}}. \quad (1.10)$$

The first two terms amount the divergence of the enthalpy flux $\vec{F}_{\text{enth}} = (e + p_{\text{th}}/\rho) \rho \vec{v}$, the third the kinetic energy flux $\vec{F}_{\text{kin}} = \vec{v}^2/2 \rho \vec{v}$, the fourth the the viscous flux $\vec{F}_{\text{visc}} = \tau_{ij} \cdot \vec{v}$, and, the finally the radiative energy flux \vec{F}_{rad} . Then, we immediately overview all source and sink terms for the total energy with

$$\partial_t e_{\text{tot}} = -\vec{\nabla} \cdot \left(\vec{F}_{\text{enth}} + \vec{F}_{\text{kin}} + \vec{F}_{\text{rad}} + \vec{F}_{\text{visc}} \right). \quad (1.11)$$

We note that the divergence of the sum of the energy fluxes is zero for the quasi-stationary state, which is the equivalent to the conservation of the total energy, $\partial_t e_{\text{tot}} = 0$. The variation in one value is transformed into another one, e.g., enthalpy flux into radiative flux.

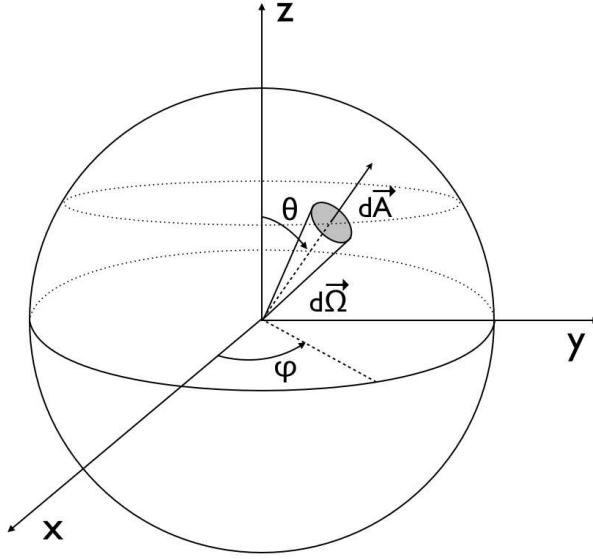


Figure 1.3: The solid angle $d\vec{\Omega}$ in spherical polar coordinates, illustrating the direction of the specific intensity radiate.

The thermodynamic pressure, p_{th} , is the sum of the gas and radiation pressure, i.e.

$$p_{\text{th}} = p_{\text{gas}} + p_{\text{rad}}, \quad (1.12)$$

while the total pressure is defined as the sum of thermodynamic and turbulent pressure, i.e.

$$p_{\text{tot}} = p_{\text{th}} + p_{\text{turb}}. \quad (1.13)$$

We emphasize that it is vital to choose a clear notation, since the turbulent pressure is neglected in 1D calculations, however, in the superadiabatic region its influence can become substantial.

1.2.2 Radiative transfer

The radiative transfer equation describes the interaction between the radiation field and the matter, which we want to discuss in the following. When we consider the energy dE_{λ} irradiated through the surface dA in the direction $d\vec{\Omega}$ (see Fig. 1.3) in the time interval dt in the wavelength range $d\lambda$, then we can amount the specific radiative intensity, I_{λ} , or surface brightness with

$$dE_{\lambda} = I_{\lambda} (\cos \theta) \cos \theta dA d\vec{\Omega} d\lambda dt, \quad (1.14)$$

which is the macroscopic quantity for the evaluation of the radiative losses. The total (bolometric) intensity is the specific monochromatic intensity integrated over all wavelength, $I = \int I_{\lambda} d\lambda$.

The coupling of radiative energy flux is taking place in the internal energy equation (Eq. 1.3), where the radiative heating and cooling rates serve as a source or drain for the energy. The radiative heating and cooling rate is the divergence of the radiative energy flux, i.e.

$$q_{\text{rad}} = -\vec{\nabla} \cdot \vec{F}_{\text{rad}}, \quad (1.15)$$

while the radiative flux is evaluated with

$$\vec{F}_{\text{rad}}(\vec{r}, \vec{n}, t) = \int_{\lambda} \int_{\Omega} I_{\lambda}(\vec{r}, \vec{\Omega}, t) \vec{\Omega} d\vec{\Omega} d\lambda,$$

where I_λ is the monochromatic radiative intensity (Eq. 1.14) at the wavelength λ emitted in the direction $\vec{\Omega}$ from the location \vec{r} . The radiative intensity is determined with the radiative transfer equation

$$\hat{n} \cdot \vec{\nabla} I_\lambda(\vec{s}) = \rho \kappa_\lambda (S_\lambda - I_\lambda) \quad (1.16)$$

with \vec{s} being the light path, κ_λ the monochromatic opacity, and, S_λ the radiative source function. The radiative transfer equation states that when the radiative intensity is lower than the the source function, cooling is taking place, in particular, in the optical surface layers, where the opacities decrease and the radiation can escape. The source function is given by

$$S_\lambda = \frac{j_\lambda}{\alpha_\lambda}, \quad (1.17)$$

with j_λ being the emission coefficient and the α_λ extinction coefficient. The extinction the coefficients are derived from the continuous bound-free and the discrete bound-bound atomic transitions, and is given by

$$\alpha_\lambda = \sigma_\lambda n,$$

where σ_λ are the atomic cross-section and n the number density of the atoms. To simplify the calculations one make often the use of the assumption of the local thermodynamic equilibrium (LTE). Then, due to the frequent collisions between the atoms, ions and electrons, thermodynamic equilibrium is established, and the atomic level populations can be determined by the local kinetic temperature, T , alone without considering the influence of the radiation field through scattering. Therefore, under assumption of LTE the non-local effects of scattering are expected to be negligible in the excitation-ionization equilibrium for the atomic level populations. One determines the (kinetic) velocity distribution with the Maxwell distribution

$$n(v) dv = \left(\frac{m}{2\pi kT} \right)^{1/2} 4\pi v^2 \exp[-mv^2/(2kT)] dv, \quad (1.18)$$

with v being the velocity, m the mass of the particle, and, k the Boltzmann constant. Furthermore, the excitation between energy levels i and j are calculated with the Boltzmann distribution

$$\frac{n_{r,i}}{n_{r,j}} = \frac{g_{r,i}}{g_{r,j}} \exp[-(\chi_{r,i} - \chi_{r,j})/kT], \quad (1.19)$$

with $n_{r,i}$ the i th level population in the ionization stage r , g_i the statistical weight of level i , and $\chi_{r,i}$ the excitation energy. And the ionization state r is determined with the Saha distribution

$$\frac{n_{r+1,1}}{n_{r,1}} = \frac{1}{n_e} \frac{2g_{r+1,1}}{g_{r,1}} \left(\frac{2\pi m_e kT}{h^2} \right)^{3/2} \exp[-\chi_r/kT], \quad (1.20)$$

with n_e the number density free electrons, m_e the mass of electrons, h the Planck constant, χ_r ionization energy. Then, under the assumption of strong LTE the source function (Eq. 1.17) can be approximated with

$$S_\lambda = B_\lambda(T), \quad (1.21)$$

i.e. the source function is equal to the Planck function

$$B_\lambda(T) = \frac{2hc^2}{\lambda^5} \frac{1}{e^{\frac{hc}{\lambda kT}} - 1}. \quad (1.22)$$

Usually the radiative transfer equation is evaluated instead of the geometrical depth on optical depth

$$\frac{dI_\lambda}{d\tau_\lambda} = I_\lambda - S_\lambda \quad (1.23)$$

with

$$\tau_\lambda = \int \rho \kappa_\lambda ds, \quad (1.24)$$

which denotes the monochromatic optical depth along the geometrical path ds . Furthermore, it is more convenient to express the radiative intensity with monochromatic mean intensity averaged over the entire solid angle

$$J_\lambda = 1/4\pi \int_{\Omega} I_\lambda d\Omega, \quad (1.25)$$

then the radiative heating and cooling rate can be expressed with

$$q_{\text{rad}} = 4\pi\rho \int_{\lambda} \kappa_\lambda (J_\lambda - S_\lambda) d\lambda. \quad (1.26)$$

The radiative cooling and heating is mainly taking place in the thin photospheric transition region that is located at the optical surface. For more details we refer to Gray (2005).

Chapter 2

Methods

In this Chapter I will overview the details of the STAGGER-code (Sect. 2.1), and elucidate the methods, which I have developed and applied to compute the 3D atmosphere simulations for the present work (Sect. 2.2). Furthermore, I will explain my methods to compute the different temporal and spatial averages (Sect. 2.3), and the details of the 1D atmosphere code that is used to compute the 1D STAGGER-grid models (Sect. 2.4). For the reader who is more interested in the results and applications, instead of the technical details, this Chapter can be safely skipped. Furthermore, I want to remark that this Chapter mostly originates from two already published works (Magic et al., 2013a,b).

2.1 Multi-dimensional atmosphere modeling

The 3D model atmospheres presented here were constructed with a custom version of the STAGGER-code, a state-of-the-art, multipurpose, radiative-magnetohydrodynamics (R-MHD) code originally developed by Nordlund & Galsgaard (1995), and continuously improved over the years by its user community. In pure radiation-hydrodynamics mode, the STAGGER-code solves the time-dependent hydrodynamic equations for the conservation of mass (Eq. 1.1), momentum (Eq. 1.2), and energy (Eq. 1.3) in a compressible flow coupled to the radiation field via the heating and cooling (per unit volume) term, which is computed from the solution of the radiative transfer equation to account properly for the energy exchange between matter and radiation. We have ignored magnetic fields in the present grid of 3D convection simulations.

2.1.1 Details on the numerics

The STAGGER-code uses a sixth-order explicit finite-difference scheme for numerical derivatives and the corresponding fifth-order interpolation scheme. The solution of the hydrodynamic equations is advanced in time using an explicit third-order Runge-Kutta integration method (Williamson, 1980). The code operates on a staggered, Eulerian, rectangular mesh: the thermodynamic variables, density and internal energy per volume, are cell-centered, while momentum components are defined at cell faces. Also, in the MHD mode, the components of the magnetic field B (electric field E) are defined at the cell faces (edges). In Fig. 2.1, we show the locations within an individual cell. This configuration allows for a flux-conservative formulation of the magnetohydrodynamic equations, at the same time ensuring that the magnetic field remains divergence-free. The solution of the discretized equations is stabilized by hyperviscosity¹ which aims at minimizing the impact of numerical diffusion on the simulated flow, while providing the necessary diffusion for large-eddy simulations with finite-difference schemes (see also Nordlund & Galsgaard 1995 for further details). The values of the numerical viscosity parameters² are empirically tuned with test cases like the shock tube: they are set large enough to stabilize the numerical solution of the hydrodynamic

¹Hyperviscosity is a numerical viscosity that removes the short wavelength noise without damping the longer wavelength (see Stein & Nordlund, 1998, for more details).

²To provide stabilization and a weak dispersion of linear waves we used $n_1 = 0.005$ that should be low, and for enhanced dissipation in shocks we used $n_2 = 0.8$, which should be around unity (see Eq. 9 in Kritsuk et al., 2011).

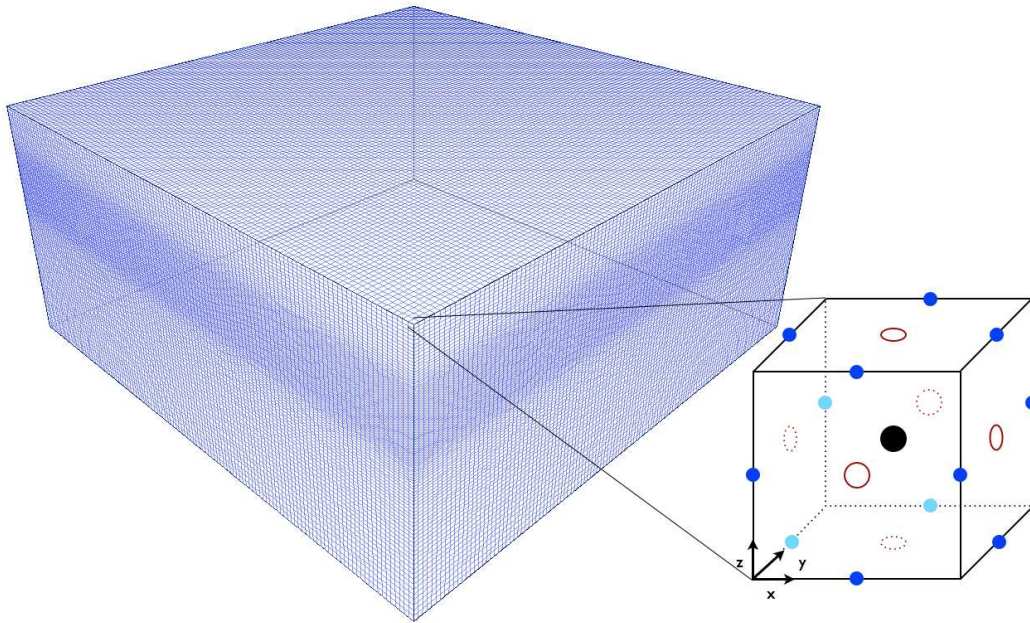


Figure 2.1: Eulerian mesh of the solar simulation with the geometrical extent of $8 \times 8 \times 4$ Mm (large blue rectangular box). Notice the equidistant horizontal spacing, while the vertical one is resolving the photosphere enhanced. Furthermore, we illustrate also an enlarged view of an individual cell (small box). Scalar values (ρ , ϵ) are defined at the cell center (black dot), while the vectorial momentum and magnetic fields are located at the cell faces (red circles), and the electric field at the cell edges (blue dots).

equations and, at the same time, kept small enough to reduce their smoothing of the flow's structures. The same optimized values of the parameters are then applied to all other simulations in the grid.

The version of the STAGGER-code we used for this work is fully MPI-parallel. The parallelization scales well with the number of cores. For this project, the simulations were typically run on 64 cores.

2.1.2 Geometrical properties

The setup of the simulations is of the so-called *box-in-a-star* type: the domain of the simulations is limited to a small representative volume located around the stellar photosphere and including the top portion of the stellar convective envelope. The boundary conditions of the simulation box are periodic in the horizontal directions and open vertically. In Fig. 2.1 we illustrate the numerical mesh of the solar simulation (notice the non-equidistant vertical resolution). Gravity³ is assumed to be horizontally and vertically constant over the whole extent of the box, i.e. $\vec{g}(x, y, z) = (0, 0, g)$, neglecting sphericity effects. However, since the size of the simulation domains correspond to only a fraction of the total radii of the stars (0.4% of the solar radius for the solar simulation, and $\sim 10\%$ for a typical red giant simulation with $\log g = 1.5$) such effects can be regarded as small for the purposes of the current grid of models. Also, for simplicity, the effects of stellar rotation and associated Coriolis forces⁴ are neglected in the present simulation setup, as it would add two more dimensions to the grid.

At the bottom, the inflowing material has a constant value of specific entropy per unit mass, which ultimately determines the emerging effective temperature. While the domains of our simulations cover only a small fraction of the convective zone, the box-in-a-star setup is still valid because the bulk up-flows at the bottom boundary of the simulations carry essentially the same entropy value as in deeper layers and are mostly unaffected by entrainment with cooler downflows. At the beginning of each simulation, the

³The surface gravity, $\log g$, is the external force term in the momentum equation (see Eq. 1.2).

⁴F-plane rotation is included in large super-granulation simulations of the Sun (see Stein et al., 2006, 2009).

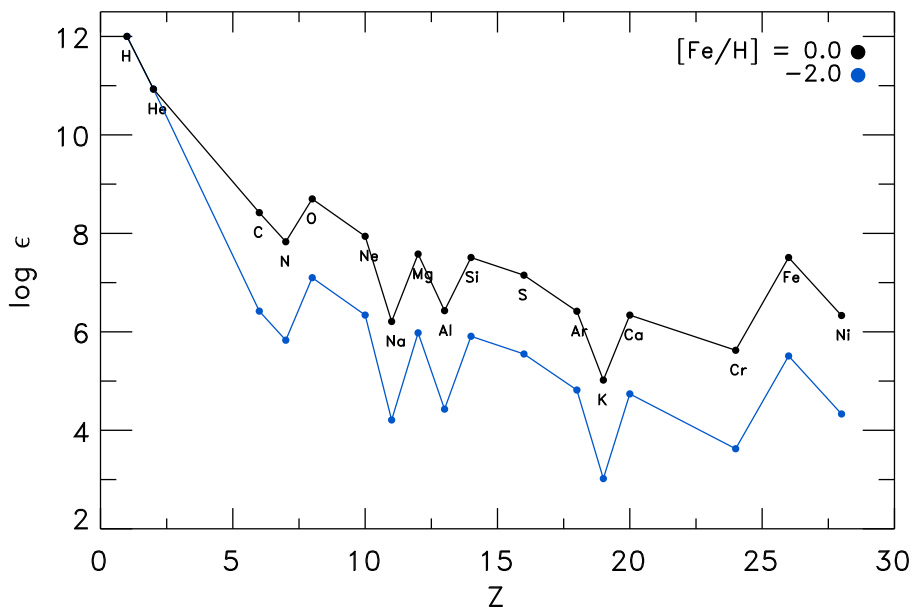


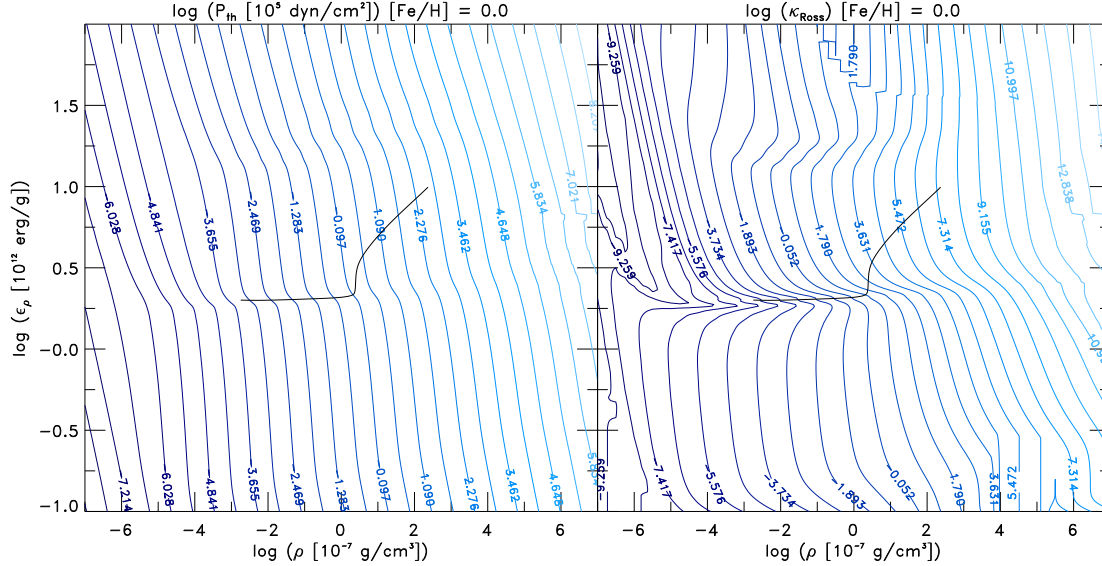
Figure 2.2: Solar abundances by AGS09 vs. the atomic number (black). A metal-poor chemical composition is also shown (blue).

entropy of the inflowing gas at the bottom is adjusted in order to yield the desired T_{eff} and, after that, is kept unchanged during the entire run (see Sect. 2.2.2). Furthermore, pressure is assumed to be horizontally constant over the whole bottom layer.

The physical dimensions in the horizontal directions are chosen to be large enough to cover an area corresponding to about ten granular cells. The vertical dimensions are extended enough for the simulations to cover at least the range of $-5.0 < \log \tau_{\text{Ross}} < +6.0$ in terms of Rosseland optical depth (in fact, they range on average from $-7.3 < \log \tau_{\text{Ross}} < +7.5$), which typically corresponds to approximately six orders of magnitude in pressure (about 14 pressure scale heights). In each simulation the Rosseland optical depth $\log \tau_{\text{Ross}} = 5.0$ refers to a different vertical geometrical depth compared to the other simulations, therefore, the contained mass will be also different for different stellar parameters, in particular, for lower surface gravity the mass is increasing, e.g., a simulation box with $\log g = 4.5/2.0$ will contain $10^7/10^{13}$ g in the region $0.0 < \log \tau_{\text{Ross}} < 5.0$. All of the simulations have a mesh resolution of 240^3 , since a resolution of about $200^3 - 250^3$ was found to be adequate to reproduce solar iron line profiles accurately (see Asplund et al., 2000a). Five layers at the bottom and the top in all simulations are reserved for the so-called *ghost-zones*: these extra layers serve to enforce boundary conditions for the high-order derivatives in the vertical direction. The spacing between cells in the horizontal direction ($\Delta x, \Delta y$) is constant, ranging from about 6 km in dwarfs to about 25 Mm in giants, while it varies smoothly with depth in the vertical direction, in order to resolve the steep temperature gradients near the optical surface. These are the layers from where the continuum radiation escapes; they are characterized by a sharp transition between stellar interior and outer layers in terms of thermodynamic quantities such as temperature, internal energy, and entropy that marks the beginning of the photosphere. Also, the steepest temperature gradients are found in the superadiabatic region just below the optical surface ($0.0 < \log \tau_{\text{Ross}} < 2.0$). Therefore, it is very important that the thin transition layer around the optical surface is well-resolved in order to ensure an accurate modeling of the radiative transfer and to avoid spurious numerical artifacts from insufficient spatial resolution (see Figs. 2.1 and 2.5).

2.1.3 Equation of state

We use the realistic equation of state (EOS) by Mihalas et al. (1988), which explicitly treats excitation to all bound states of all ionization stages, of all included elements. We have custom computed tables for a mix of the 17 most abundant elements (H, He, C, N, O, Ne, Na, Mg, Al, Si, S, Ar, K, Ca, Cr, Fe and Ni; see



grid point on long characteristics, along the vertical direction and along eight additional inclined angles (two $\mu = \cos \theta$ and four φ -angles) by tilting the (domain-decomposed⁸) 3D cube. Given the opacity κ_λ and the source function S_λ , the monochromatic intensity I_λ can be obtained by solving Eq. (1.23) and the radiative heating and cooling rate computed by integrating $\rho \kappa_\lambda (I_\lambda - S_\lambda)$ over solid angle and wavelength. We use the Radau quadrature to determine the optimal ray directions to approximate the angular integral in the calculation of the radiative heating and cooling rate as a weighted sum. For the radiative transfer calculations, we employ opacities as described above (Sect. 2.1.4).

Computing the full monochromatic solution to the radiative transfer equation in 3D at each time step is extremely expensive. The cost of the radiative transfer calculations however can be reduced enormously by opting instead for an approximated solution based on the *opacity binning* or *multi-group* method (Nordlund, 1982; Skartlien, 2000). Following this method, we sort all sampled wavelength points into different bins based on the spectral range they belong to and on their associated *opacity strength* or, better, their *formation depth*, i.e. the Rosseland optical depth τ_{Ross} ($\tau_\lambda = 1$), where the monochromatic optical depth equals unity. In this way, wavelength points characterized by similar formation heights and belonging to the same spectral interval are grouped together (see Fig. 2.6). For each simulation, we use the 1D temporal and spatial mean stratification to estimate the formation heights of the various wavelengths and sort the wavelengths into the different opacity bins. The bin selection and wavelength sorting process is performed twice during the simulation's relaxation phase after updating the individual mean stratifications, but is kept unchanged during the production runs.

To each bin, we assign a mean opacity κ_i which accounts for the contribution from both continuum and line opacities. To compute the mean opacities, we differentiate between diffusion and free-streaming limits, i.e. between the optical thick and optical thin regimes, below and above the photospheric transition zone, respectively. The mean bin-opacity κ_i is calculated as a Rosseland-like average

$$\kappa_{\text{Ross},i} = \int_{\lambda(i)} \frac{dB_\lambda}{dT} d\lambda \Big/ \int_{\lambda(i)} \frac{1}{\kappa_\lambda} \frac{dB_\lambda}{dT} d\lambda \quad (2.1)$$

in the optical thick regime, and as a mean-intensity-weighted mean opacity

$$\kappa_{J,i} = \int_{\lambda(i)} \kappa_\lambda J_\lambda d\lambda \Big/ \int_{\lambda(i)} J_\lambda d\lambda \quad (2.2)$$

in the optical thin regime, where $\lambda(i)$ is the set of wavelength points assigned to bin i . For bin i , the transition from one regime to the other around that bins optical surface is achieved by means of an exponential bridging of the two averages:

$$\kappa_i = e^{-2\tau_{\text{Ross},i}} \kappa_{J,i} + (1 - e^{-2\tau_{\text{Ross},i}}) \kappa_{\text{Ross},i}. \quad (2.3)$$

All simulations presented here have been run with the radiative transfer in the strict LTE approximation, i.e. under the assumption that the monochromatic source function S_λ (in Eq. 1.26) is the Planck function at the local gas temperature, i.e. $S_\lambda(T) = B_\lambda(T)$. For each bin i , we compute an integrated source function by summing up the contributions from all wavelength points in the bin;

$$S_i = B_i = \int_{\lambda(i)} B_\lambda d\lambda \quad (2.4)$$

Collet et al. (2011) showed that, with this opacity binning implementation, the approximation of strict LTE results in a temperature stratification is very similar to the case, where scattering is properly treated, as long as the contribution of scattering to the extinction is *excluded* when averaging the mean opacities $\kappa_{J,i}$ (Eq. 2.2) in the optically thin layers ("free streaming-regime"), but *include* it as true absorption when averaging the mean opacities $\kappa_{\text{Ross},i}$ (Eq. 2.1) in the optically thick layers ("diffusion approximation regime."). They also showed that including scattering as true absorption leads to erroneous atmosphere structures due to overestimated radiative heating in the optically thin layers. However, these findings have so far being verified for only a small sample of stellar parameters, therefore we cannot rule out that scattering

⁸For the parallel-computation of a 3D RHD simulation, the numerical box is evenly split into smaller computational subdomains for the individual CPUs.

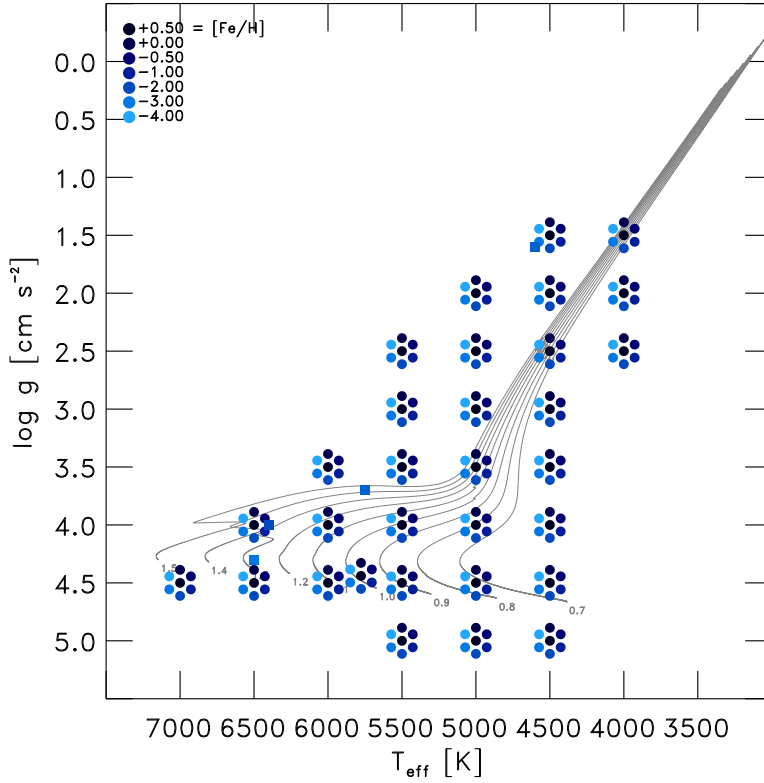


Figure 2.4: Kiel diagram ($T_{\text{eff}} - \log g$ diagram) showing the targeted STAGGER-grid parameters for the 217 models, comprising seven different metallicities (colored circles). Four additional standard stars (see text) are also indicated (squares). In the background, the evolutionary tracks for stellar masses from 0.7 to $1.5 M_{\odot}$ and for solar metallicity are shown (thin grey lines).

needs to be accounted for properly in certain cases. Nonetheless, evaluating the radiative transfer in strict LTE greatly eases the computational burden compared to the case, where the contribution of scattering is included to the total extinction (Hayek et al., 2010).

The radiative transfer equation is solved for the individual opacity bins (Eq. 1.16) for all layers that have $\max(\tau_{\text{Ross}}) < 300$, while in the deeper layers, we use instead the diffusion approximation, which is fulfilled to a high degree at such depths. With the opacity binning approximation, the radiative heating rate term (Eq. 1.26) takes then the form

$$q_{\text{rad}} = 4\pi\rho \sum_i \kappa_i (J_i - B_i) \quad (2.5)$$

where J_i is the mean intensity computed from the solution of the radiative transfer equation for bin i .

For the relaxation phase of the simulation runs, we considered six bins, while for the final models we used twelve opacity bins. We have developed an algorithm for the bin selection, which will be explained further below (see Sect. 2.2.4). Towards lower surface gravities ($\log g \lesssim 2.0$) and higher effective temperatures, numerical artifacts in the radiative transfer can occasionally develop and manifest as a Moiré pattern in the integrated outgoing intensities due to very steep temperature gradients in the photosphere. For those situations, we solve the radiative transfer equation on an adaptive mesh with finer vertical resolution, which is dynamically optimized to resolve regions where temperature gradients are steeper. The radiative heating and cooling rates computed on the adaptive mesh are then interpolated back to the coarser hydrodynamic depth scale under the consideration of energy conservation.

2.2 STAGGER-grid models

2.2.1 Stellar Parameters

The STAGGER-grid covers a broad range in stellar parameters with 217 models in total. The range in effective temperature is from $T_{\text{eff}} = 4000\text{K}$ to 7000K in steps of 500K , while the gravity ranges from $\log g = 1.5$ to 5.0 in steps of 0.5 . The grid also covers a broad range in metallicity starting from $[\text{Fe}/\text{H}] = -4.0$ to $+0.5$ in steps of 1.0 below -1.0 , and steps of 0.5 above that⁹. We decided to apply the same parameters T_{eff} and $\log g$ for all metallicities, in order to facilitate the interpolation of (averaged) models within a regular grid in stellar parameters. In addition, the grid also includes the Sun with its non-solar metallicity analogs, and four additional standard stars, namely HD 84937, HD 140283, HD 122563 and G 64-12 that are presented in Bergemann et al. (2012). For metal-poor chemical compositions with $[\text{Fe}/\text{H}] \leq -1.0$, we applied an α -enhancement of $[\alpha/\text{Fe}] = +0.4\text{dex}$, in order to account for the enrichment by core-collapse supernovae (e.g. Tinsley, 1979; Rana, 1991).

In Figure 2.4, we present an overview of our simulations in stellar parameter space. Therein, we also show evolutionary tracks (Weiss & Schlattl, 2008) for stars with masses from 0.7 to $1.5 M_{\odot}$ and solar metallicity, in order to justify our choice of targeted stellar parameters. Hence, the grid covers the evolutionary phases from the main-sequence (MS) over the turnoff (TO) up to the red-giant branch (RGB) for low-mass stars. In addition, the RGB part of the diagram in practice also covers stars with higher masses, since these are characterized by similar stellar atmospheric parameters.

2.2.2 Scaling and relaxing 3D models

Generating large numbers of 1D atmosphere models is relatively cheap in terms of computational costs, but the same is not true for 3D models. Based on our experiences from previous simulations of individual stars, we designed a standard work-flow of procedures for generating our grid. More specifically, we developed a large set of IDL-tools¹⁰ incorporating the various necessary steps for generating new 3D models, which we then applied equally to all simulations. The steps are:

- Scale the starting model from an existing, relaxed 3D simulation, and perform an initial run with six opacity bins, so that the model can adjust to the new stellar parameters.
- Check the temporal variation of T_{eff} and estimate the number of convective cells. If necessary, adjust the horizontal sizes, in order to ensure that the simulation box is large enough to enclose at least ten granules.
- If the optical surface has shifted upwards during the relaxation, add new layers at the top of it to ensure that $\langle \log \tau_{\text{Ross}} \rangle_{\text{top}} < -6.0$.
- Determine the period π_0 of the radial p-mode¹¹ with the largest amplitude, then damp these modes with an artificial exponential-friction term with period π_0 in the momentum equation (Eq. 1.2).
- Let the natural oscillation mode of the simulation emerge again by decreasing the damping stepwise before switching it off completely.
- Re-compute the opacity tables with 12 bins for the relaxed simulation.
- Evolve the simulations for at least ~ 7 periods of the fundamental p-mode, roughly corresponding to ~ 2 convective turnover times. This corresponds typically to a few thousand time-steps, of which 100 – 150 snapshots equally spaced were stored and used for analysis.

⁹We use the bracket notation $[X/\text{H}] = \log(N_X/N_{\text{H}})_{\star} - \log(N_X/N_{\text{H}})_{\odot}$ as a measure of the relative stellar to solar abundance (Asplund et al., 2009) of element X with respect to hydrogen.

¹⁰The Interactive Data Language (IDL) is a data analysis software that is developed and licensed by ITT-VIS.

¹¹The p-modes in the simulation box are determined by the center of mass velocity variations, i.e. $v_{z,\text{cm}} = \langle \rho v_z \rangle / \langle \rho \rangle$.

During these steps the main quantities of interest are the time evolution of effective temperature, p-mode oscillations, and drifts in the values of the mean energy per unit mass and of the mean density at the bottom boundary, which indicate the level of relaxation. When the drifts in these above properties stop, we regard the simulation as relaxed. If these conditions were not fulfilled, we continued running the model, to give the simulation more time to properly adjust towards its new quasi-stationary equilibrium state. Also, when the resulting effective temperature of an otherwise relaxed simulation deviated more than 100 K from the targeted T_{eff} , we re-scaled the simulation to the targeted value of T_{eff} and started over from the top of our list of relaxation steps.

The interplay between EOS, opacities, radiative transfer and convection can shift the new location of the photosphere, when the initial guess made by our scaling procedure slightly misses it. This is the case for a few red giant models leading to upwards-shifts of the optical surface and of the entire upper atmosphere during the adjustment phase after the scaling, with the average Rosseland optical depth ending up to be larger than required, i.e. $\langle \log \tau_{\text{Ross}} \rangle_{\text{top}} \geq -6.0$. In order to rectify this, we extended those simulations at the top by adding extra layers on the top, until the top layers fulfilled our requirements of $\langle \log \tau_{\text{Ross}} \rangle_{\text{top}} < -6.0$.

2.2.3 Scaling the initial models

To start a new simulation, we scale an existing one with parameters close to the targeted ones, preferably proceeding along lines of constant entropy of the inflowing gas at the bottom in stellar parameter space (see Fig. 3.2). In this way, we find that the relaxation process is much faster. In order to generate an initial model for a set of targeted parameters, we scale temperature, density, and pressure with depth-dependent scaling ratios derived from two 1D models, with parameters corresponding to the current and intended 3D model (Ludwig et al., 2009a). For this, we used specifically computed 1D envelope models (MARCS models taken from Gustafsson et al. (2008) or our own 1D models, see Sect. 3.3.1), which extend to $\log \tau_{\text{Ross}} > 4.0$. The reference depth-scale for all models in the scaling process is the Rosseland optical depth above the photosphere and gas pressure normalized to the gas pressure at the optical surface below it ($\log \tau_{\text{Ross}} > 0.0$).

After the initial scaling, we construct the geometrical depth scale z for the new simulation by enforcing the same (quasi-)hydrostatic-equilibrium condition as in the starting simulation, but with the newly scaled pressure and density. The resulting new z -scale is usually not smooth, therefore we generate a new z -scale, which is optimized to resolve the region with the steepest (temperature) gradients, as shown in Fig. 2.5. The density-, energy-, and velocity cubes are then interpolated to this new geometrical depth scale. The new z -scale is constructed using the variation with depth of the (smoothed) maximum of the derivative of the Rosseland absorption coefficient, $\max \langle d \ln \alpha_{\text{Ross}} / dz \rangle$, as a guide. The basic idea behind this approach is to vertically distribute the mesh points as evenly as possible on the optical-depth scale. With such an optimized z -scale we can efficiently resolve the same features with fewer grid-points, compared to an equidistant vertical mesh. Furthermore, a limiting vertical-to-horizontal aspect ratio ($\Delta z / \Delta x$ and $\Delta z / \Delta y$) of 1 : 4 over the whole vertical extent is enforced. We find that this value represents in practice an optimal lower limit to the aspect ratio, with respect to numerical stability and accuracy of the solution of the radiative transfer equation along inclined rays. Finally, the position of the zero-point in the depth scale is adjusted to coincide with the position of the mean optical surface, i.e. $\langle \tau_{\text{Ross}} \rangle_{(z=0)} = 1$.

At fixed surface gravity and metallicity, the mean diameter of the granules, which is used for determining the horizontal extent of the simulation, increases with higher effective temperature (see Figs. 3.11 and Sect. 3.1.6). The number of granules present in the simulation box is retrieved with the aid of the CONTOUR routine in IDL. Based on the map of the temperature below the surface (the vertical velocity would serve equally well), a contour chart of the significantly hotter granules is extracted, from which the number of granules is counted. Concerning the temporal resolution of the simulation sequences of the final production runs, the frequency, at which snapshots are stored, is based on the sound-crossing time of one pressure scale height, H_P , in the photosphere, i.e.

$$\Delta t_{\text{snap}} = \langle H_P / c_s \rangle_{(\tau=2/3)} \quad (2.6)$$

(see Cols. 14 and 15 in Table B.1). With the help of functional fits of the dependence of granule sizes and sound-crossing time scales on stellar parameters, the horizontal sizes of the simulation boxes and the snapshot sampling times can be estimated rather accurately in advance (see App. A).

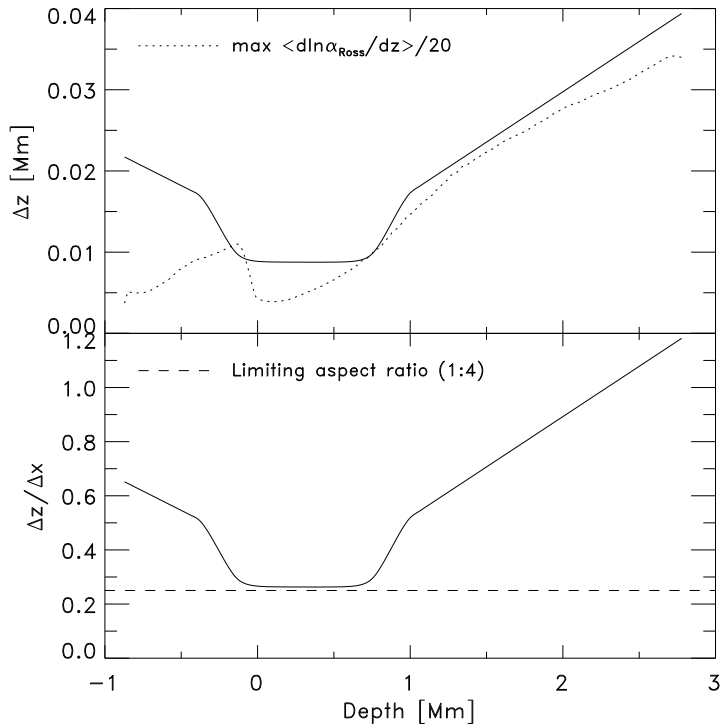


Figure 2.5: In the top panel, we display the non-equidistant vertical spacing Δz of the depth scale as a function of geometrical depth in our solar model (solid line). The z -scale is optimized to resolve the flows and thermal structure, which naturally results in the highest spatial resolution around the photosphere. Furthermore, we also show the maximum of the vertical gradient of the absorption coefficient $\max \langle d \ln \alpha_{\text{Ross}} / dz \rangle$ as a function of depth (dotted line). In the bottom panel, we show the aspect ratio $\Delta z / \Delta x$ (solid line) and we also indicated its lower allowed limit with 1 : 4 (dashed line). The actual vertical-to-horizontal aspect ratio ranges from 0.26 at the photosphere to 1.18 at the bottom of the simulation domain.

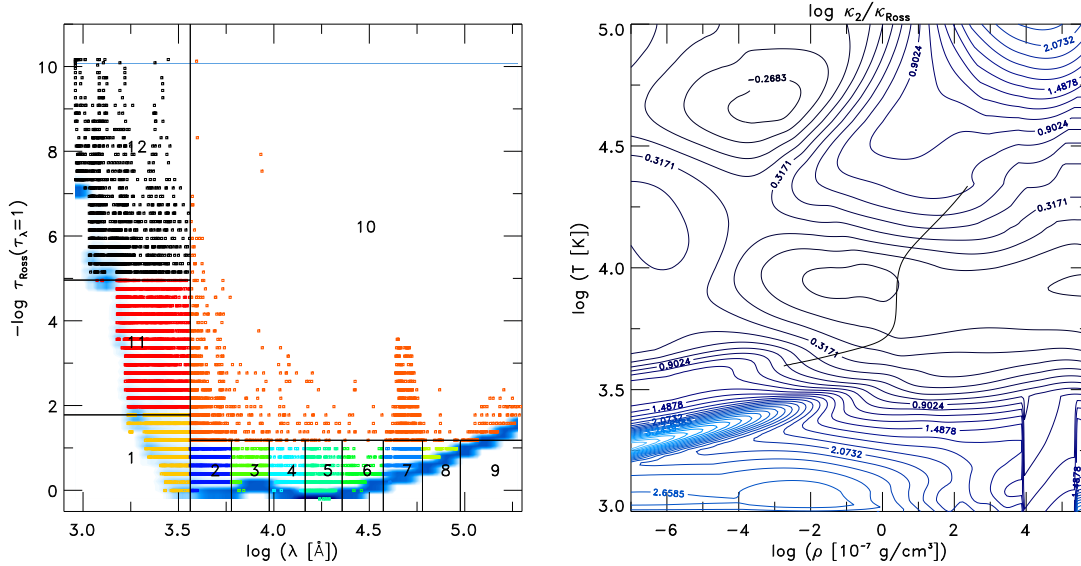


Figure 2.6: *Left figure:* We show the twelve opacity bins selected for the solar simulation by plotting the opacity strength (or, more precisely, the formation height) against wavelength for all sampled wavelength points. The individual bin elements are distinguished by different colors. For clarity, we plotted only a subset of the wavelength points considered for the opacity binning procedure. In the background, we included the smoothed histogram of the opacity strength distribution (blue contour). This shows how the majority of λ -points are mostly concentrated close to the continuum-forming layers and only a smaller fraction contributes to lines. *Right figure:* Isocontours of the relative differences of the opacity for the second bin to the Rosseland opacity in dependence of density and temperature. The solar model is also shown (black line).

2.2.4 Selection of the opacity bins

As we mentioned earlier, in Sect. 2.1.5, the purpose of the opacity-binning approximation is to reproduce the radiative heating and cooling rates as accurately as possible with a small number of opacity-bins, in order to reduce the computational burden. For the assignment of wavelength points to bins, we first compute the opacity strengths for all of the $\gtrsim 10^5$ wavelength points in the opacity-sampling (OS) data from the MARCS package (Gustafsson et al., 2008). The histogram of their distribution as a function of wavelength (see left panel of Fig. 2.6) exhibits a characteristic "L"-shape. Shorter wavelengths (UV) require more bins to resolve the wide range in opacity strength, while the lower part of the L-shaped distribution at longer wavelengths (optical and IR) calls for a better resolution in terms of wavelength. Therefore, we initially make a division in wavelength at λ_X , between the UV and the optical/IR (see boundaries of bin 1, 11 and 12 in the left panel of Fig. 2.6) and comprising approximately an equal number of wavelength points. These two regions are then in turn subdivided evenly into opacity bins according to the number of λ -points. By trial and error, we found that a binning scheme with three bins in the $\lambda < \lambda_X$ region and eight bins for $\lambda > \lambda_X$, one of which being a large one and comprising the stronger lines in the optical and IR (bin number 10 in Fig. 2.6) gives a good representation of the monochromatic radiative heating and cooling. We iterate the bin selection with slight differences (e.g., one additional division in opacity strength for the 8 bins in the lower part of the optical and IR) and by small adjustments, and choose the bin selection with the smallest relative difference between the total heating rates computed with opacity binning q_{bin} and the full monochromatic solution q_λ for the average stratification of the 3D simulation, i.e.

$$\max[\delta q_{\text{bin}}] = \frac{\max |q_{\text{bin}} - q_\lambda|}{\max |q_\lambda|}. \quad (2.7)$$

We found that the individual selection of some of the bins displays a highly non-linear response to small changes. In most cases an even distribution was favored by the minimization. Naturally, our method will

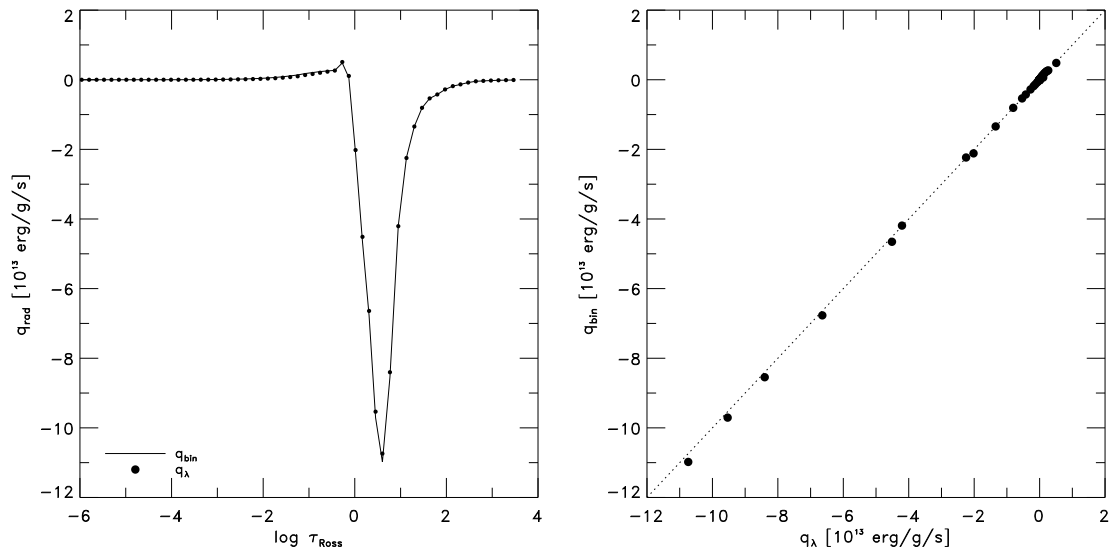


Figure 2.7: Comparison of the radiative heating and cooling resulting from monochromatic computations q_{λ} (filled dots) and the opacity binning method q_{bin} (solid line) for the solar model mean stratification. In the left figure we show both q_{rad} vs. optical depth, while in the right figure, we compare the two against each other.

typically find only a local minimum due to the small sample of iterations instead of a true global minimum. However, our method is a fast, repeatable, and automatic selection of the opacity bins, which minimizes the human effort significantly, while at the same time yielding very satisfactory results. Moreover, the possible deviation from the global minimum due to our automated bin selection and its resulting uncertainties are smaller than the overall uncertainties associated with the opacity binning method. In Fig. 2.6 (right panel), we show also the relative differences of an individual opacity bin to the Rosseland opacity. As one can see the opacity of the bins can be rather distinctive from the Rosseland and can deviate up to 10^3 .

In Fig. 2.7, we compare the resulting radiative heating and cooling rates from the monochromatic calculation against those from the opacity binning solution for the mean stratification of our solar model. The radiative heating and cooling rates from the simplified opacity binning appear rather similar to those from the monochromatic solution, thereby supporting our approach. For the solar model, our algorithm finds a bin selection that is just slightly less accurate ($\max[\delta q_{\text{bin}}] = 2.78\%$) than an optimized manual bin selection (1.86%). Incidentally, with six bins, we get $\max[\delta q_{\text{bin}}] = 3.54\%$. We obtain an average $\max[\delta q_{\text{bin}}]$ for all the grid models of $\max[\delta q_{\text{bin}}] = 2.38\%$, while with six bins we get $\max[\delta q_{\text{bin}}] = 3.0\%$. We find that $\max[\delta q_{\text{bin}}]$ increases slightly with T_{eff} and $[\text{Fe}/\text{H}]$. We note that the opacity binning method with its small number of bins states an approximation for the radiative transfer, therefore, despite the small values for $\max[\delta q_{\text{bin}}]$ further improvement is necessary, e.g., more bins or a new, more efficient binning method.

2.3 Temporal and horizontal averages

We computed various temporal and horizontal averages for a large number of physical quantities of interest. For the spatial (horizontal) averages, we computed (3D) stratifications by considering four different reference depth scales and averaging the various physical quantities on layers of constant

- geometrical height, z ;
- column mass density, $m = \int \rho dz$;
- Rosseland optical depth, $\tau_{\text{Ross}} = \int (\rho \kappa_{\text{Ross}}) dz$;

- optical depth at 500 nm, $\tau_{500} = \int (\rho \kappa_{500}) dz$,

(hereafter denoted by $\langle 3D \rangle_z$, $\langle 3D \rangle_m$, $\langle 3D \rangle_{\text{Ross}}$, and $\langle 3D \rangle_{500}$, respectively), where ρ is the gas density, and κ_{Ross} and κ_{500} are the Rosseland mean opacity¹² and opacity at 500 nm, respectively, both defined as cross-sections per unit mass.

The geometrical averages $\langle 3D \rangle_z$ are easily taken directly from the output of the STAGGER-code, since the numerical mesh of this code is Eulerian in nature. For the three other (Lagrangian-like) averages, the original data sets have to be remapped to their respective new reference depth scale by individually interpolating each column of each 3D simulation snapshot (see 2.3.2). Furthermore, we also considered four additional averages:

- flux-weighted average temperature, $\langle T^4 \rangle$;
- average brightness temperature at 500nm, $\langle T_{\text{rad}} \rangle$;
- logarithmic average, $\langle 3D \rangle_{\text{log}}$; and
- enforced-hydrostatic-equilibrium average, $\langle 3D \rangle_{\text{HSE}}$.

We determine the flux-weighted temperature stratification $\langle T^4 \rangle$ by evaluating the spatial averages of T^4 , motivated by the Stefan-Boltzmann law for wavelength-integrated radiative flux. The brightness temperature average T_{rad} is computed using the expression $B_{500}^{-1}(\langle B_{500}(T) \rangle)$, where B_{500} and B_{500}^{-1} denote the Planck function at 500 nm and its inverse, respectively (see also Sect. 3.4.1). Therefore, at the height z the average temperature, $\langle T_{\text{rad}} \rangle_z$, is equivalent to the average black-body emission at 500 nm. For $\langle 3D \rangle_{\text{log}}$, we define spatial averages of a given 3D variable X as $\exp(\langle \log X \rangle)$. Finally, since the $\langle 3D \rangle$ models do not in general fulfill the hydrostatic equilibrium condition (see Sect. 3.7), for the $\langle 3D \rangle_{\text{HSE}}$ averages we *enforce* hydrostatic equilibrium by adjusting the density and adjusting the thermodynamic pressure p_{th} consistently with the EOS, until hydrostatic equilibrium is attained. We emphasize that the proper enforcement of hydrostatic equilibrium requires that one considers both the thermodynamic p_{th} and turbulent p_{turb} contributions to total pressure p_{tot} : the gas pressure in the atmosphere is in fact, significantly reduced because of the structural support provided by turbulent pressure. Then, a new geometrical depth z is computed (see Eq. 1.8).

Classical hydrostatic 1D models of stellar atmospheres are often defined and computed on an optical depth scale, since this allows the numerical resolution to be easily adjusted where it is most needed to achieve the highest accuracy in the solution of the radiative transfer equation in the atmospheric layers, both during the modeling itself and during line-formation calculations. Therefore, especially for radiative transfer-oriented applications, these 1D models can be compared most naturally with averages of corresponding 3D models on constant optical depth, $\langle 3D \rangle_{\text{Ross}}$ or $\langle 3D \rangle_{500}$. As mentioned above, in the present work, we adopted $\langle 3D \rangle_{\text{Ross}}$ as our standard averaging choice. One of the main reasons we chose $\langle 3D \rangle_{\text{Ross}}$ over $\langle 3D \rangle_{500}$ is that during the scaling of the simulations and the construction of the initial snapshots, the top physical boundary of essentially all models reached up to $\langle \log \tau_{\text{Ross}} \rangle_{\text{top}} \approx -6.0$ (see Sect. 2.2.2). In contrast, the vertical extent of the simulations in terms of optical depth at 500 nm varies depending on stellar parameters ($\log g$ in particular) owing to the concomitant variations in opacity at 500 nm as a function of temperature and density. Therefore, the $\langle 3D \rangle_{500}$ models in general require a careful extrapolation at the top to be extended up to $\log \tau_{500} \approx -6.0$ (see Sect. 2.3.3).

While $\langle 3D \rangle_{\text{Ross}}$ or $\langle 3D \rangle_{500}$ represent natural reference depth scales for the mean photospheric stratification, $\langle 3D \rangle_z$ or $\langle 3D \rangle_m$ is better suited to describing the average physical conditions below the stellar surface; e.g., only the geometrical averages fulfill conservation of momentum and energy (see Sect. 3.7).

In late-type¹³ stellar atmospheres, the continuum opacity κ_λ in the optical is dominated by the H⁻ bound-free absorption that is sensitive to temperature ($\sim T^{10}$). Therefore, even small fluctuations in T will result in large variations in κ_λ , which in turn will lead to a high degree of spatial corrugation of layers at constant optical depth (see Stein & Nordlund, 1998). Furthermore, owing to such highly non-linear

¹²Including both line and continuum opacity.

¹³Historically, a late-type star is spectral K or M class star, while in the present a late-type star is a cool star that has a convective envelope.

behavior of the H^- opacity, temperature fluctuations around the average will be reduced by interpolation to layers of constant optical depth (see Sect. 3.5.1).

We remark briefly again that only the geometrical averages $\langle 3D \rangle_z$, sampled over a sufficient time length, preserve the conservation properties of the hydrodynamical equations, such as hydrostatic equilibrium and conservation of energy. Furthermore, depending on the intended particular application of $\langle 3D \rangle$ models, it is very important to use these carefully, since the different types of $\langle 3D \rangle$ models vary significantly among the different averaging methods.

2.3.1 Basic averaging procedure

We proceeded with the following steps in order to obtain the $\langle 3D \rangle$ models:

1. Retrieval of 3D variables of interest;
2. Interpolation to new reference depth scale;
3. Computation of horizontal averages and statistics;
4. Extrapolation of horizontal averages, if necessary;
5. Computation of temporal averages.

In case of the geometrical averages $\langle 3D \rangle_z$, steps 2 and 4 are unnecessary and are therefore skipped. Owing to the generally non-linear response of the various physical quantities as a function of basic independent variables and the EOS, the interpolation to a new reference depth scale should be performed after retrieving the variables. In particular, because of these non-linearities, we caution against the derivation of thermodynamic variables via the EOS by utilizing averaged independent variables interpolated to the new reference depth scale (see Fig. 3.41), since the spatial averaging will inevitably break the physical self-consistency present in the full original 3D data (see Sect. 2.3.2 and Appendix 3.8). Since the ghost zones do not contain physically meaningful values, we excluded them before the averaging procedure.

To speed up the calculations without noticeably degrading the statistical properties, when computing the averages we considered only every fourth column of the 3D data cubes in both horizontal directions (x and y), which means that the initial $N_x N_y = 240^2$ columns are reduced down to 60^2 . The vertical extent of the columns is unchanged with $N_z = 230$ (geometrical) or 101 (all other reference depth scales). Tests ensured that this horizontal reduction does not influence the horizontal averages owing to the still large sample of vertical columns considered and the multiple snapshots included in the temporal averaging.

For step 3, we used an arithmetic mean to compute the average values of variable X for snapshot t at each horizontal layer z :

$$\langle X \rangle_{z,t} = \frac{1}{N_x N_y} \sum_{x=1}^{N_x} \sum_{y=1}^{N_y} X_{xyz,t} \quad (2.8)$$

with N_x and N_y the number of horizontal elements. For exponentially varying variables like density and pressure, we computed also logarithmic averages, i.e., replacing X_{xyz} with $\log X_{xyz}$ in Eq. 2.8, denoting the models with $\langle 3D \rangle_{\log}$. In the final step 5, temporal averages are evaluated with

$$\langle X \rangle_z = \frac{1}{N_t} \sum_{t=1}^{N_t} \langle X \rangle_{z,t} \quad (2.9)$$

with $N_t \approx 100 - 150$ being the total number of snapshots considered for each simulation, which corresponds typically to about two turnover times. In the present work, the combined temporal and spatial averages of variable X are always denoted with $\langle X \rangle_{\bar{z}}$, where \bar{z} is the considered reference depth scale.

Since the 3D structures display a great plethora of details, for each relevant 3D variable we also determine a number of additional statistical properties (standard deviation σ , root mean square, minimum-maximum range, and histograms of the distribution of values) at each horizontal layer, which are presented and discussed in Sect. 3.5. As for the spatial averages, the standard deviation and the root mean square are evaluated in step 3 for each layer z using the same basic expression as in Eq. 2.8 and, if necessary, doubly

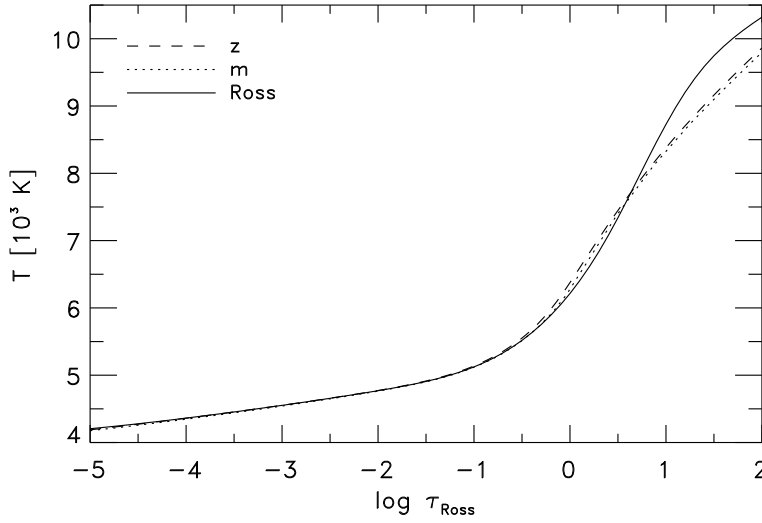


Figure 2.8: Temperature vs. optical depth from the solar simulation to illustrate the different reference depth scales; *dashed*: geometrical, *dotted*: column mass density and *solid*: Rosseland optical depth.

extrapolated at the top as in steps 2 and 4 (see Sect. 2.3.3). Finally, their temporal averages are computed in step 5.

Histograms of the distribution of values we determined separately, and we use temporal averages of the depth-dependent extrema of variable X , $\langle \min X \rangle_z$ and $\langle \max X \rangle_z$ to define a depth-dependent range $r_z = [\langle \min X \rangle_z, \langle \max X \rangle_z]$ for the histograms. For the 3D variable X at time t , we determined a set of 1D histograms, $p_{r,z,t}(X)$, for each individual layer z . The depth-dependent range r_z is resolved with $N_r = 200$ equidistant points; temporal averages $p_{r,z}(X)$ of the histograms are computed using a subset of $N_t = 20$ equidistant snapshots (see Sect. 3.5.3 for details).

Finally, we also computed averages and associated statistical properties separately for up- and downflows, which we differentiate based on the sign of the vertical component of the velocity. Of course, when computing such averages and statistics, one has to account for the correct filling factor in either case, i.e. for the number of elements $N_{x,y}$ belonging to up- or downflows, respectively (Sect. 3.5.2).

2.3.2 Interpolation to the new reference depth scale

To interpolate to the new reference depth scale (hereafter denoted as \tilde{z}) in step 2, we defined a new equidistant logarithmic reference optical depth scale, $\tilde{z} = \log \tilde{\tau}$, from $-5.0, \dots, +5.0$ in steps of 0.1 for both optical depth scales τ_{Ross} and τ_{500} . In the case of averaging based on the column-mass density scale m , we used the column-mass density \tilde{m} normalized to the mean value of m at the optical surface, i.e. $\tilde{z} = \log(\tilde{m}) = \log(m / \langle m \rangle_{\text{surf}})$ for the new reference depth scale, where $\langle m \rangle_{\text{surf}}$ was determined at $\langle \tau_{\text{Ross}} = 0 \rangle$ and considered a fixed range from $-3.0, \dots, +2.0$ in steps of 0.05 for all simulations. All variables, X , we remapped column-wise from the original geometrical depth scale to the new reference depth scale, namely $X_{xy}(z) \rightarrow \tilde{X}_{xy}(\tilde{z})$. We use linear interpolation, since quadratic interpolation introduced numerical artifacts in some (3D) models.

We note that owing to the remapping to a new reference depth scale, points at a constant optical depth or column-mass density will end up probing and spanning a range of geometrical depths, implying that the averages (and statistical properties) with respect to the new reference depth scale will be qualitatively and quantitatively different from plain horizontal averages on constant geometrical depth (see Sect. 3.6).

In Fig. 2.8 we show three temperature stratifications of the solar simulation for averages on constant geometrical depth, column-mass density and Rosseland optical depth. The stratifications are very distinctive below the optical surface, in particular, at the SAR.

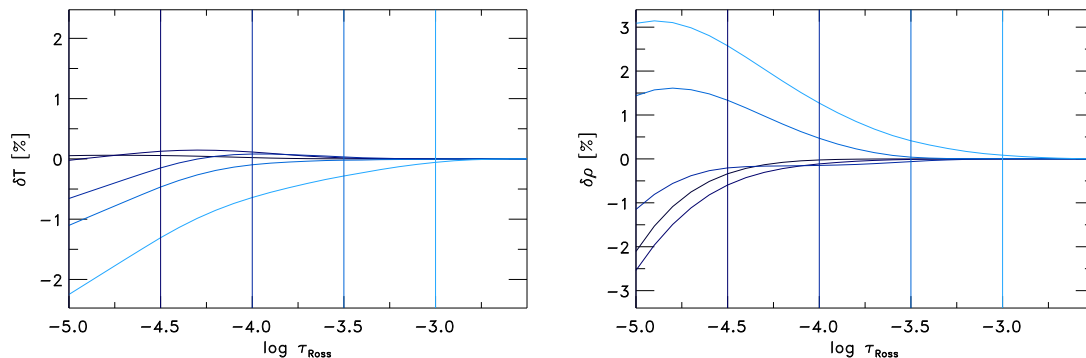


Figure 2.9: Relative differences of the temperature and density stratifications from the solar 3D model that are truncated at increasingly deeper layers ($\log \tau_{\text{Ross}} = -5.0, -4.5, -4.0, -3.5, -3.0$) and subsequently extrapolated to illustrate the level of accuracy achieved with our double-extrapolation method.

2.3.3 Extrapolation at the top

The vast majority of STAGGER-grid models are sufficiently extended vertically, in particular, at the top, to embrace the full range of $\log \tilde{\tau}$ with $[-5.0, +5.0]$. The condition $\langle \log \tau_{\text{Ross}} \rangle_{\text{top}} \leq -6.0$, is usually fulfilled for all but a few models. More specifically, surfaces of constant optical depth can become quite corrugated at the top for some giant models and fall outside the physical domain of the simulations; that is, one can occasionally have $\log \tau_{\text{Ross}}^{\text{top}} > -5.0$ for a limited number of columns. These particular columns are therefore linearly extrapolated to $\log \tau_{\text{Ross}} = -5.0$ to allow calculating of average quantities in the desired range of optical depths. Exponentially varying values like density, pressure opacities are extrapolated by considering their logarithmic values. The extrapolation is needed only for a few giant models ($\log g \leq 2.5$), and the concerned columns are usually only a small fraction ($\lesssim 0.3\%$). Therefore, we regard these extrapolations as negligible in the case of the optical depth scale τ_{Ross} .

For the optical depth scale τ_{500} , the situation is slightly different. The mean optical depth at 500 nm at the top $\langle \log \tau_{500} \rangle_{\text{top}}$ deviates increasingly towards giant models from $\langle \log \tau_{\text{Ross}} \rangle_{\text{top}}$, so that $\langle \log \tau_{500} \rangle_{\text{top}} > -5.0$. Therefore, the necessary extrapolation at the top is considerable, in particular, for giant models.

We notice that careless column-wise extrapolation at the top can lead to a largely uncertain and erroneous stratification, which would have a negative impact on spectral line formation. For instance, a wrong density stratification at the top can dramatically affect the ionization balance. To limit these extrapolation errors, we first restrict the column-wise extrapolation to the region $\log \tilde{\tau}_{500} \geq \log \tilde{\tau}_{\text{top}}$ where the value $\log \tilde{\tau}_{\text{top}} > -5.0$ is chosen so that no more than 20% of the columns would require extrapolation up to that level. We then compute the horizontal averages (step 3) and, after that, linearly extrapolate the $\langle 3D \rangle$ models a second time to the original $\log \tilde{\tau}_{\text{top}} = -5.0$ for each time snapshot. This particular extrapolation procedure produces more plausible stratifications since the horizontal $\langle 3D \rangle$ averages exhibit a smooth and monotonic behavior with depth at the top compared to individual columns of the 3D data set.

Test calculations of data sets from the solar simulation, which were truncated at the top, revealed the reliability of this *double extrapolation* approach, since for the temperature stratifications we find the maximum error around 1% at the top ($\log \tilde{\tau}_{\text{top}} = -5.0$; see Fig. 2.9). Nonetheless, we favor the use of averages on mean Rosseland optical depth, i.e. $\langle 3D \rangle_{\text{Ross}}$ rather than $\langle 3D \rangle_{500}$, since these averages are not plagued by such extrapolation uncertainties. For the extrapolated models on τ_{500} , we kept track of the extent of the applied extrapolation; in fact, only a few models with the lowest gravities ($\log g = 1.5/2.0$) exhibit a noteworthy extrapolation ($\log \tilde{\tau}_{\text{top}} \simeq -4.3/4.8$, respectively). The $\langle 3D \rangle_{500}$ averages can therefore be reduced to the extrapolation-free regime at the top afterwards.

2.4 The STAGGER-grid 1D atmospheres

The following discussion concerns solely 1D atmosphere models and MLT, therefore, similar quantities as discussed above may deviate (e.g., the convective flux F_{conv}). The numerical code that we used for computing 1D atmospheres for the STAGGER-grid models solves the coupled equations of hydrostatic equilibrium and energy flux conservation in 1D plane-parallel geometry. The 1D models use the same EOS and opacity package in order to allow consistent 3D-1D comparisons. The set of equations and numerical methods employed for their solution are similar to those of the MARCS code (Gustafsson et al., 2008) with a few changes and simplifications that will be outlined in the following. The resulting model atmospheres yet maintain very good agreement with MARCS models (see Sect. 3.3.2).

2.4.1 Basic equations

Assuming 1D plane-parallel geometry with horizontal homogeneity and dominance of hydrostatic equilibrium over all vertical flow simplifies the equation of motion (Eq. 1.2) to the hydrostatic equilibrium equation

$$\frac{d}{d\tau_{\text{std}}} (p_{\text{gas}} + p_{\text{turb}}) - \frac{\rho g}{\kappa_{\text{std}}} = 0, \quad (2.10)$$

where κ_{std} and τ_{std} are a standard opacity and corresponding optical depth (e.g., the Rosseland mean), p_{gas} and p_{turb} denote gas pressure and turbulent pressure, ρ is the gas density, and g is the surface gravity. Radiation pressure is neglected, as in the 3D simulations. Turbulent pressure is estimated using the expression

$$p_{\text{turb}} = \beta \rho v_{\text{turb}}^2, \quad (2.11)$$

with the scaling parameter β that corrects for asymmetries in the velocity distribution and the mean turbulent velocity v_{turb} that is used as a free, independent parameter.

The depth-integral of the energy equation (Eq. 1.3) reduces to the flux conservation equation,

$$F_{\text{rad}} + F_{\text{conv}} - \sigma T_{\text{eff}}^4 = 0, \quad (2.12)$$

where F_{rad} is the radiative energy flux, F_{conv} is the convective energy flux, σ is the Stefan-Boltzmann constant and T_{eff} is the stellar effective temperature. Contrary to the 3D case, effective temperature now appears as a boundary value and is thus a free parameter. Owing to numerical instabilities of the formulation, Eq. 2.12 is replaced in the higher atmosphere ($\tau_{\text{Ross}} \lesssim 10^{-2}$) with the radiative equilibrium condition

$$q_{\text{rad}} = 4\pi\rho \int_{\lambda} \kappa_{\lambda} (J_{\lambda} - S_{\lambda}) d\lambda \equiv 0, \quad (2.13)$$

where J_{λ} and S_{λ} are the mean intensity and the source function, similar to Eq. (1.23). In the 3D case, q_{rad} is explicitly calculated and is nonzero in general. Enforcing the condition of radiative equilibrium $q_{\text{rad}} \equiv 0$ in 1D leads to an atmospheric stratification where an exact balance of radiative heating and cooling in each layer is achieved, ignoring the effects of gas motion.

The mean intensity and the radiative energy flux at each depth are obtained by solving the radiative transfer equation,

$$\mu \frac{dI_{\lambda}}{d\tau_{\lambda}} = I_{\lambda} - S_{\lambda}, \quad (2.14)$$

where $\mu = \cos \theta$ with the polar angle θ off the vertical, I_{λ} is the specific intensity at wavelength λ , and τ_{λ} is the vertical monochromatic optical depth (with $\tau_{\lambda} = 0$ above the top of the atmosphere). A Planck source function $S_{\lambda} = B_{\lambda}$ is assumed. The monochromatic mean intensity and radiative flux are then delivered by the integrals

$$J_{\lambda} = \frac{1}{2} \int_{-1}^1 I_{\lambda} d\mu \quad (2.15)$$

$$F_{\text{rad},\lambda} = 2\pi \int_{-1}^1 I_{\lambda} \mu d\mu. \quad (2.16)$$

In the absence of an explicit convection treatment, convective energy transfer is estimated using a variant of the mixing length recipe described in Henyey et al. (1965). The convective flux is given by the expression

$$F_{\text{conv}} = \frac{1}{2} \alpha_{\text{MLT}} \delta \Delta c_p T \rho v_{\text{MLT}}, \quad (2.17)$$

where ρ is the gas density, c_p is the specific heat capacity, T is the temperature, and

$$v_{\text{MLT}} = \sqrt{\alpha_{\text{MLT}}^2 H_p g \delta \Delta / \nu} \quad (2.18)$$

is the convective velocity with ν being the parameter for the energy dissipation by turbulent viscosity. The well-known free mixing length parameter $\alpha_{\text{MLT}} = l_m / H_p$ sets the distance l_m in units of the local pressure scale height H_p over which energy is transported convectively. See Gustafsson et al. (2008) for details of the expressions used to obtain the convective velocity v_{MLT} and the superadiabatic excess

$$\Delta = \frac{\Gamma}{(1 + \Gamma)} (\nabla - \nabla_{\text{ad}}) \quad (2.19)$$

which scales super-adiabaticity $\nabla_{\text{sad}} = \nabla - \nabla_{\text{ad}}$ of the atmospheric stratification (see also Sect. 3.2.7), by a convective efficiency factor

$$\Gamma = \frac{c_p}{8\sigma T^3} \tau_e (y + \tau_e^{-2}) \rho v_{\text{MLT}} \quad (2.20)$$

with the optical thickness $\tau_e = \kappa_{\text{Ross}} l_m$ and y being the temperature-distribution of a convective element. We adopt the same parameters $y = 0.076$ and $\nu = 8$ as Gustafsson et al. (2008) for the additional MLT parameters that enter the above quantities. We note that in the notation by Ludwig et al. (1999), we would get $f_1 = \nu^{-1}$ and $f_4 = y^{-1}$, $f_2 = 1/2$ and $f_3 = (8y)^{-1}$.

2.4.2 Numerical methods

The system of equations is solved using a modified Newton-Raphson method with an initial stratification of temperature T and gas pressure p_{gas} on a fixed Rosseland optical depth grid. Discretized and linearized versions of the hydrostatic equation and the energy flux equation (or radiative equilibrium condition, respectively) provide the inhomogeneous term and the elements of the Jacobian matrix for the system of $2N$ linear equations, where N is the number of depth layers. The radiation field is computed for each Newton-Raphson iteration using the integral method, based on a second-order discretization of the fundamental solution of the radiative transfer equation (Eq. 2.14).

The corrections ΔT and Δp_{gas} derived from the system of linear equations are multiplied by a variable factor < 1 that is automatically regulated by the code to aid convergence. Convergence is assumed when the (relative) residuals of the $2N$ equations decrease beneath a preset threshold. Note that, contrary to the 3D simulations, the effective temperature is now an adjustable parameter; the requirement of minimal residuals automatically leads to an atmospheric stratification with correct T_{eff} through the energy flux equation.

In order to obtain a 1D model, a given $\langle 3D \rangle$ stratification provides the initial input for the Newton-Raphson iterations, along with the targeted effective temperature and surface gravity. The same EOS tables that were used for the 3D simulation provide gas density, specific heat capacity, and adiabatic gradient as a function of T and p_{gas} . Likewise, the tables containing group mean opacities and the Rosseland mean opacity provide the required microphysics for solving the radiative transfer equation, ensuring maximal consistency with the 3D simulations.

Once convergence has been achieved for the 1D stratification, the mixing length parameter α_{MLT} can be calibrated to obtain a better approximation to the $\langle 3D \rangle$ stratification in the convection zone beneath the stellar surface.

Chapter 3

STAGGER-grid

In the following, I will discuss spatially and temporally averaged global properties (Sect. 3.1) and mean 3D stratifications (Sect. 3.2) from all of our 3D models, which will be compared with classical 1D models (Sect. 3.3). For the readers that are unfamiliar with the subject of stellar atmospheres, I advice to read the short overview of the mean stratification of the solar simulation at the beginning of Sect. 3.2 first, in order to get a better access to the subsequent Sections. Furthermore, for those who are more interested in the applications of the 3D atmosphere models and their predictions, and less in the comprehensive details of the mean stratifications, I recommend to read the Section on the global properties only (Sect. 3.2), which contains the most important findings. The presented results from Sections 3.1, 3.2 and 3.3 are taken from the already published study by Magic et al. (2013a). The other five Sections of this Chapter (from Sect. 3.4 to 3.8), which encompass the comparison of the different averages, the statistical properties, the reversed granulation, the hydrostatic equilibrium and the deviations from the EOS, originate from Magic et al. (2013b).

We find a tight scaling relation between the vertical velocity and the surface entropy jump, which itself correlates with the constant entropy value of the adiabatic convection zone. The range in intensity contrast is enhanced at lower metallicity. The granule size correlates closely with the pressure scale height sampled at the depth of maximum velocity. We compare the (3D) models with currently widely applied 1D atmosphere models, as well as with theoretical 1D hydrostatic models generated with the same EOS and opacity tables as the 3D models, in order to isolate the effects of using self-consistent and hydrodynamic modeling of convection, rather than the classical mixing length theory (MLT) approach. For the first time, we are able to quantify systematically over a broad range of stellar parameters the uncertainties of 1D models arising from the simplified treatment of physics, in particular convective energy transport. In agreement with previous findings, we find that the differences can be rather significant, especially for metal-poor stars. Furthermore, the resulting (3D) stratifications for the different reference depth scales can be very distinctive. We typically find that in the upper atmosphere and in the superadiabatic region just below the optical surface, where the temperature and density fluctuations are highest, the differences become considerable and increase for higher T_{eff} , lower $\log g$, and lower $[\text{Fe}/\text{H}]$.

3.1 Global properties

In Table B.1, we have listed the stellar parameters together with the thermodynamic values fixed for the inflows at the bottom, i.e. the internal energy ϵ_{bot} , density ρ_{bot} and entropy s_{bot} , as well as important global properties for our 3D simulations. Before we consider the (3D) stratifications in Sect. 3.2, we briefly discuss some (temporally averaged) global properties.

3.1.1 Stellar parameters

Surface gravity and metallicity are input parameters for a simulation, while the effective temperature is a property ensuing from the fixed entropy of the inflowing material at the bottom s_{bot} . We calculate the effec-

tive temperature from the spatially averaged emergent radiative energy flux F_{rad} and the Stefan-Boltzmann law

$$T_{\text{eff}} = [F_{\text{rad}}/\sigma]^{1/4}, \quad (3.1)$$

with σ being the Stefan-Boltzmann constant. In Column 1 of Table B.1 we have listed the resulting temporally averaged T_{eff} of our final, relaxed simulations. These differ somewhat from the targeted T_{eff} s, since we do not know a priori, the relation between s_{bot} and T_{eff} . However, the majority of our models (72%) deviate less than 50K, and the mean deviation for the whole grid is $\overline{\Delta T_{\text{eff}}} \sim 32$ K.

3.1.2 Constant entropy of the adiabatic convection zone

The main input parameter that has to be adjusted is s_{bot} , which has the same value as the entropy in the deep convection zone due to the adiabaticity of convection, i.e. $s_{\text{bot}} = s_{\text{ad}}$ (Steffen, 1993). This is also the reason, why the results from our rather shallow boxes are valid. We set s_{bot} by specifying a fixed value for the density and energy per unit mass for the inflowing material at the bottom, ρ_{bot} and ε_{bot} . The actual values of ε_{bot} , ρ_{bot} and s_{bot} applied in our simulations are given in Table B.1. Furthermore, we provide functional fits for s_{bot} (see App. A). We compute the entropy by integrating¹ the first law of thermodynamics in the form

$$ds = \frac{1}{T} \left(d\varepsilon - p_{\text{th}} \frac{d\rho}{\rho^2} \right), \quad (3.2)$$

adding an arbitrary integration constant in order to shift the zero-point of the entropy to a similar value as in Ludwig et al. (1999). We remark that the physical aspects, such as chemical composition and ionization, implicitly enters the entropy values through the EOS. In Fig. 3.1, we show s_{bot} against T_{eff} for $[\text{Fe}/\text{H}] = 0.0$ and -0.5 , as an example. The value for s_{bot} increases exponentially with higher T_{eff} and with lower $\log g$, and linearly with metallicity with a moderate slope.

In order to increase the effective temperature solely, i.e. the emergent radiative flux F_{rad} at the top boundary, the total energy flux ascending from the convection zone has to increase by that same amount due to conservation of energy (see Sect. 3.2.8). On the other hand, when the T_{eff} is fixed and the surface gravity is reducing, this in turn will cause the density to decrease correspondingly (see Sect. 3.2.4). Therefore, to maintain the same energy flux, either the transported heat content (Δs , ε) or the mass flux (ρ or v_z) is going to enhance. When the energy flux is carried by a larger mass flux, then we speak of an enhancement in *convective efficiency*² (see Sects. 3.2.4, 3.2.2 and 3.2.8). When one considers ε_{bot} with stellar parameters, then it clearly depicts qualitatively the same characteristic changes as s_{bot} . By inserting the perfect gas law³ in Eq. 3.2 one obtains

$$ds = \frac{d\varepsilon}{T} - \frac{k}{\mu m_u} \frac{d\rho}{\rho}, \quad (3.3)$$

from which one can immediately see that the entropy increases with internal energy, $ds \propto d\varepsilon$, and also increases with lower density $ds \propto -d \ln \rho$.

On the other hand, an increase in metallicity leads to a higher entropy of the adiabat and also a larger atmospheric entropy-jump (see Fig. 3.1). Furthermore, we find increased velocities (and Δs) and decreased densities at higher $[\text{Fe}/\text{H}]$ (see Sects. 3.2.2 and 3.2.4), which in turn affects the convective efficiency. The dependence on metallicity can be unveiled with the following approximation. The opacity (and absorption coefficient) increases with higher $[\text{Fe}/\text{H}]$, since the opacity depends directly on the metallicity. The hydrostatic equilibrium can be written in terms of optical depth as $dp_{\text{th}}/d\tau_{\text{Ross}} = g/\kappa_{\text{Ross}}$. From the EOS (also ideal gas law), one can see that the pressure scales with the density, $p_{\text{th}} \propto \rho$ (for isotherms). Therefore, when one would fix T_{eff} and $\log g$, but increase metallicity (and opacity), then the hydrostatic balance will be realized at a lower density stratification (see bottom and middle panel in 3.20), which is also given by

¹The values for $p_{\text{th}}(\rho, \varepsilon)$ and $T(\rho, \varepsilon)$ are given in the EOS tables in the covered range of $\log(\rho / [\text{g}/\text{cm}^3]) \in [-14, 1]$ in 57 steps and $\log(\varepsilon / [\text{erg}/\text{g}]) \in [11, 14]$ in 300 steps.

²In 1D MLT modeling the term convective efficiency is commonly referred to the mixing-length. The latter is in 3D RHD simulations referred to the mass mixing-length, which is the inverse gradient of the mass flux (see Trampedach & Stein, 2011a).

³ $p = kT\rho/\mu m_u$, with k being the Boltzmann constant, μ the mean molecular weight, and m_u the atomic mass constant.

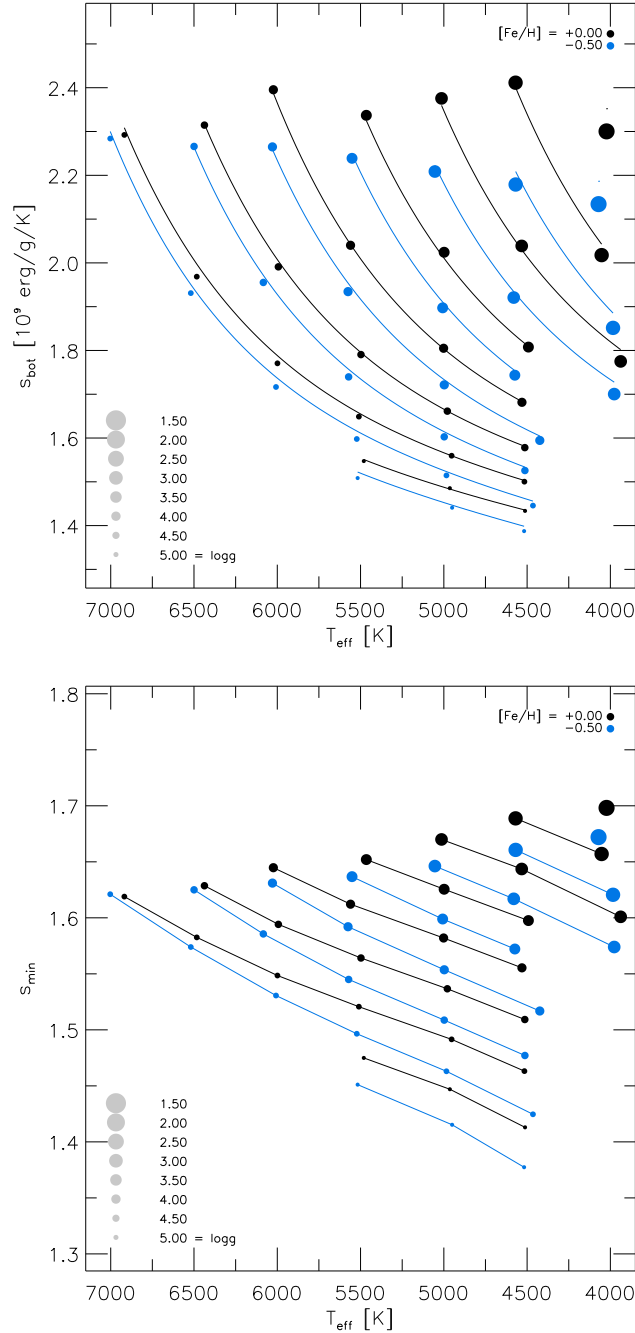


Figure 3.1: Overview of the constant entropy value of the adiabatic convection zone, which is given by the fixed entropy of the inflowing plasma at the bottom, s_{bot} , (*top*) as well as the atmospheric entropy minimum, s_{min} , (*bottom figure*) for two metallicities ($[\text{Fe}/\text{H}] = -0.5$ and 0.0 , blue and black respectively) against T_{eff} . Simulations with the same gravity are connected with functional fits for s_{bot} and s_{min} (solid and dashed lines respectively; see App. A), while similar simulations with different $[\text{Fe}/\text{H}]$ are connected with short solid black lines. Note the different ordinates in the two figures.

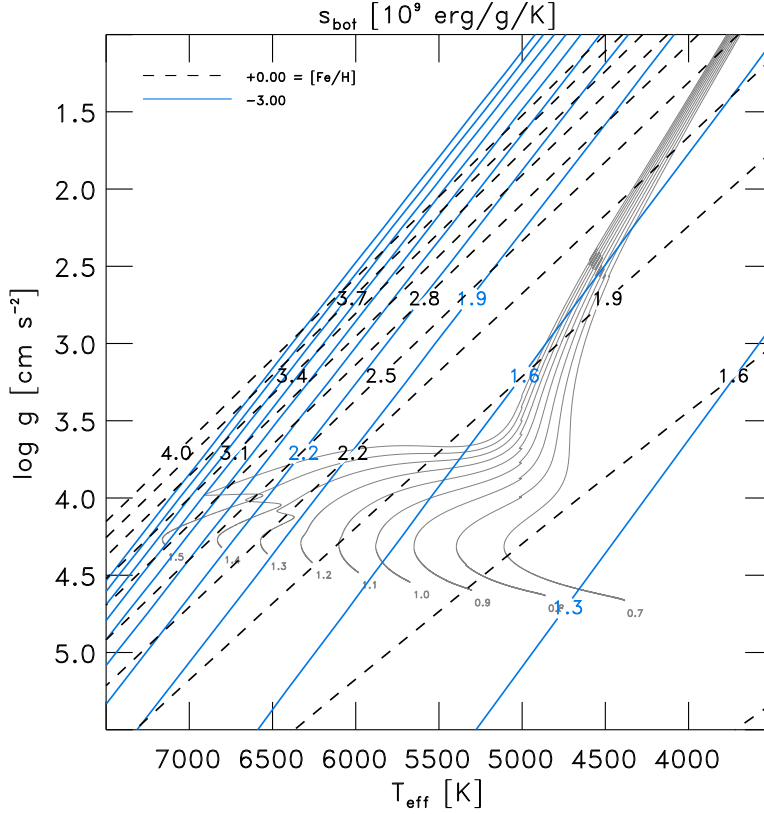


Figure 3.2: Showing lines of constant entropy of the adiabat s_{bot} from 1.3 to 4.0×10^{13} erg/g/K in steps of 0.3×10^{13} erg/g/K and for $[\text{Fe}/\text{H}] = -3.0$ and 0.0 (blue solid and black dashed lines respectively) in the Kiel diagram. Additionally, we show evolutionary tracks for 0.7 to $1.5 M_{\odot}$ with solar metallicity (thin grey lines).

1D MLT models. The lower density stratification will result in higher s_{bot} and Δs (Eq. 3.3 and top panel in 3.20).

We emphasize that the dependence of both s_{bot} and Δs with stellar parameters is quite non-trivial, since not only is it coupled to the changes in the total energy fluxes, but it is also affected by the differences in the transition from convective to radiative transport of energy with stellar parameters. In particular, the non-local radiative transfer depends non-linearly on the conditions present in stellar atmospheres, especially changes in the opacity and the EOS will strongly influence the radiative transfer. Additionally, s_{bot} will be influenced by changes in the efficiency of the convective energy transport, that is in the convective fluxes arising from the hydrodynamics (see Sect. 3.2.8 for more details).

An analytical derivation of s_{bot} as a function of stellar parameters is rather difficult, as explained above. Nonetheless, we can fit s_{bot} with stellar parameter in a functional form based on the results from our simulations (see App. A). This has been done previously, based on 2D RHD models with solar metallicity by Ludwig et al. (1999). In Fig. 3.2, we show how s_{bot} varies across the Kiel diagram ($T_{\text{eff}} - \log g$ diagram) for $[\text{Fe}/\text{H}] = 0.0$ and -3.0 . In the case of s_{bot} , our results with solar metallicity are qualitatively in good agreement with those of Ludwig et al. (1999), despite the inherent differences between 2D and 3D convection simulations, the adopted EOS, opacities, and radiative transfer treatment (see Fig. 3.3). We find that s_{bot} (which depicts s_{ad}) is regularly distributed along lines in the Kiel diagram, in fact, for the solar metallicity these lines with the same entropy of the adiabat run almost diagonally. Moreover, towards lower metallicity, we find two significant differences for the lines of constant s_{bot} , the first one being that the slopes of the lines steepen, and the second being that the distances in the $T_{\text{eff}} - \log g$ plane between the lines decrease. The latter implies metal-poor stars feature a broader range in s_{bot} compared to metal-rich ones. As we will see in Sect. 3.2, this has important consequences for the stratifications.

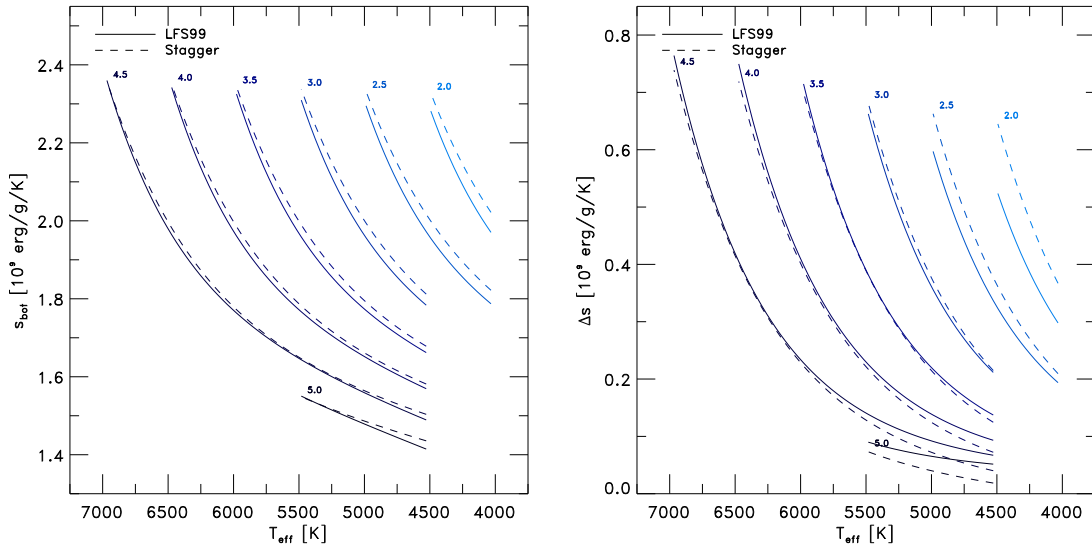


Figure 3.3: Comparison of the constant entropy value of the adiabatic convection zone, s_{bot} , and the entropy jump, Δs , between our 3D result and the 2D values found by Ludwig et al. (1999) (dashed and solid lines, respectively). The surface gravity is indicated.

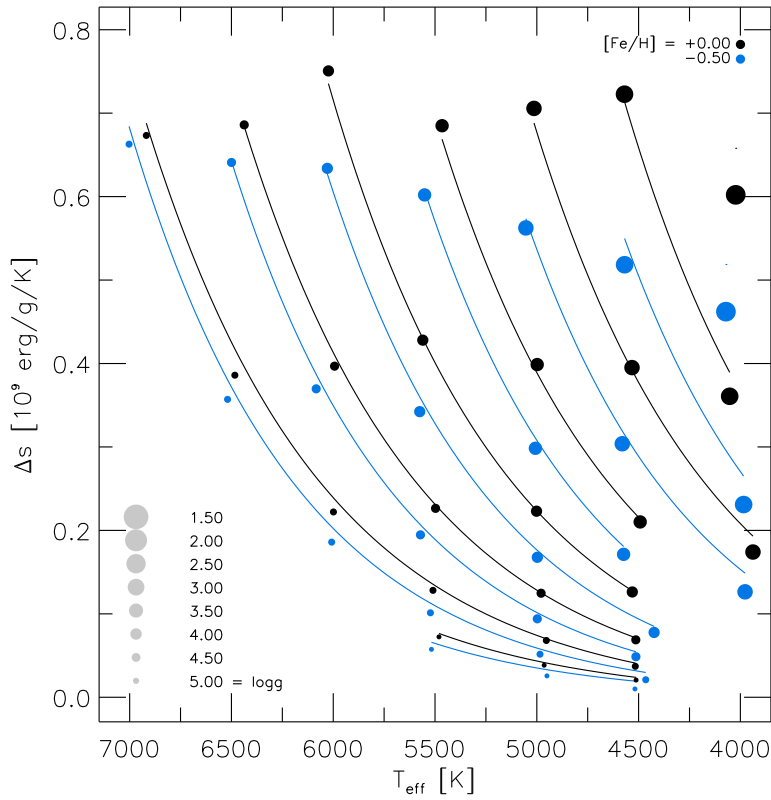


Figure 3.4: Overview of the entropy jump vs. T_{eff} for different stellar parameters.

3.1.3 Entropy jump

The upflows enter the simulation box at the bottom with the constant entropy value of the adiabatic convection zone, s_{bot} , and ascend until they reach the superadiabatic region (SAR) just below the visible surface, where the convective energy is converted to radiative energy (see Fig. 3.27). In the photosphere, the mean free path for the continuum radiation grows large enough for the gas to become transparent, and the overturning upflow at the surface loses its internal energy as photons escape and carry away entropy. Further above in the nearly isothermal atmosphere (with constant ϵ , see Fig. 3.18) with an exponentially decreasing density the entropy increases again due to the EOS (see Eq. 3.3). This leads to a minimum, $s_{\text{min}} = \min[\langle s \rangle]$, just above the surface ($\log \tau_{\text{Ross}} < 0.0$) in the temporal and horizontal averaged entropy (see Fig. 3.27). We determined the entropy jump from the difference of the entropy minimum and the fixed entropy at the bottom, i.e.

$$\Delta s = s_{\text{bot}} - s_{\text{min}}. \quad (3.4)$$

In order to calculate s_{min} , we used averages of the entropy on constant Rosseland optical depth⁴, since it is the radiation losses that cause the sharp changes in the thermodynamic state around the optical surface and, therefore, the optical depth scale offers a better reference frame for comparisons. The averages on constant geometrical height $\langle 3D \rangle_z$ smear out and thereby overestimate s_{min} increasingly towards higher T_{eff} due to the increasing level of corrugation of iso- s surfaces on the geometrical scale (see Fig. 3.27). The constant entropy at the bottom s_{bot} , on the other hand, is a fixed input value for each simulation. It is worthwhile to mention that the main contribution to the variation in Δs as a function of stellar parameters is due to s_{bot} , since s_{min} varies just slightly with stellar parameter compared to s_{bot} (see Fig. 3.1).

It is obvious that the minimum in entropy increases just slightly with increasing T_{eff} (see s_{min} in Fig. 3.1), while the jump increases with the constant entropy value of the adiabatic convection zone quasi-exponentially at higher T_{eff} and lower $\log g$ (see Δs in Fig. 3.4; compare with s_{bot} in Fig. 3.1). This can be concluded more easily from Fig. 3.20 (top panel), where we display Δs vs. T_{eff} (see also Col. 8 of Table B.1 and for Δs and s_{min} in App. A). We note that the location of the entropy jump and minimum essentially represents the boundary of stars and the jump is to be regarded as physically realistic, which is a result of 3D RHD simulations. The entropy minimum coincides with the position of the upper end of the SAR. A similar sharp drop occurs for most of the thermodynamic quantities of interest (ϵ , T and n_{el}), whereas ρ and p_{tot} display a marked change of gradient. Moreover, the jump in entropy is an important value, since it is a direct measure of the efficiency of convective energy transport (see Trampedach et al., 2013). The latter is in 1D modeling set by the four MLT parameters, especially α_{MLT} , in the framework of MLT (see Böhm-Vitense, 1958; Henyey et al., 1965). Towards cool dwarfs Δs becomes smaller, indicating a higher convective efficiency, while towards hotter stars the large entropy jumps reflect a low convective efficiency. We present a calibration of α_{MLT} based on the entropy jump in Sect. 7.5, as previously done by using multidimensional convection simulations (see Ludwig et al., 1999; Trampedach et al., 1999). The variation of Δs with stellar parameters found by Ludwig et al. (1999) is similar to our results, however, the differences are larger compared to the s_{bot} (see Fig. 3.3).

By comparing Fig. 3.1 with Fig. 3.4 one can notice the variation of Δs closely resembles the variation of s_{bot} with stellar parameters. Motivated by this, we compare directly Δs against s_{bot} in Fig. 3.5. We find a nice correlation between Δs vs. s_{bot} . At lower s_{bot} values, Δs seems to converge towards 0.0 (a negative jump is not expected, since the atmosphere is *losing* energy in form of radiation from the photosphere), while for $s_{\text{bot}} \gtrsim 1.7$, Δs grows linearly with s_{bot} and only a modest level of scatter. In Fig. 3.5, we color-coded the T_{eff} - and $\log g$ -values respectively, to show how the residuals depend systematically on atmospheric parameters. Models with higher T_{eff} (bright orange dots) and higher $\log g$ (dark grey dots) settle along higher Δs and vice versa. In order to illustrate this better, we have fitted a set of hyperbolic tangent functions (see Eq. A.4), which we show also in Fig. 3.5. We included functional fits between $T_{\text{eff}} = 4000$ and 6000 K (red/orange lines in top panel) and between $\log g = 1.5$ and 4.5 (grey lines in bottom panel). Hence, we find hotter dwarfs along lines at larger Δs , while cooler giants settle along lines at smaller entropy jumps.

Interestingly, in the linear part ($s_{\text{bot}} \gtrsim 1.7$) $\Delta s(s_{\text{bot}})$ displays a rather universal slope of $\Delta s/s_{\text{bot}} \sim 0.85$, even though for different T_{eff} and $\log g$ these are slightly offset. Another interesting aspect is that T_{eff}

⁴Averages on constant column mass density yield a very similar s_{min} .

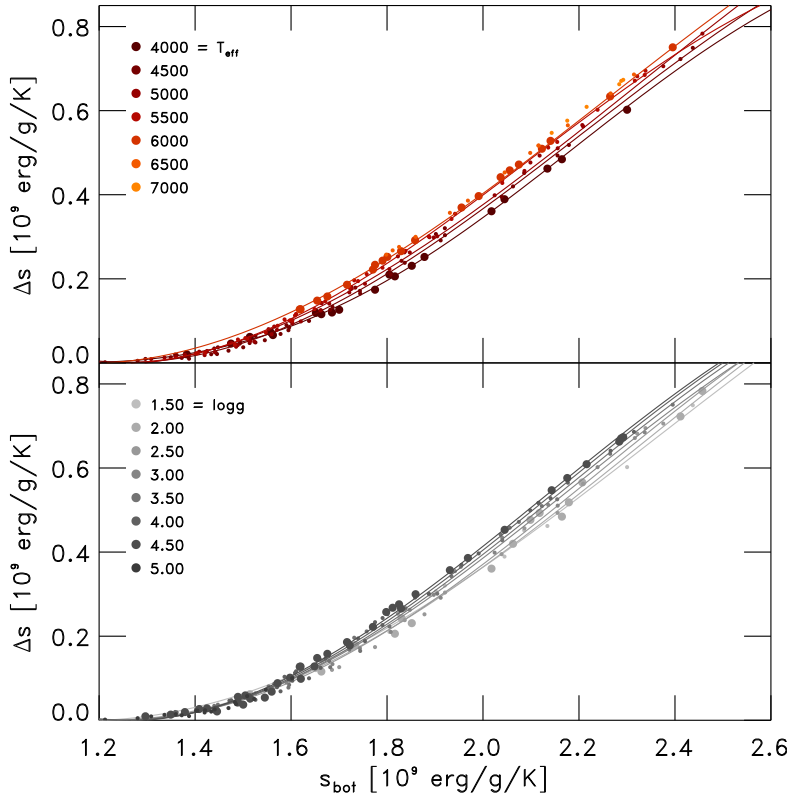


Figure 3.5: We compare the entropy jump Δs against the constant entropy value of the adiabatic convection zone s_{bot} for all grid models (filled circles; color-coding explained in the legend). Furthermore, we show also hyperbolic tangent functional fits (see Eq. A.4 and App. A) between $T_{\text{eff}} = 4000$ and 6000 K (red lines; top panel) and between $\log g = 1.5$ and 4.5 (grey lines; bottom panel).

shows a similar strong influence as $\log g$. The latter, however, is obviously expressed in logarithmic scale, therefore the influence of T_{eff} is much stronger. On the other hand, when one performs a similar hyperbolic tangent functional fit for a fixed value of $[\text{Fe}/\text{H}]$, then Δs is dispersed around the functional fit with such a large scatter that a fit is rather meaningless. Therefore, in contrast to T_{eff} and $\log g$ we find no systematic trends with metallicity.

Based on the strong correlation between the entropy jump Δs and s_{bot} , it is of interest to investigate what other *scaling relations* may be manifested for other stellar properties. With Δs as an inverse measure of convective efficiency, we expect that in light of such scaling relations, important quantities depending on the entropy jump will also similarly scale systematically with s_{bot} , in particular, density and velocity (see Sects. 3.2.2 and 3.2.4), and therefore also the calibrated mixing-length of a particular MLT implementation. We note briefly that qualitatively similar relations can be achieved with 1D MLT models with a fixed mixing length.

3.1.4 Large-amplitude fluctuations

Below the optical surface convective energy is transported to the surface in the buoyant, hot granules, and at the surface the stellar plasma becomes transparent, so that significant radiative losses generate large amplitude fluctuations in the thermodynamic properties. Convection is driven by these large amplitude fluctuations, in particular, in the entropy. The fluctuations can be quantified with the contrast of the respective value, which we will discuss more carefully in Sect. 3.5.1. The contrast of all thermodynamic properties, including the velocity field, exhibits a maximum in the SAR just below the optical surface, where the large amplitude fluctuations are taking place (see Figs. 3.37 and 3.36). In Fig. 3.6 we illustrate the maximum in the temperature-, density-, and entropy-contrast for different stellar parameters. One can retrieve that for higher T_{eff} , lower $\log g$ and higher $[\text{Fe}/\text{H}]$ the large amplitude fluctuations are increasing, which is very similar to the entropy jump and the maximum vertical rms-velocity (see Fig. 3.20). The larger temperature-contrast implies a larger temperature gradient (see Fig. 3.17), and therefore a larger transport

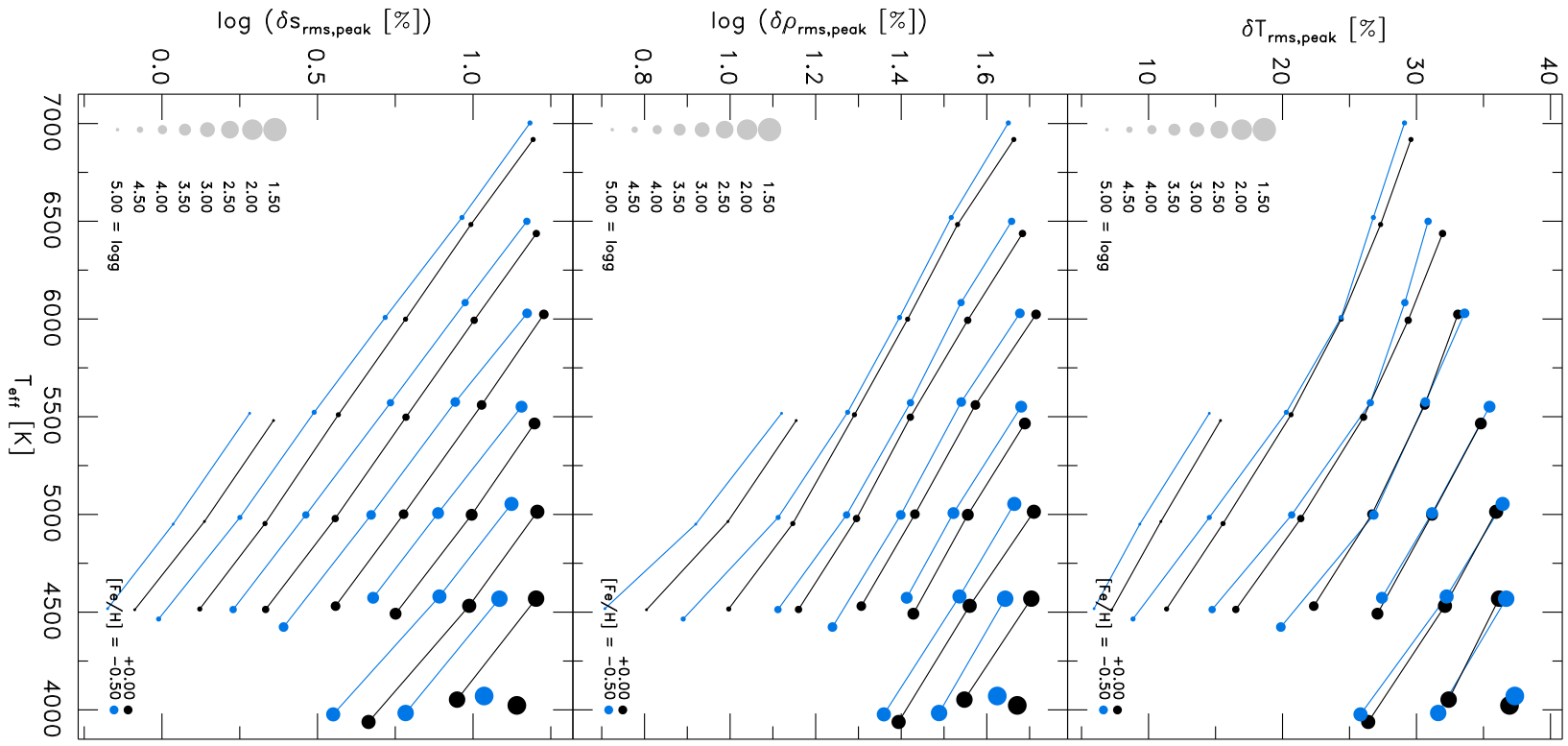


Figure 3.6: Overview of the maximum in contrast for different stellar parameters; *top*: temperature; *middle*: density and *bottom*: entropy.

of enthalpy (heat). An increasing density-contrast will result in larger buoyancy, and therefore in higher velocities. While the entropy-contrast is coupled with both of the former through the EOS. Interestingly the entropy-contrast scales very tightly with the entropy jump.

3.1.5 Emergent intensity

While classic 1D models are inherently horizontally symmetric, therefore lacking a visible granulation pattern, the emergent intensity of 3D models features inhomogeneities exhibiting rich details, which arise due to the presence of turbulent convective motions. We give an overview over the emergent intensity of our simulations in Fig. 3.7. Therein we display a main-sequence (MS) simulation (the Sun), a turnoff (TO) simulation, a K-giant, and a K-dwarf model, each with for four different metallicities. To facilitate direct comparisons among the four metallicities, we kept the horizontal sizes and the color scales for the continuum intensities fixed from $[\text{Fe}/\text{H}] = 0.0$ for the individual stellar categories (we extended the metal-poor simulations by exploiting the periodic horizontal boundary conditions). The dark regions depict the cold intergranular lanes, while the brighter areas are the hot granules. The radiation above the granules originates at higher geometrical heights, while for downdrafts it comes from much lower heights. This is because the opacity is highly non-linear due to the strong temperature sensitivity of the H^- -opacity ($\kappa_{\text{H}^-} \sim T^{10}$, see SN98), which is by far the dominant continuum opacity source in the visible for late-type stellar photospheres. Since the temperature difference between the granules and the intergranular lanes is very large ($> 10^3$ K), layers of constant optical depth will be increasingly more corrugated and become largest around the peak of the SAR. Therefore, the radiation above granules is emerging from higher geometrical depths, z_{up} , while above downdrafts it originates from deeper geometrical heights, z_{dn} (for the Sun the largest difference between the averaged geometrical heights can amount up to $\langle z \rangle_{\text{up}} - \langle z \rangle_{\text{dn}} \simeq -140$ km at $\log \tau_{\text{Ross}} = 2.0$).

An immediate, interesting aspect that leaps to the eye from the overview presented in Fig. 3.7 is the qualitative self-similarity of the granulation patterns despite the large variations in size-scales. The emergent intensity increases towards higher T_{eff} and decreases for lower surface gravities, as expected. From Fig. 3.7, it is also clear that the granule sizes decrease with metallicity (due to smaller H_P , see Sect. 3.1.6; see also Collet et al., 2007). Also apparent is the change of intensity contrast with stellar parameters, as we will discuss below.

In order to discuss the changes in the intensity, we show in Fig. 3.8 the temporally averaged histograms⁵ of the intensity I normalized to their individual mean intensity \bar{I} , thereby enabling a direct comparison between different stellar parameters. The histograms of the intensity show often two components: a peak at lower (darker, $I/\bar{I} < 1.0$) intensities, resulting from the cool downdrafts, and an often broader component at higher (brighter, $I/\bar{I} > 1.0$) intensities, arising from the upflowing hot granules. We note that these findings are qualitatively to be expected (see SN98; Trampedach et al., 2013).

As clearly depicted in Fig. 3.8, the shapes of the two components change with stellar parameters, in particular, the amplitudes and widths, thereby changing the overall shape. The two components can be clearly extracted from histograms at higher T_{eff} , where the intensity contrast is increasingly enhanced and eventually produces a distinctly bimodal distribution, which is a manifestation of the *hidden or naked granulation* (see Fig. 3.9 and Nordlund & Dravins 1990). In order to better illustrate this, we also included the full width at half maxima (FWHM) of the individual intensity histograms I_{FWHM} in Fig. 3.9. On the other hand, at lower T_{eff} the intensity contrast decreases in general, so that the two components overlap, leading to a single narrower higher peak in the histogram, thereby becoming indistinguishable from each other in the histogram. Ludwig & Kučinskas (2012) found also an unimodal intensity distribution in the context of a 3D giant model with solar metallicity. Furthermore, we find that the individual contribution to the intensity from upflows and downflows is often asymmetric, meaning that the amplitudes of the two peaks in the bimodal distribution are unequal (see Fig. 3.8). In general, for dwarfs, we find that the relative importance of downflows with respect to upflows in terms of the peak contribution to the intensity distribution increases with increasing T_{eff} . However, we also find exceptions, e.g., at lower metallicity where the behavior at $T_{\text{eff}} = 4500$ K is actually the opposite. Also, the balance between upflows and downflows varies

⁵The histogram estimates the probability distribution of a given data set, i.e. how often a value of the considered bin is given in the distribution.

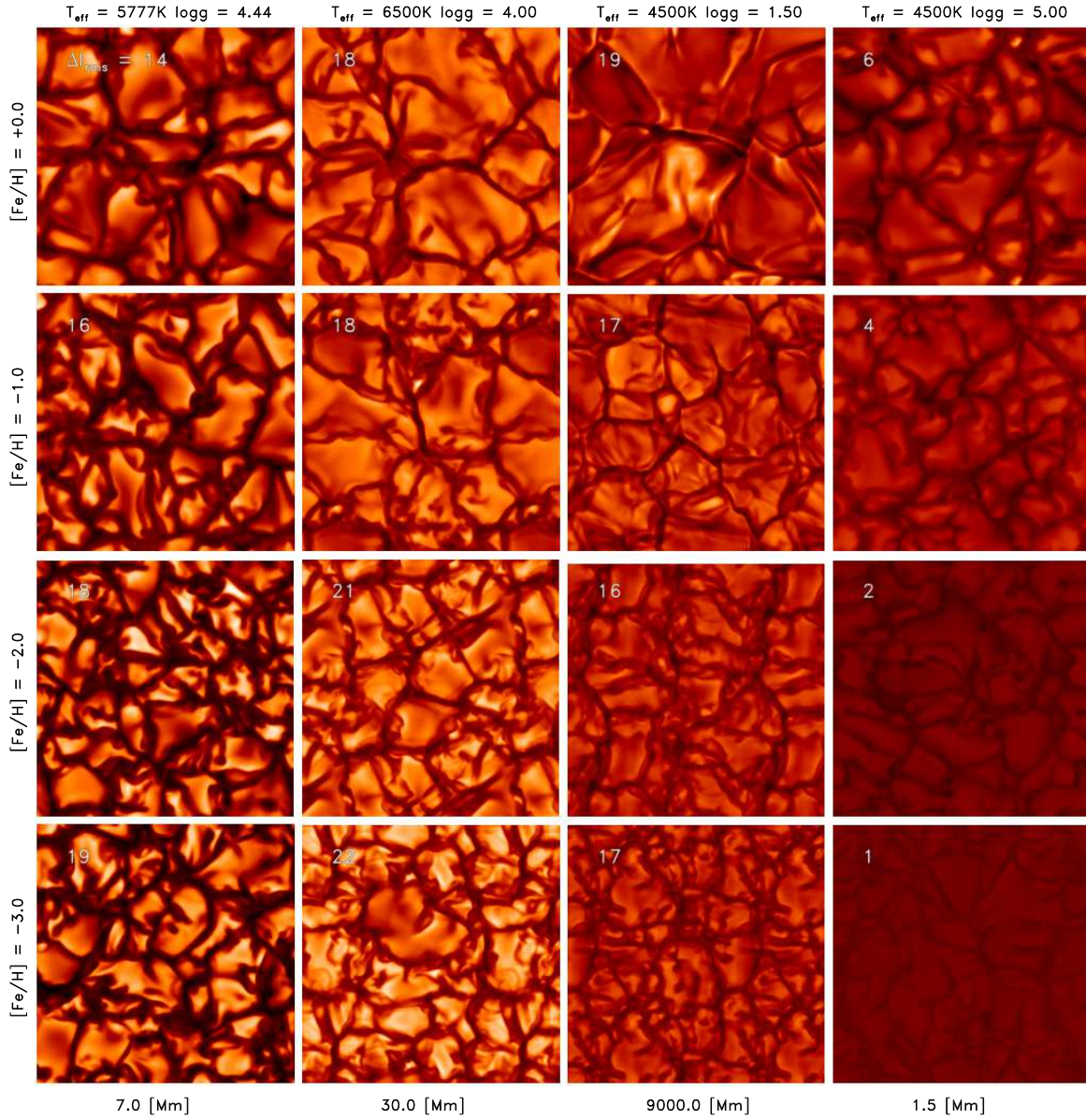


Figure 3.7: We show an overview of the emergent (bolometric) intensity ($[10^{12}\text{erg/s/cm}^2]$) for a selection of stars, namely main-sequence (MS), turnoff (TO), K-giant and K-dwarf (from left to right, respectively) at a given time instant. For each star, we show four metallicities $[\text{Fe}/\text{H}] = 0.0, -1.0, -2.0$ and -3.0 (from top to bottom, respectively). To facilitate comparisons between the different metallicity of each star, the intensity scale and the horizontal geometrical size of the metal-poor simulations are identical to $[\text{Fe}/\text{H}] = 0.0$, and the individual intensity contrasts [%] are indicated in each box.

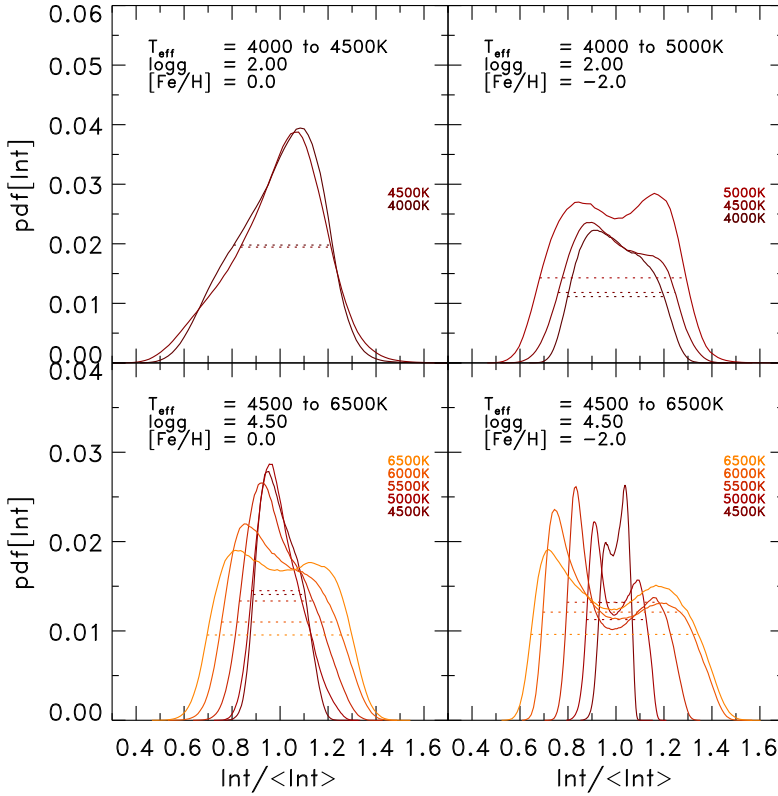


Figure 3.8: We show the temporally averaged histograms (resolved in 100 bins) of the (bolometric) intensity (solid lines) for various stellar parameters. To ease comparisons between the different stellar parameters, we normalized the individual intensity scales with its mean value. Furthermore, we have indicated the respective FWHM of the intensity histograms, I_{FWHM} , (dotted lines), a measure of the intensity contrast. Note the different ordinate scale in the top panel. The bimodal distributions are given due to the asymmetry and the large contrast in the up and downflows.

with surface gravity. The intensity histograms for giants are in general broader (higher contrast) compared to dwarfs of the same T_{eff} (see I_{FWHM}), hence exhibiting a larger intensity contrast. For dwarfs at lower metallicity (right bottom panel), the bimodality is more pronounced and the I_{FWHM} (contrast) is broader (higher) towards higher T_{eff} , while at lower T_{eff} the I_{FWHM} (contrast) becomes narrower (lower) compared to solar metallicity (left bottom panel). The latter hints at an *enhancement* of the effect of hidden or naked granulation.

To illustrate the latter in more detail, we show in Fig. 3.9 the rms of the bolometric disk center intensity fluctuations for $[\text{Fe}/\text{H}] = 0.0$ and -2.0 , which is commonly referred as the intensity contrast

$$\Delta I_{\text{rms}} = \left[\sum (I_i - \bar{I})^2 / N\bar{I}^2 \right]^{1/2} \quad (3.5)$$

with \bar{I} being the (spatial) mean intensity and N the number of data points (see Roudier & Muller, 1986). We remark that the shown ΔI_{rms} are temporal averages. It is essentially defined as the relative standard deviation, hence it reflects the width of the intensity distribution (see Fig. 3.8). This often measured value is very suitable for quantifying the range of brightness fluctuations due to granulation. The intensity contrast increases with higher T_{eff} and lower $\log g$. For our solar simulation, we get an intensity contrast of 15%, which is close to the one found by SN98 with 16% (see Col. 10 in Table B.1).

Towards higher T_{eff} , we find that s_{bot} , Δs , and the vertical velocity increase, as shown in Sects. 3.1.2 and 3.2.2. For increasingly hotter stars, the top of the convective zone, $z_{\text{top,cz}}$, penetrates higher and higher above the optical surface due to larger vertical velocities (see Fig. 3.19). Additionally, at higher T_{eff} (higher s_{bot} and Δs), the overall temperatures and their fluctuations also increase, implying that one observes increasingly higher layers, since the dominant H^- -opacity, hence the optical depth, depends sensitively on the temperature. Therefore, the granulation pattern is enhanced at higher T_{eff} , while on the contrary for lower T_{eff} the granulation becomes less visible, since $z_{\text{top,cz}}$ recedes below the optical surface in the latter case (see overview in Fig. 3.7). This phenomenon has been already described by Nordlund & Dravins (1990) as *naked granulation*.

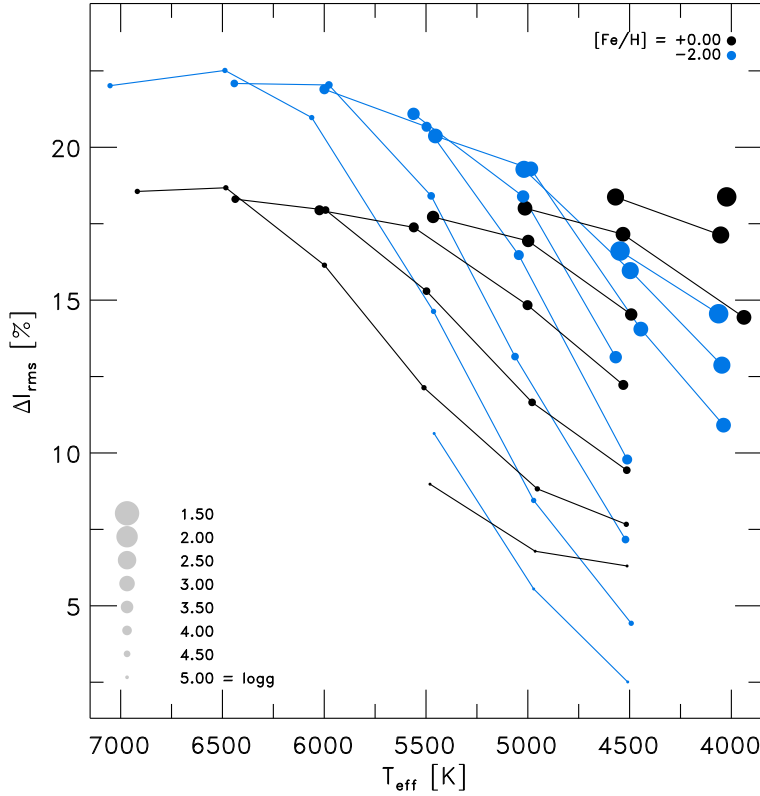


Figure 3.9: Overview of the (bolometric) intensity contrast ΔI_{rms} against T_{eff} for $[\text{Fe}/\text{H}] = -2.0$ and 0.0 (blue and black respectively). Models with the same gravity, but different T_{eff} are connected. The *enhanced* naked or hidden granulation at lower metallicity can be extracted in the larger range of intensity contrasts (see text for details).

Interestingly, in our simulations, we find for the first time on large parameter range that at lower metallicity the effect of naked and hidden granulation is more pronounced, in the sense that the range of contrast from cool, low-contrast dwarfs, to hotter, high-contrast dwarfs, is 61% larger (from 10.9 to 17.6) for our $[\text{Fe}/\text{H}] = -2.0$ simulations than for solar metallicity (see Fig. 3.9). At lower metallicity the major electron donors (metals) are depleted, therefore the formation of the dominant opacity source H^- depends primarily on the ionization of hydrogen, which is the reason for the steep increase of intensity contrast with higher T_{eff} (Nordlund & Dravins, 1990).

The variations in the intensity and in the intensity contrast with stellar parameters have important ramifications for observations. At the one hand, the enhanced naked or hidden granulation at lower metallicity affects the formation of spectral lines and the limb darkening. On the other hand, it should also lead to distinct signatures in the granulation background of asteroseismological observations and spectro-interferometric imaging.

Finally, we show in Fig. 3.10 the temporally averaged 2D spatial powerspectrum of the (bolometric) intensity. For lower wavenumber k the logarithmic powerspectrum is increasing, reaching a maximum, and decreasing again. The inverse wavenumber, where the maximum of powerspectrum is located, depicts the dominant size-scales of the emergent intensity. Since the granules correlate with brighter regions in the intensity maps that are hotter, the dominant size-scale is correlating with the typical granule size d_{gran} . We have derived the granule size in this way, which we want to discuss in the next section.

3.1.6 Granule size

The physical dimensions of the simulations boxes (s_x , s_y and s_z in Cols. 11 and 12 of Table B.1) are selected based on the mean diameter of granules (see Sect. 2.2.3 and Table B.1) and a target of about 10 granules in the box. Additionally, we measured the granule sizes by calculating the 2D spatial power spectrum of the bolometric intensity for the time series, and determining its maximum from the smoothed time average (see Fig. 3.10). This method is quite robust despite the large variations in gravity. In Fig. 3.11, we present the

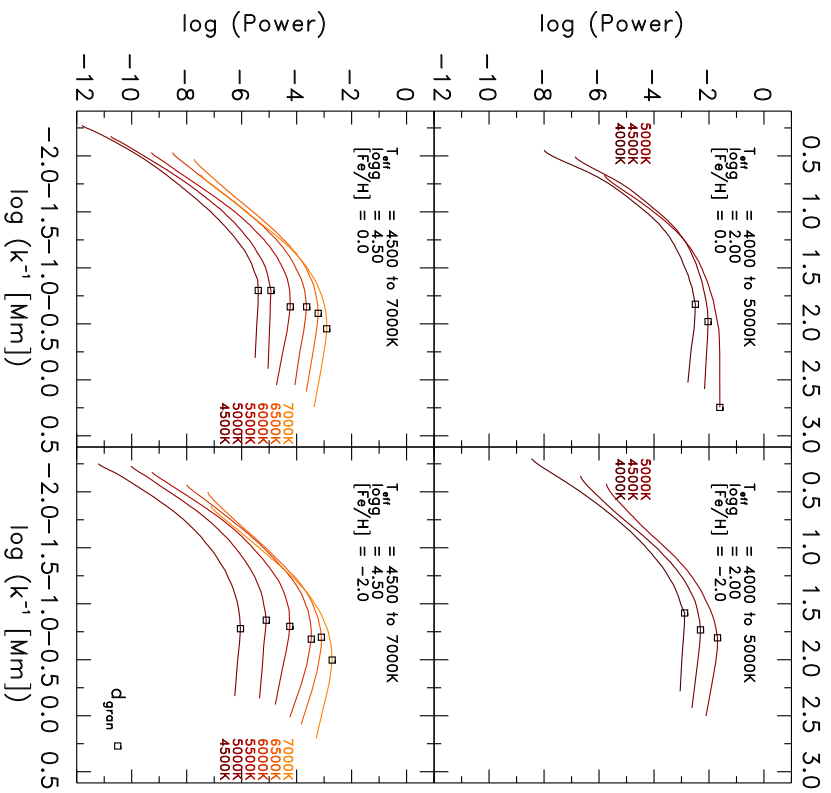


Figure 3.10: The temporally averaged 2D spatial powerspectrum of the intensity vs. the inverse wavenumber k^{-1} . We remark that the power-spectra are smoothed for clarity. Furthermore, we indicated the position of the maximal powerspectrum (box). Note the difference in abscissa of the top panel.

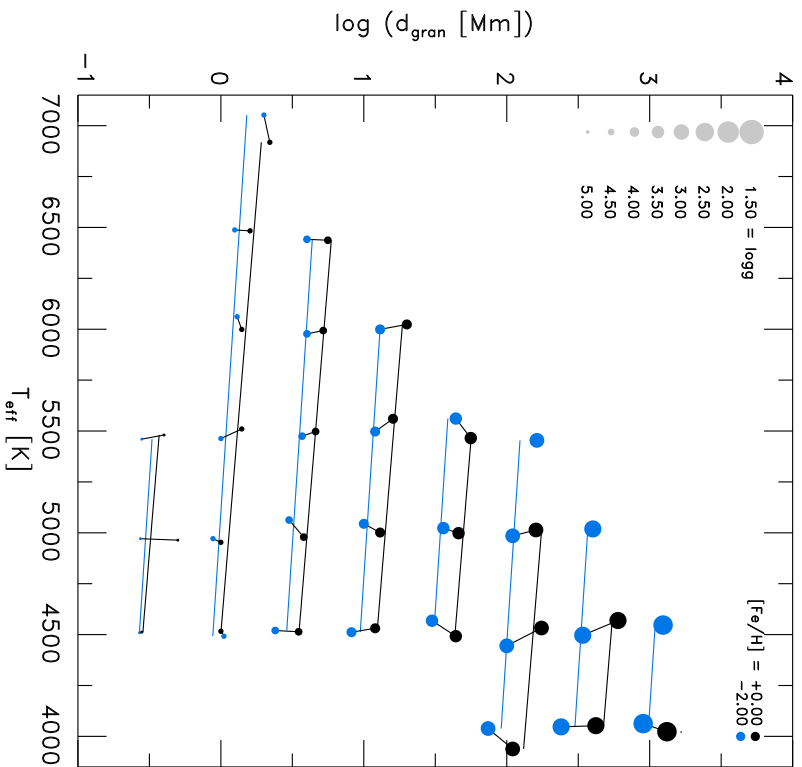


Figure 3.11: Overview of the granule diameter d_{gran} derived from the maximum of the mean 2D spatial power spectrum of the bolometric intensity against T_{eff} for $[\text{Fe}/\text{H}] = -2.0$ and 0.0 (blue and black respectively).

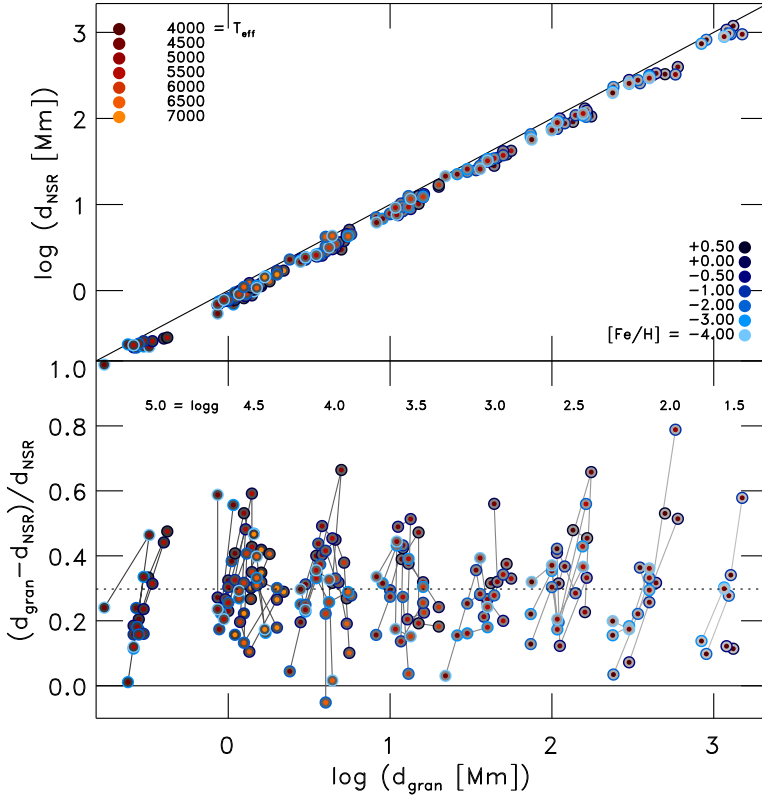


Figure 3.12: In the top panel, we compare the granule size approximated with the pressure scale height d_{NSR} (see Eq. 3.6) against the mean granule diameter d_{gran} (same as Fig. 3.11) for all models. The individual stellar parameters are indicated (T_{eff} , $\log g$ and $[\text{Fe}/\text{H}]$ with red, gray, and blue respectively). We indicated the position of $d_{\text{NSR}} = d_{\text{gran}}$ the solid diagonal line. In the bottom panel, we show also the relative residuals. We indicated also the mean residual (dotted line), which amounts to $\sim 30\%$. Here, models with the same gravity are connected (solid grey lines).

measured granule sizes d_{gran} (given in Col. 13 in Table B.1; see also App. A), showing that they become larger with smaller surface gravity. Also, the granules of the simulations with fixed $\log g$, the lowest T_{eff} are typically $\sim 50\%$ smaller compared to the simulations with the hottest T_{eff} , while for the models with the lowest metallicity they are typically $\sim 30\%$ smaller than for the metal-rich ones.

We find a remarkable validation for the approximation of the maximal horizontal extent of a granule based on mass-conservation considerations made by SN98 (see also Nordlund et al., 2009). Hereafter, we denote the following relation as the *Nordlund scaling relation* (NSR). The ascending buoyant plasma inside a cylindrical granule with radius r gives rise to a vertical mass flux with $j_z = [\pi r^2] \rho v_z$. This mass flux has to deflect and overturn increasingly towards the top. Due to conservation of mass, the upflow has to drain off sideways through the edge of the granule within approximately one pressure scale height H_P , hence resulting in a horizontal mass flux $j_h = [2\pi r H_P] \rho v_h$. The pressure is a quantity that preserves its characteristic shape with stellar parameters, i.e. the pressure of two different simulations look rather similar on a uniform depth scale, therefore the pressure scale height is preferred over the density scale height. Equating j_z and j_h we can solve for the (maximal) granular diameter, $d = 2r$:

$$d_{\text{NSR}} = 4 [v_h/v_z] H_P \approx 4H_P \quad (3.6)$$

We show in Fig. 3.12 a comparison of the granular diameters estimated with d_{NSR} and from the maximum of 2D spatial power spectra d_{gran} , which is shown in Fig. 3.11. The astonishing tight correlation can solely be interpreted as clear indication for the validity of the NSR. We find that the mean pressure scale height taken at the height of the maximum vertical rms-velocity below the optical surface ($\log \tau_{\text{Ross}} \sim 2.0$, see Fig. 3.19) gives the best match between d_{NSR} and the granule sizes. Furthermore, we also confirm that the relevant scale-height is that of the *total* pressure scale height, $H_P = p_{\text{tot}}/\rho g$, since we find a better agreement with the latter. The granular diameters found from the peak of 2D spatial power spectra are about 30% larger than the estimate from Eq. 3.6, i.e., $d_{\text{gran}} \sim 1.3d_{\text{NSR}}$ (see lower panel of Fig. 3.12). The variation of the velocity ratio v_h/v_z in the convection zone is rather small ($v_h/v_z \sim 1.0$) as both are of the order of the sound speed, therefore the variation in Eq. 3.6 stems predominantly from H_P . In hydrostatic

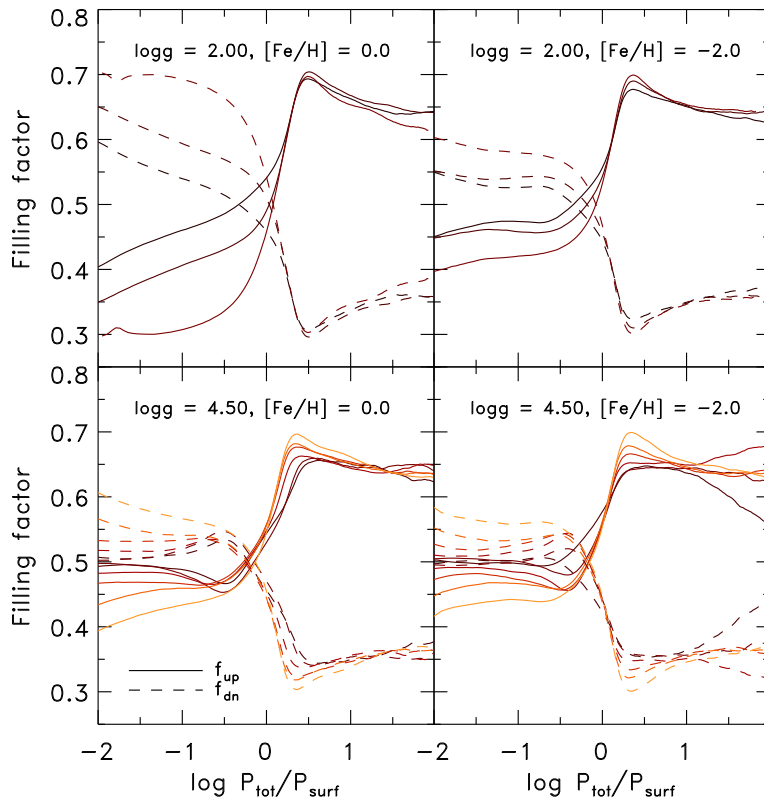


Figure 3.13: The filling factors vs. pressure normalized to the optical surface pressure for different stellar parameters.

equilibrium the pressure scale height is inversely proportional to the surface gravity ($H_P \propto 1/g$), which explains the strong correlation between the granular sizes and $\log g$. On the other hand, with increasing T_{eff} and $[\text{Fe}/\text{H}]$, the pressure scale height increases slightly because of the increase in the ratio of pressure and density ($H_P \propto p_{\text{tot}}/\rho$). The ratio actually increases even though both values decrease, since the density drops with height slightly more rapidly than the pressure.

Finally, we want to mention our finding on the filling factor for upflows and downflows, f_{up} and f_{dn} respectively. We derived the filling factor from the sign of the velocity field in the unaltered simulations on layers of constant geometrical height (see Fig. 3.13). Then we computed the mean filling factor in the convection zone, which yields on average for all simulations $f_{\text{up}} \simeq 0.65$ with a minute deviation of $\sigma = 0.014$. Therefore, we find that the mean filling factor is rather universal, and close to previous findings by SN98 with $f_{\text{up}} \sim 2/3$ and $f_{\text{dn}} \sim 1/3$. In deeper solar simulations, which reach down to 20Mm (Stein et al., 2011), we find very similar values for the filling factor.

3.2 Mean $\langle 3D \rangle$ atmosphere

In the following, we want to discuss the properties of the mean stratifications and the temporal and spatial averages of various important quantities. Unless specified otherwise, the $\langle 3D \rangle$ stratifications presented here are averages on surfaces of constant Rosseland optical depth, i.e. $\langle 3D \rangle = \langle 3D \rangle_{\text{Ross}}$. Whenever we employ alternative averages in the text, e.g., on constant geometrical height $\langle 3D \rangle_z$, we indicate that explicitly. We remark briefly that only the averages on constant geometrical height $\langle 3D \rangle_z$ strictly fulfill the equations of conservation (Eqs. 1.1, 1.2 and 1.3), therefore also the hydrostatic equilibrium, while all other averages exhibit slight deviations. For the sake of clarity, we display here only a subsample of our grid models including MS and RGB stars ($\log g = 4.5$ and 2.0) with solar and subsolar metallicity ($[\text{Fe}/\text{H}] = 0.0$ and -2.0). Whenever possible, we compare with corresponding 1D models that are obtained with our 1D code (see Sect. 2.4).

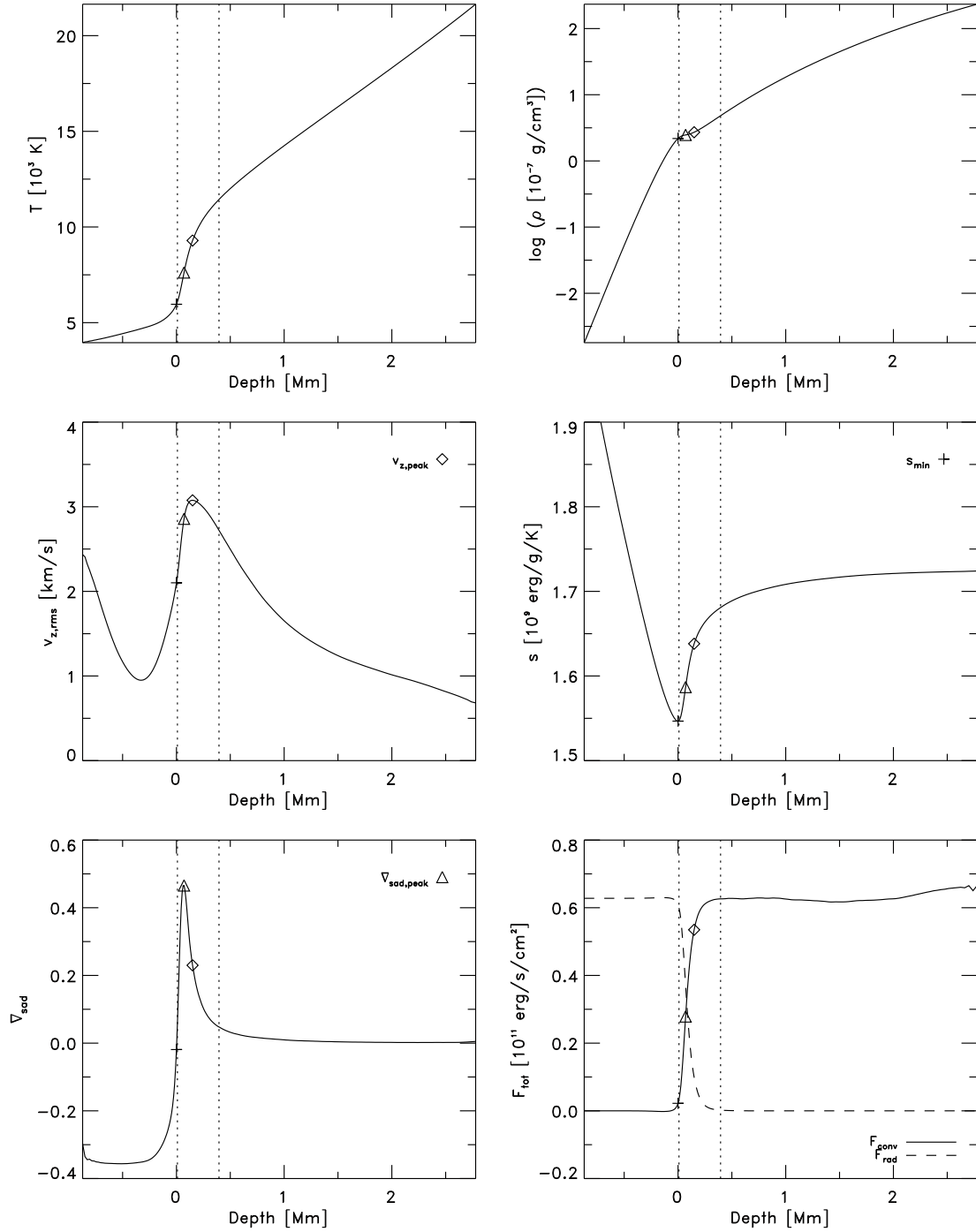


Figure 3.14: Temporal and spatial averaged mean $\langle 3D \rangle$ stratification of the solar simulation, which encompasses the temperature, T , density, ρ , vertical rms-velocity, $v_{z,rms}$, entropy, s , superadiabatic gradient, $\bar{\nabla}_{sad}$, and the radiative and convective energy flux. Furthermore, we marked the location of the superadiabatic region (SAR; vertical dotted lines) and indicated the location of the peak vertical rms-velocity (diamond), entropy minimum (plus), and the peak of the superadiabatic gradient (triangle).

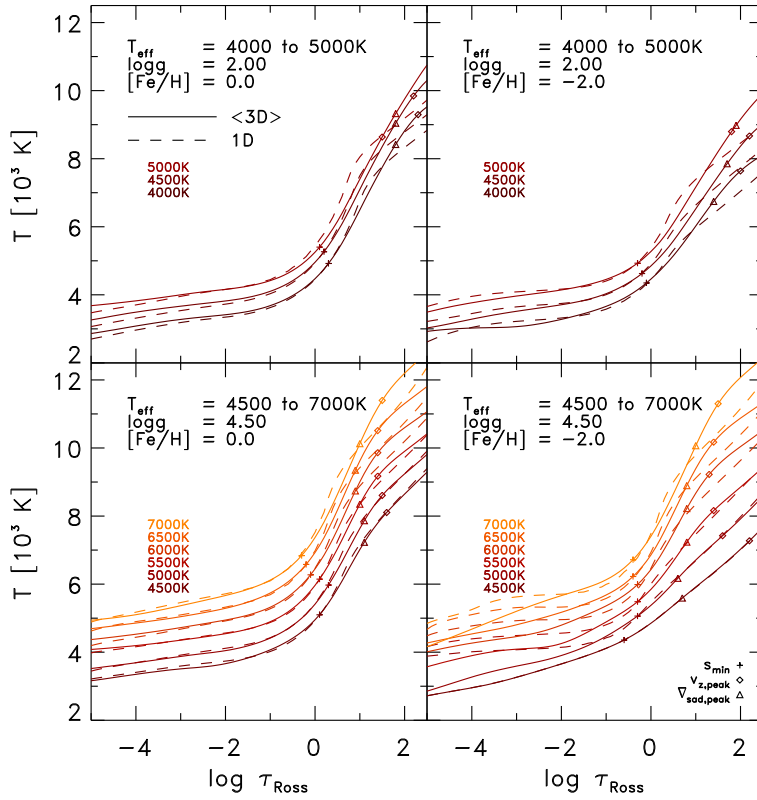


Figure 3.15: $\langle 3D \rangle$ stratifications of the temperature vs. optical depth for various stellar parameters (solid lines) and 1D models with $\alpha_{MLT} = 1.5$ (dashed lines). Furthermore, we have marked the positions of entropy minimum (plus), vertical peak velocity (diamond), and maximum in $\nabla_{sad} = \nabla - \nabla_{ad}$ (triangle).

Before continuing our discussion, we would like to briefly overview in Fig. 3.14 the temporal and spatial averaged stratification for six important variables – temperature, T , density, ρ , vertical rms-velocity, $v_{z,rms}$, entropy, s , superadiabatic gradient, $\vec{\nabla}_{sad}$, and the radiative and convective energy flux – from the solar simulation exclusively, in order to preview the stratifications more clearer, since later on in the following Sections we will display these for multiple stellar parameters. In Fig. 3.14, we show averages on layers of constant geometrical height, $\langle 3D \rangle_z$, and the optical surface is given at $z = 0$. Above the optical surface ($z < 0$) the highly stratified, almost isothermal atmosphere is located, where the temperature drops only little, while the density and pressure (not shown, but very similar to the density) are greatly declining towards higher altitudes. Below the optical surface, one finds the convection zone, where the convective motions due to the buoyancy force lead to the vertical velocities. Just below the optical surface, we would like to point out the importance of the superadiabatic region (SAR), as it will be referred repeatedly in the following (we marked in Fig. 3.14 the SAR with $\vec{\nabla}_{sad} > 0.1 \vec{\nabla}_{sad}^{peak}$). It is the region, where the transport of energy changes character, from predominantly convective to mainly radiative (see energy fluxes). The top of the SAR, where the superadiabatic temperature gradient becomes zero, i.e. $\vec{\nabla}_{sad} = 0$, marks the top the convection zone, since it is the uppermost point, where the Schwarzschild criterion is fulfilled. At the location of the peak of the superadiabatic gradient, one also finds the largest fluctuations and inhomogeneities in the thermodynamic variables due to the non-adiabatic transition to the photosphere. Furthermore, it is here in the SAR, where the entropy jump and the peak in the vertical velocity occur (see Fig. 3.14). In fact, the SAR effectively represents the physical outer boundary of the convective envelope. It is the most dynamic part in the interior of late-type stars, where the largest fluctuations are found. This is the reason why hydrostatic 1D modeling has the greatest challenges in this rather small region.

3.2.1 Temperature stratification

We first consider the temperature stratifications in optical depth, which we show in Fig. 3.15. We also show the corresponding stratifications of 1D theoretical model atmosphere with $\alpha_{MLT} = 1.5$ based on our 1D code

(dashed lines) with identical EOS and opacity tables as for 3D models. In the continuum forming layers around the optical surface ($-1.0 < \log \tau_{\text{Ross}} < 0.5$), the differences between $\langle 3D \rangle$ models with different T_{eff} s, but same $\log g$ and $[\text{Fe}/\text{H}]$, are rather small besides the shift in the temperature stratification corresponding to the difference in effective temperature ΔT_{eff} , which is to be expected since $T_{\text{eff}} \approx T(\tau = 2/3)$. Well above and below the optical surface, on the other hand, we find significant differences between the $\langle 3D \rangle$ models depending on the stellar parameters.

In the upper layers ($\log \tau_{\text{Ross}} < -2.0$) of atmospheres with solar metallicity, we find that the behavior in mean temperature is similar between 3D and 1D models. On the other hand, the metal-poor $\langle 3D \rangle$ models exhibit significantly cooler temperature stratifications compared to $\langle 3D \rangle$ models with solar metallicity ($\Delta T/T(\log \tau_{\text{Ross}} = -0.5) \sim -1\%$ and $\sim -14\%$ for $[\text{Fe}/\text{H}] = -1.0$ and -3.0 respectively), in particular, for dwarfs ($\log g = 4.5$). The temperature stratification in the upper photospheres of solar-metallicity models is largely controlled by radiative equilibrium, while for low-metallicity models this is not generally the case: for metal-poor models, the absorption features become considerably weaker, therefore, the radiative heating by spectral line re-absorption (q_{rad}) is dominated by the adiabatic cooling due to expansion of the ascending gas ($-p_{\text{th}} \vec{\nabla} \cdot \vec{v}$) in the energy balance (Eq. 1.3), leading to an equilibrium structure at cooler temperatures (Asplund et al., 1999b). For cool, metal-poor giants (e.g., $T_{\text{eff}} = 4000\text{K}$, $\log g = 2.0$), we recognize the effects of molecule formation on the structure of the high atmosphere. At sufficiently low temperatures, molecules start to form, which contribute with a large line opacity, shifting the balance from adiabatic to radiative heating and cooling, resulting in a stratification closer to the radiative equilibrium one (see Gustafsson et al., 2008). On the other hand, for giants with solar metallicity the radiative equilibrium is even more dominating, since these exhibit hotter stratifications than 1D models in the upper layers. Ludwig & Kučinskis (2012) find the same but on a much milder level. These effects are rather non-linear, and we find no simple systematic trends within our grid models.

We would now like to examine the influence of individual stellar parameters on the temperature stratification. Therefore, we show in Fig. 3.16 the temperature stratifications of models where we separately vary one at the time (T_{eff} , $\log g$, and $[\text{Fe}/\text{H}]$), while keeping the other two parameters constant. Figure 3.16 (top panel) shows, as expected, that with increasing T_{eff} , temperature becomes overall hotter above, but also below the optical surface, in order to provide the required total energy flux (higher enthalpy, Eq. 3.10). We find in our simulations (both 1D and 3D) that the increased T_{eff} s with hotter stratifications are accompanied by lower densities and higher vertical velocities below the surface (see $p_{\text{tot}}(\log \tau_{\text{Ross}} = 2.0)$ in Fig. 3.24 representatively for the ρ). The net effect on the convective flows are lower mass fluxes for higher T_{eff} s, since the decrease in density is predominating the increase in velocity, therefore resulting in a more inefficient convection. This is compensated with higher entropy jumps (see Fig. 3.20 with Δs as an inverse measure for convective efficiency), hence higher temperatures and steeper temperature gradients. On the other hand, the temperatures in the upper, radiative layers increase less with increasing T_{eff} than in the deeper, convective ones. We find with decreasing surface gravity (middle panel in Fig. 3.16) the same correlations as with increasing T_{eff} s before, the temperature stratifications become hotter below the photosphere, and due to lower densities we find a more inefficient convection, while the upper atmosphere is less affected. For lower metallicities (bottom panel), the temperature stratifications are significantly cooler, both above and below the optical surface ($\Delta T/T(\log \tau_{\text{Ross}} = 2.0) \sim -5\%$ and -15% for $[\text{Fe}/\text{H}] = -1.0$ and -3.0 respectively). At the top the stratifications are cooler at lower $[\text{Fe}/\text{H}]$ due to the dominance of adiabatic cooling over radiative heating. Below the optical surface, we find higher densities with lower velocities and entropy jumps (while the mass flux is increasing), therefore, leading to an efficient convection with shallow temperature gradients at lower metallicities. We find cooler models that fall below the opacity edge, which we describe below (compare $T_{\text{eff}} = 5000\text{K}$ in Fig. 3.18), follow an adiabatic temperature stratification even in the atmosphere, which coincides with the rather sudden change between $[\text{Fe}/\text{H}] = -1.0$ and -2.0 in Fig. 3.16 (bottom panel). Besides our standard averages on constant Rosseland optical depth, we show also the averages on constant geometrical depth scale $\langle 3D \rangle_z$ (here is z fixed and $\tau_{\text{Ross}} = \langle \tau_{\text{Ross}} \rangle_z$), which are systematically different, in particular, below the optical surface, but behave qualitatively in a similar way with stellar parameters.

In the sub-photospheric region ($\log \tau_{\text{Ross}} > 0.5$), where convection dominates, the temperature gradients $\nabla = d \ln T / d \ln p_{\text{tot}}$ ⁶ become increasingly steeper with higher T_{eff} , reflecting the hotter interior stratifica-

⁶We remark that ∇ increases, if only the thermodynamic pressure is (mistakenly) included, neglecting the turbulent component.

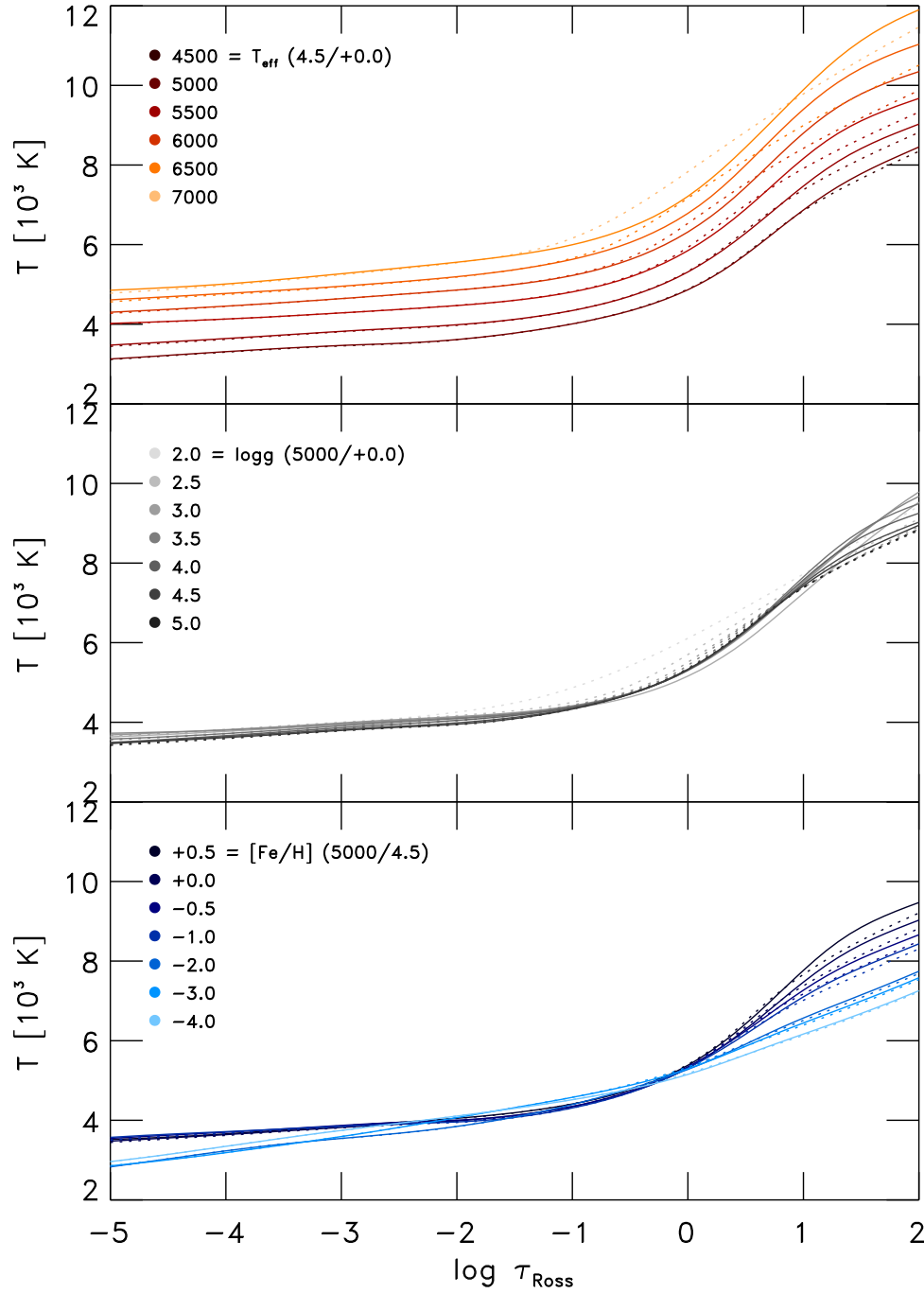


Figure 3.16: $\langle 3D \rangle$ temperature stratifications with the variation of one stellar parameter at a time, while the two others are fixed (T_{eff} , $\log g$, and $[\text{Fe}/\text{H}]$, from top to bottom, respectively). We show our standard averages on constant optical depth $\langle 3D \rangle$ (solid line) and on constant geometrical depth $\langle 3D \rangle_z$ (dotted line).

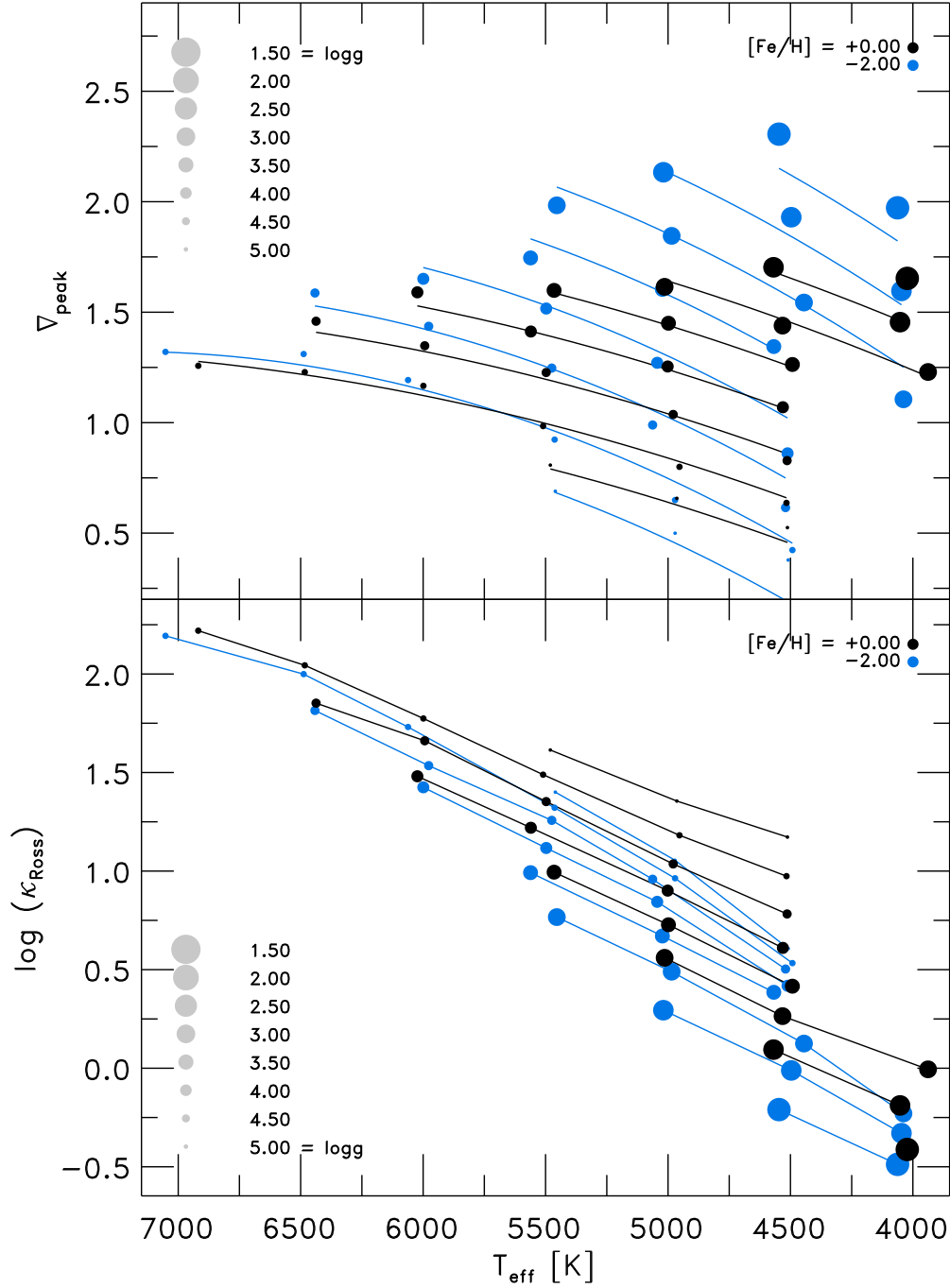


Figure 3.17: Overview of the maximum temperature gradient ∇_{peak} (top panel) and Rosseland opacity κ_{Ross} taken at the height $\tau_{\text{Ross}} \approx 3.0$ (bottom panel) against T_{eff} for $[\text{Fe}/\text{H}] = -2.0$ and 0.0 (blue and black respectively). Models with the same surface gravity are connected by their respective functional fits in the top panel (solid lines; see App. A).

tions. This can be illustrated with the maximum in temperature gradient, $\nabla_{\text{peak}} = \max \nabla$, which we show in Fig. 3.17 (functional fits are also given in App. A). The increase of ∇_{peak} with T_{eff} is close to linear, but it seems to saturate at higher T_{eff} (see $T_{\text{eff}} \geq 6500\text{K}$). We find that the maximum in temperature gradient ∇_{peak} reproduces qualitatively a similar behavior as the intensity contrast ΔI_{rms} with stellar parameter (compare Figs. 3.9 and 3.17), which is consistent with the strong temperature sensitivity of the H^- opacity. Furthermore, our metal-poor simulations exhibit a larger range of ∇_{peak} -values than their solar metallicity counterparts, and ∇_{peak} is similarly *enhanced* at lower metallicity (compare also $T(\log \tau_{\text{Ross}} = 2.0)$ for dwarfs in Fig. 3.15), as the intensity contrast (see Sect. 3.1.5). Our cool metal-poor simulations have flatter and hot metal-poor simulations have steeper temperature stratifications than the metal-rich part of our grid (see Fig. 3.16). Curiously, ∇_{peak} is close to constant with metallicity for the solar T_{eff} and $\log g$.

We identify three main effects for the given variations in temperature gradients with stellar parameters in the SAR, which are rooted in the hydrodynamics and the radiative transfer: velocity field, convective efficiency, and radiative back-warming.

1. As we discussed above (see Sect. 3.1.3), the entropy jump Δs increases with effective temperature according to a power law (see Fig. 3.20). This behavior arises due to the variations in the radiative losses (see Sect. 3.2.8), which is accompanied by changes in internal energy and density (see Fig. 3.18). The velocities rise rapidly, as exhibited by the growth of $v_{z,\text{rms}}^{\text{peak}}$ and also $p_{\text{turb}}^{\text{peak}}$ with T_{eff} (see Figs. 3.19 and 3.23 respectively). Similar to ∇_{peak} , both $v_{z,\text{rms}}^{\text{peak}}$ and $p_{\text{turb}}^{\text{peak}}$ occur in the SAR, and both increase towards higher T_{eff} and lower $\log g$.
2. The *mass mixing length* α_m changes with stellar parameters (Trampedach & Stein, 2011a). It is evaluated as the inverse gradient of the vertical mass flux, separately in the up- or downflows, hence $\alpha_m^{-1} = d \ln j_{z,\text{up}} / d \ln p$, with $j_{z,\text{up}}$ being the vertical mass flux in the upflows. Therefore, the mass mixing length is composed of the gradients of the density and the vertical velocity, i.e. $\alpha_m \propto 1/d \ln \rho + 1/d \ln v_z$. We find that α_m increases for lower Δs , $v_{z,\text{rms}}^{\text{peak}}$ and ∇_{peak} .
3. In the lower photospheric layers, where the continuum forms, radiation is absorbed (*blocked*) by spectral lines; this implies that less radiative flux can be transported at the wavelengths corresponding to spectral lines and, conversely, that more flux has to be pushed through continuum windows, an effect commonly referred to as *line-blanketing*. This in turn leads to a steepening of the temperature gradient and to additional heating of the sub-surface layers, also known as *back-warming* (see Mihalas, 1970; Nordlund et al., 2009). In 1D models it is straightforward to quantify the effect of back-warming, as done for example by Gustafsson et al. (2008), who found it to contribute a slight increase in temperatures below the surface ($\Delta T/T(\tau_{\text{Ross}} = 10) \simeq 5\%$ for solar metallicity stars with $T_{\text{eff}} \approx 5000\text{K}$ and $\log g = 3.0$). In our 3D RHD atmosphere models, line-blanketing and back-warming effects are also naturally included through our opacity-binning method. Isolating the radiative back-warming effect in our 3D simulations is, however, a little more involved than in 1D and we defer the analysis of this mechanism to a future paper in this series.

The three mentioned effects are non-linearly coupled and compete with each other, making it difficult to disentangle the individual contributions.

We would like now to examine more closely a sample of (3D) models in the $\varepsilon - \rho$ -plane, as shown in Fig. 3.18, in order to better illustrate the variations with stellar parameters. One can clearly distinguish three different regimes: the adiabatic convection zone, the photospheric transition, and the almost isothermal upper atmosphere.

At the bottom boundary, sufficiently deep in the convection zone where entropy fluctuations become small, $\langle \delta s \rangle = 0.3\%$, the models follow closely the associated adiabats with $s = s_{\text{bot}}$ (green lines). They deviate increasingly from their adiabats, as the top of the convection zone is approached. This is due to the entropy deficient downdrafts (cooled in the photosphere) becoming less diluted by the entropic upflows, as the optical surface is approached. For the 1D models (blue dashed lines), the value of the entropy at the bottom of the stratifications is evidently overestimated, particularly at higher T_{eff} , but this is because we haven't calibrated the α_{MLT} parameter here, and we have used a value of 1.5 for all models. The transition of energy transport from fully convective to fully radiative is clearly visible, since, at the optical surface, one finds a sharp isochoric ($\Delta \rho \sim 0.0$) drop in internal energy (this is basically the enthalpy-jump

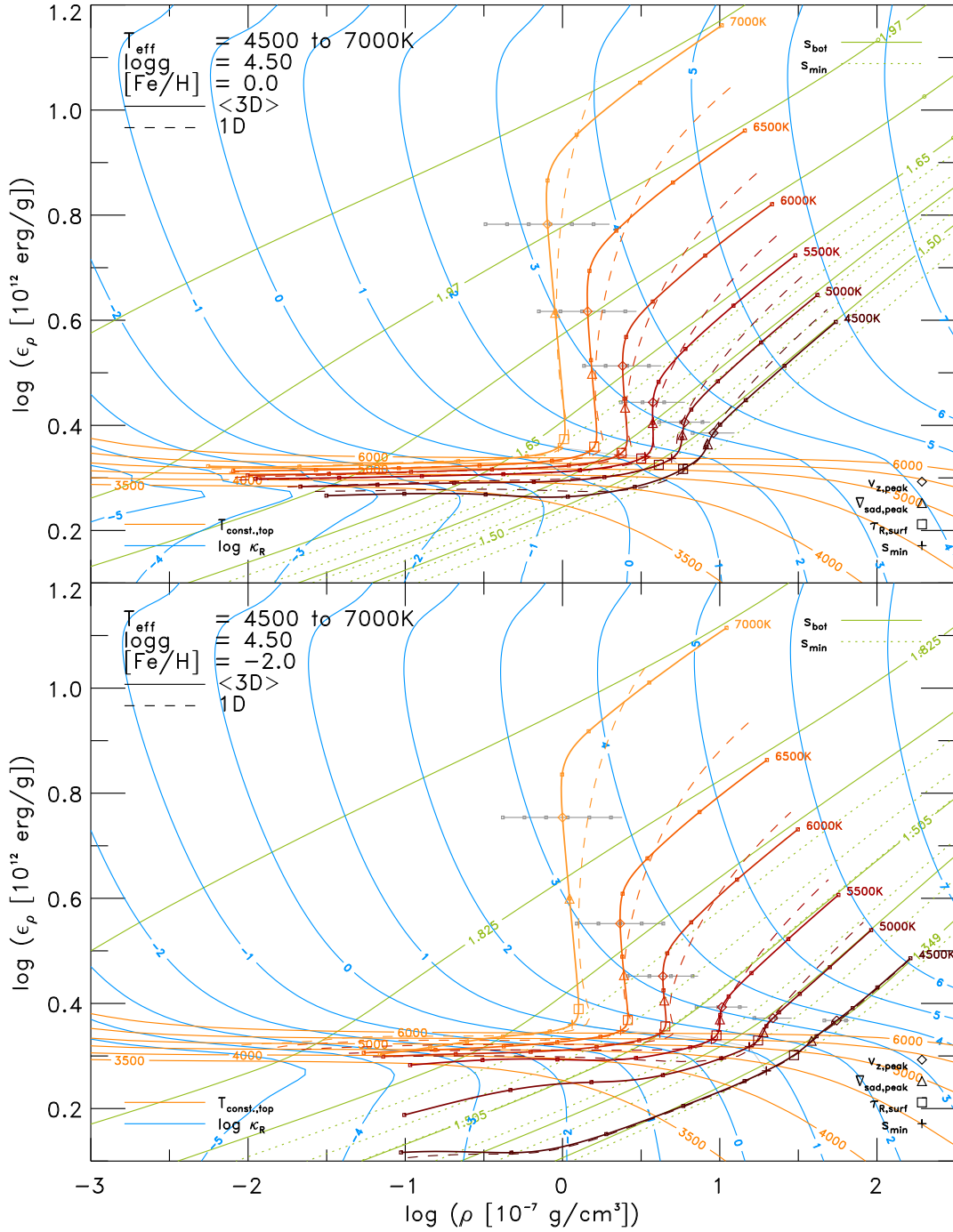


Figure 3.18: We show the mean internal energy against mean density for dwarf models ($\log g = 4.5$) with $[Fe/H] = 0.0$ and -2.0 (top and bottom panel, respectively). The specific isocontours for the entropy s_{bot} (green solid) and s_{min} (green dotted), Rosseland opacity per volume, $\rho \kappa_{\text{Ross}}$, (blue) and temperature T (orange) are underlayed. Moreover, the positions of entropy minimum s_{min} (plus), optical surface (large square), vertical peak velocity $v_{z,\text{rms}}^{\text{peak}}$ (diamonds) and maximum in ∇_{sad} (triangle) are marked respectively. The amplitude of $v_{z,\text{rms}}^{\text{peak}}$ is indicated with horizontal bars with markings in 1 km/s. We also included the 1D models with $\alpha_{\text{MLT}} = 1.5$ (blue dashed lines). The range in optical depth is shown from $\log \tau_{\text{Ross}} = -5.0$ to $+5.0$ for each dex (small squares). However, we note that our simulations boxes are much deeper ($\log \tau_{\text{Ross}} \approx +7.5$).

Δh in Eq. 3.10). The ε -jump coincides with the sub-photospheric region ($0.0 < \log \tau_{\text{Ross}} < 2.0$), where the atmosphere starts to become transparent. The transition zone ends eventually at the optical surface ($\log \tau_{\text{Ross}} \simeq 0.0$, marked with big squares). Above the optical surface ($\log \tau_{\text{Ross}} < 0.0$) the atmosphere is almost isothermal (compare with the orange isotherms in Fig. 3.18), with exponentially decreasing density and almost constant internal energy ($\Delta \varepsilon \sim 0.0$).

The entropy s_{bot} at the bottom grows exponentially with increasing T_{eff} and decreasing $\log g$. We showed above that the entropy jump increases in a similar way (see Fig. 3.5). Here we find a similar behavior for the jump in internal energy ($\Delta \varepsilon$, hence Δh) in the photosphere. Moreover, we show in Fig. 3.18 the positions of $\nabla_{\text{sad}}^{\text{peak}}$ and $v_{z,\text{rms}}^{\text{peak}}$ located in the ε -jump, and, again, we find both $v_{z,\text{rms}}^{\text{peak}}$ and $\nabla_{\text{sad}}^{\text{peak}}$ to scale exponentially with T_{eff} . For $v_{z,\text{rms}}^{\text{peak}}$, we have indicated the amplitudes as well, which also increases exponentially with T_{eff} . All of the aforementioned positions are distributed rather regularly in the $\varepsilon - \rho$ -plane, while they are less so on the $\log \tau_{\text{Ross}}$ -scale (see Fig. 3.15). The position of s_{min} is close to the optical surface and shows little variation in optical depth.

At lower energies and densities in Fig. 3.18 ($\log \varepsilon \sim 0.3$ and $\log \rho \sim 3.0$ to 0.0) we notice the effect of H I and He I opacity in form of an edge in the opacity contours ($\log \kappa_{\text{Ross}} \sim -5.0$ to -1.0), since the bound-free absorption increases (more excited states) towards higher energy below the ionization energy, and they fade away again above it. Models that fall below this edge exhibit a rather different stratification. In particular, towards cool metal-poor dwarfs, i.e. lower T_{eff} , higher $\log g$, and lower $[\text{Fe}/\text{H}]$, the models more closely follow adiabats than isotherms, in the atmosphere. This effect of the competition between radiative and dynamic heating (see beginning of this Sect.) above the convection zone becomes particularly evident at lower metallicity (for $[\text{Fe}/\text{H}] \leq -2.0$). However, for the 1D models (blue dashed lines), this is obviously not the case, since these always follow isotherms due to the enforcement of radiative equilibrium. Furthermore, the cool metal-poor (3D) models also display higher densities at the optical surface, thereby spanning a larger ρ -range for different T_{eff} s. The stratifications of simulations of hotter dwarfs, on the other hand, depend little on metallicity. For the simulations, we have only plotted the range $\log \tau_{\text{Ross}} \in [-5.0, 5.0]$, and the top of this is reached at much higher densities for the metal-poor dwarfs than for the solar metallicity dwarfs. Therefore, the density ranges covered above the optical surface by the individual atmospheres is small for metal-poor models ($\min[\log \rho] \sim -1.0$ and -2.0 , respectively; see Fig. 3.18).

3.2.2 Velocity field

Next, we consider the velocity field in our simulations, which arise self-consistently from the solution of the hydrodynamic equations. In Fig. 3.19 we show the rms-velocity of the vertical component $v_{z,\text{rms}}$, being the flux carrying component of the convective flows, and being the broadening component of spectral lines at disk center.

The buoyant uprising plasma will experience increasingly a decrease in density towards the photosphere, hence a strong density gradient, and due to mass conservation, the convective motions will eventually overturn. Therefore, $v_{z,\text{rms}}$ peaks in the SAR around $\log \tau_{\text{Ross}} \sim 1.5$ for dwarfs and ~ 2.3 for giants. Furthermore, since in the SAR, the transition region from convective to radiative transport of energy takes place due to decrease in opacity and the subsequent radiative losses, here we find the strongest turbulent motions concomitant with the greatest fluctuations in all thermodynamical quantities (in particular, entropy, temperature and density, see Figs. 3.27, 3.15 and 3.20). Further towards the interior, $v_{z,\text{rms}}$ drops as the density increases. From the slightly sub-photospheric maximum, velocities fall off to a minimum above the optical surface, then increases again in the higher atmosphere (see Fig. 3.19). Towards upper layers, $v_{z,\text{rms}}$ increases again due to p-modes, excited in the SAR but leaking out of the acoustic cavity as they have frequencies above the acoustic cut-off. The metal poor simulations show a slightly smaller increase in $v_{z,\text{rms}}$, since their density gradients are shallower due to steeper T -gradients. The declining velocity above the surface is due to the fact that the convective motions overshoot well above the top of the convection zone. We find the velocity minimum to occur between $\log \tau_{\text{Ross}} \sim -2.3$ for dwarfs and -1.5 for giants.

As to be expected from spectral observations, the magnitude of the velocity field is enhanced towards higher T_{eff} , lower $\log g$, and higher $[\text{Fe}/\text{H}]$, similar as Δs . The symmetry of the velocity profile changes with $\log g$ and metallicity, while it is little affected by T_{eff} . For lower $\log g$, the peak in the velocity field is increasingly shifted to optically deeper layers (e.g., at solar metallicity the average peak position for

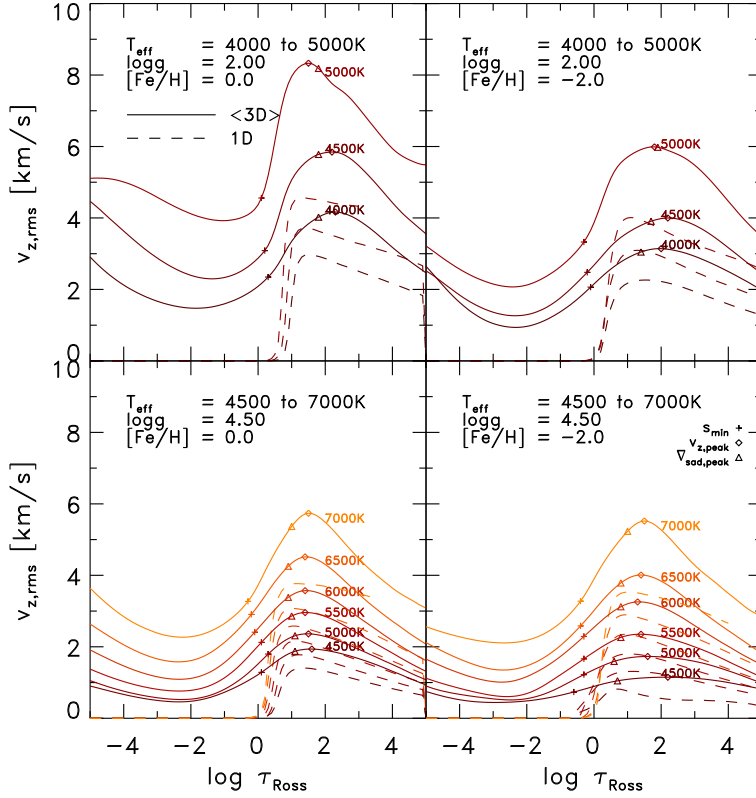


Figure 3.19: Vertical rms-velocity, $v_{z,rms}$, from the (3D) stratifications (solid lines) and convective velocity v_{MLT} from the corresponding 1D MLT models (dashed lines) as function of optical depth $\log \tau_{Ross}$ for various stellar parameters.

dwarfs is $\langle \log \tau_{Ross} \rangle \sim 1.5$, while for giants it is ~ 2.0). The coolest metal-poor simulations display a flatter profile, and the position of the minimum is increasingly shifted towards higher layers, especially for extreme metal-poor dwarfs ($[Fe/H] < -3.0$), and the profile is therefore stretched and skewed.

For comparison, we also show in Fig. 3.19 the convective velocity v_{MLT} of our 1D models determined by MLT. It is apparent that the general trends of increasing velocities with increasing T_{eff} and $[Fe/H]$ and decreasing $\log g$, are common between the simulations and the 1D MLT models, although much less pronounced in 1D. Furthermore, v_{MLT} drops rather sharply at the top of the convection zone (as given by the Schwarzschild criterion), as no overshooting is allowed for in our implementation of MLT. Several non-local variants of MLT exists, and they allow for overshooting, but none of them produce velocity profiles close to that of our simulations. We also want to mention the large asymmetry in velocities of the up- and downflows (SN98): in 3D simulations, the latter are much faster than the former (up to ~ 2 faster, in particular, for cool dwarfs), contrary to what is normally assumed in 1D descriptions of convection.

The peak vertical rms-velocity, $v_{z,rms}^{peak}$ (see bottom panel of Fig. 3.20), is a good measure of the global magnitude of velocities in the simulations. It also serves as a measure of the amount of turbulence present in the simulations. The actual values are also given in Col. 9 in Table B.1, together with a functional fit in App. A. The variation of $v_{z,rms}^{peak}$ with stellar parameters resembles that of the entropy jump Δs (compare top and bottom panel in Fig. 3.20), namely it also increases exponentially with higher T_{eff} and lower $\log g$ and linearly with $[Fe/H]$. An interesting aspect is the increase of $v_{z,rms}^{peak}$ and Δs with T_{eff} , which are close to exponential, indicating a correlation between the two. The characteristic variations of $v_{z,rms}^{peak}$ correspond to the inverse variations of the density taken at the same heights as the peaks in $v_{z,rms}$ (see middle panel in Fig. 3.20). This behavior arises due to conservation of mass (Eq. 1.1), which can be expressed as

$$\langle \partial_z \ln \rho \rangle = - \langle \partial_z \ln v_z \rangle \quad (3.7)$$

for a stationary flow ($\partial_t \rho = 0$). Of course, under this assumption, this equation is strictly speaking valid only locally, while we compare here averaged values. Despite that, we find that this relation is, in general,

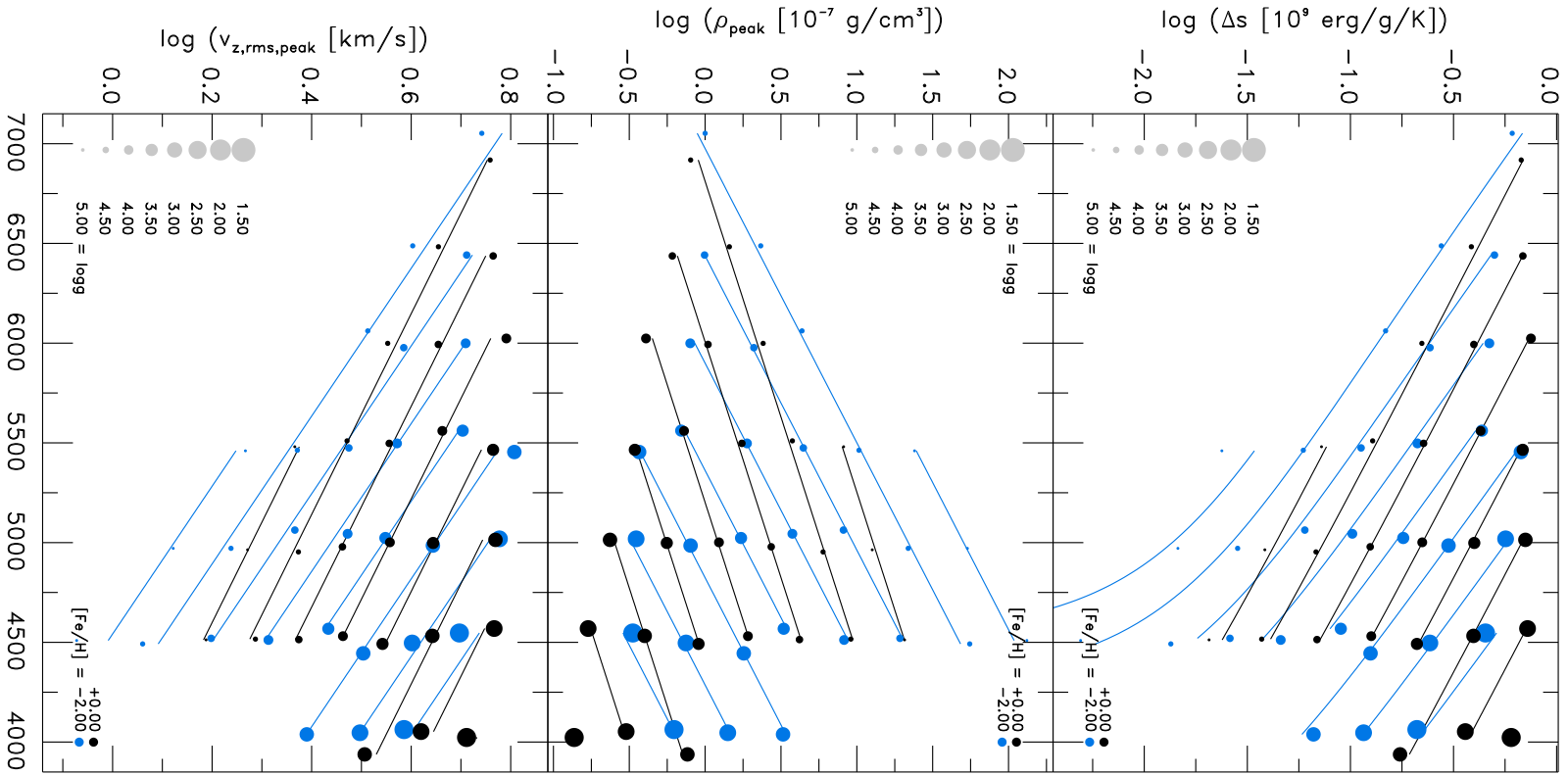


Figure 3.20: Overview of the entropy jump (top panel), maximal vertical rms-velocity below the surface $v_{z,\text{rms}}^{\text{peak}}$ (middle panel) and the density at the same height ρ_{peak} (bottom panel) vs. T_{eff} for $[\text{Fe}/\text{H}] = -2.0$ and 0.0 (blue and black respectively). Models with the same gravity are connected with their respective functional fits (solid lines; see App. A). Note the inverse correlation between density and velocity.

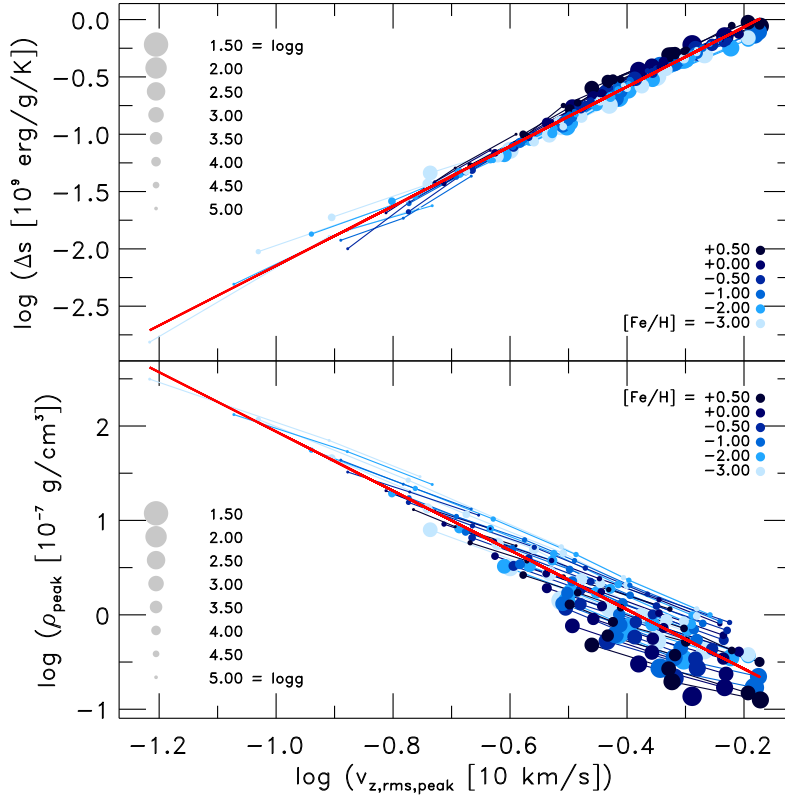


Figure 3.21: Comparison of the entropy jump Δs (top panel) and the density at the optical depth of the maximal vertical velocity below the optical surface ρ_{peak} (bottom panel) vs. maximal vertical rms-velocity $v_{z,rms}^{\text{peak}}$ for all models. A linear fit is also indicated in both panels (red lines).

qualitatively fulfilled across the whole depth of our simulations. Towards the optical surface, the density decreases, which has to be compensated by faster velocities, in order to fulfill conservation of mass as well as sustain the energy flux. The velocity field profile results ultimately from the interplay between the vertical and horizontal acceleration due to buoyancy and overturning respectively. The latter in turn is set by the radiative losses that arises from the prevailing opacity conditions according to the thermodynamic state of the plasma (see Sect. 3.2.8). Furthermore, one can also reason that at a higher effective temperature, hence hotter temperature stratification, the density will be lower (ideal gas gives for isobars $T \propto 1/\rho$; see also middle panel in Fig. 3.20), however, at the same time, more energy (enthalpy) has to be carried to the surface, which necessitates a faster flow (as is given in Eq. 3.11). The entropy jump, density, and velocity are coupled intimately with each other (the vertical mass flux is $j_z = \rho v_z$). Therefore, changes in one quantity imply corresponding variations in the values of the other quantities, and vice versa. The radiative energy losses at the photospheric transition generate the entropy fluctuations according to the prevailing opacity and the irradiation-duration, hence it sets the amplitude of the entropy jump Δs . On the other hand, the entropy deficient plasma with its density excess determines the buoyancy force, $f_B \sim \Delta\rho$, and therefore the vertical velocities v_z of the downdrafts. The downdrafts in turn will settle the upflows in order to deliver the required convective energy flux. The subtle details in the chain of causalities are non-trivial and beyond the scope of the present paper.

Similar to our finding in Sect. 3.1.3 of a scaling relation between the entropy jump and the constant entropy value of the adiabatic convection zone $\Delta s(s_{\text{bot}})$, we find here again another interesting, tight scaling relations between ρ_{peak} , $v_{z,rms}^{\text{peak}}$ and Δs , which we show in Fig. 3.21. The values are plotted on a double logarithmic scale, to more clearly illustrate the power-law character of the relations. From the above discussion, it follows that the vertical velocity is also correlated with the constant entropy value s_{bot} of the adiabatic convection zone and the density. We also show linear fits of the density ρ_{peak} and entropy jump Δs as a function of $v_{z,rms}^{\text{peak}}$ in log-log scale (red lines in Fig. 3.21), exhibiting the slopes of $\log \Delta s / \log v_{z,rms}^{\text{peak}} \sim 0.46$ and $\log \rho_{\text{peak}} / \log v_{z,rms}^{\text{peak}} \sim -1.20$, hence a scaling with the respective slopes.

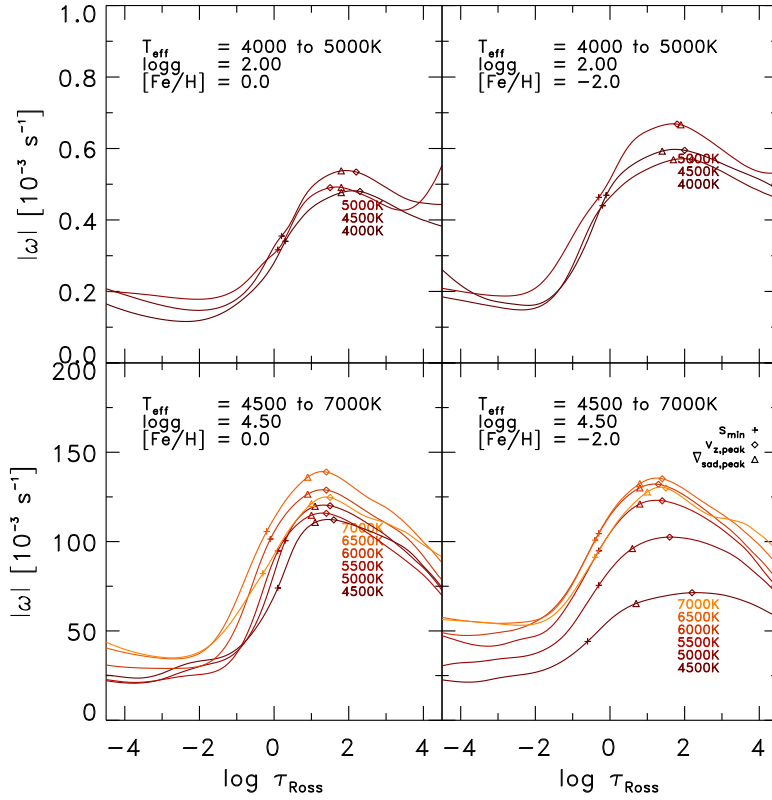


Figure 3.22: (3D) stratification of the absolute value of the vorticity $|\bar{\omega}|$ vs. optical depth is shown for various stellar parameters.

In 3D RHD simulations, the non-thermal, macroscopic velocity fields arising from convective instabilities are computed self-consistently from first principles and therefore have an immediate physical meaning. They represent the buoyant motions associated with convection and its turbulent features, and their statistical properties carry equally important physical information as the mean temperature or density stratifications. By contrast, in 1D atmosphere modeling, a free-parameter-dependent velocity field v_{MLT} is derived for the convective flux in MLT. Also, for radiative transfer and spectral line formation calculations, two ad-hoc Gaussian velocity distributions – the so-called micro- and macroturbulence (ξ_{turb} and χ_{turb} , respectively) – are usually introduced to model Doppler broadening of spectral lines associated with non-thermal (e.g., convective, turbulent, oscillatory, etc.) gas motions in stellar atmospheres. The values of the micro- and macroturbulence parameters are determined by comparing synthetic and observed spectral line profiles and line strengths. Usually, a depth-independent value of the microturbulence ξ_{turb} and one global value of the macroturbulence χ_{turb} are applied in theoretical spectrum syntheses with 1D model atmospheres. Full-3D line formation calculations using 3D models similar to those described here, have demonstrated that in late-type stars the required non-thermal Doppler line broadening is indeed primarily the result of Doppler shifts from the convective motions and to a lesser extent oscillations in the atmosphere (Asplund et al., 2000a). As such this non-thermal velocity field is clearly depth-dependent, while micro- and macroturbulence are almost always assumed to be non-varying with depth. Furthermore, v_{MLT} is solely assigned to satisfy the necessary amount of convective flux by the individual prescription of MLT. While, interestingly, v_{MLT} mimics to a certain extent the run of $v_{z,\text{rms}}$ in the interior for cooler dwarfs. We remark that this interpretation is however not physically consistently motivated. Moreover, the convective velocity varies depending on its actual implementation (e.g. Böhm-Vitense, 1958; Henyey et al., 1965) and, as such, v_{MLT} should be interpreted and used with caution. We point out that one important motivation for conducting 3D RHD atmosphere models is the fact that the before mentioned spurious inconsistent velocities become redundant. The hydrodynamical simulations account consistently for only one unique velocity field.

Another good measure for the turbulence of a velocity field is the absolute value of the vorticity $|\bar{\omega}| =$

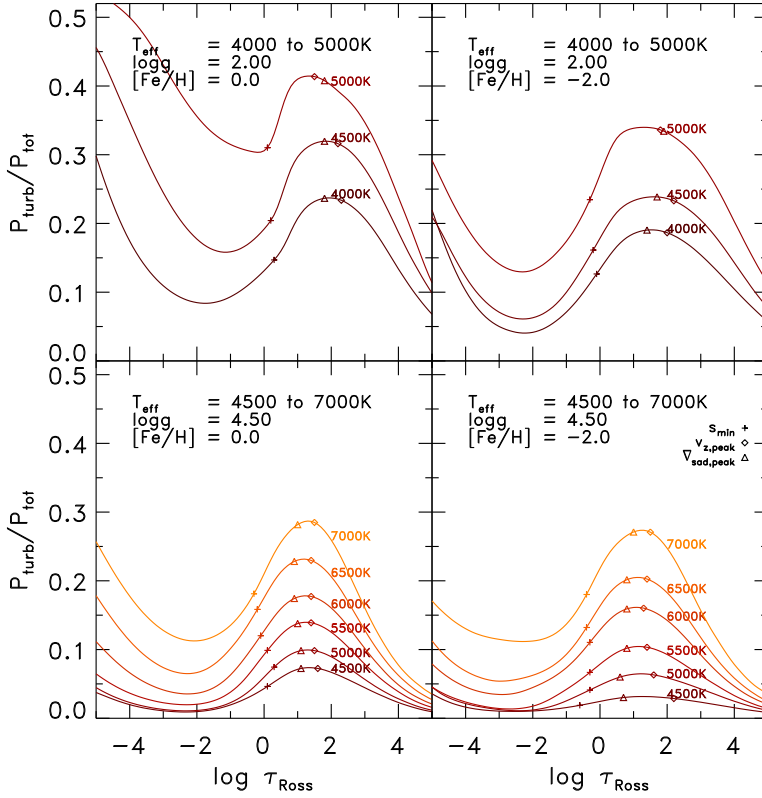


Figure 3.23: The fraction of turbulent pressure to total pressure $p_{\text{turb}}/p_{\text{tot}}$ vs. optical depth $\log \tau_{\text{Ross}}$ is displayed for various stellar parameters.

$|\vec{\nabla} \times \vec{v}|$, which is shown in Fig. 3.22. The vorticity arises below the surface in SAR due the overturning of the upflows and the turbulent downdrafts experiencing the density gradient. The peak in $\vec{\omega}$ is associated with pronounced shear flows, which arise due deflection of the horizontal flows into downdrafts of the overturning plasma (see SN98). The vorticity is concentrated in tube-like structures in the intergranular lanes around the edges of granules. The run of the vorticity follows closely that of $v_{z,\text{rms}}$ (see Fig. 3.19).

3.2.3 Turbulent pressure

The turbulent pressure, $p_{\text{turb}} = \rho v_z^2$, is an additional (dynamical) pressure that arises from the (macroscopic) vertical bulk flows due to the convective motions. It appears when considering the horizontal averages of the momentum equation (Eq. 1.2), more specifically of the advection term therein. The ratio of turbulent to total pressure, $p_{\text{turb}}/p_{\text{tot}}$, shown in Fig. 3.23, follows qualitatively very closely the run of $v_{z,\text{rms}}$ (compare with Fig. 3.19), namely, it peaks in the SAR ($\log \tau_{\text{Ross}} \sim 1.5$), reaches a minimum around $\log \tau_{\text{Ross}} \sim -2.0$, and increases in the upper layers (a functional fit for $[p_{\text{turb}}/p_{\text{tot}}]_{\text{peak}}$ is given in App. A). This is can be expected, since the p_{turb} is given by the vertical velocity. In the SAR, the shape of the $p_{\text{turb}}/p_{\text{tot}}$ profile with optical depth looks similar to a Gaussian function, however, towards lower T_{eff} and metallicity, it becomes increasingly skewed. Averages on constant geometrical depth $\langle 3D \rangle_z$ are similar, only the peak and the upper layers are slightly lower at higher T_{eff} s.

For hotter stars, in particular, metal-rich giants, the turbulent pressure becomes comparable to the gas pressure ($p_{\text{turb}}/p_{\text{tot}} \sim 0.4$) in the SAR, and the atmosphere is increasingly supported by p_{turb} . This means that neglecting the turbulent pressure, as is usually done in 1D models, would significantly overestimate the gas pressure. The consequence of this is a faulty, inconsistent stratification, since the overestimation in gas pressure comes at the cost of altering other physical quantities like the density, even when the temperature stratification looks similar compared to a $\langle 3D \rangle$ model.

We find that $v_{z,\text{rms}}$ is very close to $v_{\text{turb}} = [\langle p_{\text{turb}} \rangle / \langle \rho \rangle]^{1/2}$, since the latter is basically the density-

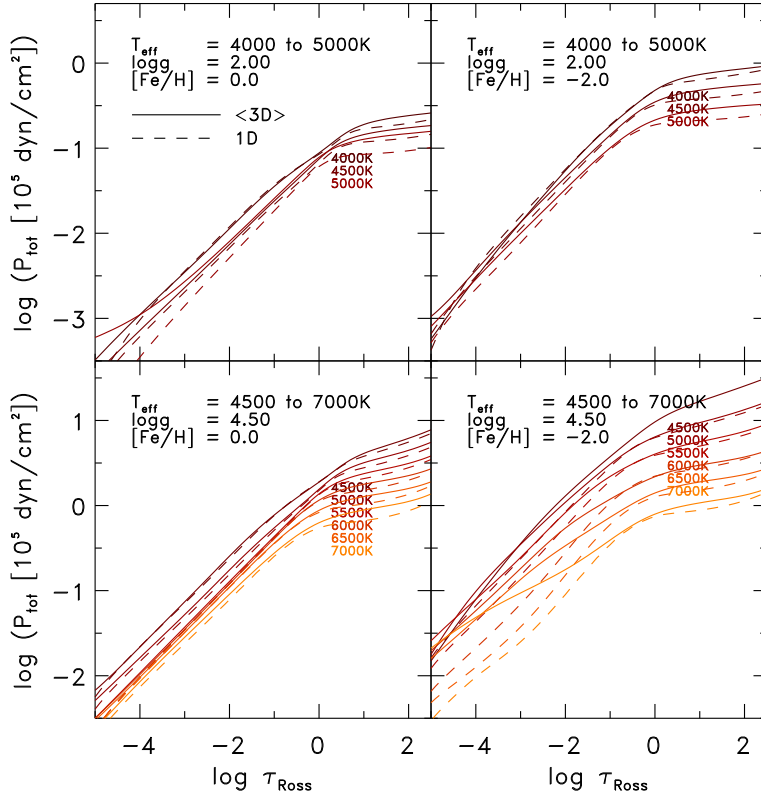


Figure 3.24: We display the ⟨3D⟩ total pressure p_{tot} against the optical depth $\log \tau_{\text{Ross}}$ for various stellar parameters (solid lines). For comparison, we also plot the 1D models neglecting turbulent pressure (dashed lines), which is the reason for the increasing differences for higher T_{eff} in the range $0 < \log \tau_{\text{Ross}} < 2$. Note the different ordinate scale in the top panel.

weighted analog of the former. In 1D stellar structure models that include turbulent pressure, the convective velocity from MLT is considered, i.e. $p_{\text{turb,1D}} = \beta \rho v_{\text{MLT}}^2$, with β being a form factor at the order of unity. However, as shown in Fig. 3.19, the convective velocities, v_{MLT} , are underestimating v_{turb} systematically towards higher T_{eff} and lower $\log g$. Therefore, the 1D models can be improved by using $v_{z,\text{rms}}$ resulting from 3D simulations, or one can fit the scaling factor β to match $v_{z,\text{rms}}$, which would clearly reduce the error. Chiavassa et al. (2011) showed that using a realistic turbulent pressure contribution to the hydrostatic equilibrium in 1D red supergiant atmospheres, greatly improves the 1D stratifications, therefore, the latter being in better agreement with ⟨3D⟩ stratifications. This extra pressure component also leads to an expansion of the atmosphere compared to a 1D model stratification without turbulent pressure. This is referred to as *atmospheric levitation* (see Trampedach, 2001). This will affect p-modes by affording them a larger cavity, and hence lowering their frequencies. This is part of the seismic near-surface effect which has plagued helio- and asteroseismology.

3.2.4 Total pressure and density

In Fig. 3.24, we show the total pressure for various stellar parameters. In contrast to the previous quantities, p_{tot} decreases with higher T_{eff} , lower $\log g$, and higher metallicity. From the three stellar parameters, the influence of the metallicity is the strongest. We find the highest pressures (and densities) in the coolest metal-poor dwarfs and the lowest pressures in the hottest metal-rich giants. In the upper layers of hot metal-poor dwarfs, we find pressures systematically increased with respect to their 1D counterparts, which is accompanied by similar behavior in ρ , p_{gas} and p_{turb} . As we showed above, a significant fraction of the total pressure is contributed by turbulent pressure in the SAR and in the upper layers (see Fig. 3.23), in particular, towards higher T_{eff} and lower $\log g$. Moreover, we note that the temporal and horizontal ⟨3D⟩_z-averages from our relaxed simulations are very close to hydrostatic equilibrium, and the turbulent pressure contributes significantly to this equilibrium.

The mean density stratifications look qualitatively similar to the total pressure ones (Fig. 3.25). Fur-

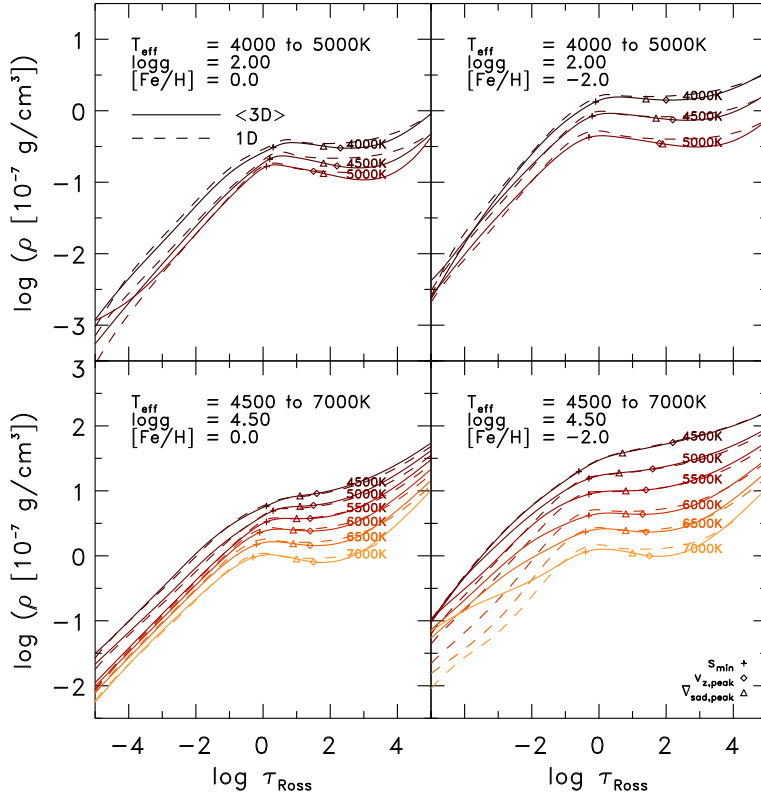


Figure 3.25: Density vs. optical depth for different stellar parameters.

thermore, in Fig. 3.20, we show the peak density⁷ ρ_{peak} , which is the density at the height of the maximum rms-vertical velocity (see Fig. 3.19). The density ρ_{peak} increases with lower T_{eff} , higher $\log g$, and lower $[\text{Fe}/\text{H}]$. These variations with stellar parameters arise due to the radiative transfer, since the cooling and heating rates (see Eq. 1.26) depend on density ρ and opacity κ . We showed in Sect. 3.1.2 that with higher metallicity and opacity, the hydrostatic stratification is set at lower ρ .

3.2.5 Electron number density

Next, we discuss the properties of the electron number density n_{el} (Fig. 3.26), which is the temporal and spatial average of the local electron density on layers of constant Rosseland optical depth. The electron number density drops by about ~ 2 dex at the transition from the interior to the photosphere. This is due to the fact that the density itself decreases here, and due to the recombination of hydrogen at the photospheric transition. The convective flux consists to $\sim 1/3$ of F_{ion} (see Sect. 3.2.8), therefore, as the hot ionized plasma reaches the surface, it radiates away energy, recombines, and overturns into downdrafts, thereby reducing the number of free electrons. The electron density increases with higher T_{eff} , lower $\log g$, and higher $[\text{Fe}/\text{H}]$. The electron pressure $p_{\text{el}} = n_{\text{el}}k_{\text{B}}T$ follows similar trends as the electron density in terms of variations with stellar parameters and depth.

3.2.6 Entropy

Local, box-in-a-star, 3D RHD atmosphere models have well defined boundary conditions at the bottom boundary because of the adiabaticity of the convection zone, even though they are relatively shallow and comprise only a small fraction of the convection zone. Indeed, the specific entropy per unit mass of the plasma stays constant across most of the convective zone, in particular, for the upflows. In Fig. 3.27, we

⁷The total pressure would lead to a very similar plot.

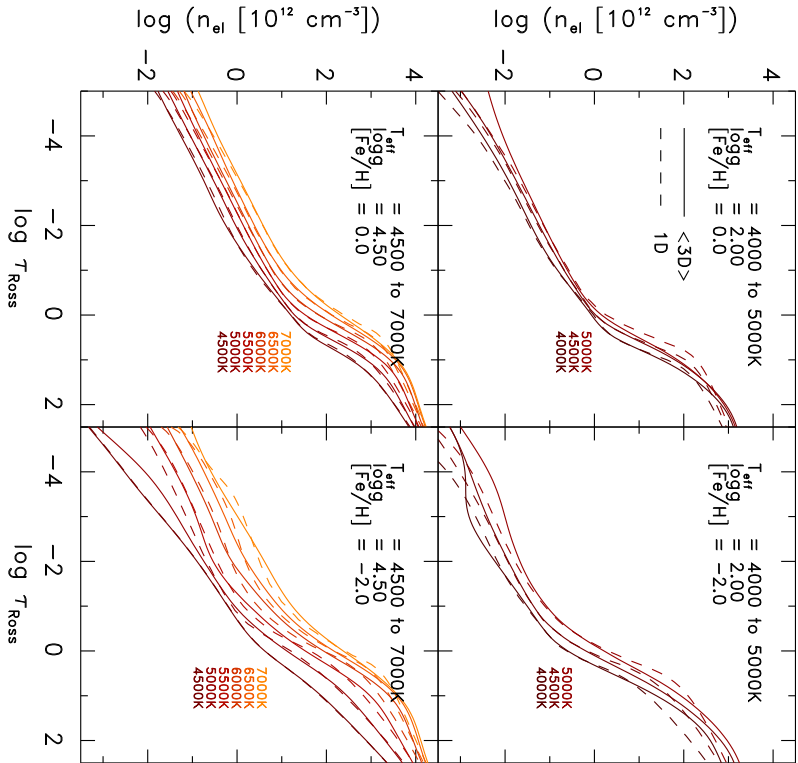


Figure 3.26: We present the $\langle 3D \rangle$ stratifications of the local electron number density n_{el} against optical depth $\log \tau_{Ross}$ for various stellar parameters (solid lines). For comparison, we also show the corresponding stratifications from 1D models (dashed lines).

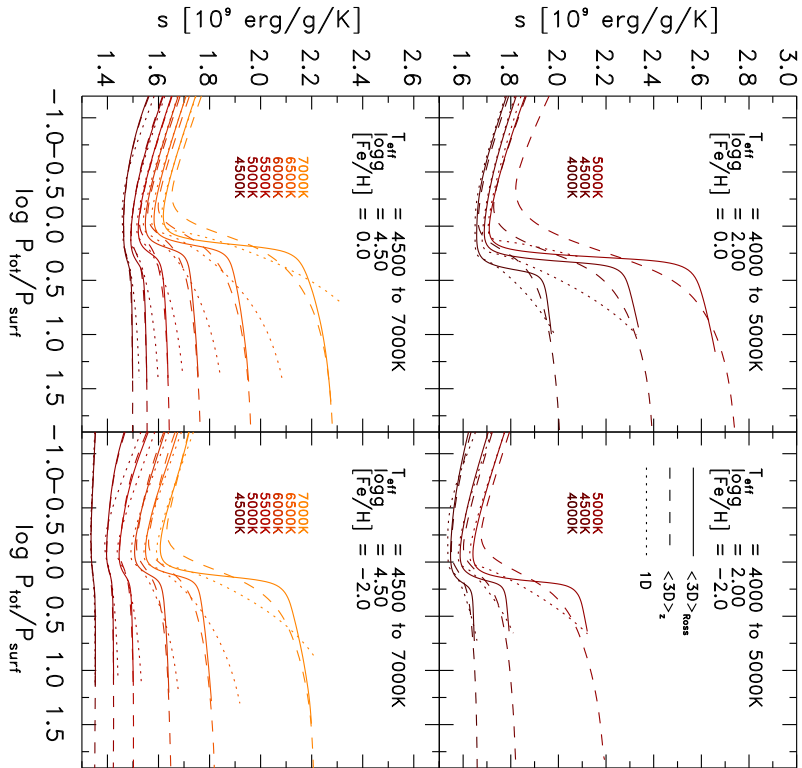


Figure 3.27: $\langle 3D \rangle$ and $\langle 3D \rangle_z$ mean stratifications (solid and dashed respectively) of the entropy s vs. the total pressure normalized to the pressure at the optical surface $\log p_{tot}/p_{surf}$ for various stellar parameters. We show also the s -stratifications of the 1D models (dotted lines). Some of the 1D models are slightly shallower due to reasons of convergence. The $\langle 3D \rangle$ models are also shorter than the $\langle 3D \rangle_z$, since $\log \tau_{Ross} = 5$ is the lower limit and covers only the shorter depth. Note the different ordinate scale in the top panel.

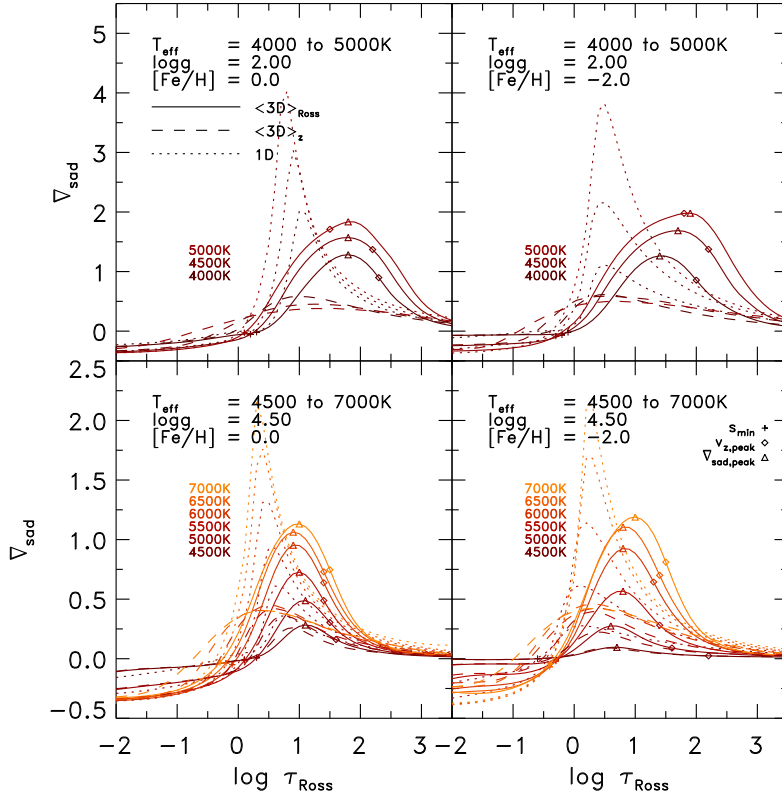


Figure 3.28: We show the $\langle 3D \rangle_{\text{Ross}}$ (solid lines) and $\langle 3D \rangle_z$ (dashed lines) superadiabatic gradient ∇_{sad} vs. optical depth $\log \tau_{\text{Ross}}$ for various stellar parameters. Furthermore, for comparison, we also show the corresponding values from 1D models (dotted lines). Note the different ordinate scale in the top panels.

show the average entropy. Below the optical surface, the entropy converges asymptotically against s_{bot} into deeper layers, especially the averages on constant geometrical height $\langle 3D \rangle_z$ (dashed lines). As the hot plasma in the granules reaches the optical surface, it becomes transparent, thereby a large fraction of the energy is radiated away. This results in a decrease in entropy, until it reaches a minimum at the top of the convection zone ($\log \tau_{\text{Ross}} \sim 0.0$). Further up, the entropy then increases again due to the decoupling of the radiation and matter above the photosphere, which results in an almost isothermal atmosphere. The 1D models (dotted lines) exhibit larger entropy stratifications in the deeper convection zone, in particular, for higher T_{eff} , thereby overestimating the entropy jump increasingly due to the fixed mixing-length parameter α_{MLT} with 1.5 for all stellar parameters.

3.2.7 Superadiabatic temperature gradient

We limit ourselves to show only the superadiabatic gradient $\nabla_{\text{sad}} = \nabla - \nabla_{\text{ad}}$, since it combines the important properties of both the total and the adiabatic temperature gradient (∇ and ∇_{ad} respectively). In Fig. 3.28, we show ∇_{sad} averaged over constant geometrical height or Rosseland optical depth. The peak in ∇_{sad} arises solely from the temperature gradient ∇ , since ∇_{ad} drops below the optical depth and reaches an adiabatic value. The superadiabatic gradient peaks around $\log \tau_{\text{Ross}} \sim 1.0 - 2.0$, and becomes $\nabla_{\text{sad}} < 0.0$, above the optical surface at $\log \tau_{\text{Ross}} < 0.0 - 0.5$. The entropy jump correlates directly with the superadiabatic gradient, since $\nabla_{\text{sad}} = 1/c_p [\partial s / \partial \ln p_{\text{tot}}]$ and one can show that $\partial s / \partial z = c_p / H_p (\nabla - \nabla_{\text{ad}})$. Hence, it is no surprise that they exhibit similarity in the peak amplitude and position. In particular, the peak amplitude increases with increasing T_{eff} and $\log g$ (see Δs in Fig. 3.20; a functional fit for $\nabla_{\text{sad}}^{\text{peak}}$ is given in App. A). The position of $\nabla_{\text{sad}}^{\text{peak}}$ on the optical depth scale $\langle 3D \rangle_{\text{Ross}}$ (triangles), hence the position of the steepest temperature gradient, changes slightly with stellar parameters. However, similar to the position of $v_{z,\text{rms}}^{\text{peak}}$ in the $\varepsilon - \rho$ -plane, the distribution of $\nabla_{\text{sad}}^{\text{peak}}$ is regular (see Fig. 3.18), namely it shifts systematically towards higher ε and lower ρ with increasing T_{eff} .

As it is clear in Fig. 3.28, one finds substantial differences in ∇_{sad} when comparing the two $\langle 3D \rangle$ stratifications with their 1D counterparts, namely, the 1D gradients exhibit distinctively larger amplitudes. These differences arise partly due the missing turbulent pressure in the 1D case, but do not resolve the discrepancies. Furthermore, we find an asymmetrically skewed shape towards the optical surface in the 1D gradients, which is shared by the geometrical averages $\langle 3D \rangle_z$, but is not the case for the averages on constant Rosseland optical depth $\langle 3D \rangle_{\text{Ross}}$. A main reason for the shown differences between $\langle 3D \rangle_{\text{Ross}}$ and 1D comes from the averaging over layers of constant τ_{Ross} . The underlying ∇_{ads} are rather insensitive to the deviations between the $\langle 3D \rangle_{\text{Ross}}$ and 1D stratifications, so the differences arise mainly due to ∇ . Between $\langle 3D \rangle_z$ and 1D the adiabatic gradients differ in the sub-photospheric gradient.

3.2.8 Transport of energy

The individual energy fluxes are quantities worthy of further consideration. The energy flux is conserved only on averages of constant geometrical height $\langle 3D \rangle_z$, therefore, we show and discuss it here. The total energy flux $F_{\text{tot}} = F_{\text{rad}} + F_{\text{conv}} + F_{\text{visc}}$ emerges from the photosphere solely in the form of radiative energy flux. The total energy flux is supplied from the convection zone by the convective energy flux, which is the sum of the enthalpy flux

$$F_{\text{enth}} = \left[\varepsilon + \frac{p_{\text{th}}}{\rho} \right] \delta j_z, \quad \text{with } \delta j_z = \rho v_z - \langle \rho v_z \rangle \quad (3.8)$$

(δj_z being the horizontal fluctuations of the vertical mass flux; the average vertical mass flux vanishes) carried in the upflows and the kinetic energy flux

$$F_{\text{kin}} = \left[\frac{1}{2} \rho v^2 \right] \delta j_z \quad (3.9)$$

arising from the downdrafts (see SN98 and Nordlund et al. 2009). Since the mean kinetic energy flux F_{kin} is negative, the positive enthalpy flux F_{enth} is the major component of the convective energy flux F_{conv} . The enthalpy flux in turn consists of the energy fluxes due to ionization⁸ $F_{\text{ion}} = \left[\varepsilon - \frac{3}{2} \frac{p_{\text{th}}}{\rho} \right] \delta j_z$, thermal heat $F_{\text{th}} = \frac{3}{2} \frac{p_{\text{th}}}{\rho} \delta j_z$ and acoustic (sound) waves $F_{\text{acous}} = \langle p_{\text{th}} v_z \rangle - \langle p_{\text{th}} \rangle \langle v_z \rangle$. In Fig. 3.29, we show the energy fluxes F_{rad} , F_{enth} , F_{kin} , F_{ion} , and F_{th} normalized to the total emergent energy flux σT_{eff}^4 (for clarity, we refrain from showing F_{visc} and F_{acous} , since their contribution to F_{tot} is very small). We vary one stellar parameter at a time, while the other two are fixed (T_{eff} , $\log g$, and $[\text{Fe}/\text{H}]$, from top to bottom in Fig. 3.29, respectively). Just below the optical surface ($0.5 < \log p_{\text{tot}}/p_{\text{surf}} < 1.0$), both F_{kin} (solid lines) and F_{enth} (dashed lines) increase towards cool metal-poor dwarfs, i.e. lower T_{eff} , $[\text{Fe}/\text{H}]$ and higher $\log g$, due to higher densities and velocities. The increased reduction of the total flux by F_{kin} (< 0.0) is compensated by a simultaneously higher F_{enth} (> 1.0). On the other hand, in deeper layers ($\log p_{\text{tot}}/p_{\text{surf}} > 1.5$), both converge to similar fractions for all stellar parameters (-0.17 and 1.14 for F_{kin} and F_{enth} respectively). This convergence to very similar values is rather remarkable. The convective motions seem to follow an exact guideline, which might be correlated to the universal filling factor (see Sect. 3.1.6). We remark that in deeper solar simulations⁹ (20Mm) that F_{enth} and F_{kin} increase with depth, while their sum remains constant (see Stein et al., 2009).

The majority of the total energy flux F_{tot} in the convection zone is carried in form of ionized hydrogen¹⁰ with $F_{\text{ion}} \simeq 0.67$, while thermal heat is the second most important component with $F_{\text{th}} \simeq 0.29$. The acoustic energy constitutes only a small fraction with $F_{\text{acous}} \simeq 0.04$. SN98 found similar fractions with $F_{\text{kin}} \sim -0.10$ to -0.15 , $F_{\text{ion}} \sim 2/3$ and $F_{\text{th}} \sim 1/3$ for the Sun. The F_{ion} and F_{th} fractions, which are the major constituents of the enthalpy flux, undergo a significant change below the surface, as we show in Fig. 3.29 for models with different stellar parameters. In particular, the fraction of thermal heat F_{th} becomes more significant at the cost of F_{ion} towards cool metal-poor dwarfs. The thermal flux F_{th} reaches a maximum (up to $F_{\text{th,max}} \simeq$

⁸The recombination of the protons at the surface is leading to F_{ion} .

⁹Our shallow solar simulation is 2.8Mm deep.

¹⁰The given fractions are averages of all grid models.

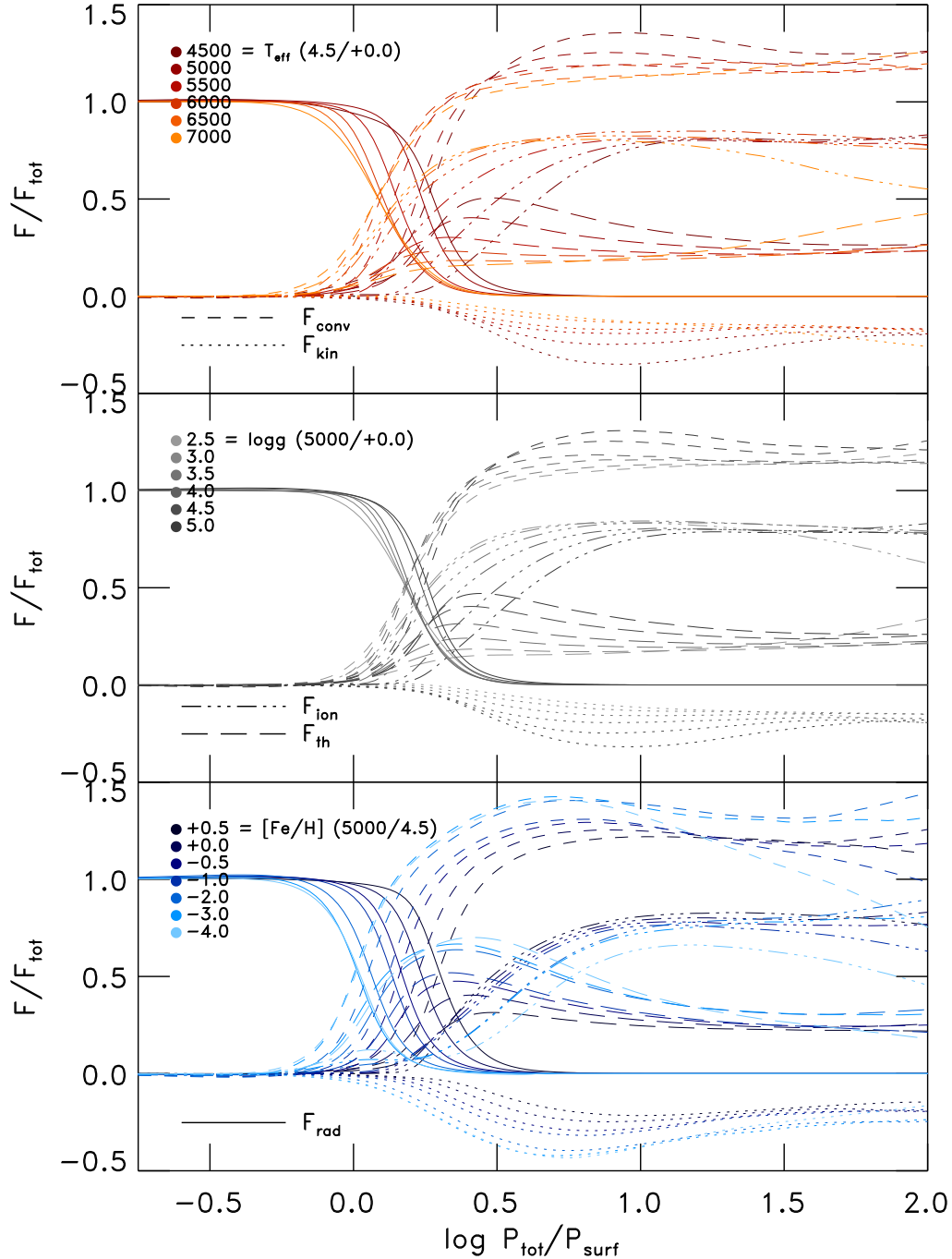


Figure 3.29: Behavior of the normalized energy fluxes F/F_{tot} against the total pressure normalized to the pressure at the optical surface $\log p_{\text{tot}}/p_{\text{surf}}$ as a function of variations in the individual stellar parameters (T_{eff} , $\log g$, and $[\text{Fe}/\text{H}]$, from top to bottom, respectively). In each panel, the various curves are shown varying one of the parameters while keeping the other two fixed. The individual normalized components of F_{tot} are F_{enth} (dashed), F_{kin} (dotted), F_{ion} (dash-triple-dotted), F_{th} (long dashed) and F_{rad} (solid). Averages are evaluated at constant geometrical height.

0.5) just below the surface, but eventually converges close to the above mentioned fractions in deeper layers (long dashed lines).

In 1D MLT models, the convective flux is assumed to consist of the enthalpy flux only, $F_{\text{conv},1\text{D}}$ (see Appendix 2.4.1). This is a result of the MLT assumption of symmetric flows which means that the kinetic energy fluxes in the up- and downflows cancel exactly. As remarked by Henyey et al. (1965), the details on F_{kin} and F_{acous} are not at hand due to the lack of a self-consistent velocity field. The energy fluxes from 3D RHD simulations, on the other hand, arise self-consistently from solving the coupled equations of radiative hydrodynamics, without further assumptions.

As mentioned above, the emergent total energy flux F_{tot} is carried in the convection zone mainly by the positive enthalpy flux F_{enth} (Eq. 3.8). Therefore, one can approximate the convective energy flux with the mean jump in enthalpy¹¹ Δh times the mean vertical mass flux of the upflows below the optical surface, hence

$$F_{\text{conv}} \approx \langle \Delta h \rangle \langle \rho v_z \rangle. \quad (3.10)$$

At the transition region, the enthalpy jump Δh is primarily caused by the strong drop in internal energy ε , hence entropy s , and the thermodynamic pressure work is rather small (note the change of p_{tot} below the surface $\log \tau_{\text{Ross}} > 0.0$ in Fig. 3.24), i.e. $\Delta h \approx T \Delta s$, where T is the temperature at the surface. By approximating $T \simeq T_{\text{eff}}$, one can expect the total energy flux $F_{\text{tot}} = \sigma T_{\text{eff}}^4$ to depend to first order on the mean entropy jump¹², density, and vertical velocity:

$$\sigma T_{\text{eff}}^3 \propto \langle \Delta s \rangle \langle \rho \rangle \langle v_z \rangle. \quad (3.11)$$

The fourth power of T_{eff} reduces to third, since we approximate $T \simeq T_{\text{eff}}$. The approximation in Eq. 3.11 can already be retrieved on dimensional grounds, however, we derived the latter in order to explain the systematic variations of Δs , $v_{z,\text{rms}}^{\text{peak}}$ and ρ_{peak} with stellar parameters, which we have observed above (see Figs. 3.1, 3.20 and 3.20, respectively). The emergent radiative energy flux is correlated with Δs , ρ and v_z , and the respective composition resulting from the individual contributions varies with stellar parameters.

The interplay between the radiative heating and cooling rates q_{rad} (Eq. 1.26) and hydrostatic equilibrium, require a different density stratification for different stellar parameters due to the dependence of opacity on thermodynamic variables, as we showed in Sect. 3.1.2. The resulting density variations will induce adjustments in the vertical velocity and entropy jump. Furthermore, we find with increasing $\log g$ or lower $[\text{Fe}/\text{H}]$ at a fixed T_{eff} , the density increases, which is compensated by lower Δs and v_z ($\Delta s \propto \Delta \rho^{-1}$, see Eq. 3.3). We would like also to emphasize the remarkably important (non-local) influence of the rather thin photospheric transition region on basically the whole convection zone, since the entropy deficiency of the turbulent downdrafts are generated mainly here. The latter sets the entropy jump and the convective driving (see Nordlund et al., 2009).

The radiative heating and cooling rates q_{rad} (Eq. 1.26) due to radiative losses enter the hydrodynamic equations as a source and sink term in the energy equation (Eq. 1.3). It is the divergence of the radiative flux $q_{\text{rad}} = -\vec{\nabla} \cdot \vec{F}_{\text{rad}}$, and a large, negative q_{rad} , the *cooling peak*, marks the transition of energy transport from fully convective below the optical surface to fully radiative close to the photosphere. To better illustrate the depth dependence of q_{rad} and the comparison among different models, in Fig. 3.30, we show the normalized cooling and heating rates $q_{\text{rad}}^{\text{norm}} = -dF_{\text{rad}}/d \ln \tau_{\text{Ross}}$. One can see that the amplitude of $q_{\text{rad}}^{\text{norm}}$ increases with higher T_{eff} , accompanied by an increase in the width of the cooling peak. The position of the maximum absolute amplitude coincides with the position of $\nabla_{\text{sad}}^{\text{peak}}$, since the cooling rate (radiative loss) is setting the entropy fluctuations, hence the superadiabatic gradient (see Sect. 3.2.7). Furthermore, this location moves into upper layers for higher T_{eff} (from $\log \tau_{\text{Ross}} \simeq 1.0$ up to 0.2 for $T_{\text{eff}} = 4000$ to 7000 K respectively). On the other hand, the width of the photospheric transition region $\Delta_{\text{ph}} = \Delta \log \tau_{\text{Ross}} (q_{\text{rad}} < 0)$ clearly widens for hotter T_{eff} , but also, in particular, for metal-poor giants (see top right panel in Fig. 3.30). While for cool dwarfs the width is typically $\Delta_{\text{ph}} \approx 3.0$ dex, for hot metal-poor giants, it reaches $\Delta_{\text{ph}} \approx 5.0$ dex (see, e.g., model with 5000 K in right top panel of Fig. 3.30).

¹¹For example, Δh can be determined at the top and bottom of the photospheric transition region (see Fig. 3.18).

¹²Here, we prefer to use Δs instead of directly Δh or $\Delta \varepsilon$ due to the adiabaticity of convection.

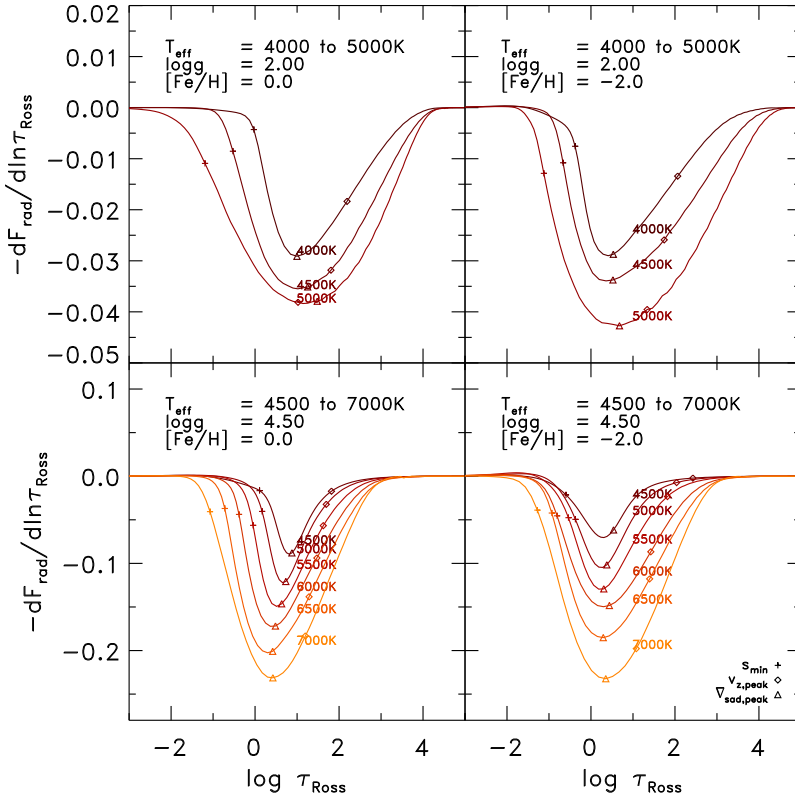


Figure 3.30: We show the normalized cooling and heating rates $q_{\text{rad}}^{\text{norm}}$ vs. optical depth $\log \tau_{\text{Ross}}$ for various stellar parameters. The shown averages are retrieved on constant geometrical height $\langle 3D \rangle_z$. Note the different ordinate scale in the top panel.

3.3 Comparison of the $\langle 3D \rangle$ with 1D models

3.3.1 1D models

A differential comparison between 1D and 3D in terms of approaches in the modeling of stellar atmospheres is of obvious relevance here. Therefore, we developed a plane-parallel, hydrostatic, 1D atmosphere code (hereafter simply referred to as the *1D code*) that is based on a similar physical treatment as the MARCS code with a few simplifications (see Appendix 2.4 and Gustafsson et al. 2008 for more details). We employ exactly the same EOS and opacities as in the individual 3D models, thereby excluding differences due to dissimilar input physics. Also, we applied the $\langle 3D \rangle$ models as initial stratifications for the 1D models. These mean $\langle 3D \rangle$ stratifications are defined on an equidistant optical depth scale from $\log \tau_{\text{Ross}} = -5.0$ to $+5.0$ in steps of 0.1. The well-resolved optical depth scale reduces discretization errors in the 1D atmosphere calculations, thereby making the 1D- $\langle 3D \rangle$ comparison more reliable.

In Fig. 3.31, we show a comparison of the 1D and $\langle 3D \rangle$ temperature stratifications. One can immediately extract that the upper layers of the atmospheres are systematically overestimated in the 1D models by up to ~ 1000 K, in particular, for metal-poor stars $[\text{Fe}/\text{H}] \leq -2.0$ (for solar models the maximal difference is ~ 500 K). In the optically thin layers of 1D models, stable against convection, radiative equilibrium is enforced. However, in the upper layers of the metal-poor $\langle 3D \rangle$ models, the effect of the non-vanishing adiabatic cooling rate is to shift the balance with radiative heating to lower temperatures due to a scarcity and weakness of spectral lines at lower metallicities (Asplund et al., 1999a; Collet et al., 2007). Interesting are also the hotter temperature stratifications for a few giants ($T_{\text{eff}}/\log g = 4500 \text{ K}/1.5$ and $5000 \text{ K}/2.0$) towards higher metallicity ($[\text{Fe}/\text{H}] > -2.0$), which results from the radiative equilibrium at higher temperatures. On the other hand, with the 1D models, we find systematically cooler temperatures below the photosphere $\log \tau_{\text{Ross}} \simeq 2.0$ with up to ~ 1000 K (here there is no difference with different metallicities). Therefore, one has to keep in mind that, with 1D atmosphere models, and for metal-poor stars in particular, these severe effects on the stratifications can lead to large systematic errors in spectroscopic abundance

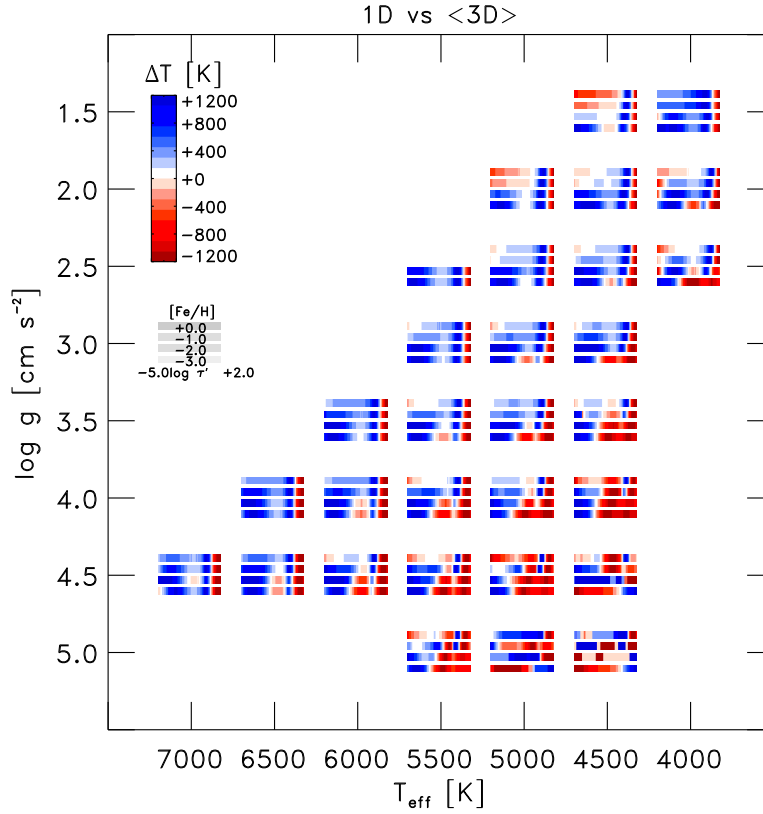


Figure 3.31: Comparison of the temperature stratification for the $\langle 3D \rangle$ and the 1D models by showing the difference $\langle 1D \rangle - \langle 3D \rangle$ (colored bars) between $\log \sigma_{\text{Ross}} = -5.0$ and 2.0 in the Kiel-diagram. We present four different metallicities ($[\text{Fe}/\text{H}] = -3.0, -2.0, -1.0$ and 0.0).

determinations, up to 0.5 dex or more in logarithmic abundance, depending on the formation height of the individual spectral lines used in the analysis (e.g. Asplund et al., 1999a; Asplund & García Pérez, 2001; Collet et al., 2006, 2007; Caffau et al., 2008, 2011; González Hernández et al., 2010; Kučinskas et al., 2013a).

In the 1D model calculations the mixing-length parameter is kept constant with $\alpha_{\text{MLT}} = 1.5$, which is the commonly applied value (see Gustafsson et al., 2008). However, it is well-known that α_{MLT} varies with stellar parameters (see Ludwig et al., 1999; Bonaca et al., 2012). Therefore, we caution that a single fixed value will lead to severe differences in atmospheric stratification. The systematic deviations beneath the optical surface in the temperature stratification between 1D and $\langle 3D \rangle$ towards cool dwarfs can be interpreted as the manifestation of the wrong α_{MLT} (see Fig. 3.31). Furthermore, p_{turb} is neglected in the 1D code, which affects the stratification by reducing the gas pressure (see Sect. 3.2.3).

3.3.2 MARCS and ATLAS models

Last, we would also like to briefly compare our $\langle 3D \rangle$ stratifications with the currently widely applied MARCS and ATLAS models (see Fig. 3.32, we show only the comparison with MARCS modes, since the ATLAS models look qualitatively rather similar). We find qualitatively similar deviations as with the 1D models above. At the same time, here we also have additional differences due to the different input physics (EOS and opacities). The largest differences between the $\langle 3D \rangle$ and 1D MARCS stratifications of metal-poor atmospheres are slightly higher, with ~ 1300 K at $[\text{Fe}/\text{H}] = -3.0$, while for solar metallicity the temperatures are underestimated in 1D by ~ 500 K at most. Below the surface, the differences amount to ~ 1000 K. The ATLAS models are up to ~ 850 K hotter at the top and ~ 1000 K cooler below the surface. In both cases, the deviations at the top increase towards lower $[\text{Fe}/\text{H}]$.

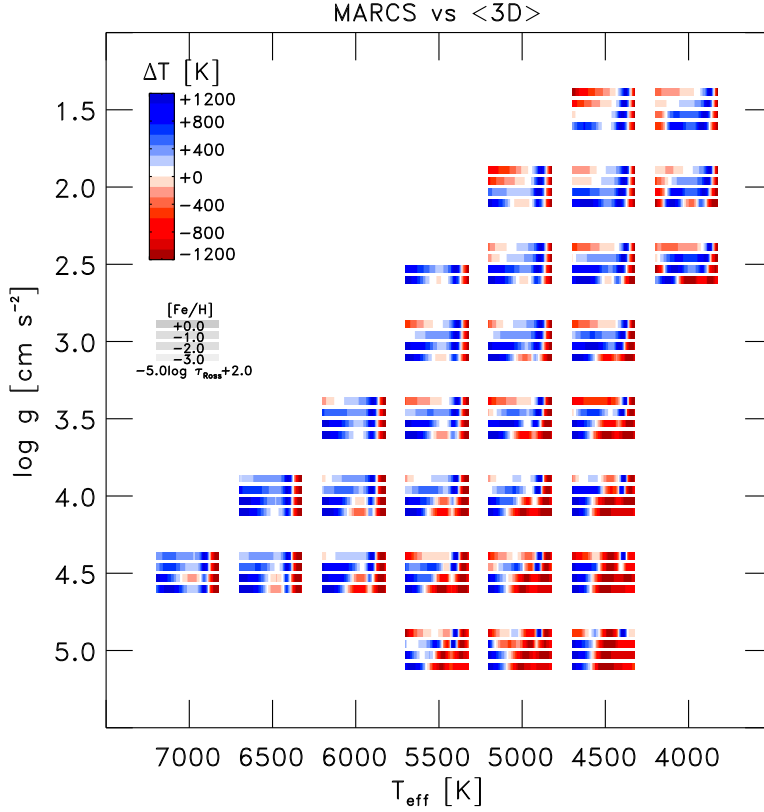


Figure 3.32: Similar as Fig. 3.31, however here we compare the $\langle 3D \rangle$ with the MARCS models for $[\text{Fe}/\text{H}] = -3.0, -2.0, -1.0$ and 0.0 . For a better comparison, we applied the same temperature range as given Fig. 3.31.

3.4 Comparison of the averaging methods

In the following, we systematically compare the different types of averaging procedures explained in Sect. 2.3 over a broad range of stellar parameters relative to Rosseland optical depth, i.e. $\langle 3D \rangle_{\bar{z}} - \langle 3D \rangle_{\text{Ross}}$. For the sake of clarity, we illustrate the properties of average stratifications only for a representative selection of STAGGER-grid models comprising dwarfs and giants ($\log g = 4.5$ and 2.0) at solar and subsolar metallicity ($[\text{Fe}/\text{H}] = 0.0$ and -3.0). Besides the most important thermodynamic state variables, temperature and density, we also investigate averages of electron number density, an important quantity for, say, calculations of ionization balance and spectral line formation.

Owing to the lack of a unique common global depth scale that is invariant between different averaging methods, we display their results jointly on the averaged Rosseland optical depth scale, $\langle \tau_{\text{Ross}} \rangle$, in order to enable a direct comparison.

3.4.1 Temperature

We consider four different reference depth scales: geometrical depth, $\langle 3D \rangle_{\bar{z}}$, column mass density, $\langle 3D \rangle_m$, Rosseland optical depth, $\langle 3D \rangle_{\text{Ross}}$, and optical depth at 500 nm, $\langle 3D \rangle_{500}$. We find that the temperature stratifications of the two optical reference depth scales, $\langle 3D \rangle_{\text{Ross}}$ and $\langle 3D \rangle_{500}$, are similar, therefore we refrain from showing these. Only at the top of the metal-poor stars do the $\langle 3D \rangle_{500}$ -averages appear cooler ($\sim 5\%$, i.e. by $\gtrsim 250$ K at $T_{\text{eff}} = 6000$ K). On the other hand, the geometrical $\langle 3D \rangle_{\bar{z}}$ and column mass density $\langle 3D \rangle_m$ averages deviate distinctively from the $\langle 3D \rangle_{\text{Ross}}$ -stratification (see Fig. 3.33). In the regime $1.0 < \log \tau_{\text{Ross}} < 3.0$, both $\langle 3D \rangle_{\bar{z}}$ and $\langle 3D \rangle_m$ are cooler by $\sim 5 - 10\%$. At the surface ($\tau_{\text{Ross}} = 0$), the geometrical averages deviate considerably, while the $\langle 3D \rangle_m$ -averages are closer to the optical depth scale (see Fig. 3.33). In the deeper layers below the superadiabatic regime (SAR), the various averaging methods are practically indistinguishable. In the upper atmosphere the differences are smaller at higher $[\text{Fe}/\text{H}]$ due to relatively low horizontal contrast, but, these increase significantly for lower metallicity. The averages

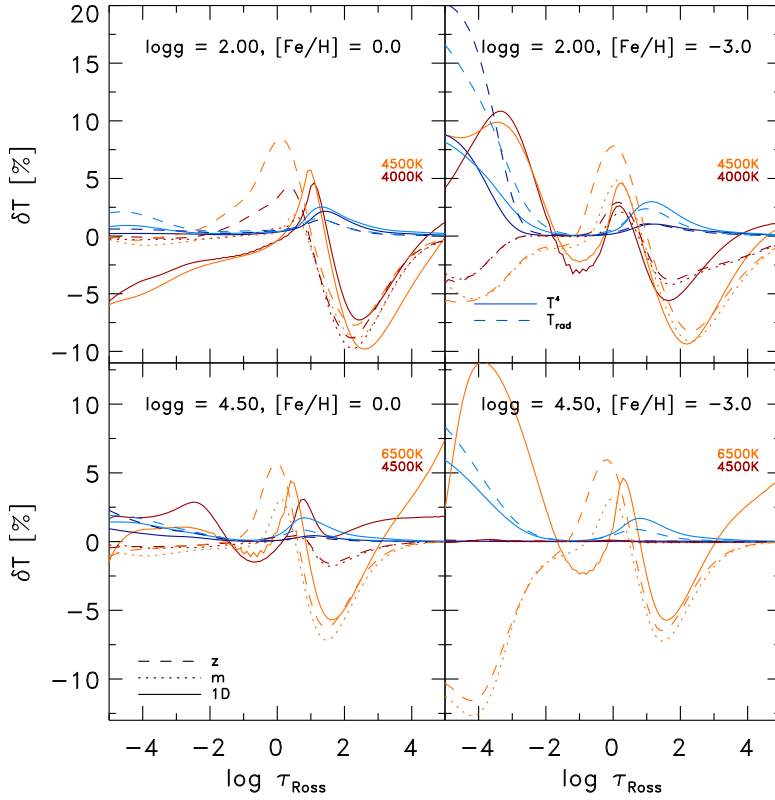


Figure 3.33: Relative differences in the temperature stratification vs. the (averaged) Rosseland optical depth for various stellar parameters. The differences are relative to the Rosseland optical depth, i.e. $\langle 3D \rangle_z - \langle 3D \rangle_{\text{Ross}}$. *Orange dashed lines*: averages on layers of constant geometrical height $\langle 3D \rangle_z$; *orange dotted lines*: averages on layers of constant column mass density $\langle 3D \rangle_m$; *orange solid lines*: 1D MLT models. The flux-weighted T^4 -stratifications (*blue solid lines*) and the brightness temperatures T_{rad} (*blue dotted lines*) averaged on surfaces of constant Rosseland optical depth are also shown. Note the differences in the y-axes.

$\langle 3D \rangle_z$ and $\langle 3D \rangle_m$ are marginally cooler than $\langle 3D \rangle_{\text{Ross}}$ by $\sim 1 - 2\%$ at solar metallicity. In the metal-poor case $[\text{Fe}/\text{H}] = -3.0$, the temperature stratifications are distinctively cooler, which will certainly influence the line formation calculations with $\langle 3D \rangle$ stratifications. Furthermore, the differences increase with higher T_{eff} and lower $\log g$.

As mentioned earlier, in the atmospheres of late-type stars, minor temperature fluctuations are amplified disproportionately into large variations in the line and continuum opacity κ_λ owing to the strong T -sensitivity of the H^- -opacity ($\kappa_\lambda \propto T^{10}$, see Stein & Nordlund 1998). Therefore, surfaces of constant optical depth appear strongly corrugated in terms of the range of geometrical heights that they span. The transformation to layers of constant optical depth will naturally even out these corrugated surfaces and, at the same time, smooth the temperature fluctuations, since the latter are the source of the former (see Sect. 3.6). Therefore, these are noticeably smaller on layers of constant optical depth compared to layers of constant geometrical depth, which is portrayed in the temperature contrast and histogram (see also Figs. 3.37 and 3.40). The SAR exhibits large-amplitude fluctuations as a result of the release of thermal and ionization energy at the photospheric transition, which are the reason for the observed enhanced differences between the averaging methods (see Sect. 3.5.1).

Steffen & Holweger (2002) found a beneficial mean $\langle T \rangle$ -representation for the Sun in the flux-weighted temperature averages, T^4 , taken on constant Rosseland optical depth from their 2D simulations. The idea behind this approach is that the T^4 -averages render radiation-oriented T -stratifications, therefore resulting in 1D line profiles that are closer to the multidimensional ones (see also Steffen et al., 1995). To allow for a similar comparison for our models, we computed such average T^4 -stratifications. In Fig. 3.33, the T^4_{Ross} -stratifications generally appear hotter at the top and in the SAR compared to the simple T -stratification. Averages taken at the fourth power will weight higher values more, which leads to hotter average temperatures. This could lead to pronounced differences for molecular lines that form high up in the atmosphere. At solar metallicity, the T^4 -stratifications at the top are fairly similar to the plain T -averages ($\sim 1 - 2\%$) in agreement with the findings of Steffen & Holweger (2002). This is different at lower metallicity ($[\text{Fe}/\text{H}] = -3.0$), namely the T^4 -averages are clearly higher by $\sim 5 - 10\%$. At higher

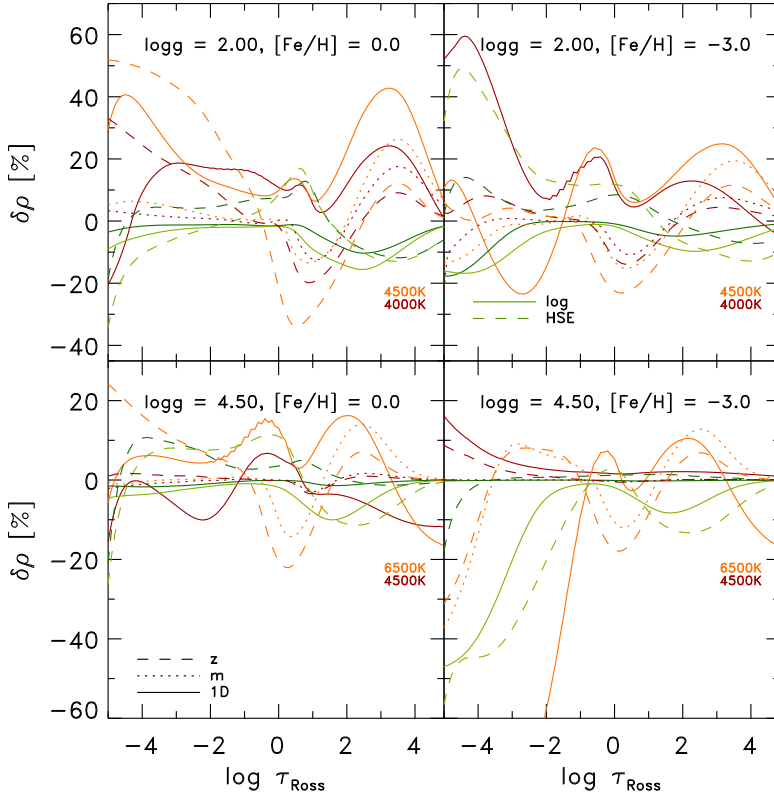


Figure 3.34: Relative differences in the density stratification vs. the (averaged) Rosseland optical depth for various stellar parameters. The differences are relative to the Rosseland optical depth, i.e. $\langle 3D \rangle_z$ – $\langle 3D \rangle_{\text{Ross}}$. *Orange dashed lines*: averages on layers of constant geometrical height $\langle 3D \rangle_z$; *orange dotted lines*: averages on layers of constant column mass density $\langle 3D \rangle_m$; *orange solid lines*: 1D MLT models. The logarithmic density averages $\langle 3D \rangle_{\text{Ross}}^{\log}$ (*blue solid lines*) and hydrostatic averages $\langle 3D \rangle_{\text{Ross}}^{\text{HSE}}$ (*blue dotted lines*) are shown. Note the differences in the y-axes.

T_{eff} and lower $\log g$, the temperature differences are greater, in particular, for the metal-poor giants, owing to the enhanced temperature fluctuations (see Sect. 3.5.1).

Under the assumption of local thermodynamic equilibrium (LTE) and neglecting the effects of scattering, the source function is given by the Planck function, $S_\lambda = B_\lambda(T)$. Within this approximation, we can thus consider the brightness temperature average T_{rad} defined earlier in Sect. 2.3 as a good representation of the mean temperature stratification from the point of view of the radiative emission properties: brighter parts in each depth layer are given more weight with this averaging method. The differences between the average T_{rad} at 500nm and average T -stratifications are displayed in Fig. 3.33. Their variations with stellar parameters are very similar to those of T^4 -averages, however, slightly more pronounced, in particular, the metal-poor giants exhibit hotter stratifications by up to $\sim 20\%$ at the top.

3.4.2 Density

In Fig. 3.34, we also illustrate the results of averaging in the case of the density stratifications. In the deeper interior, the different $\langle 3D \rangle$ models converge toward the same density stratification. In the SAR, below the optical surface at $\log \tau_{\text{Ross}} \gtrsim 0.0$, the geometrical averages $\langle 3D \rangle_z$ are smaller than the $\langle 3D \rangle_{\text{Ross}}$ averages by up to $\sim 30\%$, while at the top these are much denser by up to $\sim 40\%$. The differences increase towards higher T_{eff} and lower $\log g$. We find a different behavior in the metal-poor dwarfs, which turn lower towards the top after the initial increase ($\sim 10\%$). The density stratifications averaged on column mass density $\langle 3D \rangle_m$ are larger in the SAR and in the upper layers closer to $\langle 3D \rangle_{\text{Ross}}$. However, we find that at lower metallicity $\langle \rho \rangle_m$ they are smaller by up to $\sim 30\%$. We note that thermal pressure qualitatively shows the same characteristics as the density.

The shape of the density distribution is symmetric and narrow on layers of constant column mass density, thanks to the exponential stratification of the atmosphere and to the additional damping of density fluctuations on the column mass scale (see Fig. 3.40). As a result, the $\langle 3D \rangle_m$ averages feature the narrowest contrast and density ranges, which, on the contrary, are usually greatest for geometrical averages $\langle 3D \rangle_z$;

for the $\langle 3D \rangle_{\text{Ross}}$ averages, these are noticeably reduced due to the mapping onto the optical reference depth scale (Fig. 3.37). Overall, the density fluctuations at the top of the $\langle 3D \rangle_{\text{Ross}}$ stratifications are similarly as small as those by $\langle 3D \rangle_m$ and $\sim 20\%$; however, for metal-poor dwarfs they reach up to $\sim 80\%$ (see Fig. 3.37). As shown in Sect. 3.5.3, we find that the corrugation of the layers of constant optical depth in the upper part of 3D model stellar atmospheres at lower metallicity increases considerably towards higher T_{eff} because of an enhanced T -contrast by the so-called reversed granulation (see Rutten et al., 2004). This in turn broadens the density distribution during the remapping to the optical depth scale, shifting the mean density value and leading to the observed deviations between $\langle \rho \rangle_{\text{Ross}}$ and $\langle \rho \rangle_m$ at lower metallicity (see Sect. 3.6), which will affect the $\langle 3D \rangle$ line formation calculations.

The highly stratified structure of stellar atmospheres features an exponential decrease with height. Linear density averages will therefore tend to give more weight to higher density values, leading to a systematic overestimation of the mean densities. For this reason, we consider the logarithmic averages $\langle \rho \rangle_{\log}$, which we compare to the linear ones in Fig. 3.34. As expected, we find the logarithmic ρ -averages are smaller than the linear ones, with the difference between the two increasing with higher T_{eff} and lower $\log g$ by up to $\sim 30\%$. The mean densities in the upper layers are lower by $\sim 10\%$ and $\sim 40\%$ at solar and low metallicity, respectively. For quantities that vary more moderately (e.g., temperature), the differences between logarithmic and linear averaging are rather small.

The transformation to constant optical depth and the subsequent averaging will change the physical self-consistency as shown in Sect. 3.7. To rectify this, we followed the recommendation of Uitenbroek & Criscuolo (2011) and also computed ρ -stratifications, which are enforced to be in hydrostatic equilibrium¹³, $\langle \rho \rangle_{\text{HSE}}$ (Fig. 3.34). These deviate significantly from the plain $\langle \rho \rangle$ -stratifications, in particular, at the top. Incidentally, we note however that their dynamic nature and the effects of convective flows and turbulent pressure mean that the 3D models themselves are not strictly speaking in hydrostatic equilibrium at any one time.

In Fig. 3.33 (both panels), we also compare the 1D MLT models with the $\langle 3D \rangle_{\text{Ross}}$ stratifications. The 1D models in general show qualitatively similar behavior as the geometrical averages. The metal-poor 1D models are distinctively hotter, since these enforce radiative equilibrium in the upper layers.

3.4.3 Electron number density

We find large differences among the various averages of the electron number density, n_{el} , which we show in Fig. 3.35 (right panel). In the SAR the geometrical averages $\langle n_{\text{el}} \rangle_z$ are distinctively larger than the averages on surfaces of constant Rosseland optical depth $\langle n_{\text{el}} \rangle_{\text{Ross}}$, while the column mass density averages $\langle n_{\text{el}} \rangle_m$ are found in between the two. The deviations increase for higher T_{eff} and lower $\log g$ considerably, while at lower T_{eff} the differences are significantly smaller. We show in Sect. 3.6 that the interpolation to a new reference depth scale changes the statistical properties by redistributing properties from different heights, so the resulting mean horizontal average will look different depending on the reference depth scale. This effect seems to be most pronounced in the case of electron density.

To determine the ionization fraction in spectral line calculations, the electron number density is either already provided by the model atmosphere or looked up from an EOS using the independent thermodynamic variables (typically (T, p) or (T, ρ)). The latter has to be done carefully in the case of the $\langle 3D \rangle$ models, since, besides potential differences in the EOS compared to the one used for calculating the model atmosphere, electron densities derived from the EOS based on averaged independent variables, $n_{\text{el}}^{\text{EOS}} = n_{\text{el}}(\langle T \rangle, \langle p \rangle)$, can deviate significantly from the more physically consistent averaged $\langle n_{\text{el}} \rangle$ (see Sect. 3.8).

3.4.4 Vertical velocity

It is worthwhile to compare how the vertical velocity, $v_{z, \text{rms}}$, changes with the respective averaging methods. For comparison, we show in Fig. 3.36 (left panel) the rms of the vertical velocity. In the upper layers, we find the $v_{z, \text{rms}}$ on geometrical averages to be higher compared to other averages, while it is lower in the deeper layers. On optical depth the peak in $v_{z, \text{rms}}$ below the surface is somewhat symmetric and slightly higher, while for averages on geometrical height and column mass density their peaks are flatter and more

¹³The density and pressure are varied until hydrostatic equilibrium is restored.

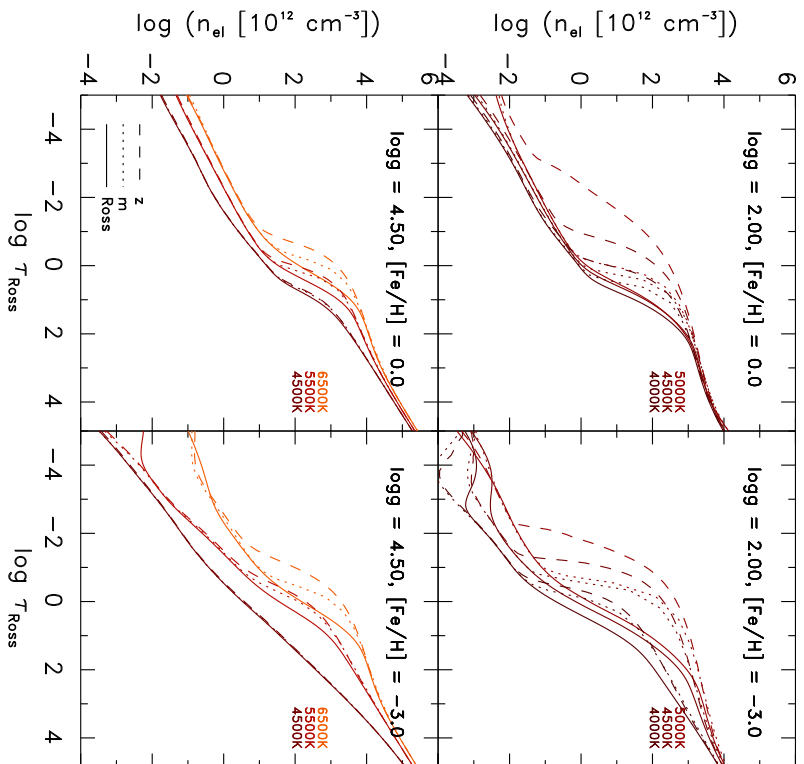


Figure 3.35: Root mean square (rms) of the mean electron number density n_{el} vs. optical depth. *Dashed lines:* $\langle 3D \rangle_z$ averages; *dotted lines:* $\langle 3D \rangle_m$; *solid lines:* $\langle 3D \rangle_{Ross}$.

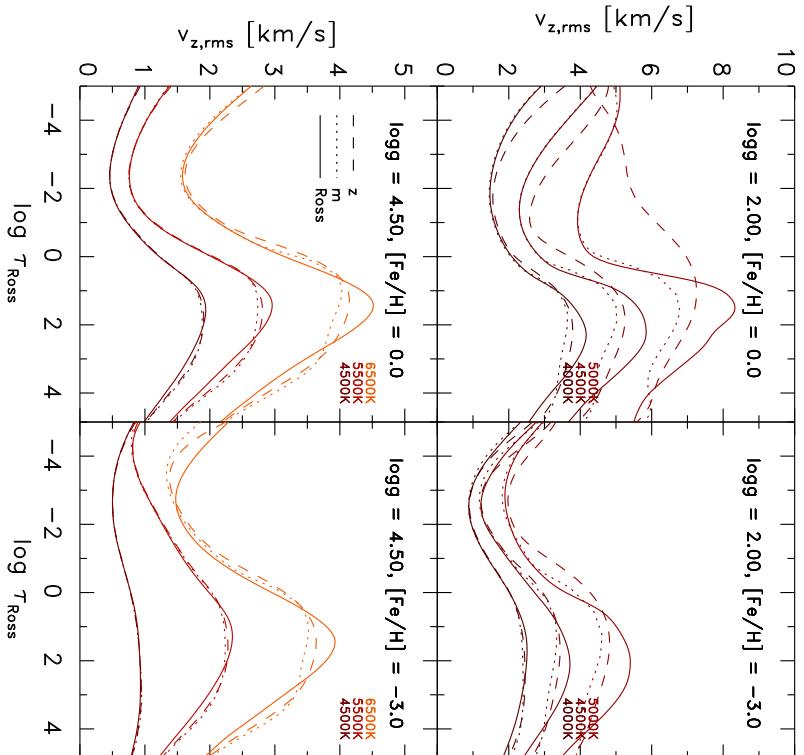


Figure 3.36: Root mean square (rms) of the vertical velocity $v_{z,rms}$ vs. optical depth. *Dashed lines:* $\langle 3D \rangle_z$ averages; *dotted lines:* $\langle 3D \rangle_m$; *solid lines:* $\langle 3D \rangle_{Ross}$.

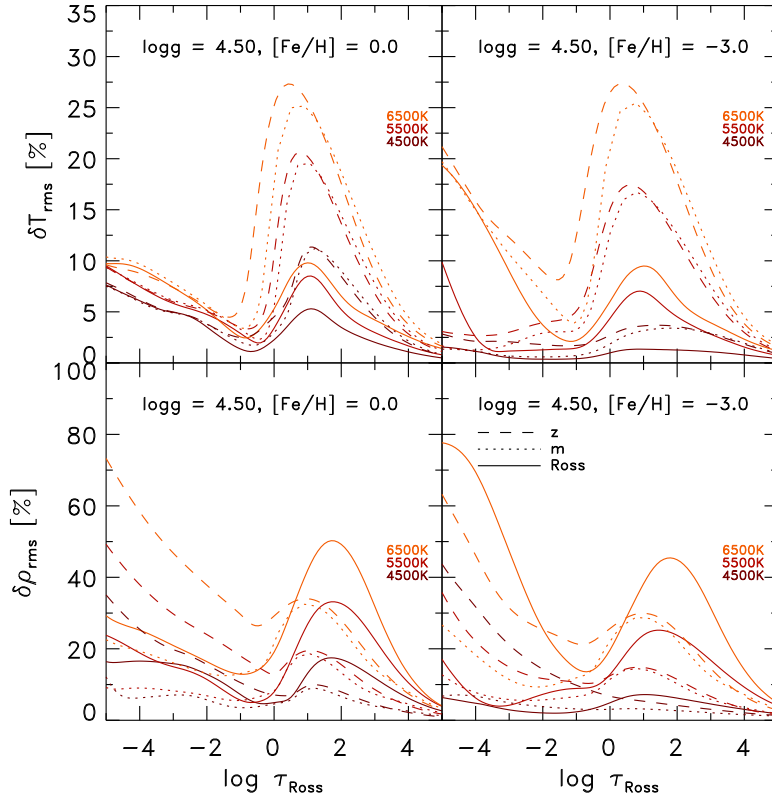


Figure 3.37: Temperature (top) and density (bottom) contrasts vs. averaged Rosseland optical depth. *Dashed lines:* $\langle 3D \rangle_z$ averages; *dotted lines:* $\langle 3D \rangle_m$; *solid lines:* $\langle 3D \rangle_{\text{Ross}}$.

skewed towards higher layers, and the peak location is realized in slightly upper layers. For lower T_{eff} and higher $\log g$, the differences diminish more and more, so that for the coolest models, the difference are small. The differences in the velocity arise as well due to the redistribution of velocity during the mapping to the new reference depth scale (see Sect. 3.6).

3.5 Statistical properties

To explore the origins of the differences among the various average $\langle 3D \rangle$ structures and the resulting ramifications for line formation calculations, we discuss here the statistical properties of the temperature, density, and velocity stratifications. Since the statistical properties of $\langle 3D \rangle_{500}$ and $\langle 3D \rangle_{\text{Ross}}$ are fairly similar, we focus only on the latter.

3.5.1 Contrast

The 3D RHD models usually exhibit a broad range of values at a given height thanks to the fluctuations arising from the convective motions. The amplitude of these fluctuations can be quantified using the root-mean-square of the relative deviation from the horizontal mean value,

$$\delta X_{\text{rms}} = \sqrt{\frac{\sum_{i=1}^N (X_i - \bar{X})^2}{N\bar{X}^2}}, \quad (3.12)$$

which we refer to as the *contrast* (\bar{X} is the mean value of X). It is equal to the normalized standard deviation; i.e., $\delta X_{\text{rms}} = \sigma_X / \bar{X}$.

The translation to another reference depth scale changes the statistical properties as variables are remapped, which in turn is reflected in changes in contrast. Among the various averaging methods, geometric averages $\langle 3D \rangle_z$ typically feature the highest contrast. We also find that the level of fluctuations

generally increases with increasing T_{eff} and decreasing $\log g$. The highest contrast typically prevails in simulations with the highest T_{eff} and located in the vicinity of the maximum superadiabatic gradient, $\vec{V}_{\text{sad}}^{\text{peak}}$, and maximum rms-velocity, $v_{z,\text{rms}}^{\text{peak}}$. These arise from the photospheric transition from convective to radiative energy transport, and the resulting overturning of the entropy-depleted plasma. At the top of the convection zone, the fluctuations reach a minimum, and they decrease towards the bottom of the model atmosphere.

In top and bottom panels of Fig. 3.37, we show the temperature and density contrasts, δT_{rms} and $\delta \rho_{\text{rms}}$, respectively. In the case of the optical depth $\langle 3D \rangle_{\text{Ross}}$, the temperature contrast is significantly reduced compared to the other reference depth scales ($\delta T_{\text{rms}}^{\text{peak}}$ reduced by a factor of ~ 3), while the density contrast is slightly enhanced ($\delta \rho_{\text{rms}}^{\text{peak}} \sim 20 - 60\%$ compared to $10 - 50\%$). For averages on column mass density $\langle 3D \rangle_m$, $\delta \rho_{\text{rms}}$ is lower, in particular, in the upper layers, and δT_{rms} is slightly smaller compared to the $\langle 3D \rangle_z$ case. Fluctuations of variables that correlate with the new reference depth scale will be reduced during the transformation. As the translation to layers of constant optical depth partly evens out the corrugated τ -isosurface, fluctuations of the opacity κ_λ will be reduced, since the dominant H^- opacity is very sensitive to temperature. Therefore, the temperature fluctuations are also smoothed out. Layers of constant column mass density will similarly suppress density variations (see Sect. 3.6). At the top, $\delta \rho_{\text{rms}}$ is almost similar between $\langle 3D \rangle_m$ and $\langle 3D \rangle_{\text{Ross}}$ in the case of the solar metallicity ($\delta \rho_{\text{rms}}^{\text{top}} \sim 40\%$); however, at lower metallicity, $[\text{Fe}/\text{H}] = -3.0$, we find considerable disparity with $\delta \rho_{\text{rms}}^{\text{top}} \sim 80\%$.

The thermal stratification in the upper atmosphere is determined by adiabatic cooling thanks to mechanical expansion and radiative heating because of spectral line re-absorption (Asplund et al., 1999b; Collet et al., 2007). In metal-poor stars, radiative reheating in upper layers is significantly reduced owing to the weakness of spectral line features, while the mechanical expansion cooling term is virtually unaffected. The reversed granulation takes place at increasingly lower geometrical height with higher T_{eff} and lower $\log g$, causing the distribution of the thermodynamic variables to become increasingly broader and more skewed (see Sect. 3.5.3). This is the reason for the enhancement in δT_{rms} and $\delta \rho_{\text{rms}}$ towards the top boundary in metal-poor simulations in Fig. 3.37. Replicating the results of full 3D line formation calculations in low-metallicity stars with $\langle 3D \rangle$ models is therefore challenging, since the averages have to correctly account for such temperature and density fluctuations. Interestingly, the temperature contrast saturates at 6500 K, similar to the saturation of the intensity contrast shown in Sect. 3.1.5 (see Fig. 3.9).

The strength of spectral lines is sensitive to temperature, and the remapping to constant optical depth decreases δT_{rms} , making $\langle T \rangle$ closer to $\langle T \rangle_{\text{rad}}$. However, the transformation to layers of constant optical depth exhibits the side effect of redistributing the other variables, too, in particular, the gas density; $\delta \rho_{\text{rms}}$ is thus much higher than averages on column mass density, due to the additional influence of opacity on the depth scale (see Sect. 2.3). This in turn will likely affect the line formation calculations with the different $\langle 3D \rangle$ models.

The strong contrast in the upper part of the convection zone ($\log \tau_{\text{Ross}} \geq 0$) is induced by the large amplitude fluctuations owing to the radiative energy losses at the photosphere and the asymmetry of the up- and downflows, which we discuss further in Sect. 3.5.2. An interesting aspect is that the contrast in thermodynamic variables is very similar to the rms of the vertical velocity (Fig. 3.36), which is indicative of the correlation between the mass flux and the fluctuations in the thermodynamic variables. Namely, vertical velocity is generated by density contrast $\delta \rho$ via to the buoyancy force, $f_B = -g\delta \rho$, which results from an imbalance of pressure and gravity terms in the hydrodynamical equation for conservation of momentum (see Sect. 1.2.1) in the highly stratified atmosphere. Lighter fluid elements ($\delta \rho < 0$) experience positive buoyancy and thus upward acceleration, while denser elements ($\delta \rho > 0$) experience negative buoyancy and are pulled downward. Buoyancy forces will vanish eventually, when the density of the up- or downflowing element levels with the surrounding gas.

The entropy contrast δs_{rms} (not shown here), qualitatively depicts a very similar dependence on stellar parameter and reference depth scale as δT_{rms} . Both are very similar in optical depth, while for the averages $\langle 3D \rangle_z$ and $\langle 3D \rangle_m$ the overall amplitude is a factor ~ 2 smaller. In Sect. 3.2.8, we showed that the convective energy flux depends on the entropy jump, density, and vertical velocity. Interestingly, here we also find additional *scaling relations* concerning the peak contrast in entropy, $\delta s_{\text{rms}}^{\text{peak}}$, and density, $\delta \rho_{\text{rms}}^{\text{peak}}$, with the vertical peak velocity $v_{z,\text{rms}}^{\text{peak}}$. This can be interpreted as convective driving, where the radiative losses generate large fluctuations in the entropy, temperature, and density.

For the different averaging methods, the variations in the minimum-maximum range for the temperature

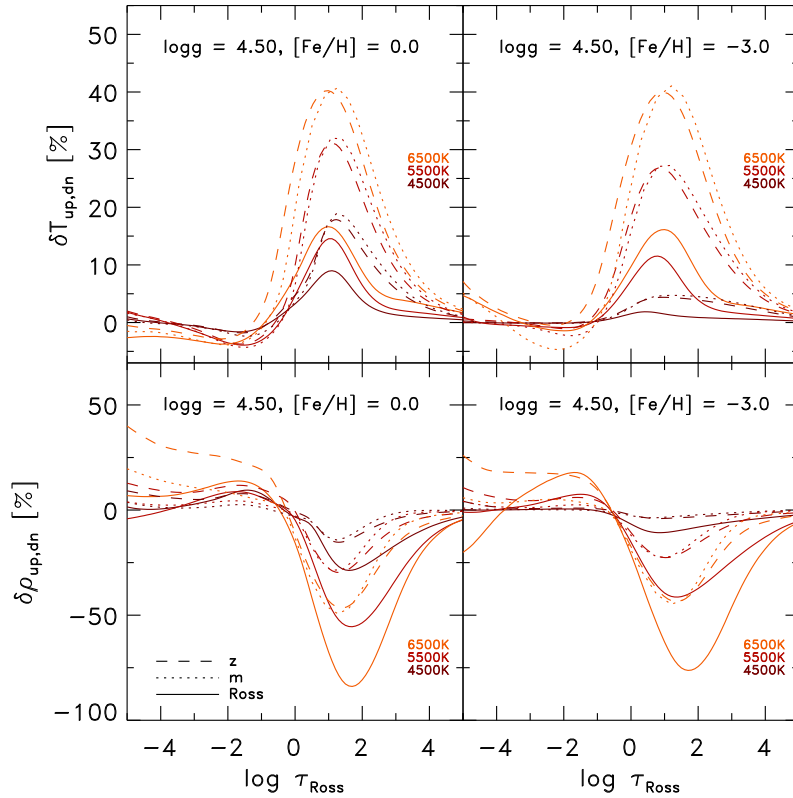


Figure 3.38: Similar as Fig. 3.37 but showing the relative difference between averages in up and downflows, $\delta T_{up,dn}$ and $\delta \rho_{up,dn}$.

and density are qualitatively very similar to the contrast (even though with larger amplitudes $\sim 5 - 8$), therefore, we refrain from discussing these explicitly.

3.5.2 Upflows and downflows

The properties of the convective motions in stellar atmospheres are highly asymmetric in up- and downflows. The upflows overshoot into the photosphere leading to non-thermal Doppler shifts imprinted on spectral line features. We first compute the mean values of various variables separately for up- and downflows based on the sign of the velocity at a given height. We then determine the relative difference between up- and downflows with $\delta X_{up,dn} = (X_{up} - X_{dn})/\bar{X}$ (Fig. 3.38). As expected, the buoyant upflows are hotter and lighter compared to the subsiding downflows. Furthermore, the asymmetries are especially pronounced in the convection zone below the optical surface. Above the photosphere, the convective motions decay quickly, and the asymmetries in $\delta T_{up,dn}$ and $\delta \rho_{up,dn}$ are distinctively smaller. The remaining asymmetries at the top stem from reverse granulation.

The convective flows in granules, slow and almost laminar, radiate away their energy and overturn into the intergranular lanes characterized by cool, dense, narrow turbulent downdrafts. The subsequent large-amplitude fluctuations in the thermodynamical properties are caused by the turbulent mixing of the downflows with the upflows, typically located in the intergranular lane below the optical surface in the SAR. These regions are arranged in tubelike structures around the granules, and can be identified with their excessive vorticity. It is remarkable that, across all stellar parameters, the filling factor of the up- and downflow in the convection zone remains almost constant, with $f_{up} \sim 2/3$ and $f_{dn} \sim 1/3$, respectively (see Sect. 3.1.6).

The variable $\delta T_{up,dn}$ is reduced, and $\delta \rho_{up,dn}$ is enhanced on the optical reference depth scale $\langle 3D \rangle_{Ross}$ compared to the other averages. The column mass density shows a smaller asymmetry in density. This behavior, similar to what we discussed earlier for the temperature and density contrasts, is not entirely surprising, since the fluctuations are caused by the presence of the up- and downflows (see also 3.6).

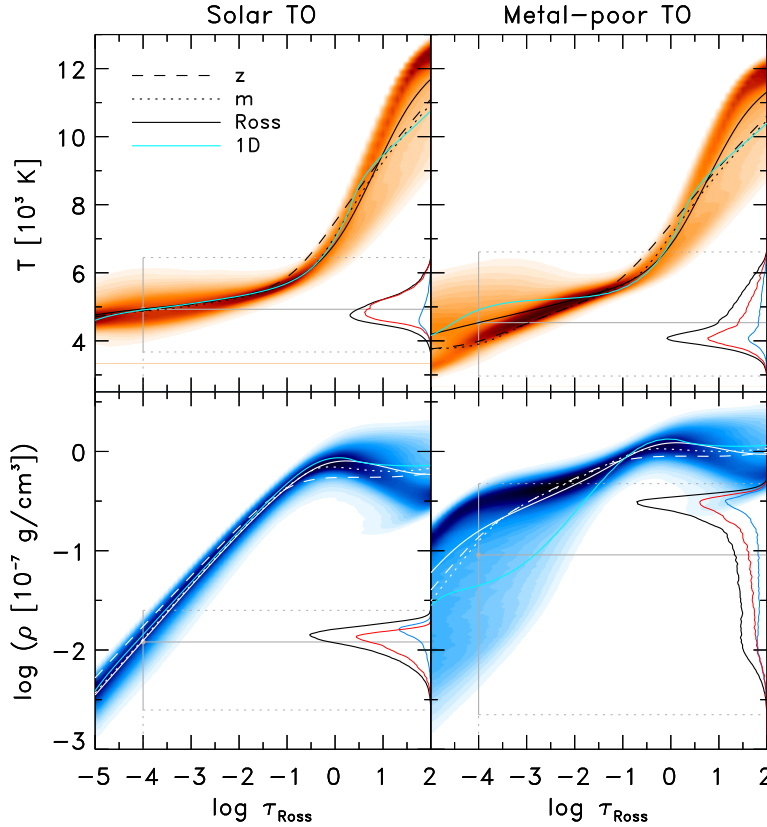


Figure 3.39: Histogram of the temperature (top) and density (bottom) vs. optical depth for the TO simulation ($T_{\text{eff}} = 6500$ K / $\log g = 4.0$) with solar and subsolar metallicity ($[\text{Fe}/\text{H}] = -3.0$). Additionally, the histogram of a single layer ($\log \tau_{\text{Ross}} = -4.0$) is indicated for the whole layer (black) and separated in up- and downflows (blue and red, respectively). *Dashed lines:* $\langle 3D \rangle_z$ averages; *dotted lines:* $\langle 3D \rangle_m$; *solid lines:* $\langle 3D \rangle_{\text{Ross}}$; *blue solid lines:* 1D MLT models.

3.5.3 Histograms

In Fig. 3.39, we illustrate temporally¹⁴ averaged histograms of the temperature, $p(T)$, and density distributions, $p(\rho)$ for the turnoff simulation with two different $[\text{Fe}/\text{H}]$ evaluated on layers of constant Rosseland optical depth, in order to illustrate the differences in the statistical properties. The histogram of the metal-poor case differs substantially in upper layers from the solar one. Furthermore, in Fig. 3.40, we show $p(T)$ and $p(\rho)$ in the upper layers ($\langle \log \tau_{\text{Ross}} \rangle = -4.0$) for dwarf models with different T_{eff} and $[\text{Fe}/\text{H}]$. In both cases we compare the distributions on constant geometrical height z , constant column mass density m and constant Rosseland optical depth τ_{Ross} .

At solar metallicity (Fig. 3.40), the temperature distributions are very narrow and symmetric. With increasing T_{eff} , the average T is as expected higher and the width of the distribution broadens slightly. The mean values are very similar between the different $\langle 3D \rangle$ methods and in principle indistinguishable, which also agrees with Fig. 3.33. Furthermore, the mean values are located very close to the mode.

At $[\text{Fe}/\text{H}] = -3.0$, the temperature distributions change considerably. While at cooler T_{eff} the shape is very narrow and symmetric, for $T_{\text{eff}} \geq 5500$ K we find a distinct broadening of the T -distribution on geometrical reference depth scale $\langle 3D \rangle_z$, which is given by a long tail at high T and a decreasing peak at lower T (see Figs. 3.39 and 3.40). In the column mass density averages $\langle 3D \rangle_m$ the temperature peak is slightly more pronounced at higher T_{eff} , while the high- T tail is slightly reduced. The situation is pretty different for the averages on Rosseland optical depth $\langle 3D \rangle_{\text{Ross}}$, where we find that the temperature peak drops faster towards higher T_{eff} , and at 7000 K the T -distribution shows an almost unimodal distribution. The mean values disagree at higher T_{eff} between the different reference depth scales.

The density distributions behave differently depending on the reference depth scale. On $\langle 3D \rangle_z$ the histograms are in general slightly skewed with a fat tail towards lower ρ for all metallicities (Figs. 3.39 and 3.40). The density distributions for the averages on column mass density are very symmetric and narrow for both solar and low metallicities. At solar metallicity, the density histograms on constant optical depth

¹⁴We compute for each layer its histogram individually, and average these over 20 snapshots.

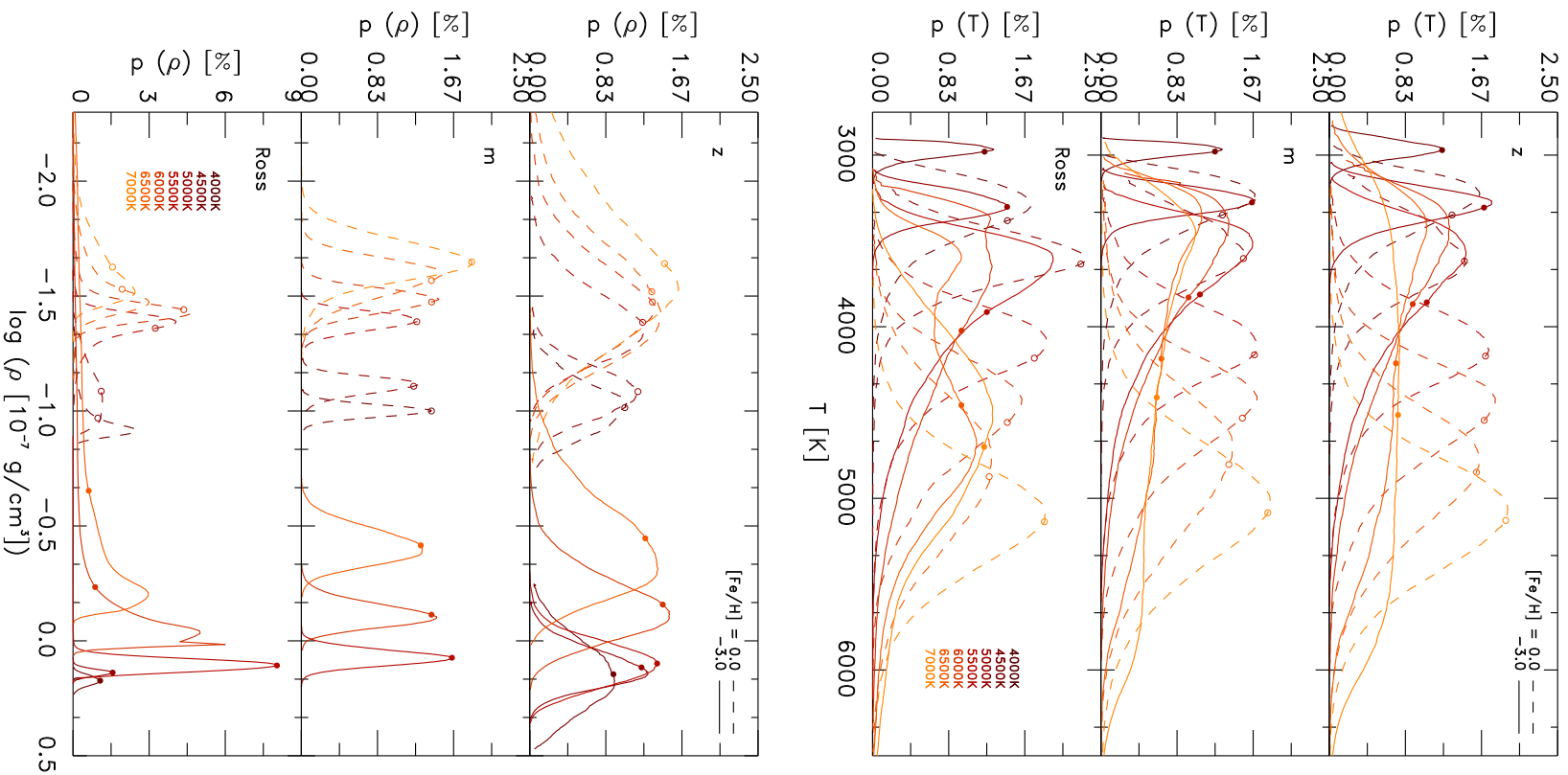


Figure 3.40: Histograms of the temperature (left) and density (right panel) distributions taken at $\langle \log \tau_{\text{Ross}} \rangle = -4.0$. We show the histograms averaged on constant geometrical height (top), column mass density (middle) and Rosseland optical depth (bottom). The surface gravity of displayed models is $\log g = 4.5$ and the metallicity is solar (dashed lines) and subsolar with $[\text{Fe}/\text{H}] = -3.0$ (solid lines). The mean values are indicated by open and filled circles for $[\text{Fe}/\text{H}] = -3.0$ and 0.0 , respectively).

are narrower and higher than the geometrical analogs, but skewed in contrast to $\langle 3D \rangle_m$. In the metal-poor case, $\langle \rho(\rho) \rangle_{\text{Ross}}$ becomes very narrow and symmetric at lower T_{eff} , but towards higher T_{eff} we find the ρ -distribution to also be broader. The mean density stratification varies considerably among the different averaging methods.

As mentioned above, adiabatic cooling due to mechanical expansion and radiative reheating are competing with each other in the upper photosphere and contribute to the phenomenon of reversed granulation. At lower metallicity, the reversed granulation is enhanced, so that the optical depth is increasingly strongly corrugated towards higher T_{eff} , which in turn will amplify the differences in statistical properties during the translation to the optical depth scale from the geometrical depth scale. This leads to the systematic broadening in the statistical distribution that we encounter at lower metallicity.

3.6 Reversed granulation

To illustrate the effects of the remapping of the 3D atmospheric structures on new reference depth scales, we show slices of temperature contours from our TO-simulation in Fig. 3.41. We show horizontal temperature maps taken in the upper atmosphere (top panel) and three vertical slices with different reference depth scales, which include geometrical z (second panel), column mass density m (third panel), and Rosseland optical depth (bottom panel). Furthermore, we indicate three different isocontours of the temperature (yellow) and density (blue lines) in Fig. 3.41, and we also show lines of constant optical depth τ_{Ross} (white lines in top panel) or geometrical depth z (middle and bottom panels).

The downdrafts just below the optical surface, which are denser and cooler than the lighter and hotter surrounding granules, are easily identified (by the prominent changes in T, ρ and τ_{Ross} above the downflows, e.g., $x \approx 1.8 \text{ Mm}$). Owing to the lower temperatures in the downdrafts compared with the granules, the same optical depth value is reached at lower geometrical depths, meaning that the emergent radiation in the intergranular lanes originate in much deeper geometrical heights. The corrugation of the optical depth on geometrical depth scale is therefore most pronounced in the downdrafts (see isocontour of $\log \tau_{\text{Ross}} = 2.0$ in second panel of Fig. 3.41).

The opposite is true for the upper atmospheric layers because of the phenomenon of *reversed granulation* (Rutten et al., 2004; Cheung et al., 2007), namely, above the granules, cooling by adiabatic expansion is dominant, while above the inter granular lanes the radiative reheating and mechanical compression are more important for the energy balance. At lower metallicity and higher T_{eff} , the radiative reheating above granules is reduced by the weakening of spectral line features. The resulting reduction in radiative reheating leads to significantly cooler temperatures (see top panel in 3.41) and a lower pressure support, and as a consequence the atmospheric layers at a given constant optical depth subside toward lower geometrical heights, closer to the optical surface. Therefore, the temperature contrast is enhanced in the upper atmosphere. The subsiding of the atmosphere is similar to what we found earlier, namely that the density range spanned in the atmosphere is significantly reduced at lower metallicity (see Fig. 3.18). Finally, the *enhancement* of the reversed granulation and the temperature contrast results in strongly corrugated surfaces of constant optical depth at the top of metal-poor simulations. We note that we also found an *enhanced* intensity-contrast for metal-poor stars (see Sect. 3.1.5).

The remapping of the individual columns of the 3D structure from geometrical depth to optical depth entails a change of perspective between the old and the new scales in terms of the distribution of values of a particular physical variable at a given constant reference depth. This is again most obvious in the downdrafts in the convection zone (see line of constant geometrical depth at $z = 0.2 \text{ Mm}$ in bottom panel of Fig. 3.41). Properties from deeper geometrical heights are mapped onto layers at lower optical depth, and the temperature differences between upflowing and downflowing regions are reduced, which results in a less of a temperature contrast and in minimum-maximum ranges (see Sect. 3.5.1). On the other hand, the deviations in the density are significantly *enhanced*, which will clearly alter the statistical properties, in particular, the mean values.

In the upper atmospheric layers of the solar metallicity case, the optical depth is corrugated only a small amount, therefore the transformation does not affect the temperature and density much (compare the upper flat blue line with the two lower corrugated ones in the bottom panel of Fig. 3.41). However, the corrugation of the optical depth in the upper atmosphere is rather large for hotter metal-poor stars

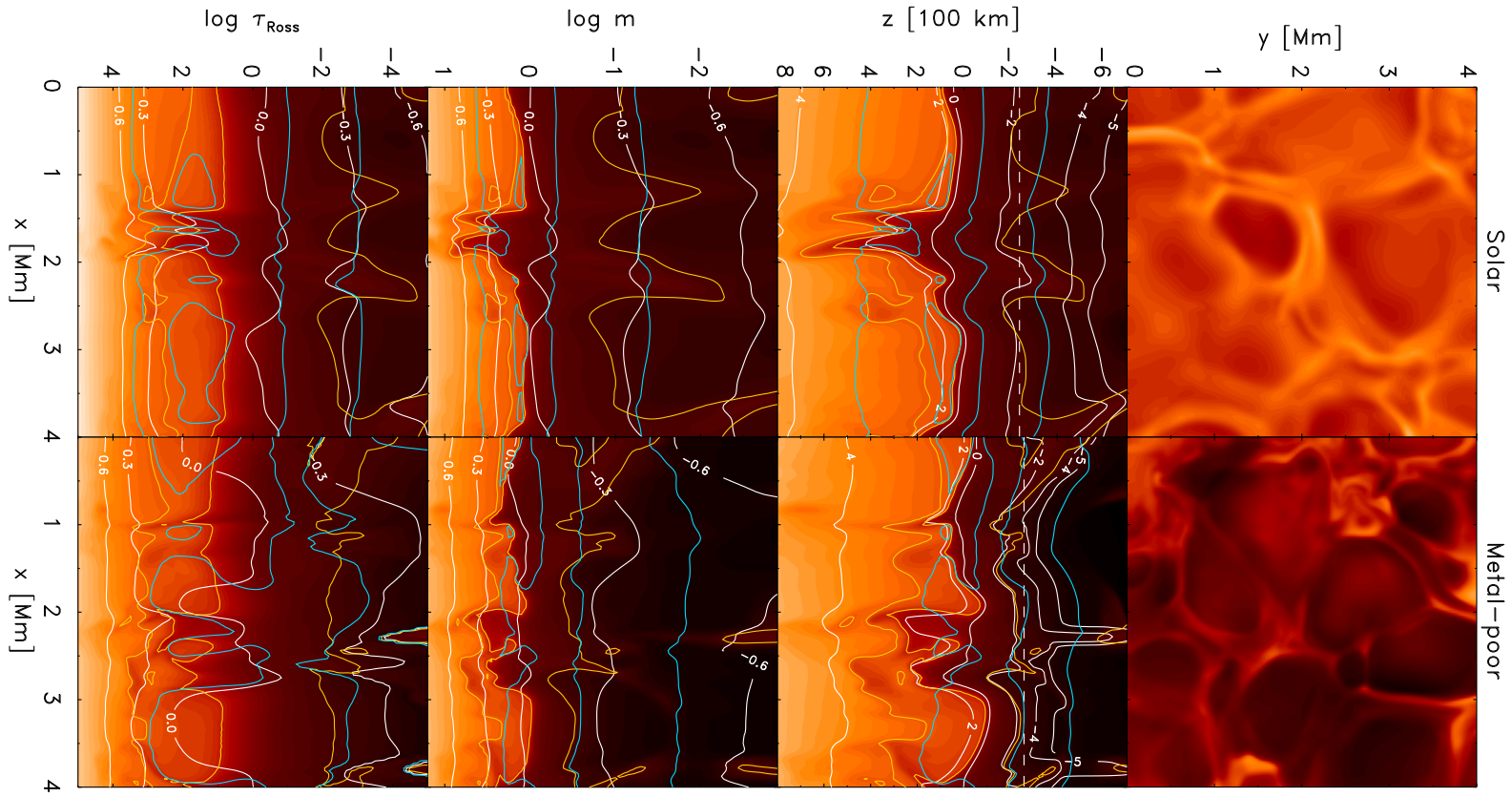


Figure 3.41: Temperature-contours from our model with $T_{\text{eff}} = 6500\text{K}$ and $\log g = 4.5$ with $[\text{Fe}/\text{H}] = 0.0$ (left) and -3.0 (right). The top panels display horizontal slices with the reversed granulation pattern imprinted in the temperature map (from 3 to $7 \times 10^3\text{K}$) taken at $\sim 230\text{km}$ above the surface, which is also indicated in the second panel (dashed lines). The panels below show vertical slices (T -contours from 2 to $17 \times 10^3\text{K}$) ranging from $-5.0 \leq \log \tau_{\text{Ross}} \leq 5.0$ on layers of constant geometrical height (second), column mass density (third) and Rosseland optical depth (last panel). These panels include isocontours of the temperature (5 , 10 and $12 \times 10^3\text{K}$; yellow lines) and density (0.1 , 1.0 and $2.5 \times 10^{-7}\text{g}/\text{cm}^3$; blue lines) and both increase with decreasing vertical depth. We show also lines of constant optical depth (second) and geometrical depth (third and last) indicated with white lines.

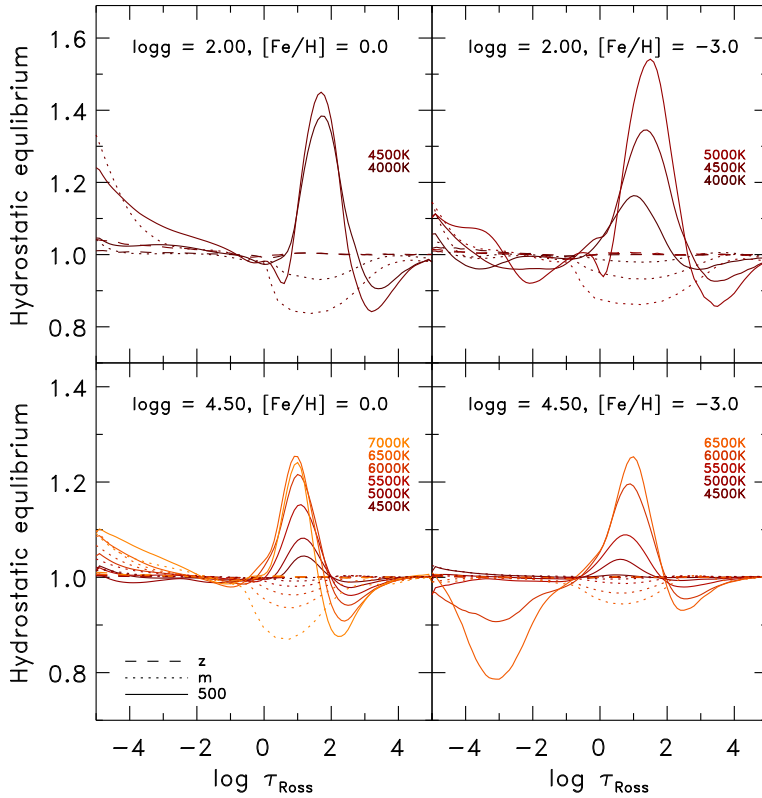


Figure 3.42: Deviations from the hydrostatic equilibrium vs. optical depth. *Dashed lines:* $\langle 3D \rangle_z$ averages; *dotted lines:* $\langle 3D \rangle_m$; *solid lines:* $\langle 3D \rangle_{\text{Ross}}$.

owing to the enhanced reversed granulation. As a result, the effects of remapping on the optical depth scale for the temperature and density is fairly substantial in these simulations. And the distribution of the thermodynamic properties is broadened, such that the meaning of the horizontal average is weakened (see Fig. 3.40).

In a similar way, the translation to column mass density naturally reduces the variations in density thanks to its definition of the reference depth scale, which is the depth-integrated density. Therefore, the resulting density fluctuations are rather small in layers at constant column mass density. The variation in temperature is slightly lower than in the averages on geometrical depth, but larger than in the averages on optical depth, as one would expect.

We stress once again that the different reference depth scales are equivalent to each other in terms of the spatial remapping of the 3D atmospheric structures. What differs of course is the statistical properties of physical variables on layers of constant depth, which vary depending on the choice of reference depth scale. One has to consider two important aspects concerning the horizontal averaging, the first being what kind of quantity is considered, and the second which reference depth scale is accounted for. Therefore, the statistical properties of the density and temperature are relatively distinctive depending on which reference depth scale is considered (see Sect. 3.5).

3.7 Hydrostatic equilibrium

The STAGGER-code directly solves the discretized time-dependent, radiative-hydrodynamical equations (see Sect. 1.2.1) for the conservation of mass, momentum, and energy. The conservation properties are reflected in the mean $\langle 3D \rangle_z$ stratifications of relaxed, quasi-stationary 3D hydrodynamical models averaged on layers of constant geometrical depth. In particular, the geometrical averages appear over time to

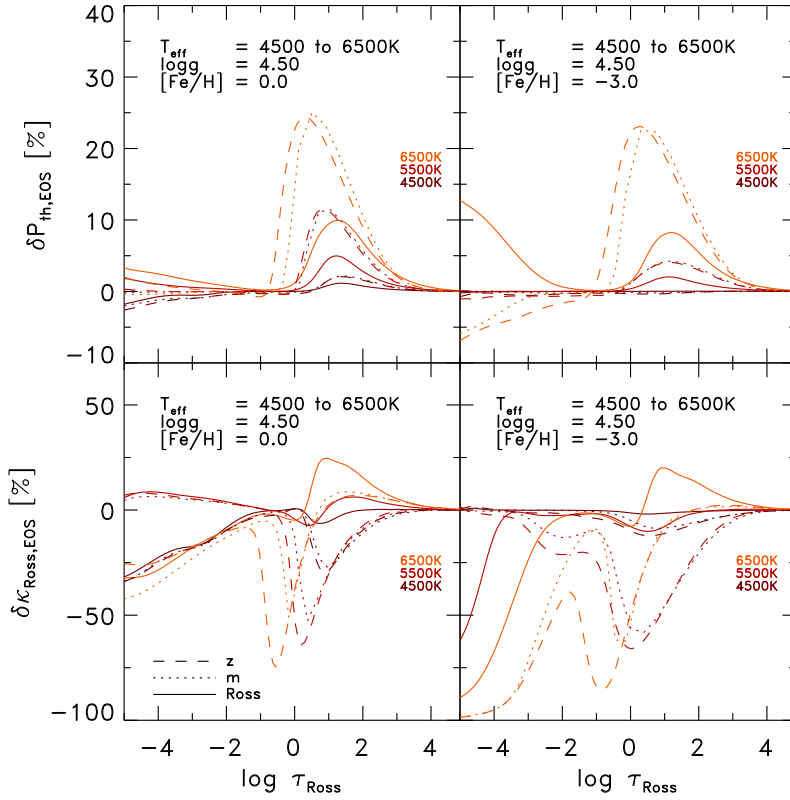


Figure 3.43: Deviations between the spatially and temporally averaged pressure (*top*) and opacity (*bottom*) and the values derived from the EOS, i.e. $X(\langle \rho \rangle, \langle \epsilon \rangle)$, vs. optical depth. *Dashed lines*: $\langle 3D \rangle_z$ averages; *dotted lines*: $\langle 3D \rangle_m$; *solid lines*: $\langle 3D \rangle_{\text{Ross}}$.

be close to hydrostatic equilibrium.¹⁵ In Fig. 3.42 we show the hydrostatic equilibrium in the form of $\rho g dz/dp_{\text{tot}} = 1$ for the *temporal* and *geometrical* averaged $\langle 3D \rangle_z$ stratifications, which are very close to hydrostatic equilibrium. We emphasize that the hydrostatic equilibrium is only fulfilled by considering the *total* pressure p_{tot} , as given in Eq. 1.8, which includes the non-thermal *turbulent pressure* that occupies a significant fraction of p_{tot} at the top and in the SAR (see Fig. 3.23).

Furthermore, one can find in Fig. 3.42 that the averages on a new reference depth scales feature distinctive deviations from hydrostatic equilibrium (see $\langle 3D \rangle_{\text{Ross}}$ and $\langle 3D \rangle_m$). The transformation to a new reference depth scale maps all three components of Eq. 1.8 – geometrical depth z , density ρ , and total pressure p_{tot} – away from its hydrostatic equilibrium state. Also, the geometrical depth z loses its strict physical meaning through such a transformation as a mean value. The mean stratifications on constant Rosseland optical depth $\langle 3D \rangle_{\text{Ross}}$ deviate slightly at the top and significantly in the SAR from the hydrostatic equilibrium ($\langle 3D \rangle_{500}$ is very similar). The largest departures can be found in the SAR. Furthermore, the amplitude of the discrepancy from hydrostatic equilibrium increases for higher T_{eff} and lower $\log g$.

3.8 Deviations from the EOS

In 3D RHD simulations, the thermodynamic state of a simulation is self-consistently determined by the EOS. This means in particular, that any thermodynamic variable depends on only two independent variables (namely the gas density ρ and the internal energy ϵ) in a well-defined way under the assumption of a constant chemical composition. However, the internal self-consistency is broken by reductions like temporal or spatial averaging.

This can be easily understood by investigating the behavior of a function $f(X)$ on a 3D cube of quantity X . For small fluctuations $X' = X - \langle X \rangle$ around the horizontal average at a given depth in the model

¹⁵This statement only holds when considering sufficiently long temporal sequences of snapshots: the individual simulation snapshots at a given instant in time are not in hydrostatic equilibrium.

atmosphere, a Taylor-expansion of f up to second order yields

$$f(X) = f(\langle X \rangle + X') \quad (3.13)$$

$$\approx f(\langle X \rangle) + \left. \frac{df}{dX} \right|_{\langle X \rangle} X' + \frac{1}{2} \left. \frac{d^2f}{dX^2} \right|_{\langle X \rangle} X'^2. \quad (3.14)$$

The horizontal average of this expression evaluates to

$$\langle f(X) \rangle \approx \langle f(\langle X \rangle) \rangle + \left. \frac{df}{dX} \right|_{\langle X \rangle} \langle X' \rangle + \frac{1}{2} \left. \frac{d^2f}{dX^2} \right|_{\langle X \rangle} \langle X'^2 \rangle \quad (3.15)$$

$$= f(\langle X \rangle) + \left[\frac{1}{2} \left. \frac{d^2f}{dX^2} \right|_{\langle X \rangle} \langle X'^2 \rangle \right] \delta X_{\text{rms}}^2, \quad (3.16)$$

where the definition of the contrast δX_{rms} was used in the last equation (see Eq. 3.12 in Sect. 3.5.1). The linear term in Eq. 3.15 vanishes as $\langle X' \rangle = 0$ by definition. It is immediately clear that $\langle f(X) \rangle = f(\langle X \rangle)$ holds for linear functions. It is thus the non-linearity of f that causes a departure of $\langle f(X) \rangle$ from $f(\langle X \rangle)$, because the departure scales with the square of the contrast δX_{rms} . The discussion can be easily expanded to functions of two variables $f(X, Y)$, since they are found in the EOS.

As a consequence, deriving thermodynamic quantities from averaged independent variables, $\langle \rho \rangle$ and $\langle \varepsilon \rangle$, will lead to inconsistent outcomes. The mean pressure in a given layer of the 3D cube will deviate from the pressure calculated with the EOS from mean density and mean internal energy, $\langle p_{\text{th}} \rangle \neq p_{\text{th}}(\langle \rho \rangle, \langle \varepsilon \rangle)$. Therefore, with $\langle 3D \rangle$ we face another level of complexity.

To quantify the deviations, we compute the temperature T , pressure p_{th} , opacity κ_{Ross} , and electron number density n_{el} from the EOS by employing the mean independent variables $\langle \rho \rangle$ and $\langle \varepsilon \rangle$. Then, we determine the relative disagreement as $\delta X_{\text{EOS}} = (\bar{X}_{\text{EOS}} - \bar{X})/\bar{X}$. In Fig. 3.43, we display the deviations of thermal pressure $\delta p_{\text{th}}^{\text{EOS}}$ and opacity $\delta \kappa_{\text{Ross}}^{\text{EOS}}$. As suggested by Eq. 3.16, we find the maximal deviations typically below the optical surface in the SAR, where the large fluctuations take place due to the overturning and to the presence of convective motions with their highly asymmetric up and downflows. The mean value thus toddles between the bimodal distribution. Furthermore, we find a strong variation in the δX_{EOS} with stellar parameter, which increases for higher T_{eff} and lower $\log g$. Depending on which reference depth scale is applied, the disagreement δX_{EOS} are distinct.

This loss of consistency caused by dimensional reduction means that mean $\langle 3D \rangle$ models can never entirely substitute full 3D models, especially for spectral line formation applications (Uitenbroek & Criscuoli, 2011). The mean stratifications are nothing more than statistically meaningful representations of stellar atmospheres, while only the complete 3D data set describes their physical state completely. In 1D model atmospheres, such internal consistency is maintained at all times, since no spatial averaging of non-linear variables is involved in the construction of 1D models.

Chapter 4

Stellar granulation

Our host-star, the Sun, shows a distinct granulation pattern on its observable (optical) surface, which is simply the manifestation of the subsurface convection that transports energy to the surface. The solar granulation pattern has been subject to manifold observational studies over the last decades with progressively increasing resolution due to technological advances (e.g. Roudier & Muller, 1986; Hirzberger et al., 1997; Schrijver et al., 1997; Bovelet & Wiehr, 2001). Nowadays high-resolution solar observations are comparable to the typical numerical resolution with ~ 77 km (see Abramenko et al., 2012a). Until the advent of realistic 3D RHD simulations, which solve the hydrodynamic equations coupled with a realistic radiative transfer, direct comparisons of theoretical predications with the solar granulation properties were absent, since the 1D models are incapable to predict the typical stellar granulation pattern imprinted in the emergent (bolometric) intensity map emerging from the stellar surface. Stein & Nordlund (1998) found similar solar granule sizes compared to the observations from the quiet-sun with typical diameters of ~ 1 Mm.

In this Chapter I want to address the two key questions: how realistic are the solar granule properties in our simulation? And, also how do the stellar granules properties change for different stellar parameters? I will explain the granule recognition method I have used to detect the individual granules from the intensity map of the 3D simulations (Sect. 4.1), and subsequently I will discuss the various properties of individual granules, such as their diameter, intensity, temperature, density, velocity and geometry (Sect. 4.2). Moreover, I will consider the fractal dimension (Sect. 4.3), the properties at the optical surface (Sect. 4.4), and finally the topology of the solar granules (Sect. 4.5).

We find in all of our 3D RHD simulations a dominant granule size very similar to the solar case. The granules can be divided in a smaller and larger population relative to the dominant granule size, which generally distinguish in their properties. As the most interesting result in this Chapter, I want to highlight the Section on the fractal dimension (Sect. 4.3), in particular, the two distinct values with $D_1 = 1.04$ and $D_2 = 1.85$ for the smaller and larger granules in the solar simulation, respectively. The smaller granules are regular shaped and dimmer, while the larger ones are fragmenting granules, therefore, these exhibit an increasingly irregular, complex shape and intensity contrast.

4.1 Granule recognition

Several methods for detecting granules in the observed intensity have been developed over the years. Classically, a single-level clip of an intensity image is used for the granule recognition, where the small and large features are filtered out by spatial passband Fourier filtering. These "Fourier-based recognition" (FBR) techniques have been the most commonly applied ones in the past, and are fast, but also very inaccurate (see Roudier & Muller, 1986; Hirzberger et al., 1997). Another possible approach is to trace granules with a single fixed relative intensity-levels, e.g., between 0.97 and 1.03, as proposed by Abramenko et al. (2012b). However, in this present work we prefer, the more robust "multiple level tracking" algorithm that was developed by Bovelet & Wiehr (2001). It is a simple, yet very powerful tool to extract the granules from the (bolometric) intensity map alone. The basic idea behind this method is to find (granular) shapes

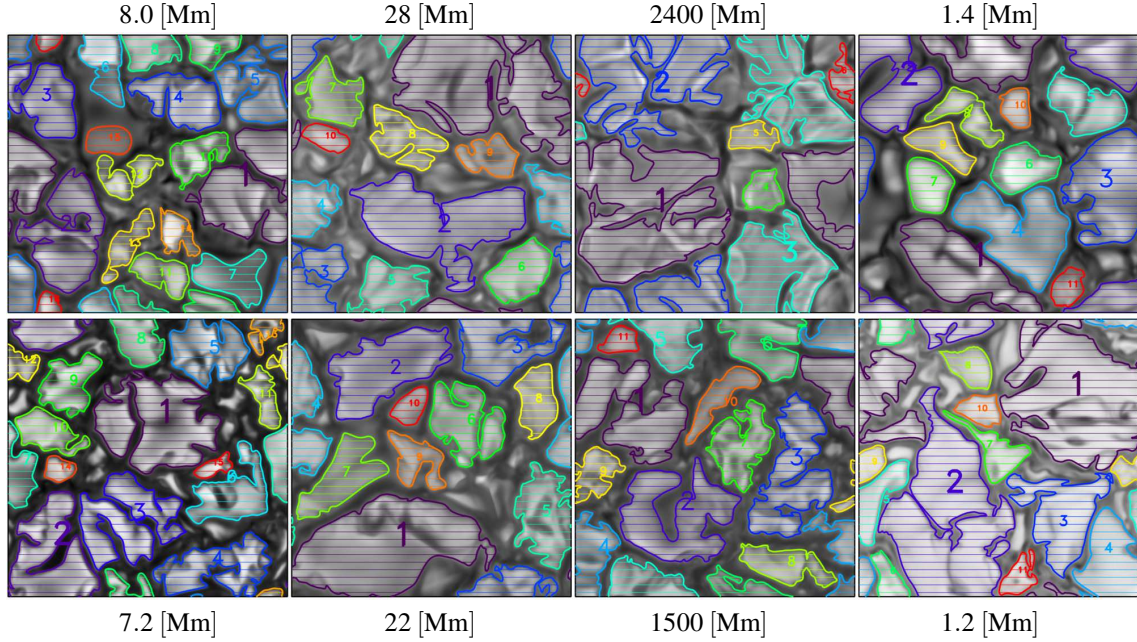


Figure 4.1: Emergent (bolometric) intensity map (*gray contours*) over-plotted with the (colored) contours of the recognized granules (*left to right*) for the Sun ($T_{\text{eff}}/\log g = 5777\text{K}/4.44$), turnoff star (6500 K, 4.0), K-giant (4500 K, 2.0) and K-dwarf (4500 K, 5.0) with solar and sub-solar metallicity with $[\text{Fe}/\text{H}] = -3.0$ (*top and bottom*, respectively). The granules are numbered in the order of decreasing granule size at its respective barycenter (large characters refers to large granule size).

repeatedly for decreasing intensity level clips, thereby increasing their filling factors, until a predefined threshold filling factor is matched. Then, one obtains unambiguously the granules with a single input parameter being the filling factor for the upflows, f_{up} . Since the latter is basically the same for all stellar parameters with $f_{\text{up}} \approx 2/3$, the granule-recognition is in principle unambiguous with the multiple level tracking algorithm (see Sect. 3.1.6). Furthermore, we find the latter algorithm being very fast, robust, and works for different stellar parameters similarly as good as for the Sun. To demonstrate this, we show the results for the Sun, a turnoff star, a K-giant, and a K-dwarf and their metal-poor analogs in Fig. 4.1.

Following the multiple level tracking algorithm, we traced the granules in our simulations with the IDL CONTOUR routine and computed the respective filling factor, f_i , of the considered intensity-level. We started at the relative intensity $\bar{I} = 1.2$ and decreased the intensity level down to 0.97 in steps of 0.01, until f_i reached the threshold value¹ with $f_{\text{up}} = 0.60$ for all stellar parameters. As next, we enlarged the intensity maps by exploiting their horizontal periodicity, and we determined the area and equivalent diameters and further properties for each granule. Then, we dismissed very small patches and granules outside the simulation box located entirely in the enlarged domain, matched the fragmented parts of granules that were located at the edge, and classified them in two populations: small (fractional) granules, A_1 , and large granules, A_2 , with the latter being larger than the one-third of the average area, i.e., $A_2 \geq 1/3\bar{A}$. Furthermore, we singled out dark spots and bright points. Following Abramenko et al. (2010) we enhanced the contrast of the intensity by subtracting the smoothed values \hat{I} (window size of 5 pixels), and computed the rms for $I_{\text{rms}} = I - \hat{I}$. Then, the bright points were detected at the 2σ -threshold relative to the other granules. We performed the granule-recognition for each snapshot of the time-series, thereby leading to large sample of granules with typically several thousand granules for an individual simulation (e.g., Sun ~ 3800 for 150 snapshots), which improves the statistics.

From the area of the granules we determined the equivalent diameter with

$$d_{\text{gran}} = 2\sqrt{A_{\text{gran}}/\pi}, \quad (4.1)$$

¹We have chosen the threshold value slightly lower than $f_{\text{up}} \approx 0.66$ to yield a better distinction between the granules.

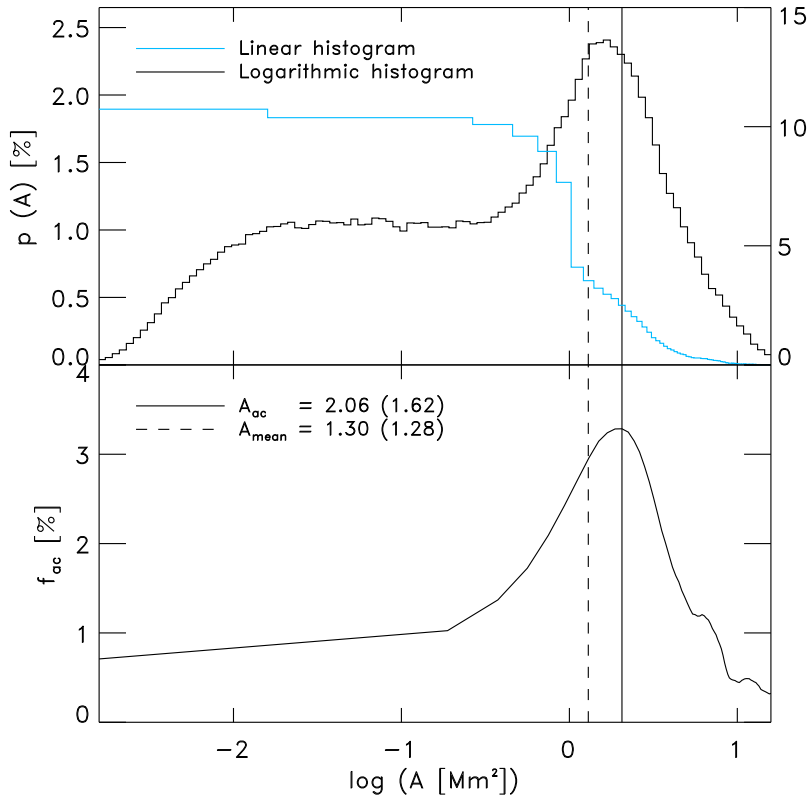


Figure 4.2: The linear and logarithmic histogram of the granule area, A , (top panel; blue and black line, respectively) and the area contribution, f_{ac} , (bottom) derived from our solar simulation. We indicated the location of the mean granule area (dashed) and the maximum of f_{ac} (solid line).

which is the the diameter of a circle that has the same area A_{gran} . With the granule size we refer to d_{gran} or A_{gran} in the following. Furthermore, we determined the unique geometric center, which is the barycenter

$$\vec{x}_{bc} = \sum \vec{x}_i A_i / A_{gran}, \quad (4.2)$$

where the summation runs over all pixels enclosed by the contour of the granule, and \vec{x}_i is the vector pointing to the cell i , and A_i is the pixel area.

The above mentioned granule detection methods assume that bright regions in the intensity maps associate with the hotter and lighter stellar plasma leading to the bulk, upflowing granules, which is very good fulfilled, as we demonstrate in Sect. 4.4.2. Therefore, the remaining dark regions in the intensity maps inherently consist of cool, dense gas, which one usually refers as the (negatively buoyant) downdrafts.

4.2 Granule properties

The granule size is the first property we want to address, therefore, we show the histogram of the granule areas of the Sun in Fig. 4.2. The range in granule sizes is very large (typically spanning four orders), therefore, a histogram considering linear equidistant granules sizes for the bins would overestimate the smallest values by employing very large bins for the histogram (see Fig. 4.2). This would lead to a bottom-heavy distribution, which might lead to the misleading conclusion of a dominant a large number of small granules (see Roudier & Muller, 1986; Hirzberger et al., 1997; Abramenko et al., 2012b). Therefore, we advise strongly against a linear binning of the histograms for strongly varying quantities like the granule size. To avoid this mistake we considered the logarithmic granule area for the histograms. Then, the smallest granule sizes are better resolved, and one yields more accurate distribution, while a linear bin size would group the smallest granules into just a single bin, thereby leading to an apparently large probability. In Fig. 4.2 one can withdraw that the histogram exhibits a maximum close the mean granule size, which

we refer to as the mode of granule size

$$d_h = \max[p(A)]. \quad (4.3)$$

The distribution around the mode of the granule size is very asymmetric. For larger granule sizes than the mode, the distribution drops rapidly within a short range, while for lower values it also drops after a plateau, but the range of the smaller half is distinctively larger. These two regimes represent on the one hand the oversized fragmenting granules and the other hand the resulting fragments. The (fragmented) small-scale granules were found in high-resolution solar observations by Abramenko et al. (2012b). The fragmentation of granules is a continuous process, therefore, the distribution of granule sizes is also continuous, and it covers a fairly large range in size.

Also another possibility to quantify the granule size distribution is the the area contribution function, which is given by

$$f_{ac} = n_i A_i / A_{tot}, \quad (4.4)$$

with n_i being the number of elements within the area-bin A_i , and $A_{tot} = \sum n_i A_i$ being the total area of all granules. The area contribution function is in principle a histogram of granule size, which is weighted with the contribution of area to the total area (see Roudier & Muller, 1986). We noted above that a linear granule size is overestimating the histogram for smaller granules. The contribution function has the intrinsic advantage that a large number of small granules contributes only little to the f_{ac} , since their area is small. It depicts the dominant granule size, which contributes most to the radiation, independently of the linear or logarithmic bin sizes. In Fig. 4.2 we show the area contribution function resulting from the solar simulation. Here, we can also uniquely label the dominant granule size with the maximum, i.e.

$$d_{ac} = \max[f_{ac}]. \quad (4.5)$$

Similar to the above finding with d_h , the dominant granule size divides the distribution into two regimes at a very similar value, which supports further the location of the "significant" granule size. The decline towards larger granule sizes is similar, but the lower part is noticeably smaller than the histogram (both are not expected to coincide entirely due to their different definitions). We remark that the lower values of f_{ac} towards smaller granules sizes illustrates that employing a logarithmic scale for the histograms of the granule size is essential to yield correct conclusions on the "real" declining distribution of the smallest granules. We find for the solar simulation a dominant scale of $A_{ac} = 2.06 \text{ Mm}^2$, which is $d_{ac} = 1.61 \text{ Mm}$. Observational findings have similar values with $d_{ac} \approx 1 \text{ Mm}$ (Roudier & Muller, 1986; Hirzberger et al., 1997), and the given difference arises probably from atmospheric and instrumental effects (see Stein & Nordlund, 1998).

4.2.1 Diameter of granules

In the following we want discuss the resulting granules sizes for different stellar parameters. Therefore, we show in Fig. 4.3 the (smoothed) histograms of the granule diameters, d_{gran} (Eq. 4.1; the area histograms are the same). For higher T_{eff} and $[\text{Fe}/\text{H}]$ the mean granule sizes are slightly larger, while towards giants (lower $\log g$) these are significantly larger, since the pressure scale height scales with the surface gravity directly (see Sect. 3.1.6). In general, the shapes of the histogram are similar to the solar one and also exhibit a mode in their granule sizes. In the case of dwarfs, the peak at the d_h is less pronounced towards lower T_{eff} and we find increasingly a bimodal distribution with a distinct second peak from the small-scale granules (in particular, for giants). The second peak at smaller granule sizes varies with stellar parameter, so that in some cases the two peaks are similar, and in a few the second peak at smaller d_{gran} is even higher than that at the larger ones. This indicates that in these models the granules fragment into smaller pieces more frequently (see Sect. 4.3). However, most of radiation still emerges from the larger peak, since the area contribution function exhibits a single peak, which is located at larger granules sizes (see Fig. 4.3 and Sect. 4.2.2). Furthermore, the decline towards larger fragmenting granules is steeper with higher T_{eff} , which means that these granules disintegrate within a smaller range of granule sizes. The lower half of the histograms are similar despite a shift and the second peak.

Our findings carry some uncertainty that might be rooted in the granule detection method or in the simulation boundaries. However, we assume that our results are robust, since these are qualitatively similar

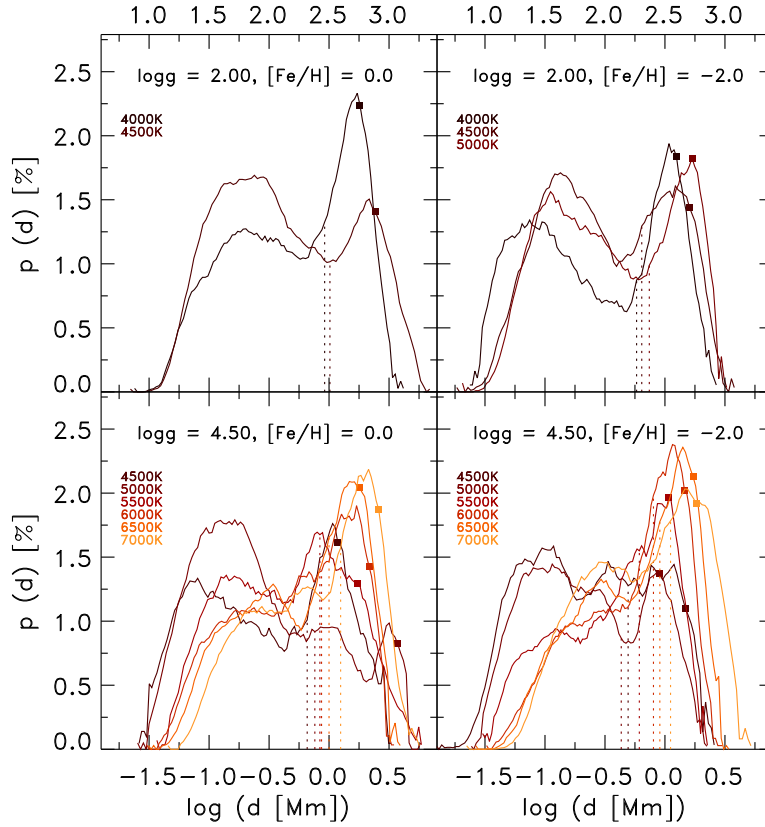


Figure 4.3: The logarithmic histograms of the granule size, d_{gran} , smoothed with a window of 10. Furthermore, we indicated the mean granule diameters (dotted lines) and the dominant scales, d_{ac} (filled squares). Note the difference in abscissa between the top and bottom panel.

to those by Beek et al. (2013). They find also an asymmetric distribution exhibiting a dominant granule size with a depressed tail for the small-scale granules. Moreover, they also find the mean granule diameter being similar and their filling factors are also around $f_{\text{up}} \approx 2/3$.

4.2.2 Intensity distribution of granules

In Fig. 4.4, we show the mean (bolometric) intensities of granules (seen at the disk-center), $\langle I_g \rangle$, that are normalized by the temporal average of the entire simulation, $\langle I \rangle$, against their granule sizes, including also their ranges of the extrema. Smaller granules are darker ($\sim 5 - 9\%$) and larger granules are brighter, and around the dominant granule size, d_{ac} , one finds the brightest granules ($\sim 5 - 15\%$). This means that the most abundant granules with sizes similar to d_{ac} cover most of the stellar surface and are the brightest, i.e. these dominate the bolometric intensity not only due to their size and abundance. Therefore, most of the radiative energy is lost in these granules. The mean intensities of granules larger than d_{ac} are lower than the maximal, since these large fragmenting (exploding) granules develop dark spots due to pressure excess and mass flux reversal (see Stein & Nordlund, 1998), which is then reducing the mean intensity. Hirzberger et al. (1997) finds also a similar granule size dependence for the mean intensity in the observed solar granules: for the smaller granules, the intensity is rising towards larger d_{gran} and slightly decreasing above the dominant granule size.

Furthermore, the larger granules have larger extremal ranges in intensity in Fig. 4.4, and around the mean granule size one finds a distinct enhancement in the darkness (minimum) that arises due to presence of dark spots typically preceding the granule splitting. For higher T_{eff} , smaller granules are dimmer and the larger ones are brighter, while for different $\log g$ the changes are only subtle. In the case of metal-poor simulations, the same small-scale granules are darker for hotter T_{eff} and brighter for cooler T_{eff} compared to the solar case, which correlates with the enhancement of the intensity contrast at lower metallicity (see Sect. 3.1.5). Namely, due to the lack of metals at lower metallicity, the importance of neutral hydrogen as primary electron-donors increases for higher T_{eff} , and since the electron density is controlling the formation

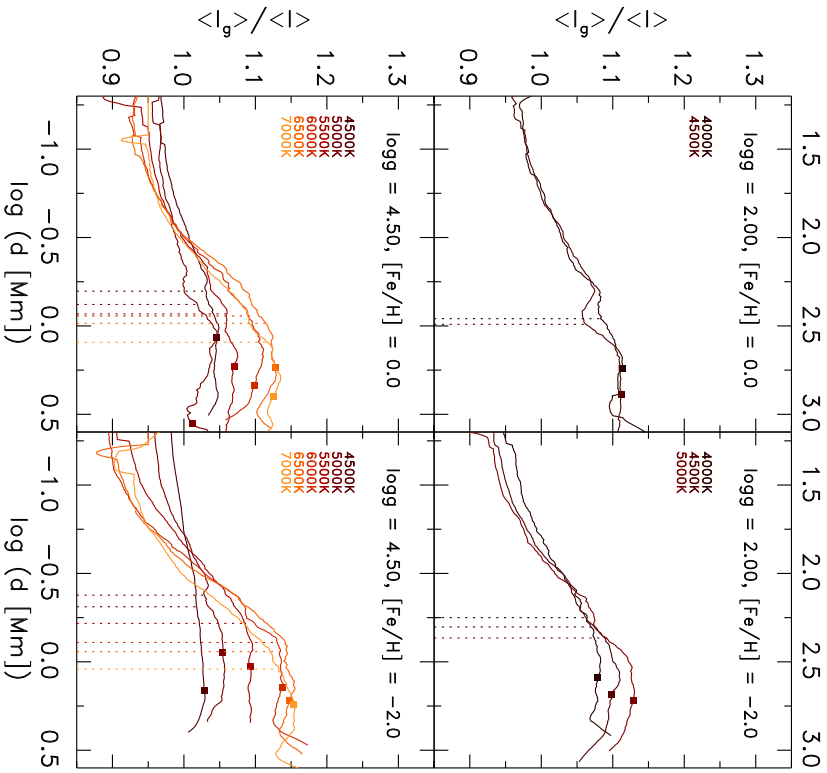


Figure 4.4: Mean normalized intensity vs. granule size. Furthermore, we indicated the mean granule diameters (*dotted lines*) and the dominant scales, d_{ac} (*filled squares*). Note the difference in abscissa between the top and bottom panel.

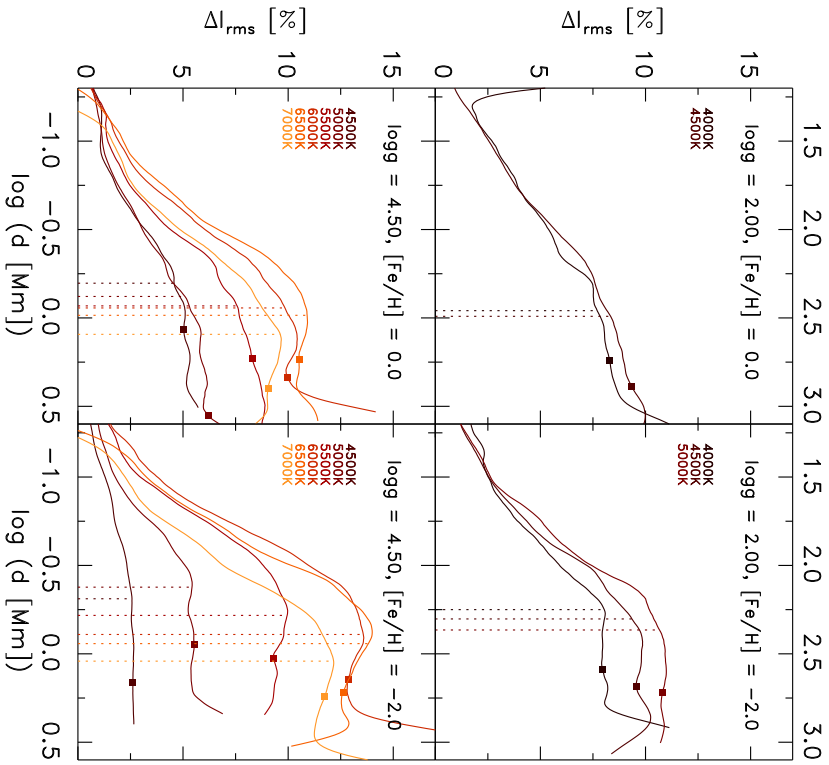


Figure 4.5: Mean intensity contrast vs. granule size. Furthermore, we indicated the mean granule diameters (*dotted lines*) and the dominant scales, d_{ac} (*filled squares*). Note the difference in abscissa between the top and bottom panel.

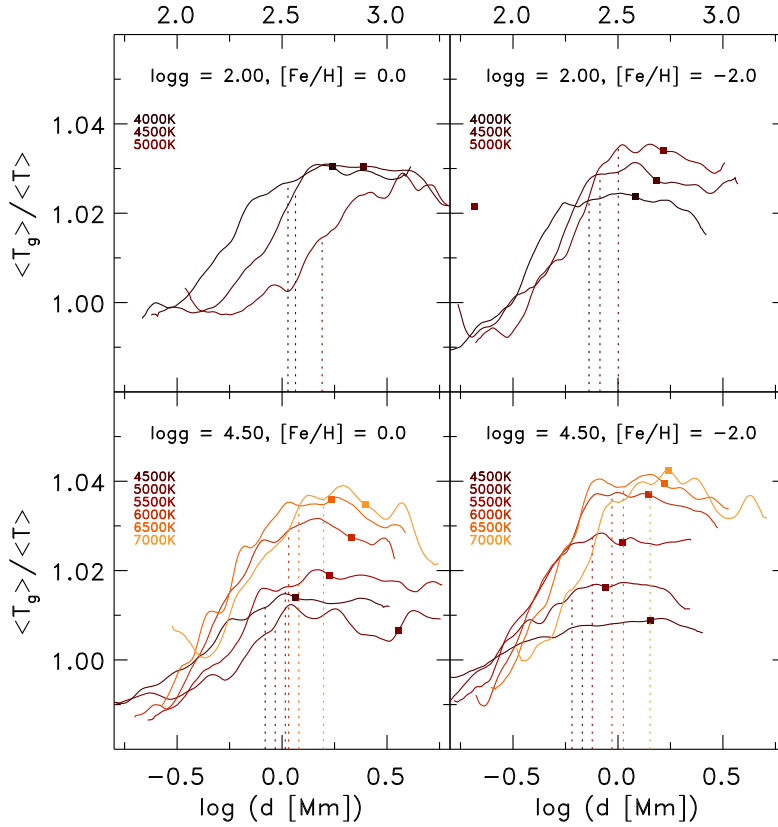


Figure 4.6: Mean normalized granule temperature vs. granule size, which is obtained on layers of constant Rosseland optical depth. Furthermore, we indicated the mean granule diameters (dotted lines) and the dominant scales, d_{ac} (filled squares). Note the difference in abscissa between the top and bottom panel.

of negative hydrogen – the dominant opacity source – the opacity is therefore more sensitive to an increase in temperature.

In Fig. 4.5, we show the intensity contrast of the granules vs. their size. The trends are similar to the intensity with stellar parameters. The intensity contrast is lower for small granules, typically reach a maximum at the mean granule size, and decreasing above it. Higher intensity contrast correlates with more complex substructures in the granules with dark spots and bright edges. These arise due to differences in the temperature excess of the granules originating from the granular dynamics (e.g., Hirzberger et al., 1997; Stein & Nordlund, 1998).

4.2.3 Temperature and density of granules

We averaged the temperatures and densities of the recognized granules (Sect. 4.1) on layers of constant Rosseland optical depth at the optical surface, which we show in Figs. 4.6 and 4.7 against the granule sizes for different stellar parameters. Furthermore, to improve the comparison the displayed mean values of the granules, $\langle T_g \rangle$ and $\langle \rho_g \rangle$, are normalized with the temporal and horizontal averages, $\langle T \rangle$ and $\langle \rho \rangle$, of the complete layer at the surface ($\tau_{\text{Ross}} = 1$) determined on layers of constant Rosseland optical depth. In general, larger granules feature higher mean temperatures and lower densities. A inverse correlation between the temperature and density is to be expected (from ideal gas law follows $T \sim p/\rho$). The temperature excess peaks around the mean granule diameters ($\sim 1 - 4\%$), while these are the most under-dense granules at the same time ($\sim 1 - 15\%$). The T -peak and ρ -minimum are increasing for higher T_{eff} and lower $\log g$. The smallest granules exhibit lower-than-average temperatures and higher-than-average densities, since these are small granule fragments located in the downdrafts. Furthermore, we find a distinctively tight correlation between the mean granule temperature and intensity with typical values around $\sim 97\%$ with very small variation of different stellar parameters, while the density is anti-correlated with the intensity by values around $\sim -55\%$, but with a large variation with stellar parameters. We note that the normalized mean thermodynamic pressure of granules, $\langle p_{\text{th}} \rangle$, exhibits very similar dependence with the granule size

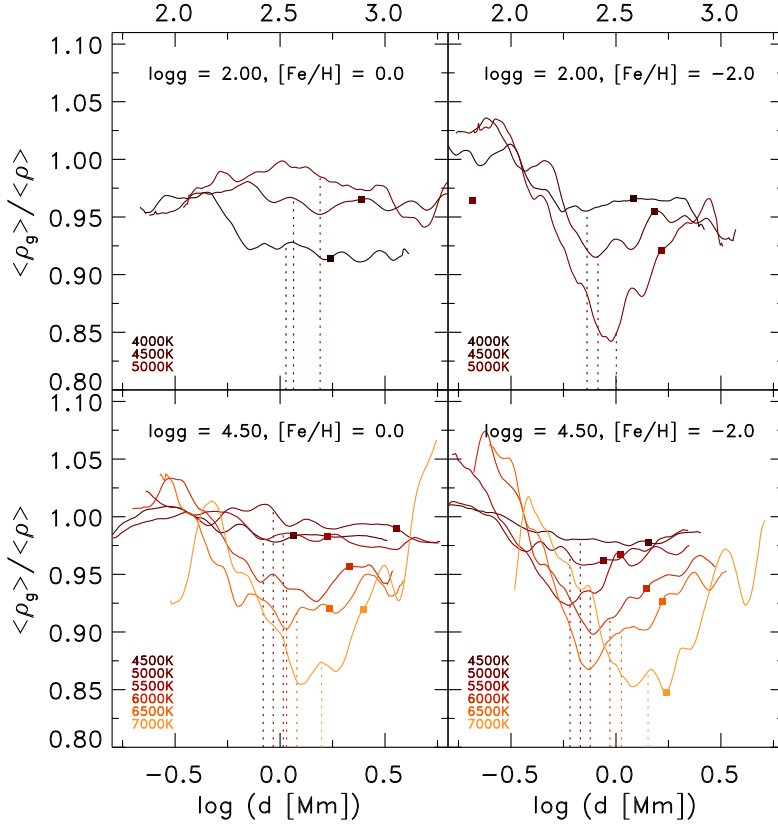


Figure 4.7: The same as Fig. 4.6, however, we show here the mean normalized density of the granules.

as the density, while the mean entropy resembles the temperature, but on a smaller scale (not shown).

4.2.4 Velocity of granules

In Fig. 4.8, we show the mean rms of the vertical velocity derived for the individual granules on layers of constant Rosseland optical depth at the optical surface. The rms velocity are for higher T_{eff} , lower $\log g$ and higher $[Fe/H]$, and these are in general flat for cooler T_{eff} s, while for hotter effective temperatures, one can find a distinct peak close to the mean granule diameter. We have seen above (Sect. 4.2.3) that these granules with mean diameters have lower densities due to higher temperatures, therefore, these lighter granules will experience a larger buoyancy acceleration. We remark that the characteristic variations of the rms velocities arise mainly from the upflows, since the majority of the cells of the granules are flowing upwards. We find that the lower mean densities around the mean granule diameters are not decreasing the mean upwards directed vertical mass flux, since the higher velocities are raising the upwards mass transport.

4.2.5 Geometrical properties

To quantify the geometrical properties of the complex granule shapes, we followed Hirzberger (2002) and determined

$$f_r = 4\pi A/P^2, \quad (4.6)$$

$$f_c = d_{\text{gran}}/d_{\text{MF}}, \quad (4.7)$$

$$f_i = w_{\text{MF}}/d_{\text{MF}}, \quad (4.8)$$

$$f_e = b/a. \quad (4.9)$$

The roundness factor (Eq. 4.6) is the area-perimeter relation for the roundness of a shape that measures the deviation from a perfect circle, and is also known as the isoperimetric quotient. The isoperimetric

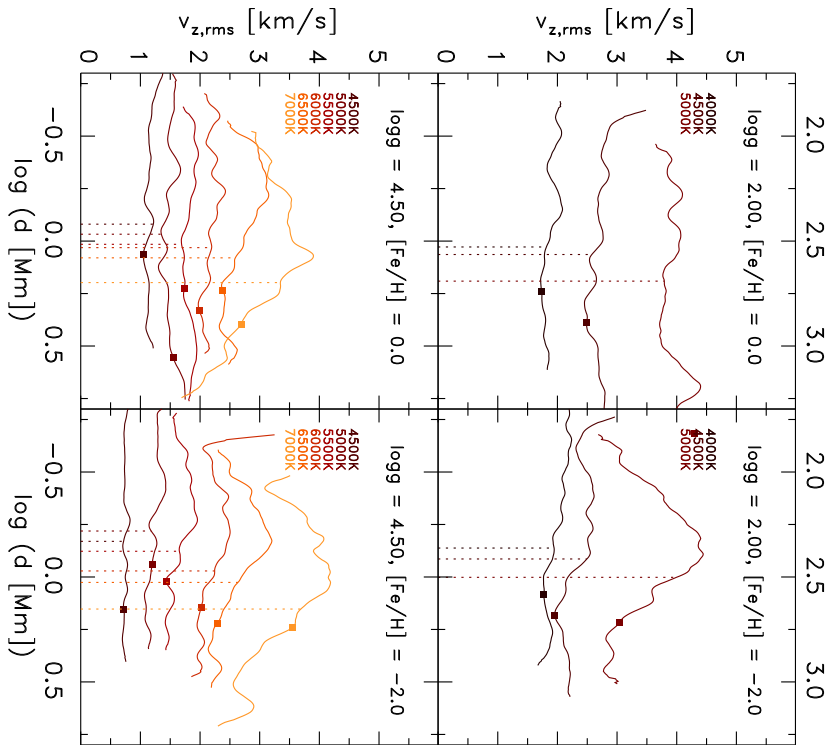


Figure 4.8: Mean rms vertical velocity of granules vs. granule size, which is obtained on layers of constant Rosseland optical depth. Furthermore, we indicated the mean granule diameters (*dotted lines*) and the dominant scales, d_{ac} (*filled squares*). Note the difference in abscissa between the top and bottom panel.

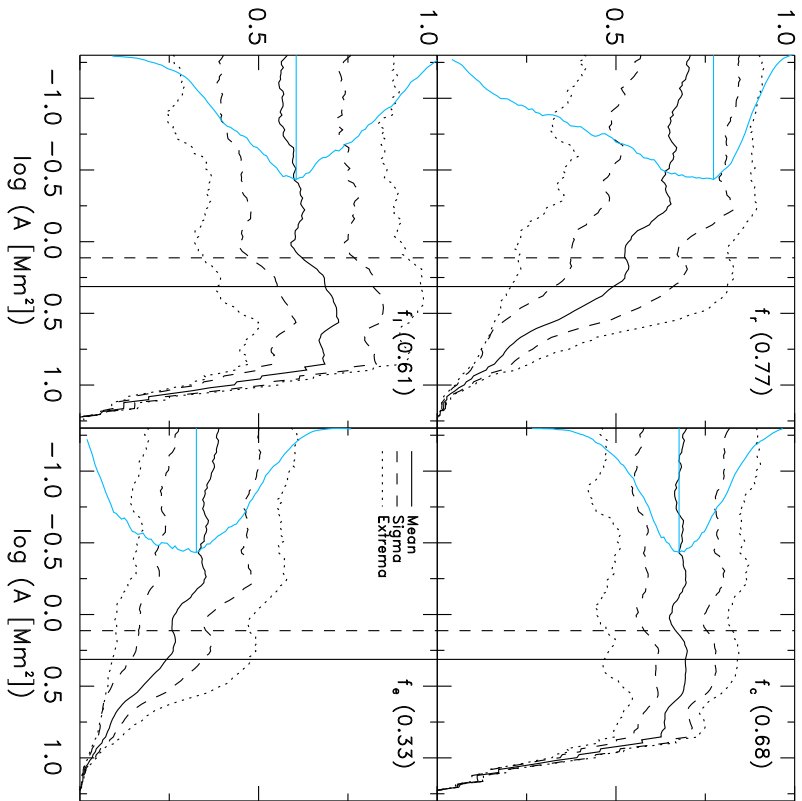


Figure 4.9: The smoothed distribution of the geometrical shape factors for roundness, circularity, elongation and ellipticity vs. granule area derived from the solar simulation. We outlined the mean (*solid*), the standard deviation around mean (*dashed*) and the extrema (*dotted lines*). Furthermore, we included also a (smoothed) histogram of the shape factor (*blue lines*), in order to render its distribution. The maximum of the latter is indicated (*horizontal gray line*). The vertical lines indicate mean and dominant granule area (*black vertical dashed and solid line*).

inequality, $f_s \leq 1$, holds for any arbitrary shape, and yields equality only for the circle. The circularity factor (Eq. 4.7) is the ratio between granule size, d_{gran} , and the maximal Feret-diameter, d_{MF} , which is the diameter of the principal axis, i.e. the maximum diameter at the barycenter for all degrees of rotation. It quantifies the evenness along the boundary, e.g., an even shape will lead to a value close to 1, while a star-shape will result very low ones. The elongation factor (Eq. 4.8) is determined with w_{MF} being the width perpendicular to d_{MF} , i.e. it is the aspect ratio of the principal axis, and values towards unity are close to a circle. Finally, the ellipticity factor (Eq. 4.9) is combined by $a = \xi + (\xi^2 - A/\pi)^{1/2}$ and $b = A/(\pi a)$ with $\xi = [(A/\pi)^{1/2} + P/\pi]/3$, and compares the shape with an ellipse (see Hirzberger, 2002).

The geometrical properties are shown for the Sun in Fig. 4.9. For granules smaller than the dominant granule size, the geometrical properties are in general similar. While above d_{ac} one finds a transition, in particular, f_r and f_e are dropping towards zero above the dominant granule size, since the granules start to fragment and split, and the perimeter is increasing much more faster than the area ($f_r \propto P^{-2}$). This is in agreement with the second, larger fractal dimension, D_2 , we found in Sect. 4.3. The shape factors f_c and f_l are independent of the perimeter, therefore, these are changing only little. The histograms of the shape factors are symmetrically distributed around a well-defined maximum with different widths. However, the roundness factor is an exception, it exhibits a skewed distribution that covers almost the whole range between zero and unity, and the maximum is located at $f_r = 0.77$. As given in Fig. 4.9, the contributions arise from different granules sizes. Smaller granules tend to be in general more regular at their boundaries (larger f_r) with smooth edges, while the fragmenting granules that are larger than d_{ac} have increasingly irregular, complex boundaries (small f_r) that are fringed and convoluted (see Fig. 4.1). The granule shapes are in overall very regular, circular shapes ($f_c = 0.68$ and $f_l = 0.61$) independently from d_{gran} . Furthermore, the granules are quite elongated with $f_e = 0.33$. When we compare our four shape factors with those by Hirzberger (see 2002), then these are qualitatively very similar, only the maximum of the roundness factor is at much lower values with $f_r = 0.1$, which might be due to difference in the recognition methods (FBR). Therefore, we remark that our solar simulation harbors a very realistic granulation pattern. Since the shape factors are very similar for different stellar parameters, we restrict ourselves to the discussion of the solar values.

4.3 Fractal dimension

The fractal dimension is a suitable, measurable value to quantify the complexity of a geometrical shape (Mandelbrot, 1977). In the case of granules, this is given by the area-perimeter relation

$$P = kA^{D/2} \quad (4.10)$$

with k being a shape factor and D the fractal dimension (Roudier & Muller, 1986). Then, the fractal dimension can be retrieved from the Eq. 4.10 with

$$D = 2\Delta \log P / \Delta \log A. \quad (4.11)$$

In planar geometry, perfect objects have an integer fractal dimension, e.g., circles or squares have $D = 1$ (dimension of a line), but with different shape factors $k = 2\sqrt{\pi}$ and 4, respectively. However, real objects are of fractal nature, i.e. most of patterns in nature exhibit a non-integer dimension. It is an important measure for the regularity of granules; more regular ones will have a lower D , while more irregular granules will have higher area-perimeter ratios.

We show the 2D histogram of the area and perimeter determined from the granules of the solar simulation in Fig. 4.10. Interestingly, we find for both a very tight linear correlation. At the dominant granule size, we find a distinct change in the slope of the correlation, indicating a multi-fractal nature of granulation. Therefore, we determined two fractal dimensions with two separate linear least-square fits. The first one is performed for the small-scale granules ($A < \bar{A}$), and the resulting fractal dimension is very close to unity with $D_1 = 1.04$, which means that the smaller granules are very regularly shaped. One can also consider this in the way that for an expanding granule with a larger area the perimeter is increasing with the square root power of the latter (same to a circle), and therefore, these granules are less fringed. The second linear fit is performed for larger granules ($A > \bar{A}$), and the fractal dimension is distinctively larger

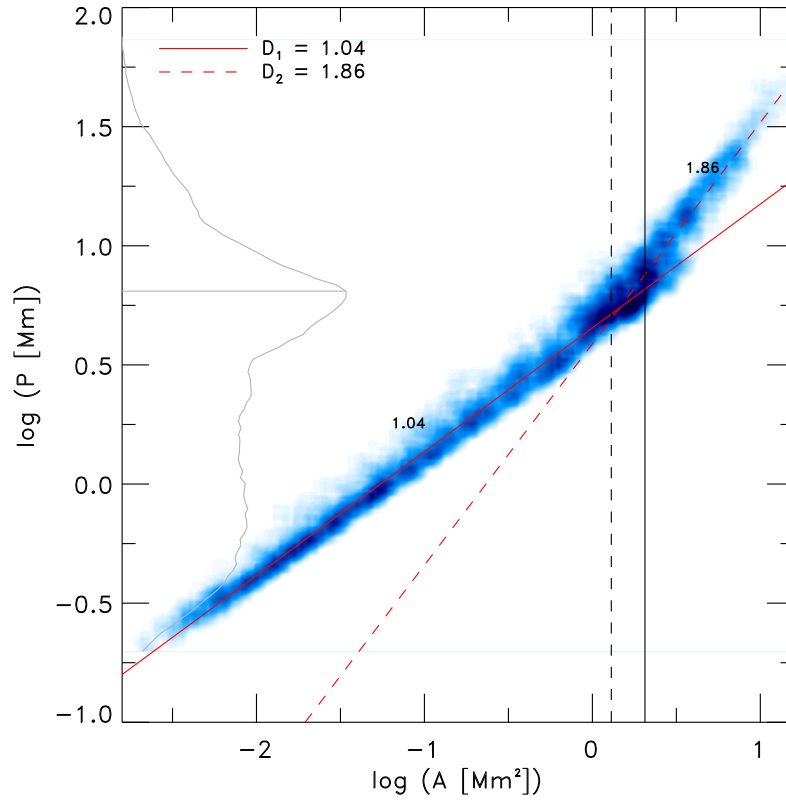


Figure 4.10: We show the (smoothed) histogram of the area-perimeter relation determined from the solar simulation. We indicated the histogram of the perimeter (*gray line*), the location of the mean granule area (*black dashed*) and the maximum of f_{ac} (*black solid line*). Also the linear fit for the small-scale (*red solid*) and the large granules (*red dashed lines*) are also included.

with $D_2 = 1.86$ (see Fig. 4.2). This means that large granules, growing above the dominant granule size, feature increasingly over-proportional larger perimeters, which accounts for the fact that these start to split and fragment. One could also argue that such a behavior should be expected simply based on geometrical argumentation, meaning that splitting granules will display incisions in a continuous manner.

The fractal dimensions are often determined from solar observations. In agreement with our result, Roudier & Muller (1986) also found two clearly distinct fractal dimensions with $D_1 = 1.25$ and $D_2 = 2.15$ (with FBR). Moreover, our fractal dimensions coincide also with Hirzberger et al. (1997), who determined for smaller granules $D_1 \approx 1.3$ and for larger granules $D_2 \approx 2.1$ (with FBR). Also, Bovelet & Wiehr (2001) derived similarly (with FBR) $D_1 = 1.2$ and $D_2 = 1.96$. On the other hand, they determined with their multiple layer tracking method, which we also employ, distinctively lower values for the fractal dimensions with $D_1 = 1.09$ and $D_2 = 1.28$. Their smaller fractal dimension is similar to ours, however, the second one for the larger granules is much lower, and therefore contradicting our results. They find that the FBR method is recognizing smaller granules as a larger single one compared to the multiple layer tracking method. However, since we do not use a FBR method, our results should be similar to their findings. We also performed a single linear fit, which resulted in $D = 1.10$, but the latter is clearly insufficient to depict the larger granules (not shown). In all of these before mentioned cases, the fractal dimensions are slightly larger than our values, which originates probably from the different granule recognition method (FBR), but also from the reduced resolution of their observations including atmospheric effects. We find that the solar simulation yields two clear distinct slopes in their area perimeter relation, which is not affected by observational constraints.

As next, we want to consider the variations of the area-perimeter ratio based on D_1 and D_2 for different stellar parameters. The area-perimeter relations are very similar to the solar one, therefore, we refrain from showing them (in fact these coincide for smaller granules, and are indistinguishable). The branching at the dominant granule size scale is always given with a slope close to unity for the smaller granules and a steeper slope for larger granules, in particular for lower T_{eff} and higher $[\text{Fe}/\text{H}]$. In Fig. 4.11, we show the fractal dimensions from the linear fits for various stellar parameters. The first fractal dimension

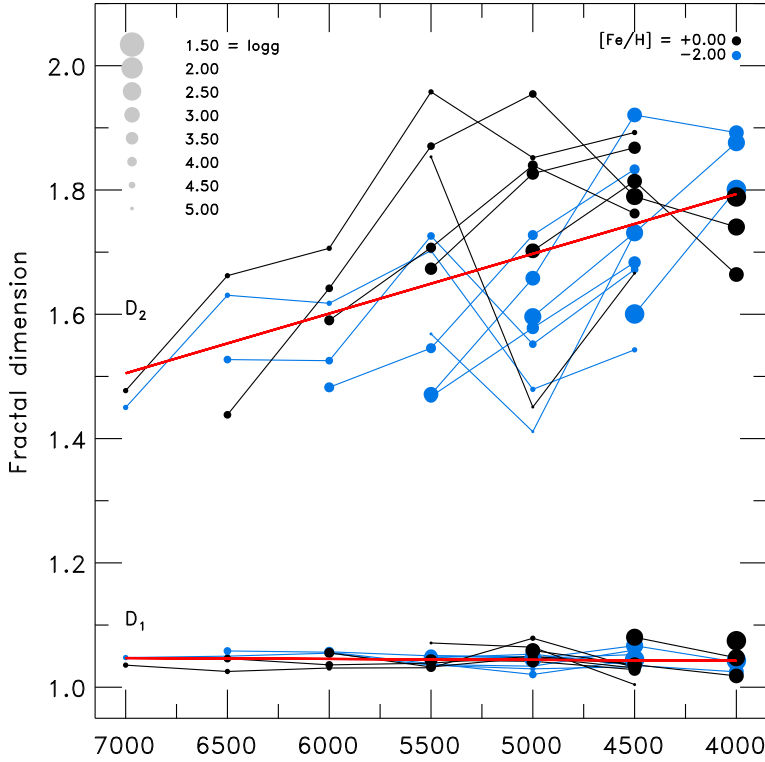


Figure 4.1: The smoothed histogram of the area-perimeter relation of the solar model. We over-plotted the fractal dimension. We show linear fits for D_1 and D_2 , the slopes being $\Delta_1 \approx 1.06$ and $\Delta_2 \approx 2.18$.

for the smaller granules is strikingly close to unity with the average value being $D_1 = 1.05 \pm 0.02$, and therefore basically universal in all simulations. The granules smaller than the dominant granule size are often regularly shaped. Furthermore, a value close to unity ($D_1 \sim 1$) implies that the perimeter increases to the square root with the area, i.e. $P \propto A^{1/2}$, for the smaller granules (see Eq. 4.10). The second dimensions are clearly larger, being on average $D_2 \approx 1.7 \pm 0.3$ with a significant level of scatter. Moreover, D_2 is sensitive to the stellar parameters, featuring a general decreasing trend for higher T_{eff} and $[\text{Fe}/\text{H}]$, and lower $\log g$. The values of D_2 never exceed 2 in all of our simulations. The larger granules above the dominant granule size are irregularly shaped, and $D_2 \sim 2$ translates into a linear area-perimeter relation of $P \propto A$, i.e. for larger granules, the perimeter increases linearly with the area. This is in principle the manifestation of the fragmentation of oversized, unstable granules. When we consider a hotter and cooler dwarf ($T_{\text{eff}} = 7000, 5500 \text{ K}$, $\log g = 4.5$ in Fig. 4.11), then the values for D_2 are ~ 1.5 and ~ 1.9 . If we compare two granules with the same (larger) area, A_0 , from both dwarfs, then the granules of the cooler dwarf will exhibit much larger perimeters, $P_{\text{hot}}(A_0) < P_{\text{cool}}(A_0)$, i.e. its granules will be in general more fragmented. This might be due to the higher densities and the lower vertical velocities, thereby shifting the balance of the characteristic length scales.

The granulation patterns in our simulations exhibit a striking self-similarity despite the large variations in the horizontal length scales and convective flow properties (see Fig. 4.1). This apparent observation is backed by the linear correlation of the area-perimeter relations, and the similar fractal dimensions between the different stellar parameters. Surface convection appears to operate scale-invariant over large ranges. With the fractal dimension we can support further this aspect. This is true, in particular, for the small-scale granules. Furthermore, the branching of the two fractal dimensions is taking place at the dominant granule size for all stellar parameters, since above the latter the granules cannot be supported by the pressure excess and start to fragment, thereby increasing the granule perimeter and becoming more irregular. Therefore, the branching area between D_1 and D_2 can be regarded as the maximal granule size, and granules with larger sizes are unstable, in particular, the second fractal dimension D_2 is the manifestation of the exploding granules. This simple geometrical fact supports the necessity for a larger second branch, despite the granule

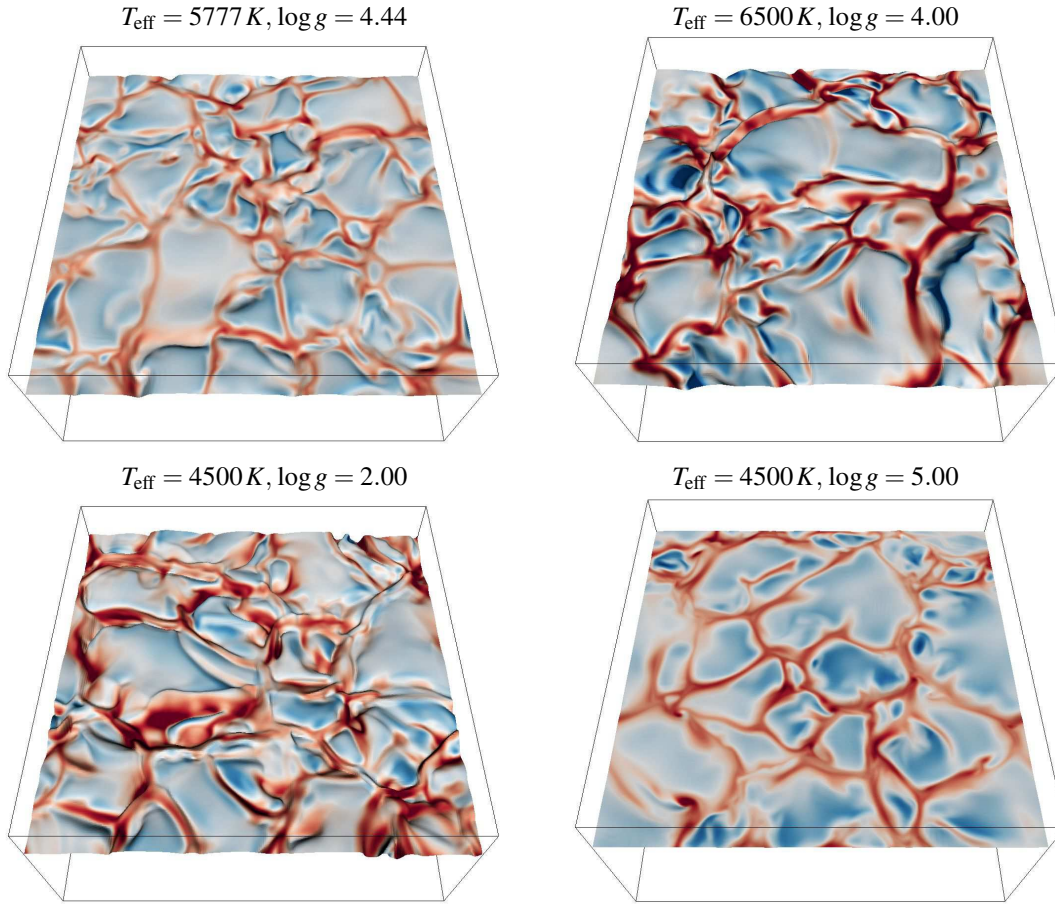


Figure 4.12: The corrugated optical surface including the vertical velocity to illustrate the up- and downflows (*blue* and *red*; each with a range of 8 km/s) for a selection of stars: main-sequence, turnoff, K-giant, K-dwarf.

detection method and observational effects.

4.4 Optical surface

4.4.1 Corrugation of the optical surface

The optical surface is defined as the layer with the constant optical depth unity ($\tau_{\text{Ross}} = 1$), and marks the photospheric transition boundary from the stellar interior to the outer. The optical surface is corrugated depending on whether one is considering a region above a granule or one above the intergranular lane, since the optical depth depends on the temperature and its gradient. Namely, at larger temperature gradients higher temperatures, hence higher opacities, are reached on shorter geometrical distances (see Stein & Nordlund, 1998). Therefore, we observe the emitted light above granules from higher layers, while the radiation from the intergranular lanes originates from slightly deeper layers. In Fig. 4.12, we show the optical surfaces for four different stellar parameters, encompassing the Sun, a turnoff star, a K-giant and a K-dwarf. Furthermore, we also illustrate the vertical velocity at the optical surfaces, and one can depict that the downflows are located in the intergranular lane, while the bulk granules are flowing upwards at the surface. The level of corrugation differs distinctively for the different stellar parameters. The level of corrugation can be quantified with the temporal averaged rms deviation of the geometrical depth for the layers of constant optical depth unity, i.e. $\langle z_{\text{rms}}(\tau_{\text{Ross}} = 1) \rangle$. The solar simulation is slightly corrugated

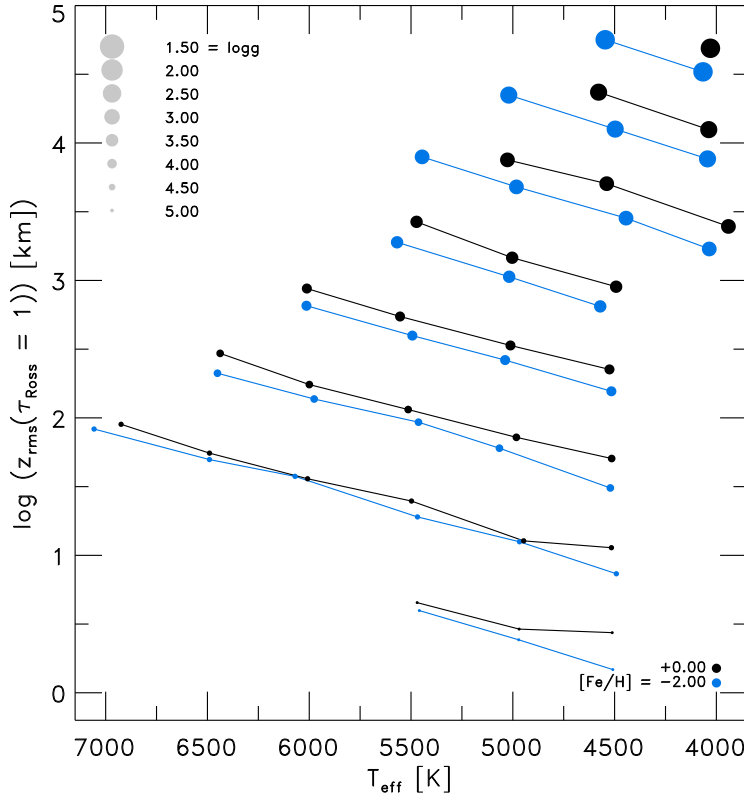


Figure 4.13: Overview of the rms deviation of the geometrical depth for the optical surfaces with different stellar parameters.

with ~ 33 km, which is close to the value found by Stein & Nordlund (see 1998) with ~ 30 km. Compared to the solar radius this is a very small relative variation with $\sim 5 \times 10^{-3} \%$. The earth has a tolerance of 0.17% from a spheroid, which is ~ 1.5 dex (~ 30 times) larger than the (quiet) Sun. The turnoff and giant simulation exhibit distinctively larger corrugated optical surfaces compared to the Sun with ~ 300 and ~ 23000 km respectively, while the dwarf model has a very smooth optical surface with ~ 3 km. One can estimate that the turnoff star has approximately the twice solar radius, while the K-giant has the twenty-fold, then their relative variations are with 0.02 and 0.17% respectively larger than compared to the Sun and comparable to the earth, however, this would still seem for an observer still very spheric. The K-dwarf would have the half of the solar radius and a very small relative variation with $\sim 1 \times 10^{-3} \%$.

To illustrate the systematic variation of the corrugation we overview the standard deviation of $\langle z(\tau_{\text{Ross}} = 1) \rangle$ in Fig. 4.13. The corrugation increases primarily with lower surface gravity and higher effective temperatures, since from hydrostatic equilibrium ($dp/dz = \rho g$) follows $dz \propto 1/g$ and the dominant negative hydrogen opacity source is very temperature sensitive ($\kappa_{\text{H}^-} \propto T^{10}$). Furthermore, at higher metallicity the corrugations are also larger due to the lower densities.

4.4.2 Surface velocity correlations

In order to study the surface properties more closely, we determined the temporal averaged (2D) histograms for the temperature, T , density, ρ , and intensity fluctuations, δI , as a function of vertical velocity at the optical surface on layers of geometrical depth ($\langle \tau_{\text{Ross}} \rangle = 1$) or constant Rosseland optical depth ($\tau_{\text{Ross}} = 1$), which are shown in Fig. 4.14. The thermodynamic properties correlate very well with vertical velocity, and the vertical velocity is separating the different properties between the up- and downflows (see SN98). All the thermodynamic properties exhibit a bimodal distribution due to the inherent asymmetric nature of the convective energy transport. On the one hand the stellar plasma in the upflows has hotter temperature and lower density with brighter intensities located in the granules. On the other hand the downflows are composed by cooler temperature and higher density with in the darker intensity found intergranular lane.

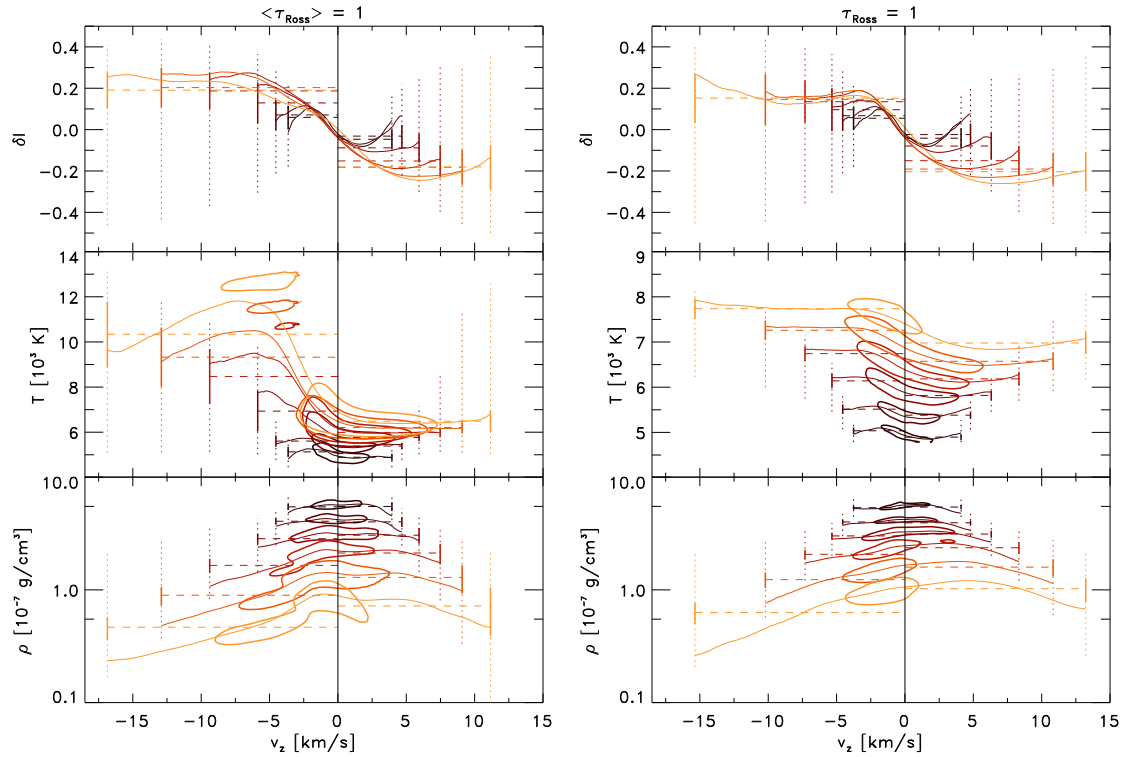


Figure 4.14: Correlation of the relative intensity fluctuations, temperatures, and densities with the vertical velocities at the optical surface for different stellar parameters (top, middle and bottom panel respectively) shown by the distribution of their histogram (thick lined contour at 0.2). We indicated the mean value (solid line), and for the up- and downflow separately their mean (horizontal dashed line), range (vertical dotted line) and standard deviation (vertical solid line). Furthermore, we show the geometrical averages taken the height with $\langle \tau_{\text{Ross}} \rangle = 1$ (left panel) and the averages on layers of constant optical depth $\tau_{\text{Ross}} = 1$ (right panel).

Furthermore, the (slow) upflows correlate with higher entropy and ionization, while the (fast) downflows associate with lower entropy and ionization. In Fig. 4.14 we show the mean values of the histograms for T , ρ and δI , which exhibits typically a s-shape like feature. Moreover, we display the contours of the one-fifth of the maximal probability for the T and ρ , from which one can estimate the distribution of the histogram. Then one can obtain a temperature jump from the histograms derived on layers of constant geometrical depth (left panel in Fig. 4.14), where we determined the height of the optical surface on the temporal average, i.e. $\langle \tau_{\text{Ross}} \rangle = 1$. At higher a effective temperature the density decreases, while the velocity rises, thereby leading to an enhancement in the overshooting of the convective upflows, which is also known as the so-called "naked granulation" (see Nordlund & Dravins, 1990). In agreement with the latter, we find that the T -jump becomes more distinct for hotter T_{eff} , and the bimodal distribution between the up- and downflows is more evident (compare the mean values between the up- and downflows). The upflows have distinctively larger values compared to averages on layers of constant optical depth (right panel in Fig. 4.14). The velocity correlation is tighter at layers of constant optical depth ($\tau_{\text{Ross}} = 1$), since the opacity is very T -sensitive due to the negative hydrogen opacity, and layers with similar temperatures are mapped during transformation to the optical depth (see Sect. 3.4). The fluctuations of the upflows are broader in temperature and narrower for the density (see Fig. 4.14), while the downflows feature a broad distribution in ρ and smaller range in T .

4.5 Topology of granulation

The superadiabatic convective flow at the surface correlates very tightly with the fluctuations of the thermodynamical properties. Therefore, the fluctuations can be utilized to conveniently illustrate the granulation pattern. In Fig. 4.15 we display renderings of the temperature, $\delta T_z = \Delta T_z / \langle T \rangle_z$, and density, $\delta \rho_z = \Delta \rho_z / \langle \rho \rangle_z$, fluctuations, which we have separated between excess and deficit (over and under-density). The granules consist of under-dense, pillar-like shaped, confined regions of temperature excess below the optical depth. The convective flow loses its heat-excess at the optical surface due to radiative losses and overturns into over-dense, turbulent downdrafts. The fluctuations are largest around the peak of the superadiabatic gradient, and towards deeper layers the fluctuations decline fast due to efficient mixing of the of the low-entropy downflows.

In Fig. 4.16 a comparison of the (bolometric) intensity map and the projected temperature excess, which we yield with

$$\Theta = \int_{\tau=1}^{\text{bot}} \delta T_z (\delta T_z > 1.1) dz.$$

One can obtain that the superadiabatic "convective pillars" (under-dense regions with heat-excess) correlate with bright granules, while the over-dense regions with dark intergranular lane.

To depict the turbulent downflows in the superadiabatic region, the amplitude of the vorticity is suitable quantity (see Fig. 4.17). At the interface between an upflow and downflow one finds strong shear flows, which is giving rise to the high vorticity. Therefore, in the vicinity of the optical surface vortex tubes are located around the granules, with vortex arcs emerging above the optical surface. Furthermore, the largest velocities are located in the downdrafts due to the overturning of the granular stellar plasma, often transonic or even supersonic flow-speed, in particular, for simulations with higher T_{eff} , lower $\log g$ (see Fig. 4.18).

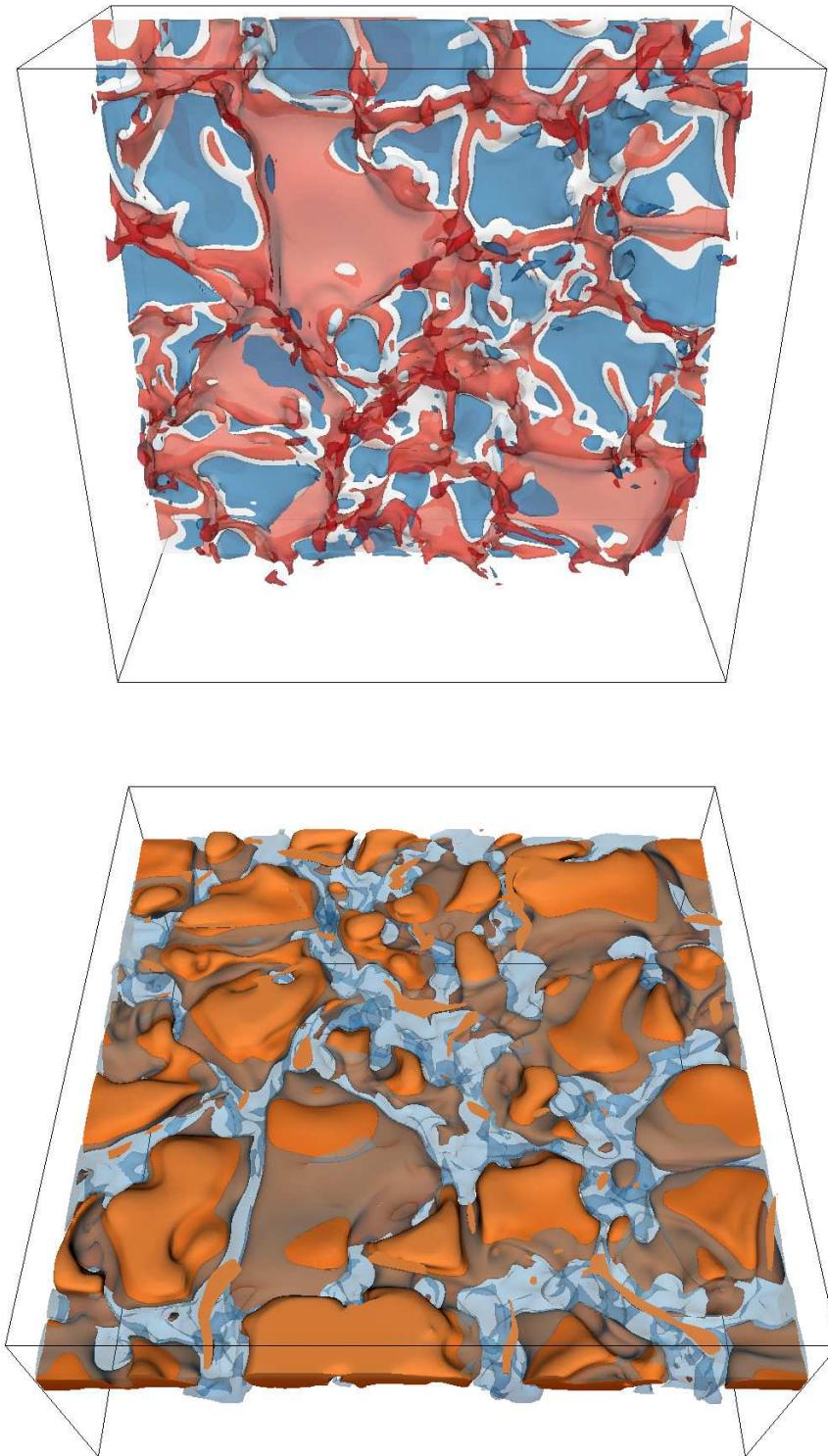


Figure 4.15: The subsurface granulation pattern visualized with the temperature and density fluctuations (*bottom* and *top*, respectively) for the solar simulation. The excess (orange) and deficit (blue) for the temperature is 5%, and the rendering threshold for the over (blue) and under-density (red) is given at 20%. The top figure shows the upwards view towards the optical surface, while the bottom figure is a top-down view.

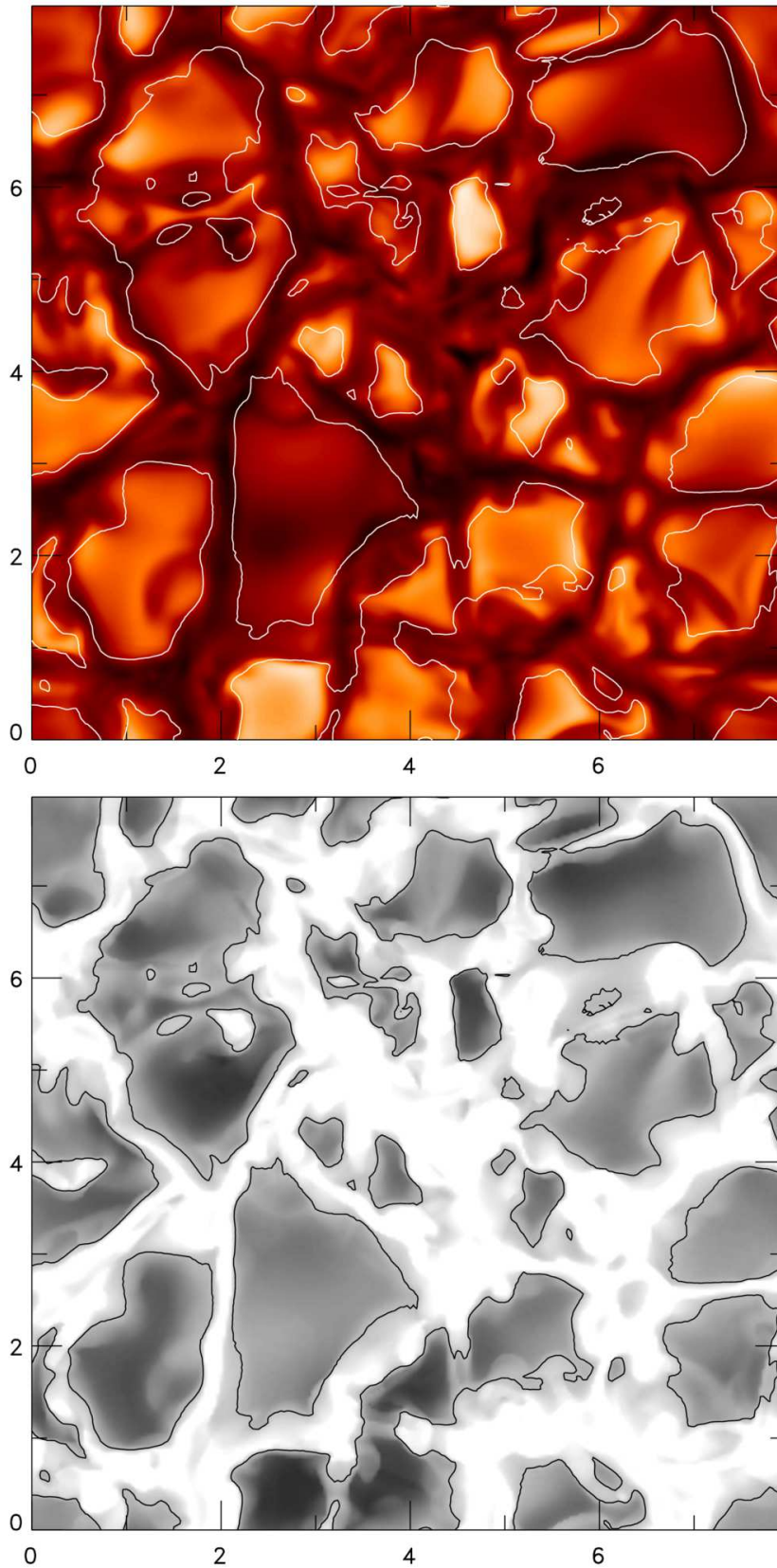


Figure 4.16: The bolometric intensity map of the Sun (top) compared with the projected temperature excess located below the optical surface in the superadiabatic region (bottom figure).

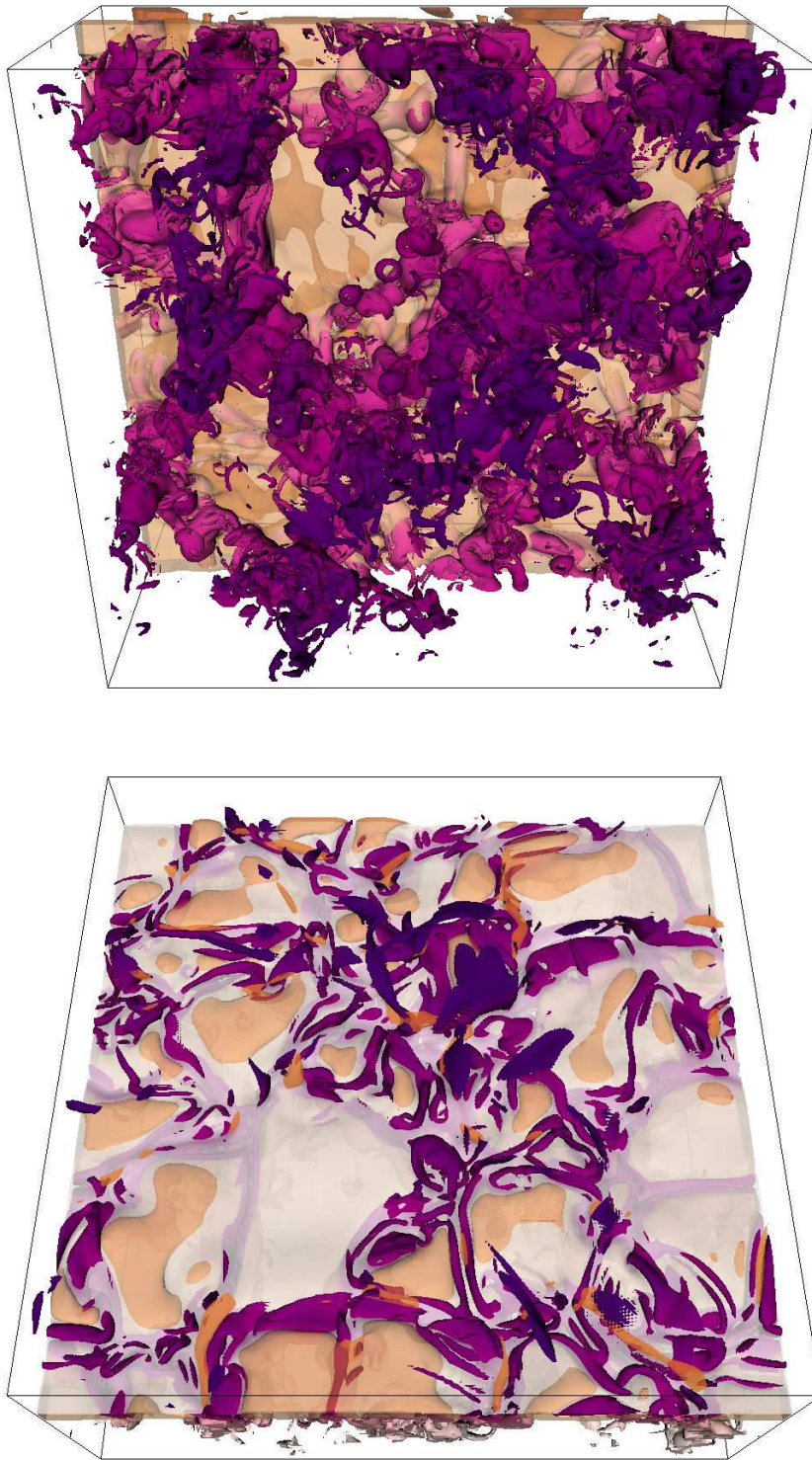
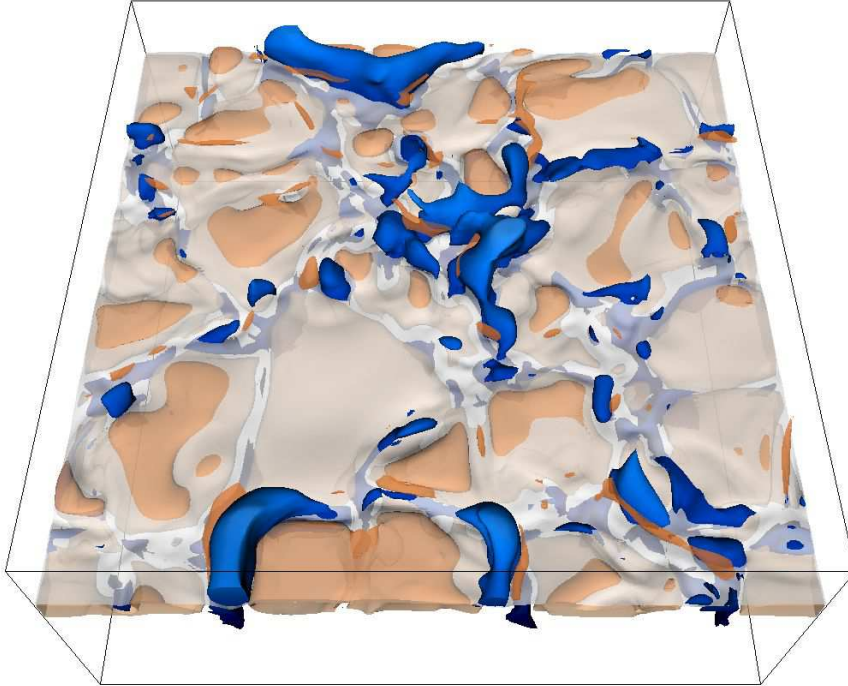


Figure 4.17: The turbulent downdrafts depicted by the amplitude of the vorticity (purple) for solar simulation. Furthermore, we display the optical surface (white) and the granules (orange). The top panel illustrates the fingering plumes of the turbulent downdrafts, while the bottom figure features the vortex tubes with vortex arcs located close to the optical surface. The vorticity is color-coded by the optical depth, where darker colors indicate deeper (higher) layers in the top (bottom) panel. The top figure shows the upwards view towards the optical surface, while the bottom figure is a top-down view.

$$T_{\text{eff}} = 5777 \text{ K}, \log g = 4.44$$



$$T_{\text{eff}} = 6500 \text{ K}, \log g = 4.00$$

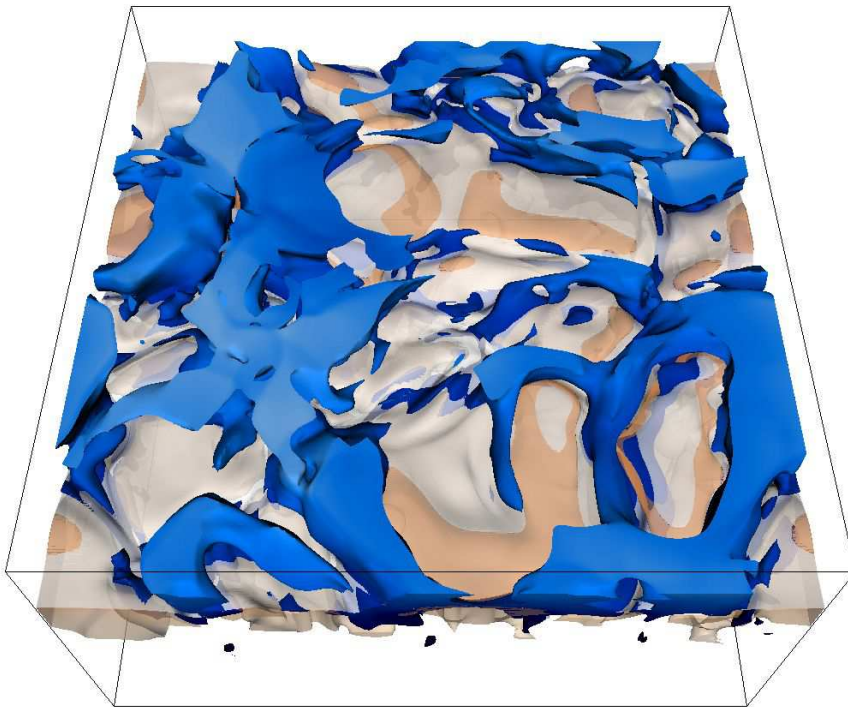


Figure 4.18: *Top figure*: Transsonic Mach numbers ($M > 0.8$; blue contours) in the solar simulation. *Bottom figure*: supersonic Mach numbers ($M > 1.0$) in a turnoff simulation. Furthermore, we display the optical surface (white) and the granules (orange). The views are shown from the top-down perspectives.

Chapter 5

Spectral line formation

Cool stars are distinguished by their convective envelopes below the optical surface and the concomitant velocity field and its typical manifestation as granulation patterns are imprinted in the observable spectral line profiles in form of line shifts and asymmetries. Realistic line profiles are broadened by natural, thermal, pressure, van der Waals, radiative and collisional broadening, and usually these are considered by convolving them into the line absorption coefficient α_ν . Spectral lines depend mainly on the number of absorbers (atomic level population), therefore, it is very sensitive to the temperature due to exponential and power dependence of excitation-ionization ($\propto e^{-\chi/kT}$; see Eqs. 1.19 and 1.20 in Sect. 1.2). Moreover, due to the convective velocities additional non-thermal broadening takes place in form of Doppler shifts. Line wings are formed in deeper layers close to the continuum forming depth, while the line cores are formed above in higher layers, therefore, these sample different heights with distinctive physical conditions, in terms of velocity amplitudes, correlation between temperature and density inhomogeneities, asymmetries between regions with up- and downflowing material, thereby leading to characteristic asymmetries in the emergent intensity and flux line profiles (see Asplund et al., 2000a).

Classical theoretical atmosphere models made use of several simplifications in order to facilitate calculations with the computing power at hand in the past (see Gustafsson et al., 2008; Castelli & Kurucz, 2004). The treatment of convection has been the most challenging part in modeling stellar atmospheres, since a complete theory of convection including a full closure is today still absent, and therefore, in one-dimensional (1D) modeling simplified treatments have been made use of, such as the mixing-length theory (MLT; see Böhm-Vitense, 1958; Henyey et al., 1965) or the full spectrum of turbulence model (Canuto & Mazzitelli, 1991) with a priori unknown free-parameters that has to be calibrated by observations. Then, for the 1D line formation calculations the lack of knowledge on the convective velocity field is partially compensated by introducing fudge parameters: micro- and macroturbulence.

However, for the accurate interpretation of high-resolution spectroscopical observations from the latest ground-based large-aperture or space-born instruments spectroscopical analysis based on classical theoretical models is insufficient, therefore, the demand on improved theoretical atmosphere models has emerged. For the precise modeling of realistic line profiles including line shifts and asymmetries one has to compute realistic three-dimensional (3D) atmosphere models, where the convective velocity field emerges from first principles by solving the hydrodynamic equations coupled with non-grey radiative transfer (Nordlund, 1982; Stein & Nordlund, 1998; Nordlund et al., 2009). The major application for 3D radiative hydrodynamic (RHD) atmosphere models is the computation of synthetic full 3D line profiles or spectra as post-processing based on the former in order to derive accurate stellar parameters and abundances (Asplund et al., 2000a,b, 2005, 2009). The 3D RHD models demonstrated their predictive capabilities powerfully in comparison with observed line profiles for several different stars. Asplund et al. (2000a) found almost perfect agreement between observed solar iron line profiles and theoretical predictions without any trends in the derived abundances with line strength. The line strength is evaluated by the equivalent width, which is the area-integral of the spectral absorption line profile, i.e. $W_\lambda = \int (1 - F_\lambda/F_c) d\lambda$. Furthermore, comparisons of line shifts and asymmetries derived from high-resolution spectroscopical observations of different types of cool stars advocated additionally for the realistic nature of the theoretical 3D RHD models (see Nordlund & Dravins, 1990; Atroshchenko & Gadun, 1994; Allende Prieto et al., 2002; Ramírez et al.,

2008, 2009, 2010; Gray, 2009).

The aim of this Chapter is intended to tackle the following two key questions: how do spectral lines based on $\langle 3D \rangle$ models compare to full 3D models? And also, how do Fe line properties vary with stellar parameters? More specifically, I intend to analyze line shifts and asymmetries carefully for a selection of Fe I and Fe II lines, in order to better understand the variation of spectral line features with stellar parameters, which is important for stellar parameter determination, particularly for the metallicity, and for the characterization of stellar surface convection. Iron lines are often considered useful for this purpose, since it is an abundant element with accurate atomic data at hand. I will explain the methods for the calculations of the 3D spectra (Sect. 5.1), decompose the 3D lines into up- and downflows (Sect. 5.2), compare spectral lines from $\langle 3D \rangle$ and full 3D models (Sect. 5.3), and, study the lines shapes, shifts and asymmetries of a number of Iron lines (Sect. 5.4). Furthermore, I note that the Section 5.3 originates from the publication Magic et al. (2013b).

The differential comparison of spectral line formation computed from $\langle 3D \rangle$ and 3D models shows distinctive differences, depending on which reference depth is considered for the $\langle 3D \rangle$ stratification. The averages over layers of constant column-mass density yield the best mean $\langle 3D \rangle$ representation of the full 3D models for LTE line formation, while the averages on layers at constant geometrical height are the least appropriate. Unexpectedly, the usually preferred averages over layers of constant optical depth are prone to increasing interference by reversed granulation towards higher effective temperature, in particular at low metallicity. Furthermore, the resulting variations in line strength, shift, width and bisectors are rather systematically, and these can be related to the respective physical conditions at the height of the line formation in the stellar atmospheric environment, in particular the amplitude of the vertical velocity field. Line shifts and asymmetries arise due to the presence of convective velocities and the granulation pattern that are ubiquitously found in observed stellar spectra of cool stars. As a major novelty I point out the surprisingly well working $\langle 3D \rangle$ two-stream line formation in Sect. 5.2.

5.1 Multi-dimensional line formation calculations

We used the 3D radiative transfer code SCATE (Hayek et al., 2011) to calculate full 3D synthetic spectral line disk-center intensity and flux profiles with 3D STAGGER model atmospheres. SCATE assumes local thermodynamic equilibrium (LTE). Furthermore, in the present work, we also neglected the effects of scattering; i.e. we approximated the source function with the Planck function, $S_\lambda = B_\lambda$. We caution that LTE is can be a poor approximation, especially for Fe I spectral line formation calculations at low $[\text{Fe}/\text{H}]$ (e.g. Bergemann et al., 2012), which should be kept in mind for analyzing the LTE-based abundance corrections presented here. For the sake of consistency, we used the same EOS (Mihalas et al., 1988) and continuum opacity data (from the MARCS package; see Gustafsson et al., 2008) as in the 3D STAGGER simulations.

To reduce the computational costs for line formation calculations, we consider a subset of $N_t = 20$ temporally equidistant snapshots – the same as used for the temporal $\langle 3D \rangle$ averages – sampling the entire time spans of the individual 3D simulation sequences. Additionally, we reduce the horizontal spatial resolution from $N_x N_y = 240^2$ to 60^2 by considering only every fourth column in each horizontal direction. Test calculations carried out at full resolution show that differences are negligible for all practical purposes (see Asplund et al., 2000a). Concerning the vertical direction, while we did not subsample the number of depth points, we considered only those layers with the temporal and horizontal averaged Rosseland optical depth being $\min(\langle \log \tau_{\text{Ross}} \rangle) \leq 3.0$. The resulting disk-center (3D) intensity and flux profiles are spatially and temporally averaged, and then normalized with the respective continuum intensity or flux.

To systematically illustrate the differences between $\langle 3D \rangle$ and 3D line formation, we computed fictitious atomic lines for neutral and singly ionized iron, Fe I and Fe II, for the selected STAGGER-grid models and metallicities (see Fig. 5.1). All lines are defined at the same wavelength, $\lambda = 500 \text{ nm}$, and we considered two lower-level excitation potentials, $\chi_{\text{exc}} = 1.0$ and 4.0 eV . Furthermore, we varied the oscillator strength, $\log gf$, in order to cover a range of line strengths, from weak to partly saturated lines, with equivalent widths from $W_\lambda = 5$ to $80 \text{ m}\text{\AA}$. We assumed an iron abundance of $\log \epsilon_{\text{Fe}} = 7.51$ (Asplund et al., 2009) and $\log \epsilon_{\text{Fe}} = 4.51$, for the solar metallicity and $[\text{Fe}/\text{H}] = -3.0$ case, respectively.

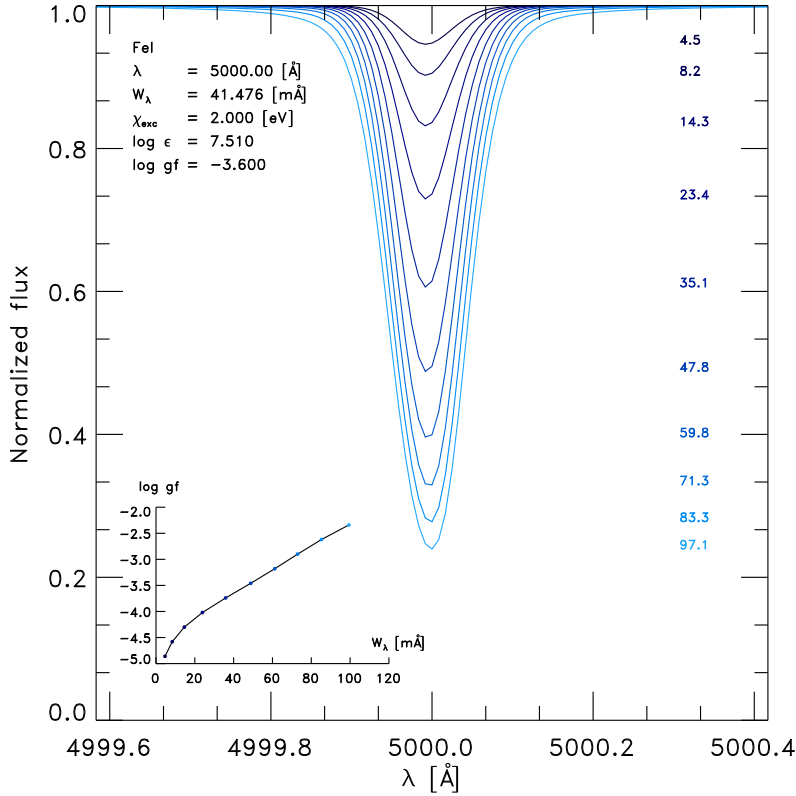


Figure 5.1: Various solar Fe I line profiles with increasing line strength (equivalent width, W_λ , indicated by blue numbers) with higher $\log gf$ values to illustrate the curve-of-growth. Furthermore, the equivalent width vs. oscillator strength $\log gf$ (curve-of-growth) is given in the inserted plot.

The spectral line calculations with $\langle 3D \rangle$ models were also performed with SCATE, to guarantee a consistent comparison. SCATE employs atmospheric structures on geometrical height and computes the optical depth, τ_λ , for the individual line. Therefore, we provide the geometrical height by integrating $dz = d\langle \tau_\lambda \rangle / \langle \kappa_\lambda \rangle$, which is of course unnecessary for $\langle 3D \rangle_z$. Furthermore, tests revealed that including just an averaged velocity, e.g., $|\bar{v}|/3$, is insufficient to reproduce the influence of the 3D velocity field on the line shape. Analyzing the influence of the velocity field on the line formation surpasses the scope of the present work. In this study, for the calculations with $\langle 3D \rangle$ models we neglected the information about the actual velocity field and instead assumed a fixed microturbulence of $\xi_{\text{turb}} = 1.0$ km/s for all considered stellar parameters. To include an average velocity field, we find that a two-stream approach only is capable of doing so, since otherwise a single-direction oriented average velocity field is overestimating the Doppler shifts into this direction.

Since the line formation calculations with $\langle 3D \rangle$ models are obviously much faster, we use the $\langle 3D \rangle_{\text{Ross}}$ averages first to estimate the $\log gf$ range, which would result in the designated range in W_λ . We then consider ten equidistant $\log gf$ values within that range for the $\langle 3D \rangle$ and full 3D models. Finally, we interpolate the curves-of-growth ($\log gf$ vs. W_λ) using a spline interpolation and retrieve the $\Delta \log gf$ difference between $\langle 3D \rangle$ and 3D synthetic lines at a given equivalent width; i.e., $\Delta \log gf = \langle 3D \rangle - 3D$. This curve-of-growth approach is commonly applied to derive the differences between $\langle 3D \rangle$ and 3D lines. For trace elements, changes in line strength due to $\Delta \log gf$ are equivalent to changes due to abundance variations $\Delta \log \epsilon$; hence, the $\Delta \log gf$ differences can be interpreted as $\langle 3D \rangle - 3D$ abundance corrections. With four fictitious lines and four representative models with two metallicities, we covered 32 cases in total. In Fig. 5.1 we show a series of fictitious Fe I spectral line profiles with increasing line strength for higher $\log gf$ values computed from the solar simulation, including an illustration of the curves-of-growth as an example.

Full 3D line profiles are marked by line shifts and asymmetries owing to the non-thermal Doppler broadening introduced by the up- and downflows of the convective motions, which are present in the photosphere due to overshooting (Asplund et al., 2000a). In 3D RHD modeling, the velocity field emerges

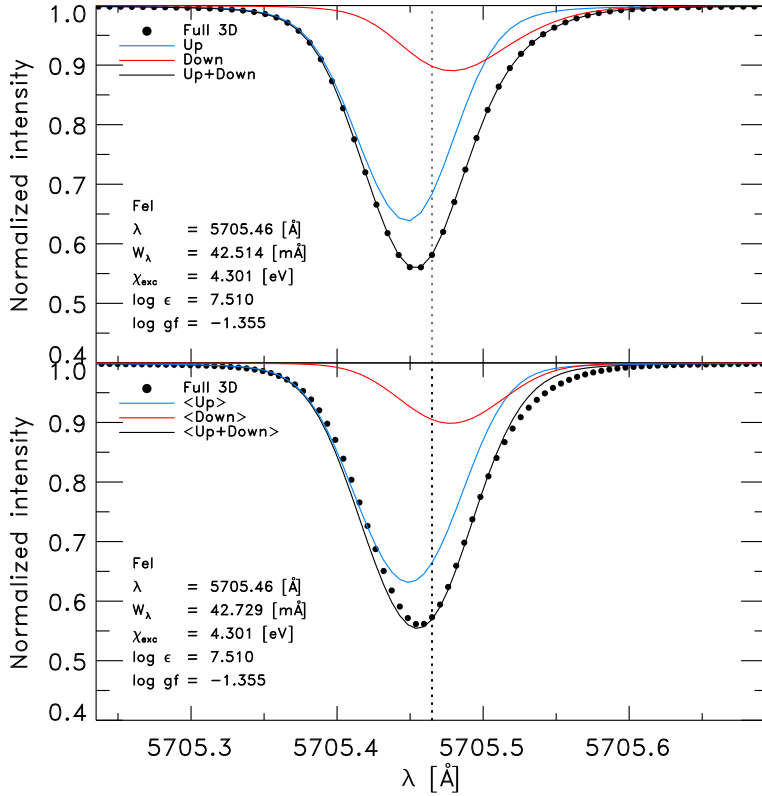


Figure 5.2: The normalized spectral intensity profile vs. wavelength for a single intermediate Fe I line ($\lambda = 5705.5$, $\lambda_{\text{exc}} = 4.3$) resulting from the solar simulation. For comparison, we illustrate the full 3D spectral line profile from the (filled circles), the profile from the upflows (blue) and downflows (red line), and the superposition of the both (black solid line). *Top panel*: the decomposition of a full 3D line profile; *bottom panel*: the two-stream model computed with (3D) models for the up- and downflows.

naturally from first principles. The buoyant hot rising plasma in the granules blue-shifts the line, while the fast downdrafts introduce a redshift. Besides the convective motions, another source of line broadening are the inhomogeneities in the thermodynamic independent variables, ρ and T . The ascending granules are hotter and less dense than the downdrafts (see Fig. 3.38). The velocities and inhomogeneities prevailing at formation height of the individual lines will lead to line shifts and asymmetries. The (3D)-based lines are symmetric without any shifts, however, we can compare the equivalent widths of lines from calculations based on full 3D models and on the different average stratifications.

We probed different formation heights with the parameters of our fictitious lines. The Fe II lines form deeper in the atmosphere, closer to the continuum forming layers, while the Fe I lines are more sensitive to the intermediate heights of the atmosphere. Spectral lines with lower (higher) excitation potential form at smaller (larger) optical depths. We showed in Sect. 3.4 that the metal-poor model stellar atmospheres exhibit rather different temperature stratification at the top depending on the averaging method, consequently the latter should show the largest differences between the $\langle 3D \rangle$ models.

5.2 Two components of the line profile

In order to elucidate the individual contribution from the granules and the intergranular lane on the line shape and asymmetry, we show in Fig. 5.2 (top panel) a Fe I line computed from a single solar simulation snapshot (black filled circles). We averaged the spatially resolved line profile separated into (bright) granules and (dark) intergranular lane (up- and downflows; blue and red lines respectively) based on a threshold at 90% from the mean continuum intensity, $I_c = \langle I_c \rangle$, which resulted in a filling factor of $f_{\text{up}} \sim 2/3$ and $f_{\text{dn}} \sim 1/3$ (see Stein & Nordlund, 1998,) for the up- and downflows respectively. We find the following renormalization to work well for the intensity profile,

$$\tilde{I}_{\text{up}} = (\langle \tilde{I}_{\text{up}} \rangle_{\lambda} - \Delta \tilde{I}_{\text{up}}^c) f_{\text{up}} + f_{\text{dn}} \quad (5.1)$$

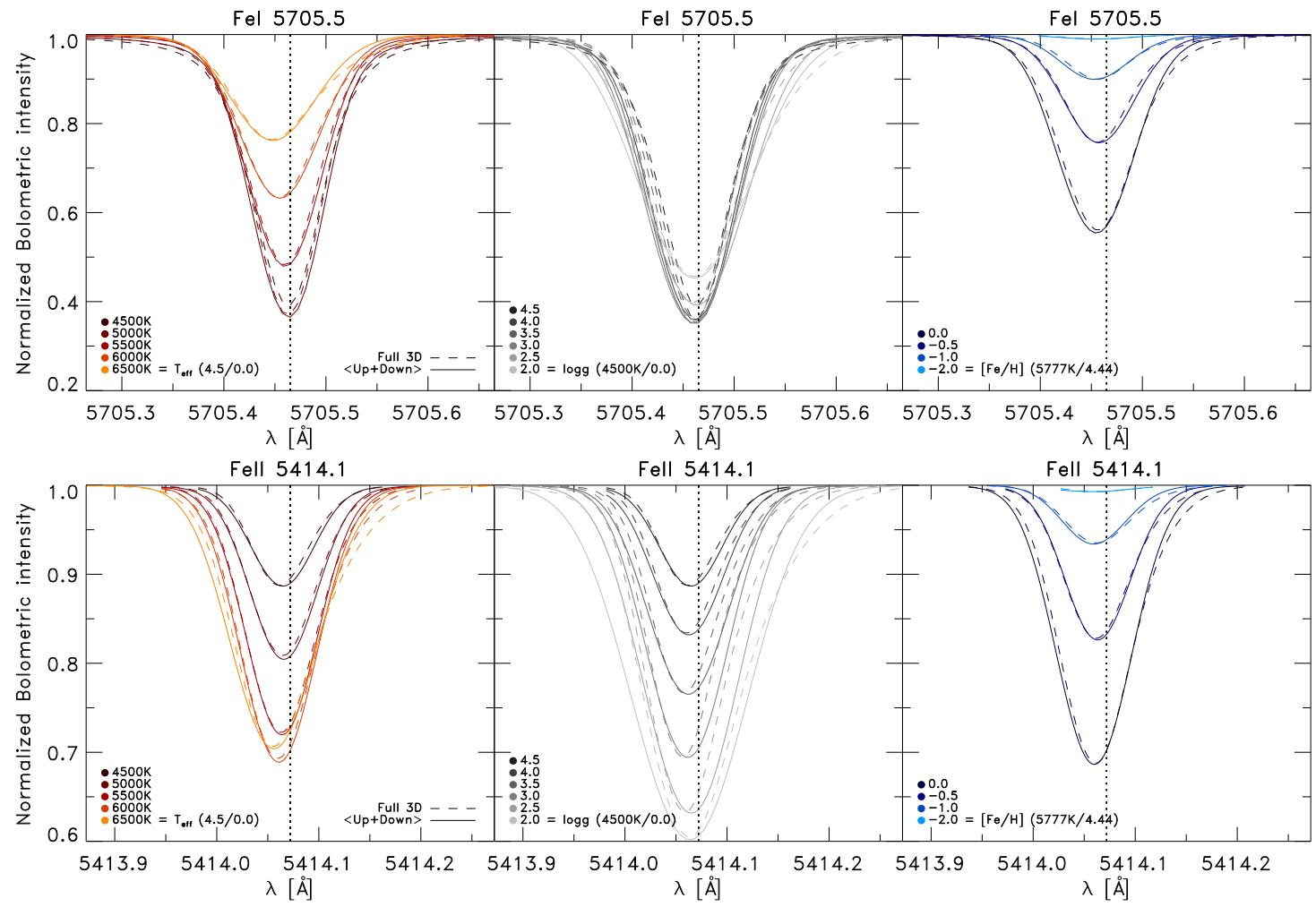


Figure 5.3: Normalized flux vs. wavelength for a Fe I and Fe II line (top and bottom panel respectively) for different stellar parameters comparing full 3D and the <3D> two-stream models (solid and dashed lines, respectively). In each column, one stellar parameter is varied, while the other two are fixed (indicated); *left panel*: effective temperature; *middle panel*: surface gravity; *right panel*: metallicity. Furthermore, the respective lines computed with the <3D> models are also shown (dotted lines). Note the different the ordinates.

$$\tilde{I}_{\text{dn}} = (\langle \tilde{I}_{\text{dn}} \rangle_{\lambda} - \Delta \tilde{I}_{\text{dn}}^c) f_{\text{dn}} + f_{\text{up}} \quad (5.2)$$

with $\tilde{I} = I/I_c$ being the normalized intensity, $\langle \dots \rangle_{\lambda}$ the average over the wavelengths and $\Delta \tilde{I}_{\text{ud}}^c = \langle I_{\text{ud}}^c/I_c \rangle - 1$ the continuum-correction of the up- and downflows. The bracketed term in Eq. 5.1 (5.2) for the upflows (downflows) is weighted by its respective filling factor f_{up} (f_{dn}) and renormalized to continuum level of 1 with the shift by the complementary filling factor f_{dn} (f_{up}). By considering relative intensity values we find the separation being more accurate compared to absolute values. The superposition of the individual components is achieved with $\tilde{I} = \tilde{I}_{\text{up}} + \tilde{I}_{\text{dn}} - 1$ (black line), which restores the undivided line profile (black filled circles), since the separation is still keeping the total line depression constant (the shift by 1 is the continuum-correction). From Fig. 5.2 one can depict the individual components, being the stronger blue-shifted upflows and the weaker red-shifted downflows that leads to the complete line profile. Furthermore, one can notice a distinct difference in the line depth of the individual components, which unveils the fact that the effect of the downflows being restricted to the upper part of the bisector, while the lower part is dominantly arising from the upflows in the granules.

Furthermore, we performed line formation calculations in the framework of a two-stream model approach with two mean $\langle 3D \rangle$ models separated in the up- and downflows (see bottom panel in Fig. 5.2). Therefore, we computed two line profiles individually based on the $\langle 3D \rangle_{\text{up}}$ and $\langle 3D \rangle_{\text{dn}}$ model, which include temperature, density stratification and rms-velocity retrieved from the up- and downflows separately. We find that weighting the rms-velocity by the depth-dependent filling factors leads to better results, since otherwise these are overestimating the velocity field. Then, the resulting two normalized intensity profiles, \tilde{I}_{up}^* and \tilde{I}_{dn}^* , are weighted and renormalized with a single filling factor, $f_{\text{up}} = 2/3$ and $f_{\text{dn}} = 1/3$, similar to the above ($\tilde{I}_{\text{ud}}^* = \dots$) in Eqs. 5.1 and 5.2). Finally, the two components are superposed to a single line profile as well with $\tilde{I}^* = \tilde{I}_{\text{up}}^* + \tilde{I}_{\text{dn}}^* - 1$. We note that the two intensity profiles, \tilde{I}_{up}^* and \tilde{I}_{dn}^* , include the same microturbulence that leads to the same line strength for a standard $\langle 3D \rangle$ model compared to the full 3D line. Finally, the combined intensity profile is convolved with macroturbulence (Gaussian broadening) in order to match the line depth, and the matching value is also applied for \tilde{I}_{up}^* and \tilde{I}_{dn}^* . The resulting line profiles are also shown in Fig. 5.2 (bottom panel), which are interestingly often very close to the full 3D profile. However, we note some slight variations in accuracy with different lines or stellar parameters (see Fig. 5.3, which includes more line profiles for other stellar parameters).

5.3 Spectral line formation: $\langle 3D \rangle$ and 3D LTE calculations

To explore the differences between the line formation based on $\langle 3D \rangle$ and full 3D models, we have chosen a set of representative models consisting of a main-sequence (MS) star ($T_{\text{eff}}/\log g = 5777 \text{ K}/4.44$), a turn-off (TO) star (6500/4.0), a red-giant (RG) star (4500/2.0), and a dwarf (4500/5.0). For all these models, we considered metal-poor analogs with $[\text{Fe}/\text{H}] = -3.0$ in addition to the solar metallicity.

5.3.1 Comparison of $\langle 3D \rangle$ and 3D line formation

We show an overview of the differences between the $\langle 3D \rangle$ and the full 3D calculations in Figs. 5.4 and 5.5. The first noticeable observations are the systematic trends in form of a slope towards higher line strength, which are due to the fixed value of the microturbulence, ξ_{turb} , with 1 km/s in the $\langle 3D \rangle$ models. An increasing slope with line strength indicates an underestimation of ξ_{turb} , in particular, for the TO and RG (see panel 5 to 12 in Fig. 5.4 and 21 to 28 in Fig. 5.5). By contrast, in cool dwarfs, the adopted ξ_{turb} seems to be overestimated due to the increasing negative trends in $\Delta \log \epsilon$. These findings agree with comparisons of 1D models with observations (e.g., Edvardsson et al., 1993; Bensby et al., 2009), where they needed only a small microturbulence to correct for trends in $\Delta \log \epsilon$. We tested this by applying a number of ξ_{turb} values¹, which showed that a fine-tuning can rectify the present slope. However, for the sake of clarity, we prefer to limit the already large number of stellar and line parameters to just a single ξ_{turb} .

¹We find a reduction of the slope in the curve-of-growth with $\xi_{\text{turb}} = 0.5, 1.5, 2.0 \text{ km/s}$ for the dwarf, RG and TO models respectively (while a fine-tuning could flatten it completely).

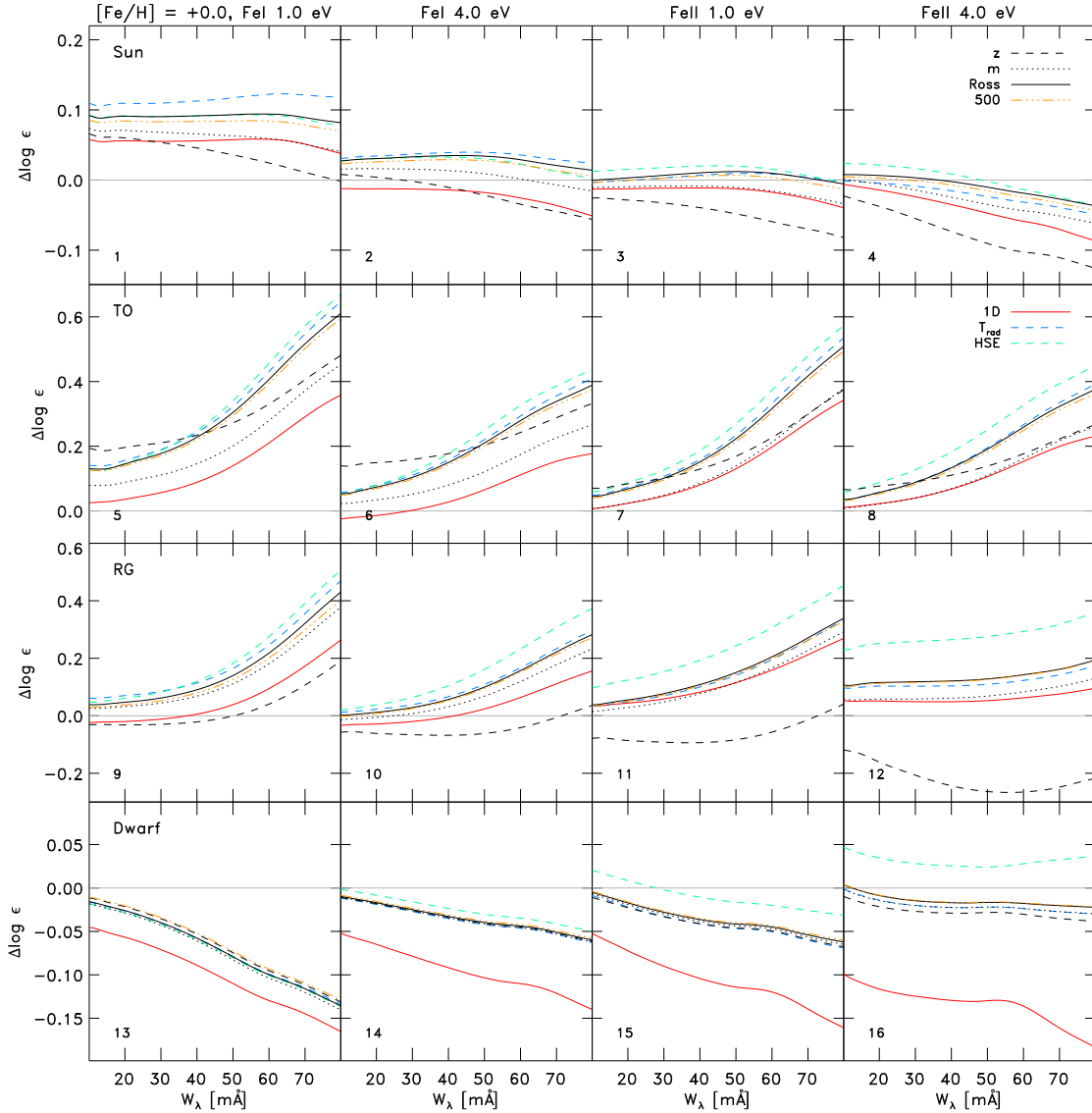


Figure 5.4: Overview of the $\langle 3D \rangle - 3D$ line formation differences given in abundances displacement $\Delta \log \epsilon$ vs. equivalent width W_λ for the Fe I and Fe II fictitious spectral lines with the excitation potentials $\chi_{\text{exc}} = 1.0$ and 4.0 eV . Showing the representative selection including the Sun, TO, RG and dwarf (from top to bottom; notice their different ordinates). The averages on layers of constant geometric height $\langle 3D \rangle_z$ (blue dashed), constant column mass density $\langle 3D \rangle_m$ (black dotted), constant Rosseland optical depth $\langle 3D \rangle_{\text{Ross}}$ (black solid lines) and at 500 nm $\langle 3D \rangle_{500}$ (red dashed triple-dotted lines) are indicated. For these averages, we show the solar (black) and sub-solar (blue lines) metallicity. Furthermore, we show 1D models (red solid), $T_{\text{rad}}^{\text{Ross}}$ -averages (green solid) and $\langle 3D \rangle_{\text{Ross}}^{\text{HSE}}$ (green dashed lines). The microturbulence of $\xi_{\text{turb}} = 1.0 \text{ km/s}$ has been used throughout.

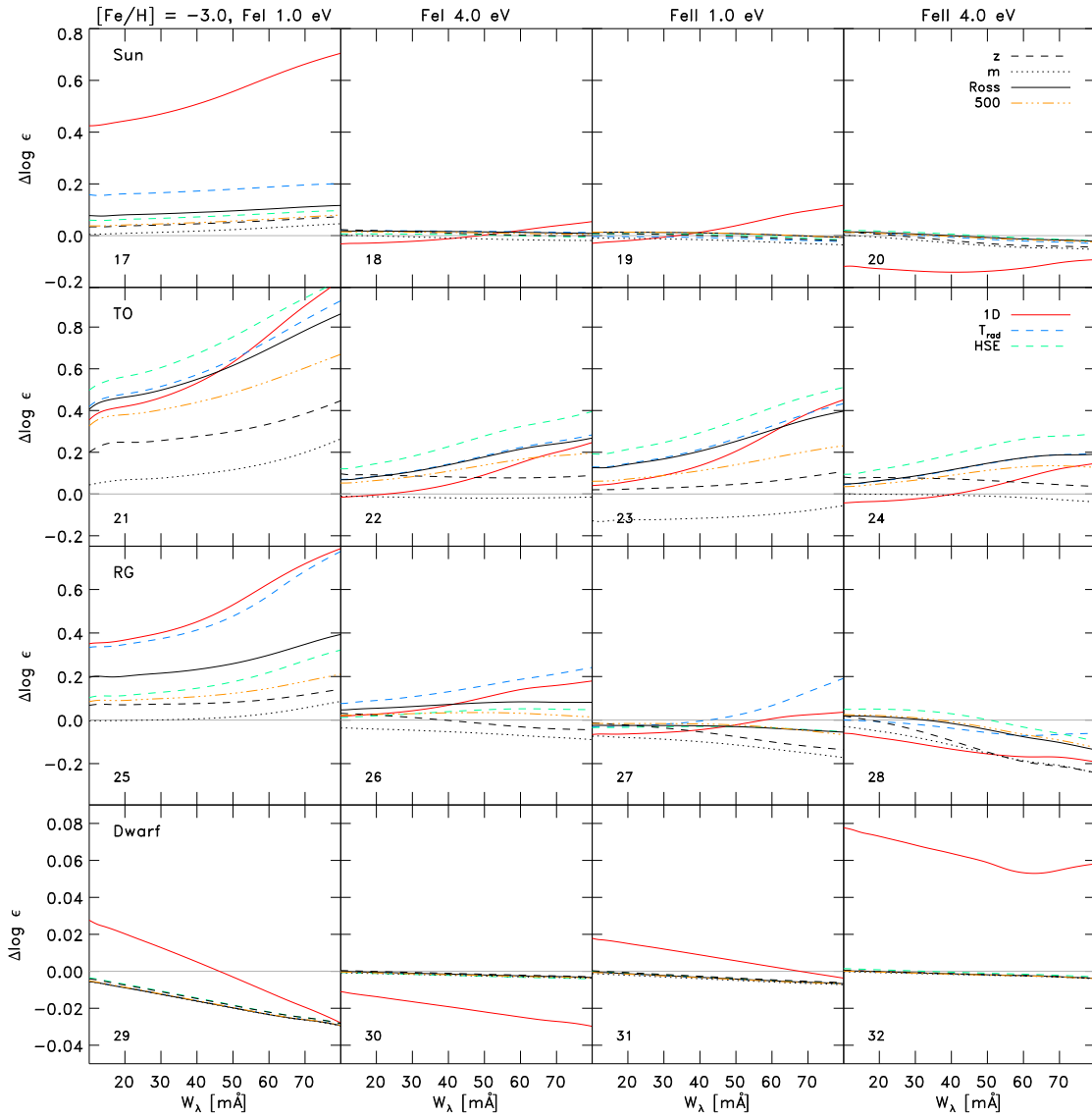


Figure 5.5: Similar as Fig. 5.4 but showing overview of the abundance corrections for metal-poor models. Note the larger ranges of the y-scales.

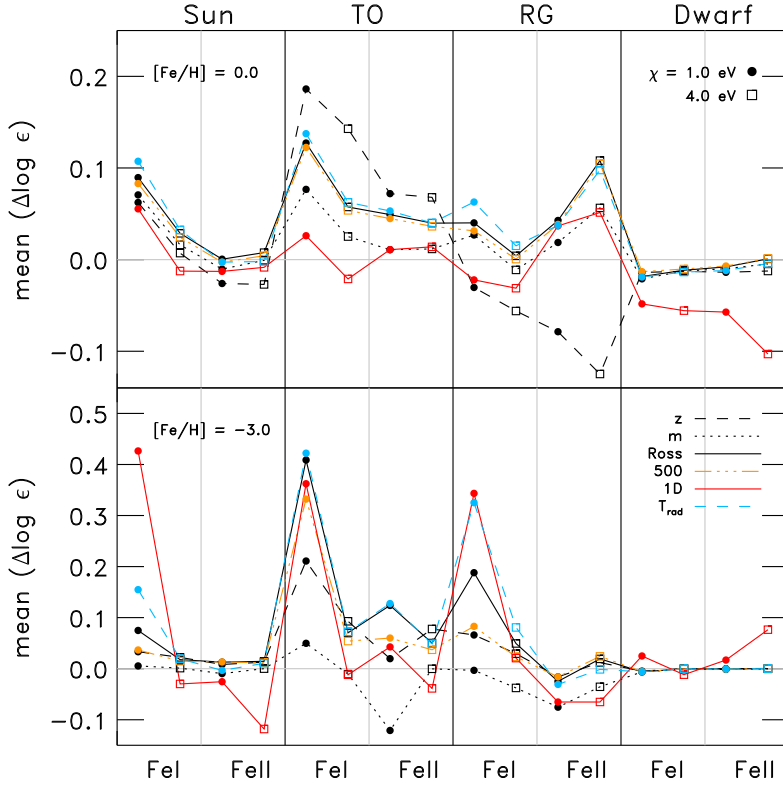


Figure 5.6: The mean $\Delta \log \epsilon$ (evaluated between 5 – 20 mÅ) is illustrated against Fe I and Fe II given at $\chi_{\text{exc}} = 1.0$ and 4.0 eV for the different selected models. Solar metallicity (top) and the metal-poor (bottom) case are shown, and the averages $\langle 3D \rangle_z$ (blue dashed), $\langle 3D \rangle_m$ (purple dotted), $\langle 3D \rangle_{\text{Ross}}$ (solid black), $\langle 3D \rangle_{500}$ (red dashed triple-dotted) and 1D models (solid blue lines).

Weak lines are insensitive to ξ_{turb} , yet they show variations in strength, which can be attributed to differences in the mean $\langle 3D \rangle$ stratifications of temperature and density. Interestingly, when one compares this regime between the different averages in Fig. 5.4, the averages on column mass density are often the closest to the full 3D spectral lines and perform in this respect often better than the averages on constant Rosseland optical depth. The stratification on constant optical depth at 500 nm always shows spectral line features slightly closer to the full 3D case compared to the Rosseland optical depth. However, this is because we chose our fictitious iron lines at 500 nm, which leads to an inherent advantage of $\langle 3D \rangle_{500}$ over $\langle 3D \rangle_{\text{Ross}}$. The geometrical averages show large deviations in the case of the TO and RG star at solar metallicity (see panels 5 to 12).

The differences in the metal-poor case (Fig. 5.5) are clearly greater than in the solar metallicity models (Fig. 5.4). It is obvious that $\langle 3D \rangle$ models at low $[\text{Fe}/\text{H}]$ struggle to reproduce the 3D case properly, in particular, Fe I lines with small excitation potential, and the differences are particularly pronounced for the hotter metal-poor TO stars (panel 21). This is in accordance with our findings from Sects. 3.4 and 3.5 at low metallicity and high T_{eff} . The differences in the statistical properties among the various $\langle 3D \rangle$ averages increase at low $[\text{Fe}/\text{H}]$. In particular, the widths of the temperature and density distributions become broader at lower metallicity (Fig. 3.40), and their mean values become increasingly less well-defined in its statistical representation. The reason for the broadening is the enhanced contrast of the reversed granulation due to the reduced radiative re-heating with weak spectral line features at low metallicity (see Sect. 3.6).

To facilitate an overall comparison between the different averages with respect to line formation, we show in Fig. 5.6 (left) the mean abundance deviations for weak lines that are determined between $W_\lambda = 5 - 20 \text{ mÅ}$. For the model representing the Sun, the differences between $\langle 3D \rangle$ and 3D are in general small: $\lesssim 0.1$ dex. For the TO stars at solar $[\text{Fe}/\text{H}]$, the differences are considerably larger: $\lesssim 0.2$ dex. We find the largest deviations for Fe I lines with small excitation potential $\chi_{\text{exc}} = 1.0 \text{ eV}$, which are the most temperature sensitive; in particular, the geometrical averages exhibit strong differences. At lower metallicity, the differences increase, in particular, for the TO and RG model with $\lesssim 0.4$ dex, and the line profiles resulting from the mean stratification on Rosseland optical depth shows the largest deviation to the

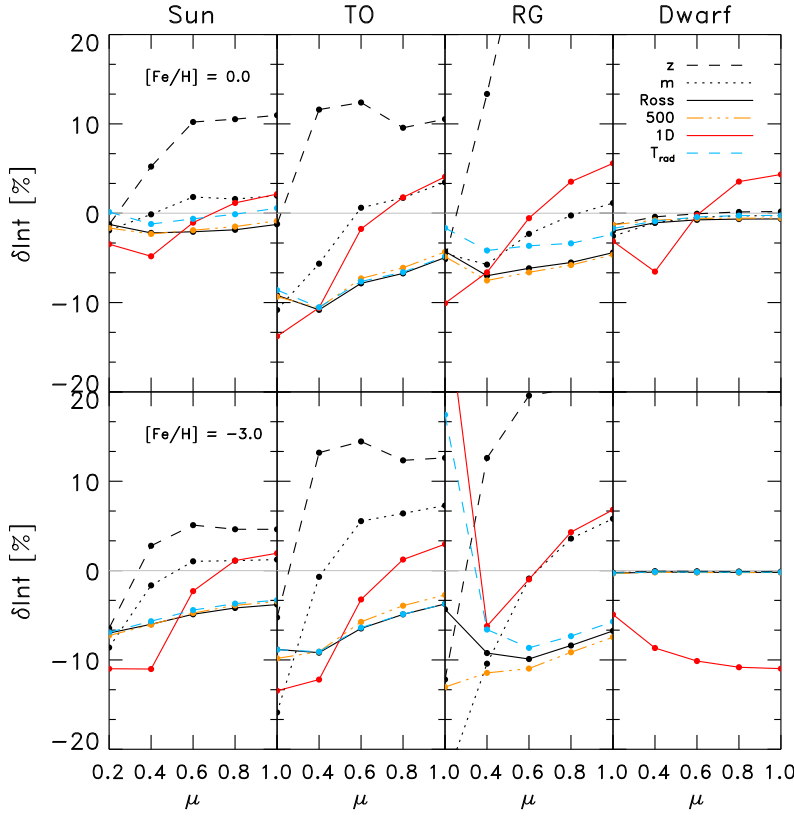


Figure 5.7: Similar to Fig. 5.6, here we show the relative difference with $\langle 3D \rangle - 3D$ of the continuum intensity, δI_μ , vs. μ angle is displayed.

full 3D line profiles for metal-poor TO star. In general the deviations become smaller at higher χ_{exc} and for Fe II lines. The dwarfs show very small differences compared to the full 3D case. These models exhibit the lowest velocities and temperature contrast with the mean stratifications closely resembling the 1D models based on same EOS and opacities.

The averages on column mass density $\langle 3D \rangle_m$ typically exhibit the best agreement with the predictions of the full 3D model, in particular, at low metallicity. This stems from the fact that a lower contrasts will result in more accurate and realistic averages. The geometrical averages $\langle 3D \rangle_z$ exhibit large deviations (in agreement with Uitenbroek & Criscuoli, 2011), especially for the TO stars. When one considers the comparison of the temperature and density in Figs. 3.33 and 3.34, then one can deduce that the models with cooler stratifications are closer to the full 3D line strength. Both models, averaged on constant optical depth, $\langle 3D \rangle_{Ross}$ and $\langle 3D \rangle_{500}$, lead to systematically larger deviations from the full 3D line formation calculations than those obtained with $\langle 3D \rangle_m$ models, in particular, for low excitation Fe I for the metal-poor TO star.

The resulting spectral line features with the logarithmic averages $\langle 3D \rangle_{log}$ are similar to plain $\langle 3D \rangle_{Ross}$ (therefore we refrain from showing the latter), while averages enforcing hydrostatic equilibrium, $\langle 3D \rangle_{HSE}$, clearly fail to closely reproduce the results from 3D line formation (similar to Uitenbroek & Criscuoli, 2011) and lead to rather large errors in the line formation, in particular, for the metal-poor TO model (Fig. 5.5). Furthermore, both the flux-weighted and brightness-temperature averages, T^4 and T_{rad} , are in general very close to the plain average, but often slightly less accurate, which is a somewhat surprising result (see T_{rad} in Fig. 5.6).

Another meaningful way to test the performance of the different averages can be accomplished by comparing the deviation of the center-to-limb variation (CLV) of the continuum intensity. In Fig. 5.7, we show the differences of the continuum intensity, $\delta I_\mu = (I_\mu^{(3D)} - I_\mu^{3D})/I_\mu^{3D}$, i.e. between the $\langle 3D \rangle$ and full 3D models. We find in general that the $\langle 3D \rangle$ models overestimate the continuum intensity at disk center ($\mu = 1$), while towards the limb ($\mu = 0.2$) the $\langle 3D \rangle$ often underestimate the intensity. The deviations of the different averages are similar to the above findings with the comparison of the curve of growth. The disk-center intensities of the 3D RHD models are matched best by the averages on column mass density $\langle 3D \rangle_m$,

whereas the geometrical averages $\langle 3D \rangle_z$ display the largest discrepancies, in particular, for the RG model at solar metallicity with an overestimation by $\sim 60\%$. The results for the averages on optical depth are once again midway between the two other kinds of averages. An interesting aspect is that the brightness-temperature averages T_{rad} fail to render the continuum intensities exactly, which has to be interpreted as a consequence of the non-linearity of the Planck function. Our findings are qualitatively similar to those by Uitenbroek & Criscuoli (2011).

5.3.2 Cautionary remarks

We remind the reader that LTE is often a very poor assumption at low $[\text{Fe}/\text{H}]$ (e.g. Asplund, 2005) and thus that the abundance differences presented in Figs. 5.4 and 5.5 should not be added indiscriminately to results from standard 1D LTE abundance analyses. In LTE, the difference between 3D and 1D models can be very substantial for metal-poor stars for especially low excitation and minority species like Fe I (e.g., Asplund et al., 1999b; Collet et al., 2007), but those same lines also tend to be sensitive to departures from LTE (e.g., Bergemann et al., 2012; Lind et al., 2012) in 1D and $\langle 3D \rangle$ models, mainly due to over-ionization and over-excitation in the presence of a hotter radiation field than the local kinetic temperature (i.e., $J_\lambda > B_\lambda$). Although not explored for more than Li, one would expect that the very cool upper atmospheric layers, hence steep temperature gradients in metal-poor 3D models compared with classical 1D models, are even more prone to substantial non-LTE effects (e.g., Asplund et al., 2003; Sbordone et al., 2010). In particular, neutral species of relatively low ionization energy, such as Fe I, typically suffer from significant positive NLTE abundance corrections due to over-ionization (e.g., Asplund, 2005; Bergemann et al., 2012; Lind et al., 2012) with low excitation lines are especially prone. For low-excitation Fe I lines, one would therefore expect the 3D NLTE line strengths to be more similar to the 1D case than the 3D LTE results due to the positive NLTE corrections, partly compensating for the negative 3D LTE corrections. We therefore caution the reader that the 3D LTE abundance corrections presented here (3D LTE - 1D LTE) for Fe I lines are likely to be too negative compared to the NLTE case (3D NLTE - 1D NLTE). As a corollary, it is inappropriate to apply a 1D NLTE abundance correction to a 3D LTE-inferred abundance when the latter is very significant, as is often the case at low $[\text{Fe}/\text{H}]$.

5.3.3 Comparison with 1D models

In Sect. 3.3 we compared the $\langle 3D \rangle_{\text{Ross}}$ stratifications with 1D models computed with the same EOS and opacity as used in the STAGGER-code, in order to quantify the differences arising solely from 1D modeling based on MLT. The line formation calculations with 1D models perform quite well at solar metallicity, with the exception of the cool dwarf models (Fig. 5.4). However, in the metal-poor case, the lines based on the 1D models obviously do not correctly reproduce the full 3D lines by overestimating the T -stratifications due to the enforcement of radiative equilibrium in the upper atmosphere (Fig. 5.5). This is, in particular, distinctive for low-excitation neutral iron lines as previously found by Asplund et al. (1999b) and Collet et al. (2007). Kučinskas et al. (2013b) present similar findings for a solar-metallicity RG simulation as well, namely that neutral iron lines based on 1D MLT models are slightly closer to the full 3D lines compared to the $\langle 3D \rangle$ lines.

We note that in our 1D models the turbulent pressure is neglected, and the mixing length is fixed with $\alpha_{\text{MLT}} = 1.5$, both choices that will influence the stratification significantly. Since their effect is strongest in convective zone below the optical surface and the line formation region, the influence in terms of abundance is likely small; in fact, Kučinskas et al. (2013b) only found a very small effect < 0.02 dex for the reduction in α_{MLT} from 1.5 to 1.2. However, for metal-poor giants the influence can be greater for lines with very high excitation potential.

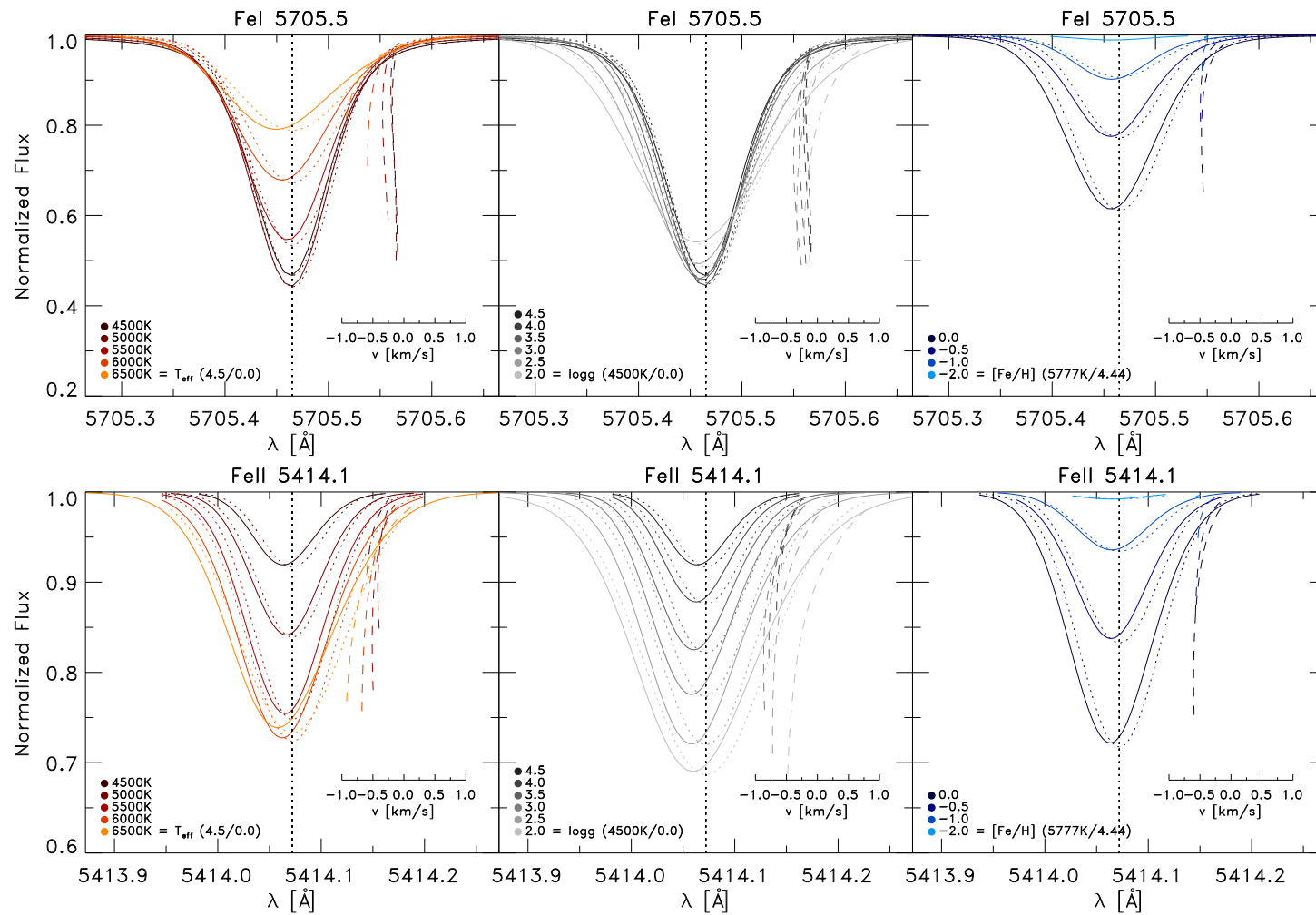


Figure 5.8: Normalized flux vs. wavelength for a FeI and FeII line (top and bottom panel respectively; solid lines) for different stellar parameters with an enlarged, off-center view of the bisector (dashed lines). In each column, one stellar parameter is varied, while the other two are fixed (indicated); *left panel*: effective temperature; *middle panel*: surface gravity; *right panel*: metallicity. Furthermore, the respective lines computed with the $\langle 3\text{D} \rangle$ models are also shown (dotted lines). Note the different the ordinates.

5.4 Fe line shapes, shifts and asymmetries

5.4.1 Line shape

Real spectral absorption lines exhibit a more complex shape than just a Gaussian or Lorentz profile due to the nature of turbulent convection prevailing at their origin in the atmospheres of cool stars, and not to mention that actual spectral lines form over a range of depths and are sensitive to local physical conditions as well as, in general to non-local effects such as radiation generated in other parts of the atmosphere. The convective velocities are imprinted in the line profile in form of Doppler shifts, which introduce shifts and asymmetries, thereby also changing the line shape and strength. In Fig. 5.8, we illustrate for a single Fe I and Fe II line (top and bottom panel respectively) overviews of profiles including the bisectors, where one stellar parameter is varied, while the two others are fixed, in order to illustrate the individual influence of T_{eff} , $\log g$ and $[\text{Fe}/\text{H}]$ on the line shape and asymmetry.

The variation of the line profiles and asymmetries is rather systematic, namely the line strength is decreasing for Fe I (increasing for Fe II) with hotter T_{eff} , while it reduces with lower $[\text{Fe}/\text{H}]$, and the asymmetries are increasing for higher T_{eff} and lower $[\text{Fe}/\text{H}]$ for both Fe I and Fe II. The opposing trends of the Fe I and Fe II line strength with T_{eff} stems from the ionization of neutral iron at higher temperatures. In the case of the Fe I line, towards lower $\log g$, the line strength is changing only little, while for the Fe II line, the line strength is rising significantly. In fact, the Fe II line strength shows always a clear ascend for lower $\log g$, while for Fe I lines this is the case only for cooler T_{eff} , and hotter ones show even smaller trends with $\log g$ (compare the range in line strength with $\log g$ in Fig. 5.9). Also, towards giants (lower $\log g$) the asymmetries are increasing considerably for both lines due to the larger amplitude and velocity asymmetry between up- and downflows (see Fig. 5.17). The wider and stronger line profiles in giants exhibit a more pronounced red-shift in the upper bisector (see lines with $\log g = 2.0$ in middle panel of Fig. 5.8) due to the increasing influence of the contribution from the downflows on the red wing. For the highest T_{eff} (6500 K) or the lowest $\log g$ (2.0) the largest span in asymmetry is achieved for both lines (see Fig. 5.8; also bottom panel of Fig. 5.12).

The height of line formation is in general very important, namely weaker lines show more pronounced line shifts and asymmetries, since they tend to be formed in deeper layers (see Sec. 5.4.6) where the maximum velocities and temperature contrasts happen ($\tau_{\text{Ross}} \sim 1$; see Sec. 5.17). Stronger lines have their formation height shifted outwards where velocity and contrast is lower and less well anti-correlated (see Fig. 5.17). Similarly, Fe II lines are formed deeper than Fe I, since their number density increases in the deeper layers with the temperature.

It is customary to distinguish between the central and outer regions of a line profile with respect to central wavelength, that is, between the core and the wings. The line core is the (unique) location depicted by the minimum in flux or intensity, i.e. $l_c = \min[F_\lambda]$. The wings are formed in deeper layers leading to a \wedge -shape in the bisector arising from the granules (see Fig. 5.2), while the line core originates from higher depths, therefore, with increasing line strength the line asymmetry of the line core (line shift) is receding after a maximum, leading with the \backslash -shape to the typical C-shape of the bisector (see Fig. 5.8). Therefore, the final shape of the bisector is the result of a superposition of the blue-shifted contribution from the upflows arising from the granules and a red-shifted part from the downflows in the intergranular lane. The line profile is often dominated by the granules, since these exhibit a brighter intensity, steeper temperature gradients and more importantly larger area contribution (filling factor) compared to the downflowing intergranular lane. However, this correlation decreases quickly above the optical surface. Furthermore, the line shape and bisector depends on the vertical velocity field, its amplitude, asymmetry and the extent of overshooting into convective stable layers (see Sec. 5.4.6). The radial p-mode oscillations generally broaden the line profile, however without altering the overall line strength, since the vertical oscillations cancel out on the temporal mean.

Additionally, we included in Fig. 5.8 also the symmetric line profiles resulting from the corresponding mean $\langle 3\text{D} \rangle$ models, in order to depict the influence from the inhomogeneities and in particular, the vertical velocity field resulting from convection and granulation. The homogenous $\langle 3\text{D} \rangle$ models include micro- and macroturbulence in order to yield the same line strength and depth respectively as the considered full 3D line, therefore, one can isolate visually the Doppler shifts arising from the realistic 3D velocity field. At cooler T_{eff} the line shape is more symmetric, therefore the differences are rather small, while towards higher

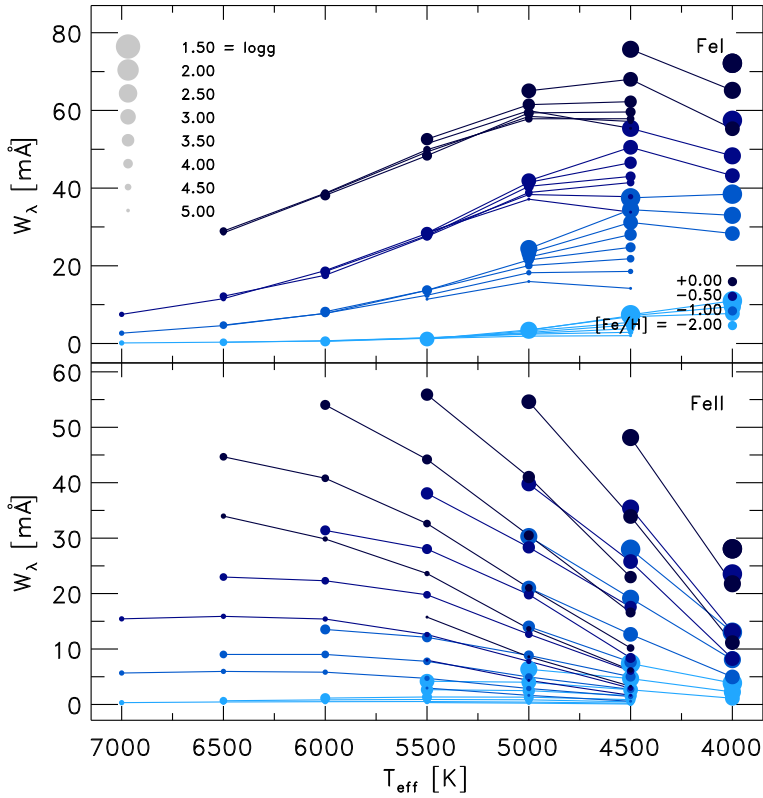


Figure 5.9: The line strength W_λ vs. effective temperature for a single Fe I line ($\lambda = 5705.5$, $\chi_{\text{exc}} = 4.3$; top panel) and Fe II line ($\lambda = 5414.1$, $\chi_{\text{exc}} = 3.221$; bottom panel).

line shifts the differences grow apparently. Due to the Doppler shifts the 3D lines are more dominantly blue-shifted, therefore one finds larger line depression (absorption) on the blue half of the profile, and a lower one on the red part compared to the symmetric (3D) line.

5.4.2 Line strength

The equivalent width is the area-integral of the spectral absorption line profile, $W_\lambda = \int (1 - F_\lambda/F_c) d\lambda$, and also referred as the line strength. Therefore, it is a quantitative measure, how effective a spectral line is absorbing radiation from the continuum radiation. In the following we want to discuss the variation of line strength for Fe I and Fe II with stellar parameters.

From the overview in Fig. 5.8 one can infer immediately that the line strength is for Fe I increasing in general for lower T_{eff} (higher T_{eff} for Fe II) and higher $[\text{Fe}/\text{H}]$. The line strength depends in the first place on the number density of the absorbing species, i.e. $n_{\text{Fe I}}$ and $n_{\text{Fe II}}$, which in turn depends on the excitation (Boltzmann eq.) and ionization level (Saha eq.). The iron abundance is given by $[\text{Fe}/\text{H}]$, therefore, the iron number density is proportional to it, i.e. $n_{\text{Fe}} \propto [\text{Fe}/\text{H}]$, hence the $n_{\text{Fe I}}$ and $n_{\text{Fe II}}$ as well. At hotter temperatures the minority species, neutral iron (Fe I), is getting increasingly ionized, therefore, the $n_{\text{Fe I}}$ decreases in favor of $n_{\text{Fe II}}$ and the line strength of Fe I lines decreases, while for Fe II it increases². At cooler temperatures the opposite is the case, namely the minority species, Fe I, is increasing dramatically in its number density and Fe II is decreasing. On the other hand, $n_{\text{Fe II}}$ is less sensitive to T_{eff} and temperature, since most of Fe is in Fe II, and therefore it is changing only little. Another reason for the decline in line strength towards hotter T_{eff} is the extremely temperature-sensitive H^- -opacity in the subsurface region of cool stars ($\kappa \propto T^{10}$), which increases its continuum opacity (see Gray, 2005) due to the higher electron pressure with hotter T . To elucidate the strong (and opposite) dependence on T_{eff} and $[\text{Fe}/\text{H}]$, we show the line strength for an individual Fe I and Fe II line in Fig. 5.9 (in particular, compare ranges and slopes

²Higher ionization degrees than the first are occur at much higher temperature for iron, and since we consider cool stars in this work, these are irrelevant.

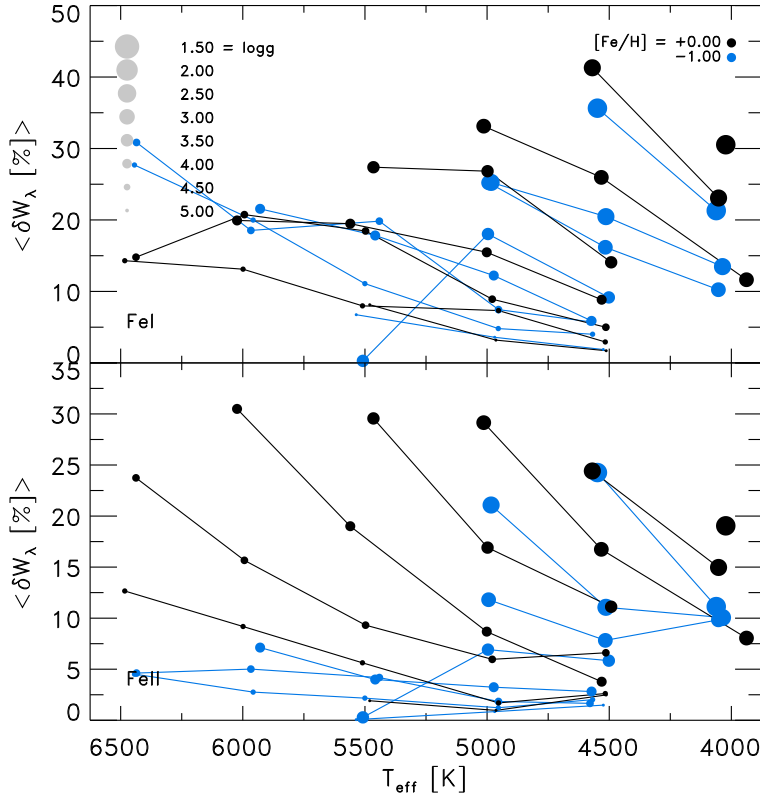


Figure 5.10: The relative difference between full 3D and (3D) line strength, δW_λ , vs. T_{eff} averaged over all Fe I and Fe II lines separately (top and bottom panel respectively).

between Fe I and Fe II in the latter). The metallicity has the strongest impact on the line strength, and the effective temperature is also very important, while the surface gravity changes the W_λ only little or much depending on the line at consideration. We note that at cooler T_{eff} we find the influence of $\log g$ being in general more pronounced for Fe I lines, while Fe II lines are less sensitive to $\log g$. Moreover, we find that the hot metal-poor stars to have very small Fe I line strength, while the cool metal-rich ones show the largest ones. In the case of Fe II lines the T_{eff} -dependence is qualitatively the opposite to Fe I, since the ionization of neutral iron increases $n_{\text{Fe II}}$, thereby the line strength. One finds also a wider range in $\log g$ for Fe II, while for Fe I the dependence is much smaller.

Now, we evaluate the difference in the line strength between the full 3D predictions and the (3D) models without any microturbulence, i.e. $\delta W_\lambda = W_{3\text{D}}/W_{(3\text{D})} - 1$. In Fig. 5.10 we display the average difference separated in Fe I and Fe II lines with stellar parameters. We remark that the individual lines exhibit distinctive values between different lines, however, the average values depict qualitatively an overview of the variations. The difference δW_λ quantifies the effect of the non-thermal Doppler broadening, since the (3D) models include no velocity field or microturbulence. As expected the Doppler broadening due to the convective velocities is enhancing the line strength of the full 3D lines, with the consequence of the latter being stronger than the (3D) lines. The enhancement in W_λ is increasing for hotter T_{eff} , lower $\log g$ and higher $[\text{Fe}/\text{H}]$, which corresponds to the variation of the vertical rms-velocity (see Fig. 5.18). The trends of δW_λ with stellar parameters are between Fe I and Fe II in general qualitatively rather similar. Lines with higher excitation potential energy feature a smaller range in δW_λ .

5.4.3 Line width and depth

In order to depict the variations of the shape of a line profile with stellar parameters, we determine the line width and depth from fictitious Fe I lines that has the same line strength ($W_\lambda = 80 m\text{\AA}$). The line width, l_w , is quantified by the full-width-at-half-maximum (FWHM) of the line profile, and states a measure for the Doppler shifts experienced from the velocity field. From Fig. 5.11 (top panel), one can obtain that

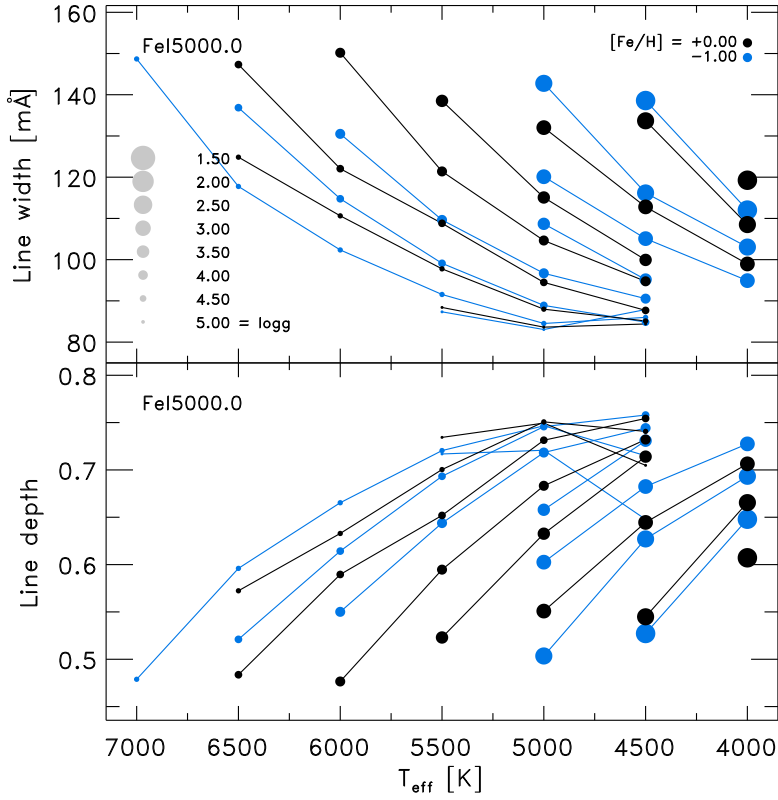


Figure 5.11: Line width l_w (top) and depth l_d (bottom panel) derived from the flux profile of the fictitious Fe I line ($W_\lambda = 80 m\text{\AA}$, $\chi_{\text{exc}} = 4.0 \text{ eV}$) for different stellar parameters.

the line width increases for higher T_{eff} and $[\text{Fe}/\text{H}]$, and lower $\log g$, which correlates with the variations of the vertical rms-velocity for the atmosphere models (see Fig. 5.18). The line depth is the relative flux or intensity of the line core, $l_d = 1 - \min[F_\lambda/F_c]$, and depicts the maximal absorption from the continuum radiation of a line. The line depth shows a clear anti-correlation with the line width for different stellar parameters (bottom panel in Fig. 5.11). However, the line depth is declining faster than the line width is increasing, which means that the line profile is becoming flatter and broader, when considering the same line strength. This broadening of the line profile for different stellar parameters is a consequence of the higher velocity amplitudes leading to larger Doppler shifts. The aspect ratio between depth and width, $a_{\text{dw}} = l_d/l_w$, is diminishing very quickly for hotter T_{eff} , lower $\log g$ and $[\text{Fe}/\text{H}]$ for Fe I lines. In the case of Fe II lines, the variation with T_{eff} is slightly different, namely it increases towards higher T_{eff} until 5500 K and drops above, and the largest a_{dw} being slightly smaller. In general the aspect ratio is increasing with W_λ , reaching a maximum around $50 m\text{\AA}$, and then decreasing, while for higher χ_{exc} it is smaller. The changes of the width, depth and their aspect ratio are for $\langle 3\text{D} \rangle$ qualitatively similar, however their amplitude is rather different. This indicates that the flattening of line profile is partly due to thermal broadening as well.

5.4.4 Line shift

When one depicts the wavelength of the line core with l_c , then the line shift is given by the difference of the line core with respect to the wavelength of the line at consideration, i.e. $l_s = \lambda_c - \lambda$, and commonly quantified in units of velocity. In Fig. 5.12 (top panel), we show an overview of the mean line shift of the Fe I lines with stellar parameters. Furthermore, we show in Fig. 5.13 an overview of the line strength against the line strength for various stellar parameters, in order to depict the influence of T_{eff} , $\log g$ and $[\text{Fe}/\text{H}]$ individually (from top to bottom respectively) for the complete Fe I and Fe II line set (circles and triangles respectively). Furthermore, for the Fe I lines we performed also least-square linear functional fits to illustrate the trends with W_λ (red lines). The linear fits consider only Fe I lines, since these cover the largest span, and the fits are clearer without the contribution of Fe II lines. We depict also the mean line shift

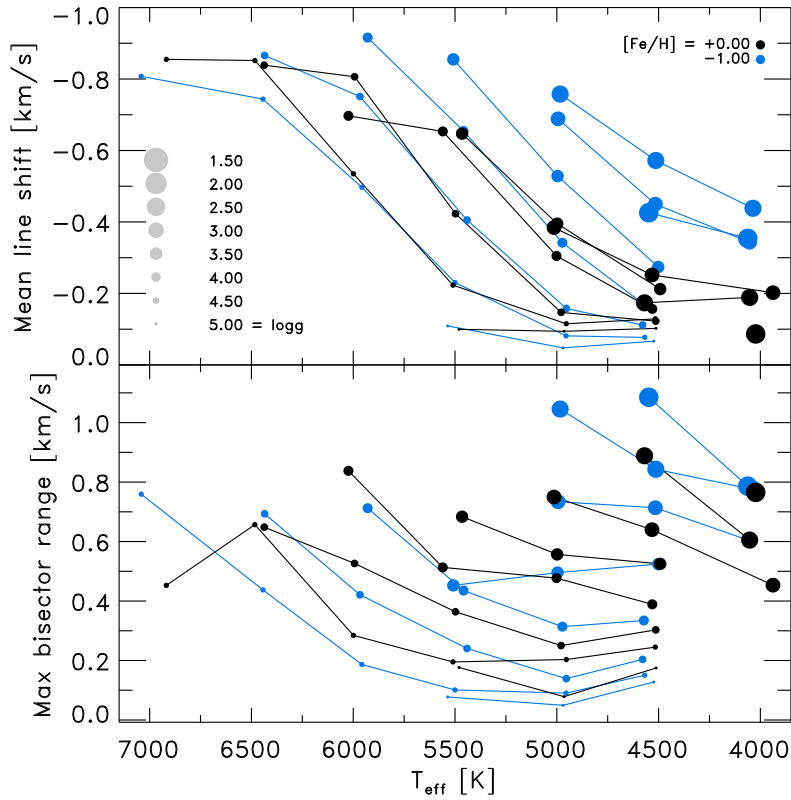


Figure 5.12: The mean (Fe I) line shift and maximal bisector for different stellar parameters. Note the inverted ordinate in the top panel, which increases towards higher blue-shifts (negative velocity).

(grey solid) and the ranges in line strength and shift (vertical and horizontal grey dashed lines respectively) for the Fe I lines. The lower excitation potential energy, χ_{exc} , and line wavelength of the lines are indicated to illustrate trends with line parameters (blue colors and symbol size respectively). We display also the line shifts from the fictitious iron lines as well.

In the following we discuss the Fe I lines first. Towards hotter effective temperatures (top panel of Fig. 5.13), we find the line shifts of Fe I lines to rise considerably (from ~ 0.1 to 0.8 km/s), while the maximal line strength is diminishing (from 140 to $40 m\text{\AA}$). At higher T_{eff} , one finds convection to operate less efficient and therefore more rigorous with higher T -contrast and rms-velocity (see Fig. 5.17 or Sec. 3.5.1 for more details). On the other hand, at higher T_{eff} , iron is more likely to be ionized and also the (continuum) H^- -opacity increases as well, hence, both effects are reducing the line strength. We noted that weaker lines originate from lower depth, where the velocity and T -contrast are larger, therefore imprinting a larger line shift. The line core of stronger lines are formed at higher altitudes, therefore, their line shift is weaker (notice the generally smaller line shifts towards stronger lines in Fig. 5.13). Moreover, for higher T_{eff} the range in line shift and the slope of the linear fits are decreasing. For lower surface gravity (middle panel), the line shift, its range and the slope of the linear fits are increasing, reach a maximum at $\log g = 3.0$ and decrease again, while the range in line strength is almost unaffected. For lower metallicity (bottom panel), the line shifts and line strength are reducing, and the slope of the linear fit are becoming steeper.

We find in general that the line shifts and strengths are anti-correlated, i.e. for weaker (stronger) lines their shifts are higher (lower), which arises from the deeper (higher) location of line formation, and the respectively larger (lower) velocity amplitude (compare top panel of Fig. 5.12 with Fig. 5.9). On the other hand, lines with lower (higher) excitation potential energy, χ_{exc} , exhibit smaller (larger) line shifts. The lines are on average blue-shifted (negative line shift; see top panel of Fig. 5.12), since the granules occupy a higher filling factors and intensity contribution over downdrafts. The mean line shift is increasing for higher T_{eff} , lower $\log g$ and enhanced $[\text{Fe}/\text{H}]$. Only a few of the strongest lines in giants exhibit red-shifted line cores, since the relative contribution of the red-shifted downdrafts in these are pronounced. We find

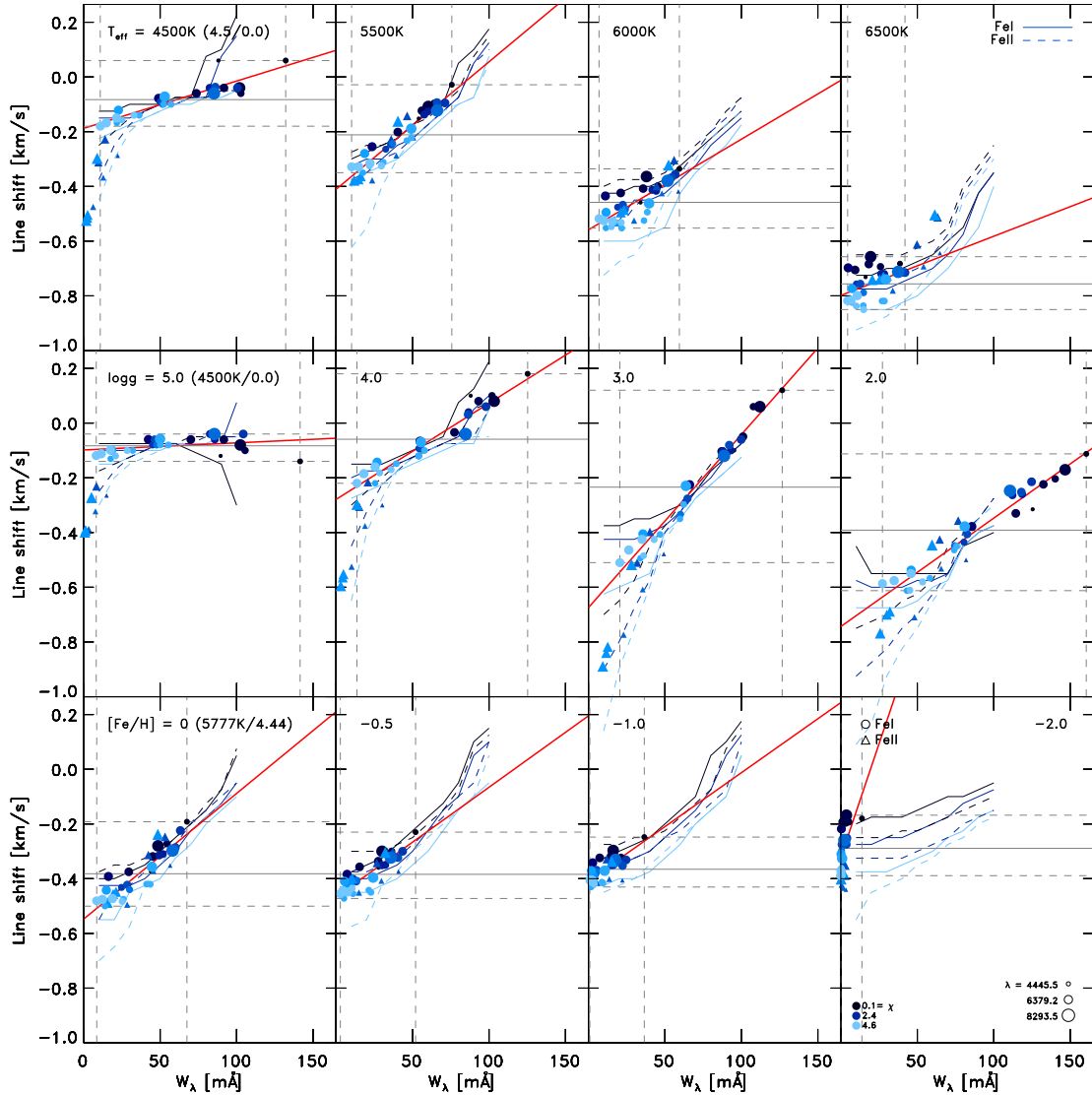


Figure 5.13: The line shift vs. line strength for the Fe I and Fe II lines (circles and triangles, respectively) for different stellar parameter. Also fictitious Fe I and Fe II lines (blue solid and dashed lines) are shown. The excitation potential energy χ_{exc} (blue colors, where brighter refers to higher χ_{exc}) and wavelength λ are indicated (symbol sizes, where bigger refers to higher λ). In each row, one stellar parameter is varied, while the other two are fixed (indicated); *top panel*: effective temperature; *middle panel*: surface gravity; *bottom panel*: metallicity. Furthermore, linear functional fits (red solid), mean (grey solid) and range in line shift and strength (grey dashed lines) are indicated.

that the fictitious Fe I and Fe II lines have qualitatively very similar line shifts as the mean line shifts shown in Fig. 5.12. The latter show a distinct dependence on the line strength.

The Fe II lines exhibit in general similar trends for line strength and shift with stellar parameter as found for the Fe I lines. However, the ranges in line strength are distinctively smaller and its variations are much less pronounced, in particular, the line strength is less sensitive to T_{eff} , since it is the majority species. Furthermore, the mean line shift and the slope of the linear fits are in general higher compared to the Fe I values.

5.4.5 Line asymmetry

The bisector of a spectral line profile is the set of midpoints that equipartitions the line segments into two equal halves, depicting the asymmetry arising from the individual Doppler shifts experienced at the respective heights. A line without asymmetries (e.g., 1D or 3D) line) has a straight bisector, while a realistic line profile exhibits a bisector with the characteristic C-shape that results from the superposition of the contribution from the (strong, blue-shifted) dominant granules and the (weak, red-shifted) intergranular lane (see Fig. 5.2).

In Fig. 5.14, we show an overview, each including five Fe I and Fe II bisectors (solid and dashed lines, respectively) that are selected based on their increasing line strength (green colors) for different stellar parameters. In general, the typical C-shape is present in most of the bisectors, however more or less pronounced and "uncovered" depending on the line strength. Weak lines feature a blue-shifted bisector with a typical \wedge -shape depicting only the upper part of the C-shape, where the line core coincides with the maximal line asymmetry, $\max[|v|]$, i.e. maximal absolute velocity shift of the entire bisector. On the other hand, stronger lines cover a larger optical path and its cores are forming in higher layers above the overshooting region, therefore, the line centers are less blue-shifted and tend towards zero, thereby increasingly featuring the entire the C-shape. The maximal asymmetry of strong lines is located around the mid-height of the line depth.

For higher T_{eff} (top panel of Fig. 5.14), the bisectors increase significantly their ranges, while the line strength becomes weaker and also more blue-shifted, until the C-shape finally disappears (6500 K). Towards giants (lower $\log g$; middle panel) the line asymmetries (range of bisectors) rise in general, and the C-shape is getting more pronounced until $\log g = 3.0$ and less below. Furthermore, the upper part of the bisector recedes towards lower velocity-shifts and are even red-shifted for the lowest surface gravity ($\log g = 2.0$), since the contribution on the red wing from the downdraft is then dominating towards the continuum flux. With lower metallicity (bottom panel) the lines are weaker, therefore the bisectors lose their C-shape until it vanishes eventually, also the range in bisector diminishes. The variations in the line asymmetry with stellar parameters result from the differences in line strength, continuum level, filling factor and Doppler shift. We note that considering the variations of a single line with different stellar parameters changes significantly its shape (see Fig. 5.8).

In Fig. 5.12 (bottom panel) we show the maximal range of the bisectors with stellar parameters, which are increasing for higher T_{eff} and $[\text{Fe}/\text{H}]$, lower $\log g$ similar to the vertical rms-velocity in the 3D atmosphere models (see Fig. 5.17). One would assume that the line asymmetries are correlating with the velocity field, since these arise from the Doppler shifts. Therefore, we compare the maximal range of the bisectors with the maximal vertical rms-velocity for different stellar parameters in Fig. 5.16. The line asymmetries correlate clearly with amplitude of the vertical velocity, only there is a slight scatter due to the different heights of line formation.

In Fig. 5.15 we illustrate bisectors from the fictitious Fe I line flux profiles for different stellar parameters, which have the same (interpolated) line strength, considering weak ($40 m\text{\AA}$) and intermediate ($80 m\text{\AA}$) line strength (top and bottom panel respectively). The basic idea behind this comparison is to isolate and illustrate the effect and signature on the line profile due to the intrinsic structural differences between the individual 3D atmosphere models arising solely from the variations in the convective flow properties. We vary one stellar parameter individually, while the other two are fixed (T_{eff} , $\log g$ and $[\text{Fe}/\text{H}]$). The three different excitation potential energies ($\chi_{\text{exc}} = 0, 2, 4$) are also considered (solid, dotted and dashed, respectively).

The intermediate strong lines feature often a more explicit C-shape compared to the weak lines with smaller maximal bisectors, otherwise, the changes with stellar parameters are qualitatively rather similar.

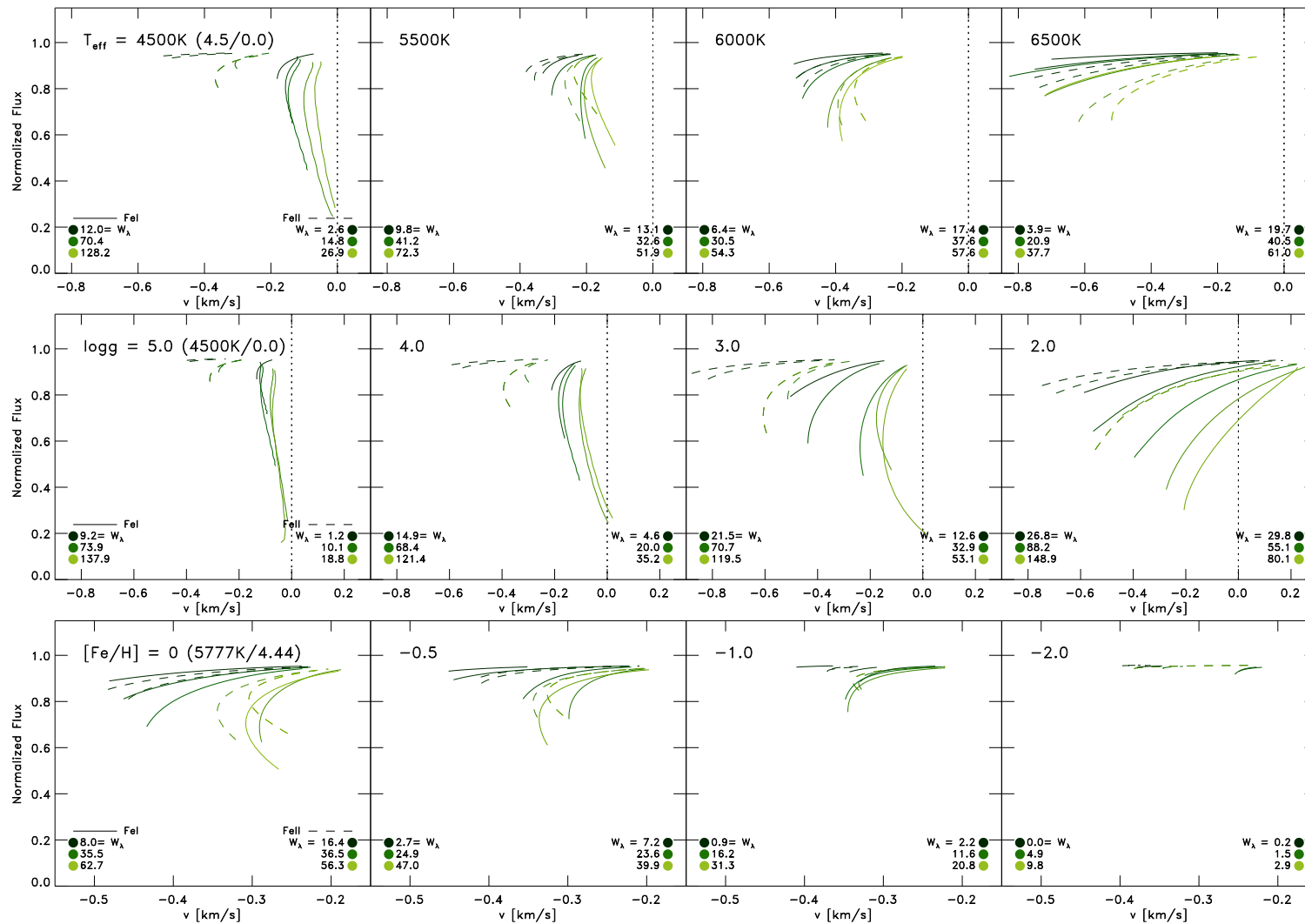


Figure 5.14: A subset of five bisectors of Fe I and Fe II lines for different stellar parameters (solid and dashed lines respectively), sorted by increasing line strength, which are indicated (green colors; brighter refers to higher W_λ). Similar to Fig. 5.13, in each row, one stellar parameter is varied, while the other two are fixed (indicated); *top panel*: effective temperature; *middle panel*: surface gravity; *bottom panel*: metallicity. Note the changes in abscissae for the different rows.

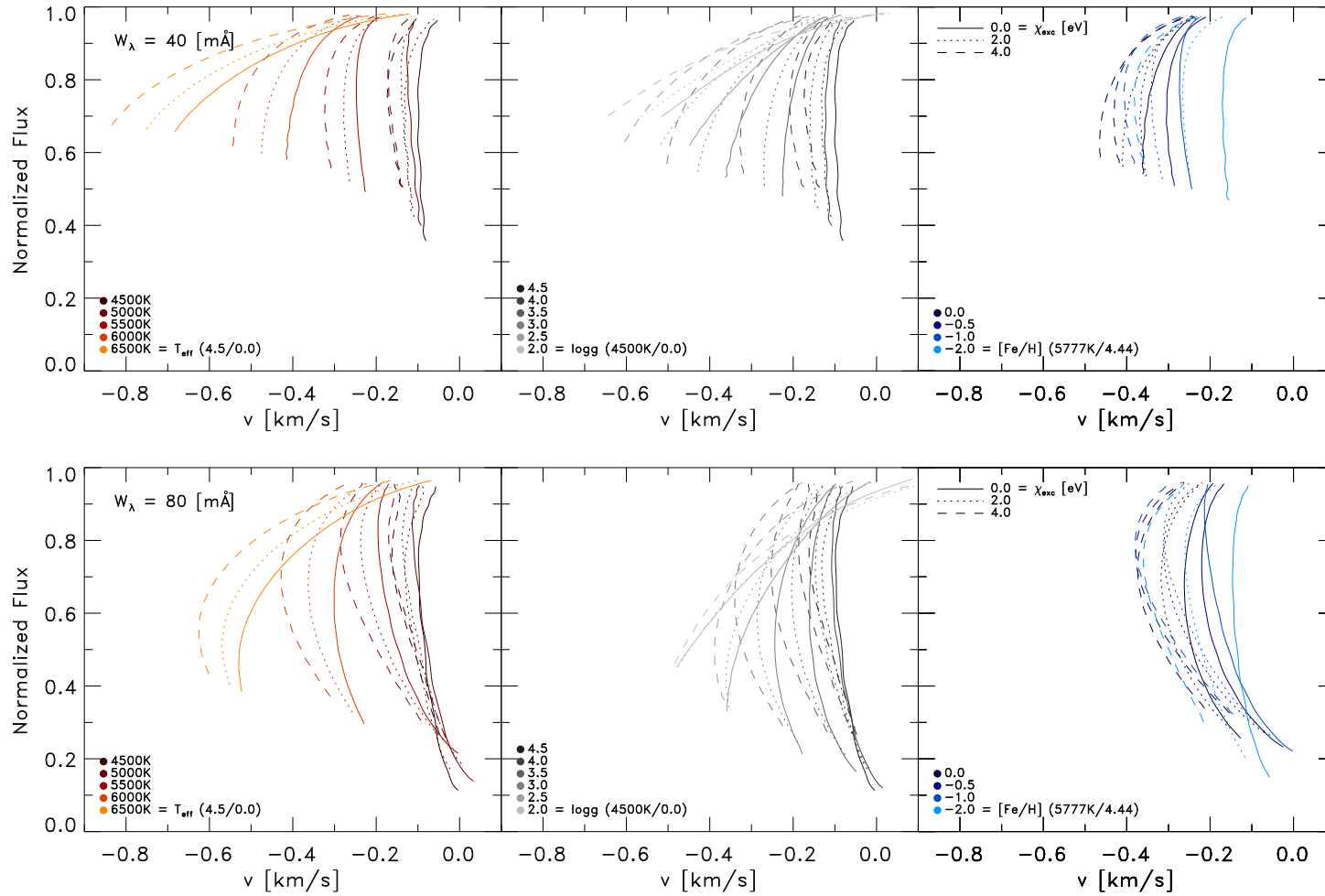


Figure 5.15: Bisectors from fictitious Fe I lines for two line strengths ($40, 80 \text{ m}\text{\AA}$; top and bottom panel respectively) and three different excitation potential energies (0, 2, 4 eV; solid, dotted and dashed lines respectively) for different stellar parameters. In each column, one stellar parameter is varied, while the other two are fixed (indicated); *left panel*: effective temperature; *middle panel*: surface gravity; *right panel*: metallicity. Furthermore, the respective lines computed with the $\langle 3D \rangle$ models are also shown (dotted lines).

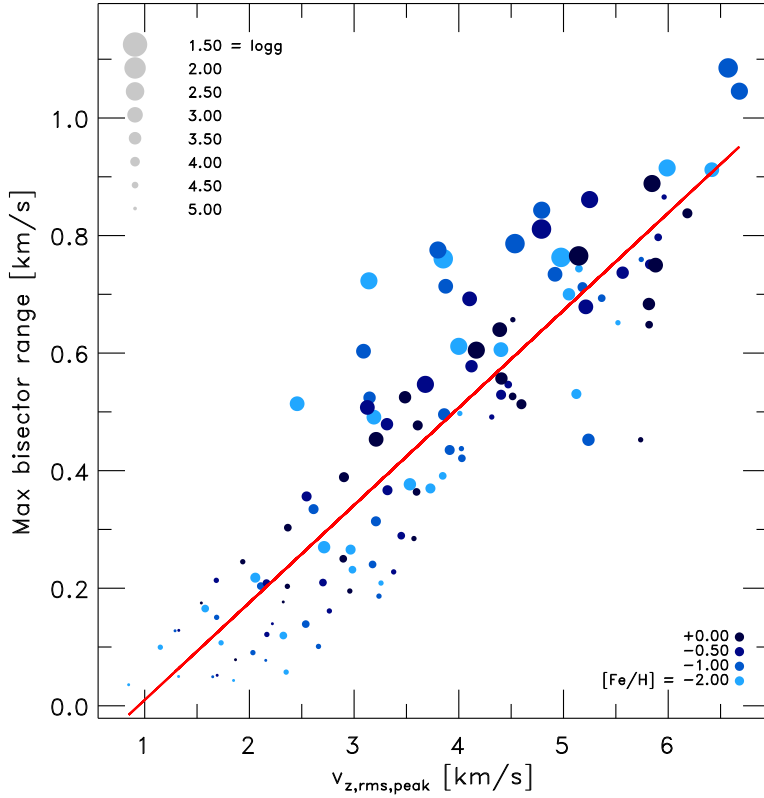


Figure 5.16: The maximal bisector vs. maximal vertical rms-velocity for different stellar parameters. A linear fit is included (red line).

For hotter T_{eff} and lower $\log g$, their effect on the weak and intermediate strong lines is rather similar, namely the line depth is decreasing (for the same line strength) and the line width is rising, which means that the line shape is becoming increasingly flatter and broader (see also Sec. 5.4.3), while the line shift and maximal bisector is enhancing considerably, primarily due to concomitant higher velocity and T -contrast (see Sec. 5.4.6). On the other hand, at lower metallicity the changes in the line shape are less pronounced, only the exhibited blue-shifts are lower due to the smaller level in velocity and T -contrast. In the case of the weak lines (top panel) with lower T_{eff} and $[\text{Fe}/\text{H}]$, higher $\log g$ the bisectors are increasingly uniform over the entire line depth, and the C-shape is less distinct, since weak lines are arising from a smaller extent in height. The variations of the fictitious Fe II are rather similar to those by Fe I, therefore we refrain from showing them. The only noteworthy differences are the slightly smaller ranges in line shift, depth and maximal bisector for fictitious Fe II lines, while the giants feature a stronger influence from the red-shifted downflows. Lines with higher excitation potential energy depict in general more blue-shifted bisectors, since these lines form in deeper layers with higher velocity and T -contrast.

5.4.6 Conditions at the height of line formation

In the following we want to discuss the different physical conditions based on the properties of the velocity and temperature prevailing in the 3D RHD model atmospheres, which are in the end responsible for the various line asymmetries we seen above. In Fig. 5.17, we show the vertical rms-velocity, $v_{z,\text{rms}}$, the asymmetry between up- and downflow rms-velocity, $\delta v_{\text{up,dn}}$, temperature contrast, δT_{rms} , the asymmetry between up- and downflow temperature, $\delta T_{\text{up,dn}}$, the correlation function of the temperature and vertical velocity, $C[v_z, T]$, and the filling factor of the upflows f_{up} .

In the superadiabatic region (SAR) just below the optical surface ($\log \tau_{\text{Ross}} > 0$) the vertical rms-velocities and temperature contrasts are reaching their maxima, since at the thin photospheric transition region the radiative losses from the upflows generate large entropy fluctuations, which drives essentially convection (see Nordlund et al., 2009, for more details). Further above the convection zone ends, there-

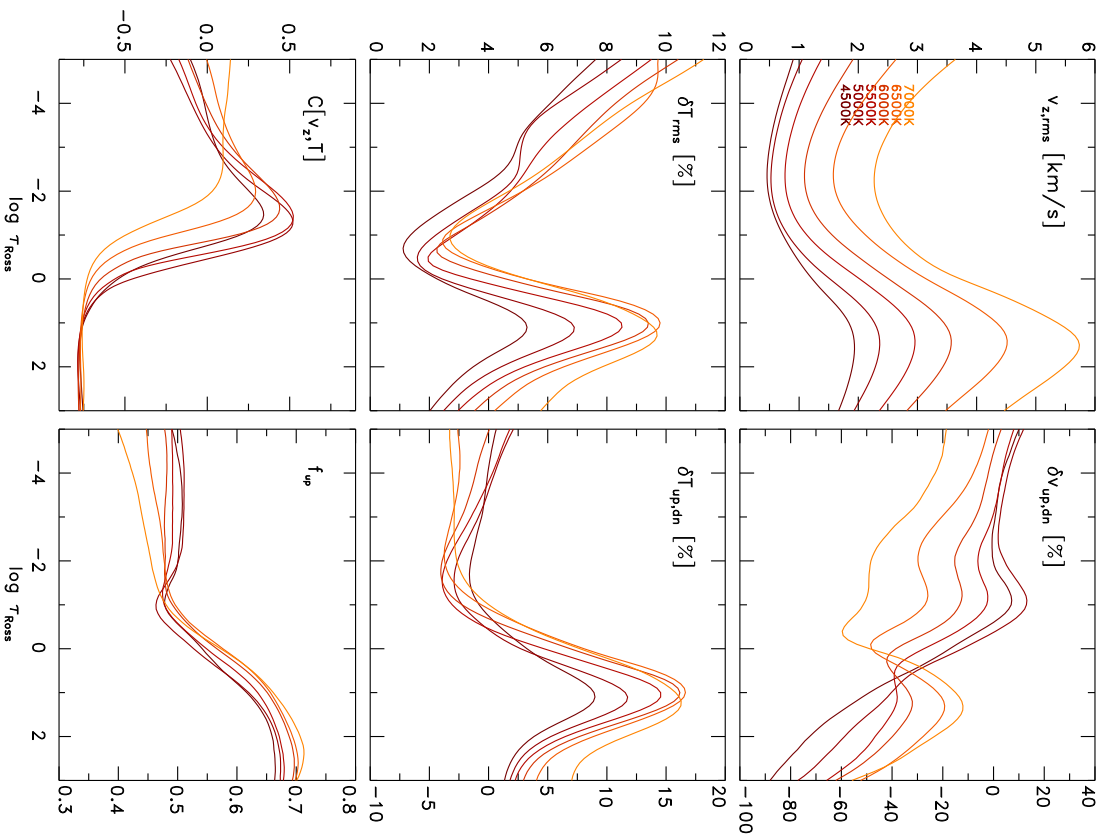


Figure 5.17: The vertical rms-velocity and its asymmetry (top); T -contrast and its asymmetry (middle); correlation function $C[v_z, T]$ and filling factor (bottom panel) shown against the optical depth for models with $\log g = 4.5$ and solar metallicity. The different T_{eff} 's are color-coded (red/orange colors).

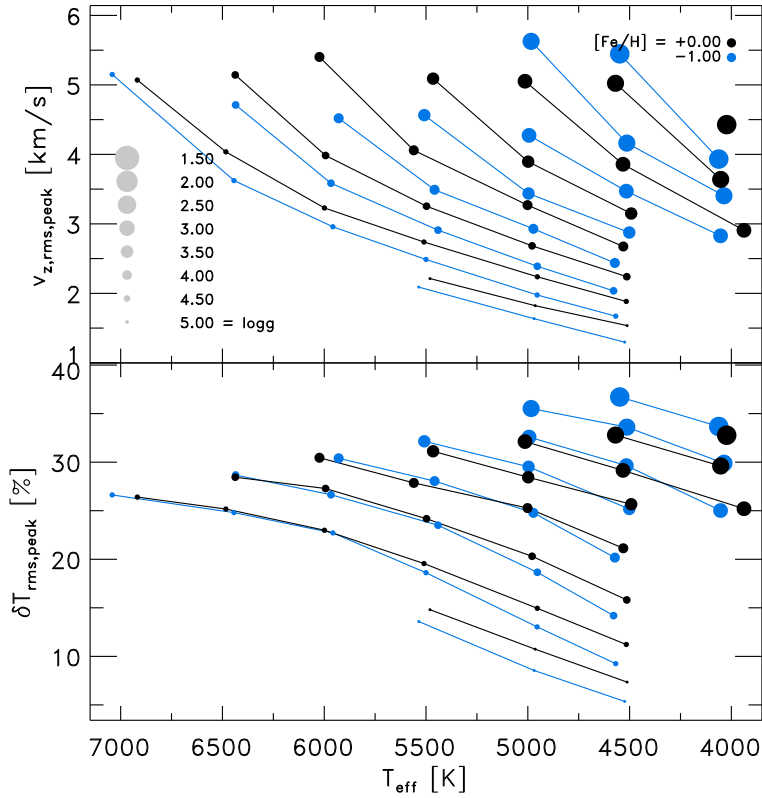


Figure 5.18: Maximal vertical rms-velocity and maximal temperature contrast vs. T_{eff} (top and bottom panel respectively) for different stellar parameters.

fore, $v_{z,\text{rms}}$ and δT_{rms} are declining towards the upper layers. Also, the asymmetries between the up- and downflows in velocity and temperature drop fast, while in convection zone, in particular, the SAR, $\delta v_{\text{up,dn}}$ and $\delta T_{\text{up,dn}}$ are rather large. Furthermore, below the optical surface, one can obtain a tight (anti-)correlation³ between the vertical velocity and temperature due to convective transport of energy, while above the correlation is distinctively smaller (see $C[v_z, T]$ in Fig. 5.17). The convective heat transport is established by the tight correlation between the buoyant upflow that carries the heat-excess to the optical surface. At the optical surface the convection zone ends, therefore the correlation declines towards zero. Due to this one can estimate the extent of overshooting with the zero crossing of the correlation function, $C[v_z, T]$, and for higher T_{eff} 's with concomitant higher velocity the overshooting is clearly reaching into higher layers. On the other hand, the convective properties change obviously with stellar parameters. In order to illustrate this, we depict the maxima of $v_{z,\text{rms}}$ and δT_{rms} in Fig. 5.18 for different stellar parameters. Both of the latter are increasing distinctively for hotter T_{eff} , lower $\log g$ and higher metallicity, in particular, for higher effective temperatures (see Sec. 3.5.1 for a detailed discussion).

Therefore, one finds in general that lines forming in deeper layers carry larger signatures from the velocity field and temperature contrast, i.e. resulting in larger line broadening and Doppler shifts, and in higher layers the opposite is the case. And also the variations of the line shifts and asymmetries with stellar parameters, which we discussed above, are in agreement with the properties in the 3D RHD models.

³The anti-correlation is due to the negative definition of the upwards direction for the vertical velocities.

Chapter 6

Limb Darkening

The emergent intensity across the surface of stars diminishes gradually from the center of the stellar disk towards the edge (limb), since the optical depth depends on the angle of view. Rays crossing the stellar photosphere near the limb reach optical depth unity in layers at higher altitude and at typically lower densities and temperatures than rays crossing the stellar disk near the center. The intensity is very sensitive to the temperature, therefore, one observes darker brightness from the limb, which emerges from higher and cooler regions of the stellar atmosphere. This effect is known as limb darkening. An accurate knowledge of the surface brightness distribution is essential for the analysis of light curves from stars with transiting objects in the line of sight, such as exoplanets and eclipsing stellar companions in binary systems. The variation in surface intensity with angular distance from the stellar disk center is usually expressed in form of limb darkening laws. Multiple functional basis have been used in the past, from simple linear to higher order non-linear laws, in order to fit the surface brightness variations predicted by theoretical model atmospheres leading to so-called limb darkening coefficients (LDC). The individual shape of a transiting light curve is important, because it contains information about the structure of the external layers of the occulted stellar object. The observed light curves are interpreted by comparisons with theoretical transit light curves that are based on limb darkening predictions arising from model atmospheres. More accurate theoretical atmosphere models will reduce the uncertainties in the comparison, and thereby improving the quality of the analysis in favor of other transit-parameters like planet-to-star ratio or the inclination of the orbit. Also, the goodness of the transmission-spectroscopy of exoplanet atmospheres relies on the underlying theoretical atmospheres of the host stars.

The first approximation of the intensity variation over the disk was performed with a simple linear law. However, with theoretical 1D model atmospheres it was shown that a linear law is insufficient to describe the limb darkening of a real star adequately (see van Hamme, 1993). Then, every conceivable alternative with a two-parameter law was introduced starting from a quadratic, over square root to a logarithmic, and finally an exponential law (e.g. see Diaz-Cordoves et al., 1995; Claret et al., 1995). These restricted functional bases are only marginally accurate for a certain range in effective temperatures, therefore, Claret (2000) introduced a new non-linear power law with four coefficients, which is powerful enough to fit the LDC for a broad range in stellar parameters, while conserving the flux to a high accuracy. Later on, limb darkening variations were fitted and provided for the community derived from extensive grids with the latest model atmospheres (ATLAS and PHOENIX) for several broad band filters, e.g. the Sloan (Claret, 2004), Kepler and CoRoT (Sing, 2010). An extensive comparison of the various limb darkening laws has been performed by Southworth (2008). All of these developments revealed that a well-considered choice of an appropriate functional basis is mandatory for a precise description of the intensity variations.

The next step in improving the systematic errors prevailing in the predicted limb darkening laws, hence transit light curves, was yielded in the underlying model atmospheres, since the limb darkening is mainly determined by the temperature gradient (see Knutson et al., 2007; Hayek et al., 2012). Therefore, flaws in the theoretical atmospheric temperature stratification will directly propagate into the predicted limb darkening. The hydrostatic 1D models make use of several simplifications, the most prominent one being the use of the mixing length theory to account for convective energy transport (Böhm-Vitense, 1958). Cool late-type stars feature a convective envelope, thereby convective motions are present in the thin photo-

spheric transition region due to overshooting of convective flows. These stars exhibit a typical granulation pattern in its emergent intensity due to inhomogeneities arising from the asymmetric up- and downflowing stellar plasma. Therefore, only 3D atmosphere models are able to predict these properties accurately. With the advent of 3D atmosphere modeling (Nordlund, 1982), which solves from first-principle the hydrodynamic equations coupled with a realistic radiative transfer, the deficiencies of the 1D models were revealed and quantified (see the review by Nordlund et al., 2009). Comparisons of the 3D models with the Sun showed that these models can predict rather accurately the intensity distribution (Pereira et al., 2013), while 1D models overestimate the limb darkening of our resolved host star. Bigot et al. (2006) studied the limb darkening of α Centauri B by comparing its interferometrically observed visibility curves with theoretical predictions. The latter is sensitive to the limb darkening, and they found a significant improvement with the predictions from 3D models. Furthermore, Hayek et al. (2012) showed on the basis of the extremely accurately measured light curves of the transiting exoplanet HD 209458 that the intrinsic residuals of the 1D models can be resolved with the more realistic 3D model atmospheres. The largest differences were found close to the limb, hence during the ingress and egress of the transition. With 1D model predictions, the well-studied close-orbit Jupiter-like transit planet HD 209458 exhibited priorly systematic residuals due to the simplified treatment of convection leading to insufficient temperature stratifications (see Knutson et al., 2007). Furthermore, Chiavassa et al. (2010) derived interferometric visibility amplitude and phase predictions from synthetic stellar disk images, including the center-to-limb variation, based on 3D RHD simulations for four K giants. They conclude that the stellar granulation pattern is affecting the observed visibility curves and closure phases, therefore, 3D corrections should be considered in interferometric studies. Chiavassa et al. (2012) compared a 3D model with interferometric observation from another well-studied star, Procyon, and the resulting stellar diameter prediction from the 3D RHD simulation is supported by additional independent asteroseismic estimation.

After the first detection of a Jupiter-like extra solar planet through radial velocity detection (Mayor & Queloz, 1995), five years later, eventually a transiting exoplanet around a solar-like star was also found (Charbonneau et al., 2000). These spectacular landmark discoveries triggered literally a gold-rush in the hunt for new exoplanets. With advanced satellite missions, like Kepler and CoRoT, nowadays up ~ 230 transiting extra solar planets have been detected. Both of the mentioned satellite missions operate in the visible spectral range, therefore, the effects of limb darkening are strong. These sophisticated observations evoke rightfully a demand in more accurate theoretical limb darkening predictions. In order to fulfill this call, we present in this work LDCs derived from realistic full 3D synthetic spectra based on a comprehensive grid of 3D RHD atmosphere models.

In this Chapter I want to address the following key question: how large are the differences in the predictions of theoretical limb darkening laws between the 3D and 1D models? The search for exoplanets is currently a very active field and relies on optimal theoretical limb darkening predictions, therefore, deriving these states an important application for the 3D RHD atmosphere models. In the following, I will introduce the different limb darkening laws (Sect. 6.1), and discuss the resulting limb darkening coefficients (Sect. 6.2). Furthermore, I will discuss the resulting predicted transit light curves (Sect. 6.3), and the differences in the limb darkening compared to previous 1D predictions (Sect. 6.4).

The discovered differences are largest at the limb between the 1D and 3D models due to the differences in the temperature gradients, however, the resulting differences in the transit light curves are very small. Nonetheless, in high-precision observed transit light curves, the differences can be measured as shown by Hayek et al. (2012). Furthermore, the use of an insufficient limb darkening law is leading to incorrect matches with strong deviations at the limb, therefore, we advise the use of the four-parameter law by Claret (2000).

6.1 Deriving the limb darkening

Based on the 3D RHD models from the STAGGER-grid, we computed a comprehensive library of full 3D synthetic spectra. Therefore, we used the OPTIM3D-code (see Chiavassa et al., 2009, 2010, for further details), which is a post-processing 3D radiative transfer code that assumes local thermodynamic equilibrium ($S_\lambda(T) = B_\lambda(T)$). The code considers the realistic velocity field due to convective motions present

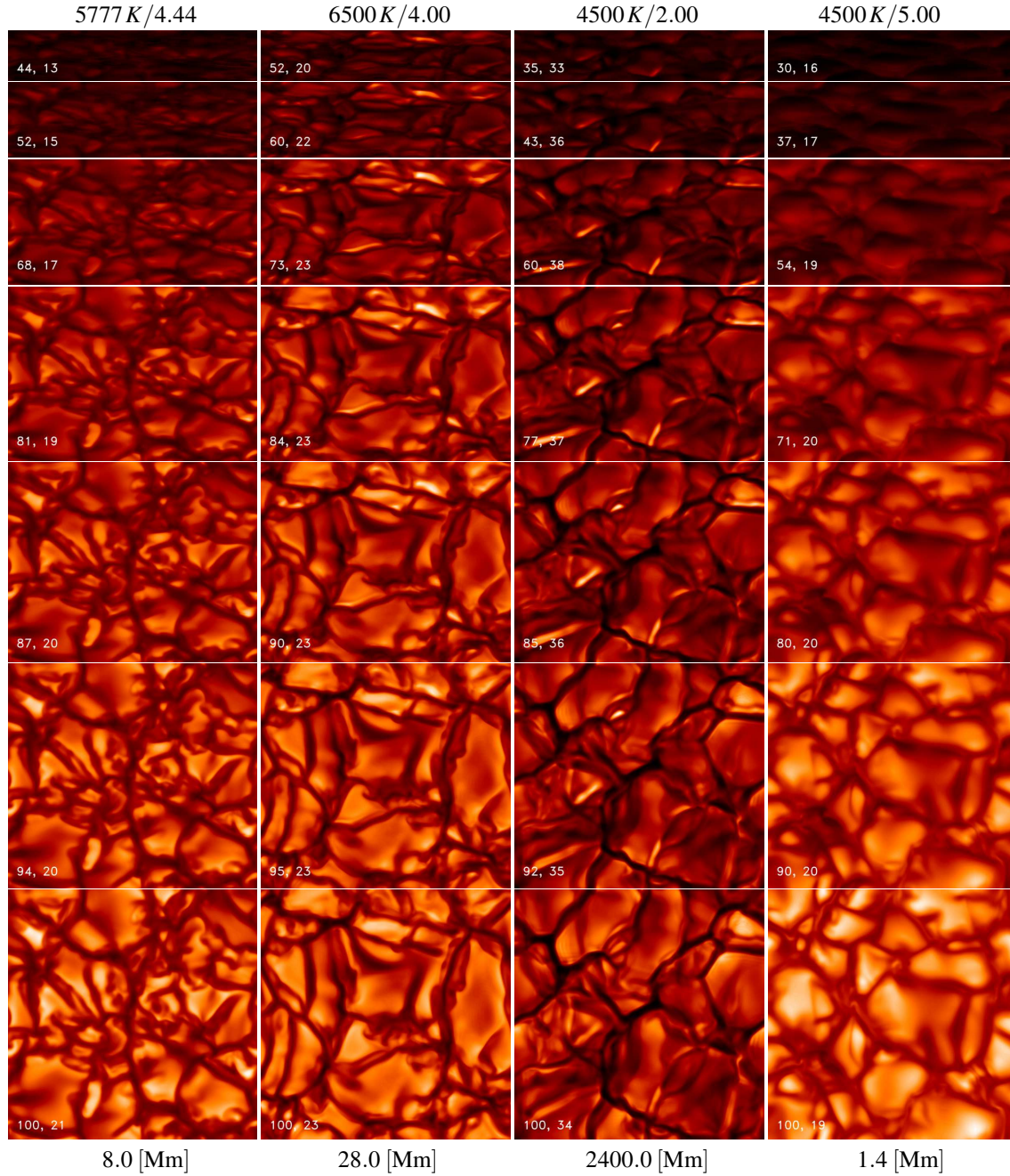


Figure 6.1: The emergent monochromatic intensity at 500nm shown for eight μ angles: 0.2, 0.3, 0.5, 0.7, 0.8, 0.9, 1.0 (from top to down, respectively) and for a selection of stars: main-sequence, turnoff, K-giant, K-dwarf (from left to right, respectively) with solar metallicity. Furthermore, we indicated the normalized mean intensity and the intensity contrast (both in percent).

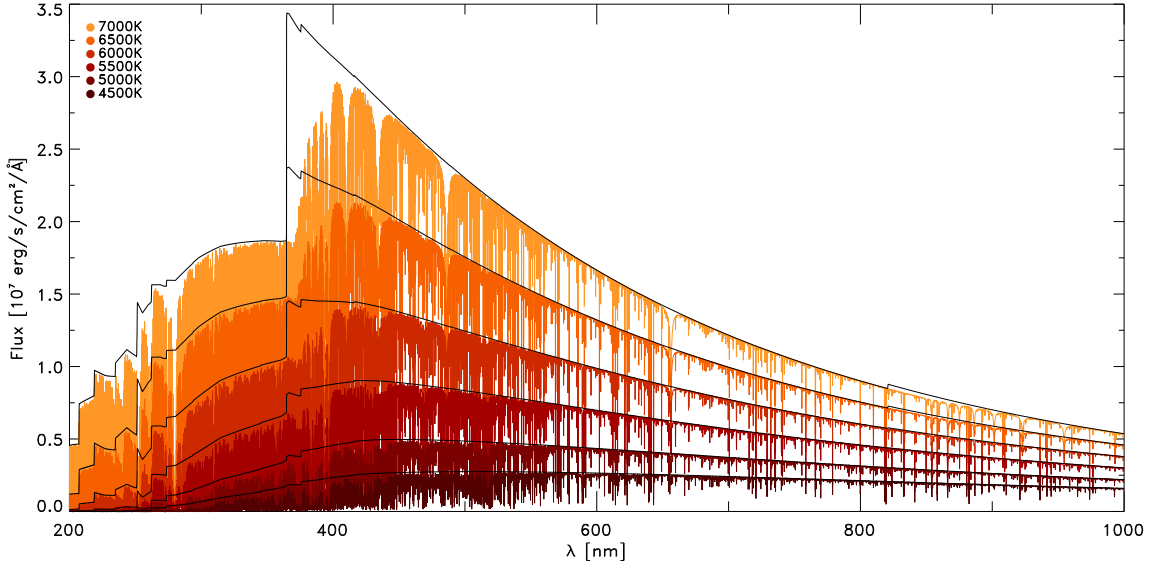


Figure 6.2: Spectral energy distribution vs. wavelength for models with $\log g = 4.5$, $[\text{Fe}/\text{H}] = 0.0$ and various T_{eff} (red/orange colors). The continuum flux is also shown (solid black).

in the 3D RHD simulations, thereby taking Doppler broadening and shifts into account. OPTIM3D employs pre-tabulated extinction coefficients, which are the same as in the MARCS code, thereby accounting for continuous and sampled line opacities (Gustafsson et al., 2008). We assumed the latest solar composition by Asplund et al. (2009) consistently in OPTIM3D as in the 3D RHD simulations performed with the STAGGER-code. In contrast to the RHD-code, the spectral synthesis code computes the large number of wavelength points with $N_\lambda = 105767$ explicitly, thereby raising the computational costs enormously. We achieve a wavelength resolution with a constant sampling rate of $\lambda/\Delta\lambda = 20000$, however, we cover a broad range with $\lambda = 1010.0$ to 199960.0\AA . We apply $N_t = 10$ snapshots for each simulation, while we keep the horizontal mesh resolution fixed with $N_{xy} = 240$. Four (equidistant) azimuthal ϕ -angles are considered ($N_\phi = 4$), while the center-to-limb resolution is resolved higher with nine μ -angles besides the disk-center ($\mu = 0.01, 0.05, 0.10, 0.20, 0.30, 0.50, 0.70, 0.80, 0.90, 1.00$). As shown by Hayek et al. (2012) the numerical resolution of our 3D RHD models and the resolution for the spectral flux computations are sufficient to predict realistic observed limb darkening laws accurately. The synthetic spectra will be discussed in a separate work (Chiavassa et al. in perp.).

We show an overview of spatially resolved intensity maps with different inclined μ angles for a selection of distinct stellar parameters (see Fig. 6.1). These exhibit the typical granulation pattern of cool stars due to convection. The bright, bulk regions are the hotter upflowing granules, which are interspersed with the dark intergranular downdrafts. From the disk-center towards the limb, the brightness is diminishing significantly, and the intensity contrast is also slightly dropping. Moreover, one can also obtain that bright features are often highly angle dependent.

In Fig. 6.2, we show a subset of the resulting averaged synthetic fluxes in the range $2000 - 10000\text{\AA}$ for a number of dwarfs with solar metallicity. Furthermore, we show also the continuum fluxes as well, and one can discern spectral absorption features, the prominent one being the Balmer lines (indicated in the figure). For higher T_{eff} the continuum flux is increasing, while individual spectral absorption features are changing as well.

The variation of the inclination of the line of sight from the disk-center is parameterized with the projected polar angle, $\mu = \cos\theta$, where θ is the angle between the line of sight and the direction of the emergent radiation. Therefore, the disk-center is depicted with $\mu = 1$, while $\mu = 0$ is the limb. The limb darkening law is expressed as the variation in intensity with μ -angle that is normalized to the disk-center, i.e. $I(\mu)/I(1)$. The resulting monochromatic intensity depends on the horizontal position x and y , the viewing angles ϕ and μ and the time, t , thus $I_\lambda(x, y, \mu, \phi, t)$. In order to yield the mean monochromatic

Table 6.1: The precision of the functional fits for the different limb darkening laws (see text for details).

Value	Lin	Quad	Sqrt	Log	Three	Four
χ^2	1.53	1.20	0.72	13.38	2.13	2.35×10^{-6}
$\max \delta$	1.20	1.79	1.56	2.00	1.37	1.65×10^{-3}
$\bar{\mu}$	0.07	0.05	0.05	0.08	0.06	0.10

intensity $\langle I_\lambda \rangle(\mu)$ from the latter, we average the intensity first spatially, then over the azimuthal angles, and finally over all time steps, i.e.

$$\langle I_\lambda \rangle(x, y, \mu, \phi, t) = \frac{1}{N_t} \sum_t \frac{1}{N_\phi} \sum_\phi \frac{1}{N_x N_y} \sum_{x, y} I_\lambda(x, y, \mu, \phi, t).$$

As next, we compute the inclination-dependent total emergent intensity $I(\mu)$ by integrating the mean monochromatic intensity $\langle I_\lambda \rangle$ over all wavelength points with

$$I(\mu) = \int \langle I_\lambda \rangle(\mu) d\lambda.$$

Then, the total surface brightness variation can be easily derived by normalizing the angular intensities with the disk-center value, I_μ/I_1 , and we can fit the various (bi-parametric) functional bases,

$$I_\mu/I_1 = 1 - u(1 - \mu), \quad (6.1)$$

$$I_\mu/I_1 = 1 - a(1 - \mu) - b(1 - \mu)^2, \quad (6.2)$$

$$I_\mu/I_1 = 1 - c(1 - \mu) - d(1 - \sqrt{\mu}), \quad (6.3)$$

$$I_\mu/I_1 = 1 - e(1 - \mu) - f\mu \ln \mu, \quad (6.4)$$

$$I_\mu/I_1 = 1 - g(1 - \mu) - h/(1 - e^\mu), \quad (6.5)$$

which are the linear (Eq. 6.1), quadratic (Eq. 6.2), square root (Eq. 6.3), logarithmic (Eq. 6.4) and exponential (Eq. 6.5) limb darkening law. Also the three-parameter non-linear limb darkening law,

$$I_\mu/I_1 = 1 - a_2(1 - \mu) - a_3(1 - \mu^{3/2}) - a_4(1 - \mu^2), \quad (6.6)$$

introduced by Sing (2010) is also considered. However, we recommend the use of the standard four-parameter non-linear functional basis (Eq. 6.7) introduced by Claret (2000), which is the default limb darkening law in the present study. The four-parameter power law is the fourth order Taylor-series expansion in $\mu^{1/2}$ given by

$$I_\mu/I_1 = 1 - \sum_{k=1}^4 a_k \left(1 - \mu^{k/2}\right), \quad (6.7)$$

This functional basis conserves the flux to better than 0.05% (see Claret, 2000). In order to fit the LDC, we applied the Levenberg-Marquardt least-square minimization, since Claret (2000) showed that this fitting method performs best.

To illustrate the performance of the individual functional basis we show in Fig. 6.3 (top panel) the limb darkening laws of the solar simulation seen in the Kepler filter. The two-coefficient laws are obviously rather inadequate and show the largest deviations at the limb ($\mu \sim 0.0$), in particular the linear, quadratic, logarithmic and exponential law (Eqs. 6.1, 6.2, 6.4 and 6.5), while the square root law (Eq. 6.3) exhibits a rather good match (it is already known that the square root law performs better for hotter stars, while for cooler stars the quadratic law is better see Claret 2000). The three-parameter functional basis (Eq. 6.6) is performing well, however, it mismatches the limb rather significantly. The standard four-parameter non-linear power law (Eq. 6.7) is an excellent functional basis, and due to its versatility the fits result in

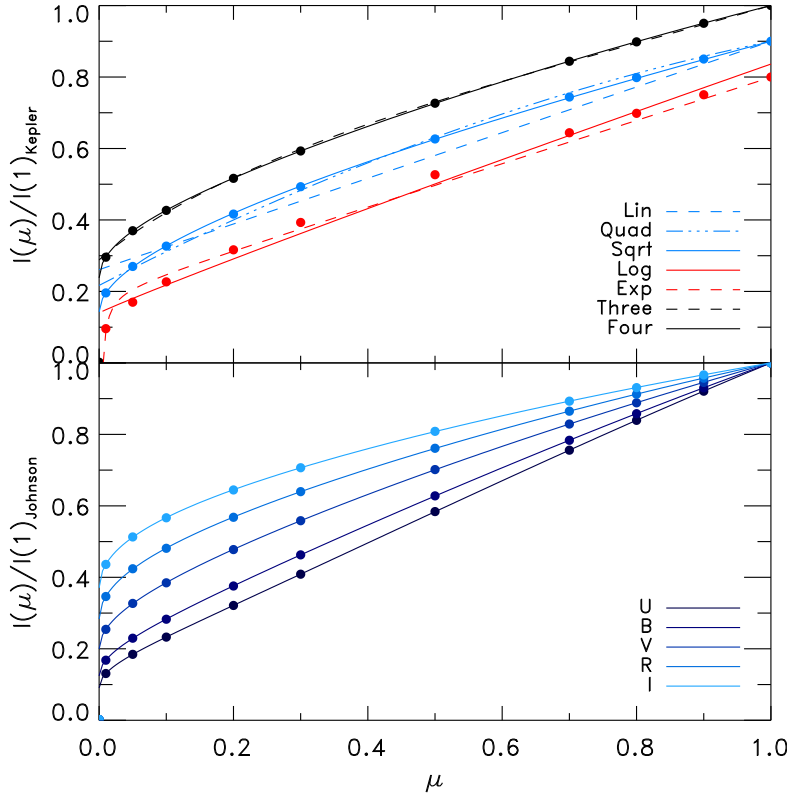


Figure 6.3: Solar intensity distribution vs. μ -angle for different limb darkening laws in the Kepler filter (top) and different bands from the Johnson filters (bottom panel). The 3D results are indicated with filled circles. In the top panel the blue and red lines are shifted by 0.1 and 0.2 respectively, while the black lines are unshifted.

extreme small residuals. In order to depict the precision of the individual laws quantitatively, we list the average χ^2 , average maximal relative deviation and average location of the latter from all stellar models in Table 6.1. The four-parameter law performs for all stellar parameters significantly much better than any other limb darkening law, therefore, we will discuss subsequently the latter only.

We consider a number of broad band filters b by convolving the response function S_λ , which considers the transmission of the filter b , with the integration of the intensity,

$$I_b(\mu) = \int S_\lambda \langle I_\lambda \rangle(\mu) d\lambda.$$

We applied multiple standard broad band filters taken from the SYNPHOT package¹, which comprises Bessel (JHK), Johnson (UBVRI) and Stroemgren (uvby). Additionally we considered individual important instruments with CoRoT, Kepler², Manua Kea (JHKLM), Sloan survey (SDSS, ugriz) and HST (ACS, STIS). In Fig. 6.3 (bottom panel) we show the five different Johnson filters for the solar model. The brightness distribution and its curvature are becoming more enhanced towards higher wavelength from the ultra-violet to the infra-red, which is a general feature for all stellar parameters. The optical depth and the temperature gradient are dependent on the considered wavelength, since radiation at higher wavelength is emerging from higher geometrical depth.

6.2 The resulting limb darkening predictions

The radiation at disk-center emerges from lower depths, while towards the limb one observes light from higher layers, where the temperature stratification has dropped very quickly, hence lower (darker) brightness ($I \propto T^4$). We mention that the limb darkening has obvious boundary constraints being that the intensity

¹<http://www.stsci.edu>

²<http://keplergo.arc.nasa.gov/>

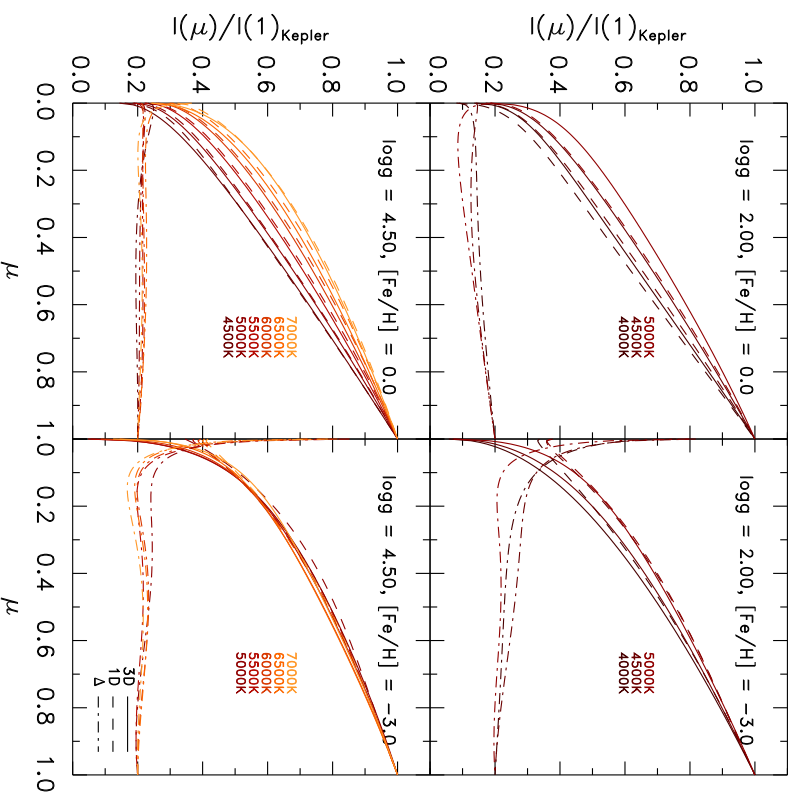


Figure 6.4: Disk-center normalized intensity, $I(\mu)/I(1)$, against the inclination, μ , in the Kepler filter showing the limb darkening for different stellar parameters. Furthermore, we illustrate also the 1D ATLAS predictions for comparison (dashed lines), and the deviations $\Delta = 1D - 3D$ (dashed dotted lines), which are enhanced by a factor of 2 and shifted by +0.2 for clarity.

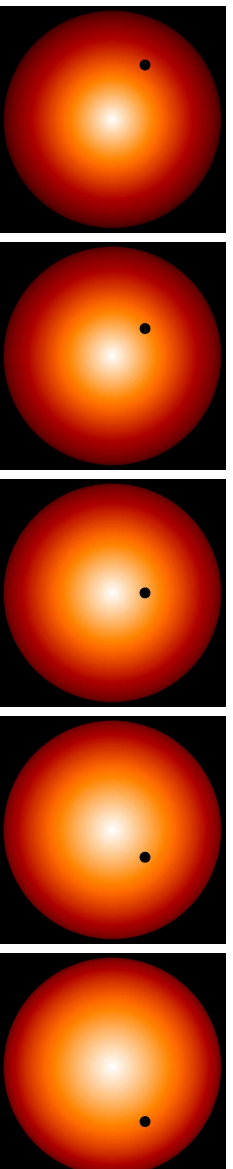


Figure 6.5: Synthetic stellar disks for stars with $\log g = 4.5$, $[\text{Fe}/\text{H}] = 0$, and increasing T_{eff} from 4500K to 6500K (from left to right) seen in the Kepler filter, and including a transiting exoplanet with $p = 0.05$ with progressing transit phase. Note the brighter limb towards higher T_{eff} .

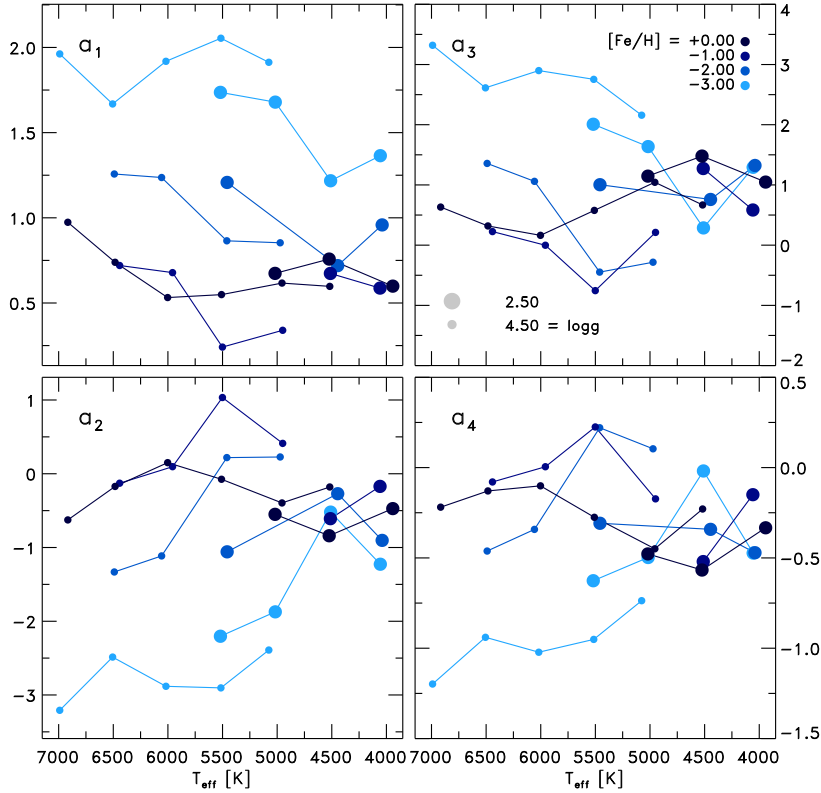


Figure 6.6: The four coefficients for the four-parameter non-linear limb darkening law (Eq. 6.7) predicted in the Kepler filter from 3D RHD models for different stellar parameters.

is maximal with $I(\mu = 1) = 1$ and minimal with $I(\mu = 0) \simeq 0$. Furthermore, we note briefly that the variation of the limb darkening with stellar parameter depends also on the considered filter, and the results can differ significantly (see Fig. 6.3).

In Fig. 6.4, we show an overview of different limb darkening variations for various stellar parameters. One finds in general that the variations are rather smooth and systematic, and the largest differences are given close to the limb ($\mu \sim 0.2$), however, the variations with T_{eff} and $\log g$ are distinctive for different metallicities. For higher T_{eff} the decline in brightness exhibits a more pronounced convex curvature between $\mu = 0.2 - 0.7$, while at cooler ones it is close to a linear drop. Therefore, hotter models end up with brighter intensities towards the limb around $\mu \sim 0.2$ and a steeper drop beyond. For instance for dwarfs with solar-metallicity we find $I_{0.2}/I_1 = 0.4 - 0.6$ for $T_{\text{eff}} = 4500 - 7000$ K. In order to illustrate the relative brightening at the limb for hotter dwarfs with solar metallicity, we show synthetic stellar disks in Fig. 6.5 with higher T_{eff} . Towards giants (lower $\log g$) the brightness is higher than for dwarfs, however the changes are more subtle compared to the effective temperature. At lower metallicity, we find the differences with T_{eff} between metal-poor dwarfs ($\log g = 4.5$, $[\text{Fe}/\text{H}] = -3$) being distinctively smaller, so that a pronounced curvature is given even for the coolest effective temperature (compare bottom panels in Fig. 6.4). In fact, we find basically no increase with T_{eff} around $\mu \sim 0.2$ ($I_{0.2}/I_1 = 0.59 - 0.61$). As we show further down, the T -insensitivity of the limb darkening at $[\text{Fe}/\text{H}] = -3$ arises due to the temperature gradient. Claret (2000) had also found an enhanced curvature at lower metallicity with 1D models. The hottest and most metal-poor dwarfs are the brightest at the edge, and the sharp drop is the steepest. Furthermore, we note that the center-to-limb variation curves for metal-poor models cross the corresponding ones for solar-metallicity models with otherwise the same stellar parameters (T_{eff}), with the exception of the models at high T_{eff} , however, this is not the case towards higher T_{eff} . On the other hand, the metal-poor giants are more similar to the solar-metallicity case, and exhibit also a clear T_{eff} sensitivity.

As next, we want to discuss the individual coefficients for the four-parameter limb darkening law (Eq. 6.7). Therefore, we show in Fig. 6.6 the four coefficients for different T_{eff} and $[\text{Fe}/\text{H}]$ and $\log g = 4.5, 2.0$. Towards higher T_{eff} both coefficients, a_2 and a_4 , are increasing until 6000 K, then above they decrease,

while the coefficients a_1 and a_3 vary the opposite at solar metallicity. For lower $[\text{Fe}/\text{H}]$ the T -dependence is inverted for a_k and the even coefficients, a_2 and a_4 , are decreasing, and the odd ones, a_1 and a_3 , are increasing. Another aspect worthy of attention is the correlation between the coefficients with half-integer exponents in μ (a_1 and a_3), and integer one (a_2 and a_4) with T_{eff} and $[\text{Fe}/\text{H}]$ (compare left with right panels in Fig. 6.6). In the Kepler filter we find the correlations to amount with $C[a_1, a_3] = 0.82$ and $C[a_2, a_4] = 0.91$ for all stellar parameters. Furthermore, the half-integer exponents anti-correlate with the integer ones (compare top with bottom panels in Fig. 6.6). While the distant coefficients are less anti-correlated with $C[a_1, a_4] = -0.76$, we find the anti-correlation between the successive coefficients being much tighter with $C[a_1, a_2] = -0.95$ and $C[a_3, a_4] = -0.99$. Claret (2000) noted also correlations between the coefficients. The coefficients a_k of the four-parameter law can be decomposed and considered individually. Then the integer exponents with the coefficients a_2 and a_4 are leading to a linear and quadratic polynomial respectively, which are describing the general slope of the limb darkening. On the other hand, the half-integer exponents with the coefficients a_1 and a_3 are square root like functions, and are responsible for the curvature towards the limb.

The coefficient u for the linear limb darkening law (Eq. 6.1) is rather crude, however, it has the major advantage of simplicity, since the linear law reduces the complex shape of the limb darkening into a single value. We display in Fig. 6.7 u against T_{eff} for different stellar parameters (top panel). A larger value in u relates to a steeper drop in intensity and indicate lower brightness at the limb, and a lower value for u results in brighter limbs (see Eq. 6.1). The coefficient u is mainly sensitive to the effective temperature and is decreasing with higher T_{eff} , and for different $\log g$ and $[\text{Fe}/\text{H}]$ the differences are rather small. As a remark we note that the linear coefficients a and c from Eqs. 6.2 and 6.3 are similar, while the quadratic and square root coefficients, b and d , behave oppositely and increase for higher T_{eff} (not shown). The values for u ranges from 0.56 to 0.77 in the Kepler filter, which would yield $I = 0.44$ and 0.23 at the limb ($\mu = 0$) respectively (the global range in u is from 0.03 to 1.05).

With a linear approximation of the Planck function one can derive the slope of the linear limb darkening law, u (e.g. Gray, 2005; Hayek et al., 2012), which depends primarily on the temperature gradient at the optical surface and is given by

$$u'_\lambda \approx \frac{\log e}{B_\lambda(T(\tau_\lambda = 1))} \frac{dB_\lambda}{dT} \Big|_{\tau_\lambda=1} \frac{dT}{d \log \tau} \Big|_{\tau_\lambda=1} \quad (6.8)$$

The approximation implies that a steeper temperature gradient at the optical surface will lead to stronger (steeper) limb darkening (larger u). In Fig. 6.7 (middle panel) we show also $u'_{500\text{nm}}$ considered at the optical surface ($\tau = 1$) vs. T_{eff} , and we find $u'_{500\text{nm}}$ to correlate well with u (top panel). Also, similar as given in u , we find $u'_{500\text{nm}}$ being T -insensitive for dwarf models with very low metallicity ($[\text{Fe}/\text{H}] = -3$), which arises from the temperature gradient term $dT/d \log \tau_\lambda$ in Eq. 6.8. The intensity is given by the source function and the lost radiation, which is stated by the radiative transfer eq., $dI_\lambda/d\tau_\lambda = S_\lambda - I_\lambda$. And under the assumption of LTE, the source function can be approximated with the Planck function at the local temperature, $S_\lambda(T) = B_\lambda(T)$. Therefore, the variation of the intensity with μ is sensitive to the temperature structure and in particular the temperature gradient. In Fig. 6.7 we show also the temperature gradient, $\vec{\nabla} = d \ln T / d \ln p_{\text{tot}}$, considered at the optical surface (bottom panel). For lower metallicity the range in temperature gradient is enhanced, which is very similar to the intensity contrast. We had already mentioned the enhancement of the intensity contrast and temperature gradient at lower metallicity in Sect. 3.1.5. We find the reason for the enhancement being the lack of metals that are usually the most important electron donors for the formation of H^- , which is the dominating opacity source (see Nordlund & Dravins, 1990). Therefore, in metal-poor models, the main contribution of electrons arises from the ionization of hydrogen. This is the reason for the strong enhancement of the temperature gradient towards $T_{\text{eff}} = 6000\text{K}$ with $[\text{Fe}/\text{H}] = -3$, which is the reason for the T -insensitivity of u and the limb darkening that we found for metal-poor dwarfs (see Fig. 6.4).

6.3 Transit light curves

During exosolar planet transits the planet eclipses its host star in the line of sight to earth, thereby diminishing the emergent intensity and leaving a characteristic imprint in the observed light curve. Theoretical

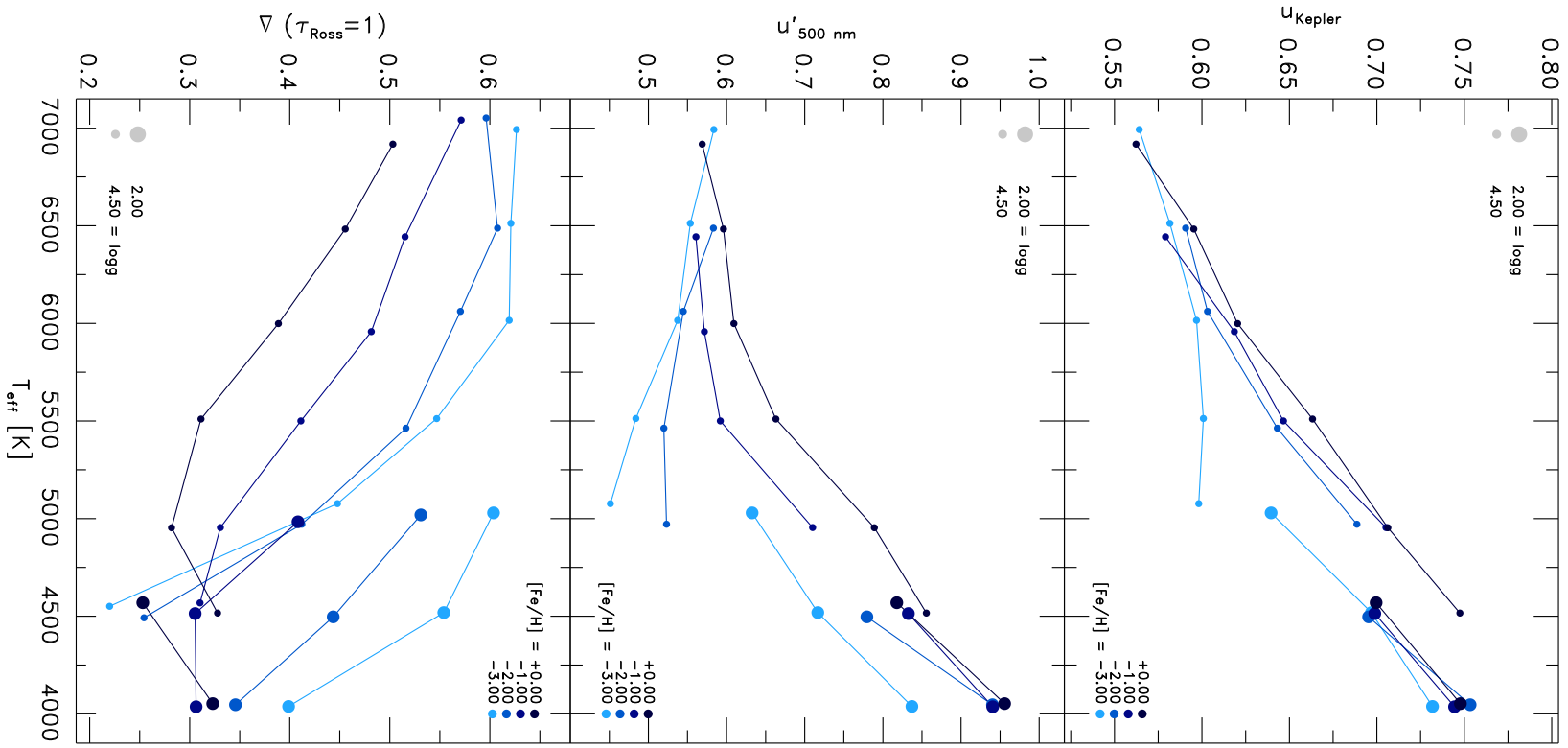


Figure 6.7: The coefficient u of the linear limb darkening law (Eq. 6.1) in the Kepler filter (top) and the approximation $u_{500\text{nm}}$ from Eq. 6.8 (middle) and temperature gradient at the optical surface (bottom panel) vs. T_{eff} for $\log g = 2.0, 4.5$ and different $[\text{Fe}/\text{H}]$.

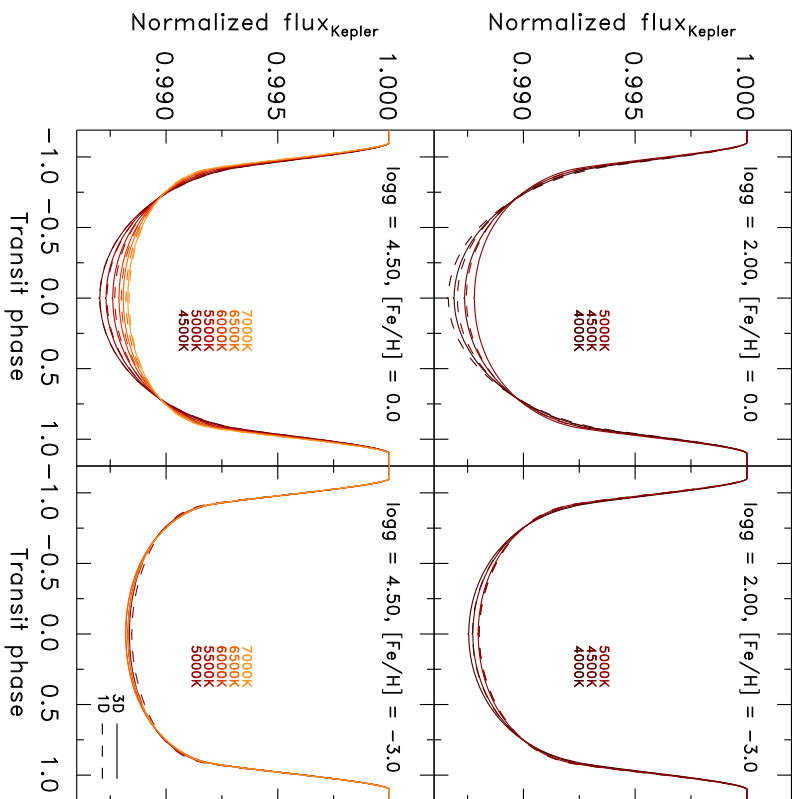


Figure 6.8: Transit light curve vs. transit phase with $p = 0.1$ in the Kepler filter for different stellar parameters. The predictions from the 1D ATLAS models are also included (dashed lines).

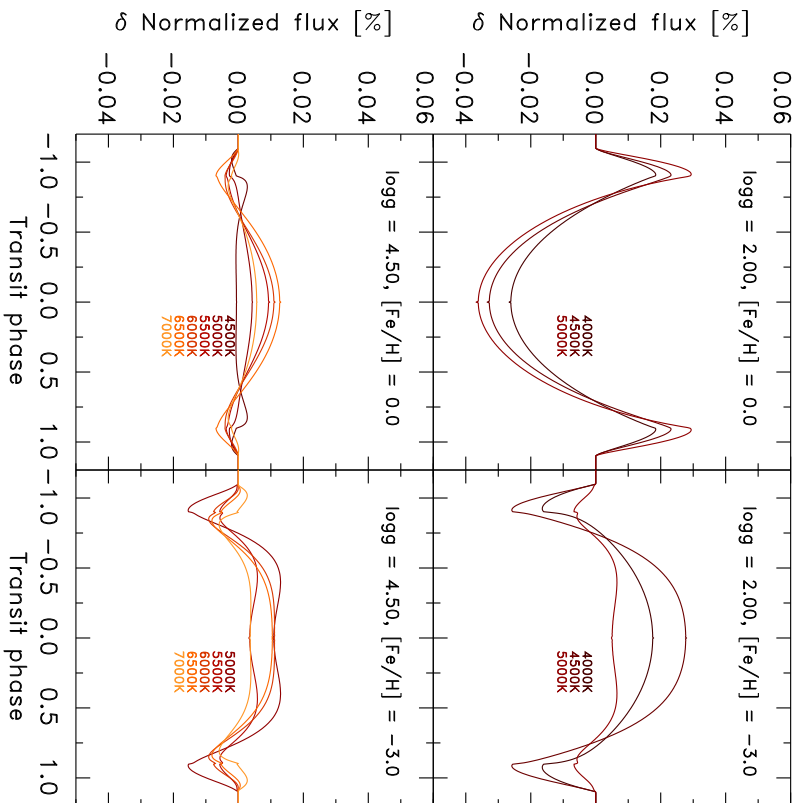


Figure 6.9: Relative deviations in the the transit light curve with $p = 0.1$ between 3D atmosphere models and 1D ATLAS models given in %. The difference is $\delta = 1D/3D - 1$.

light curve predictions are described by two main parameters, namely the ratio of the radii of planet and parent star, $p = r_{\text{planet}}/r_{\text{star}}$, and the normalized separation of the centers, $z = d/r_{\text{star}}$, with d being the center-to-center distance of the two occulting bodies. For computing the theoretical transit light curves, we used the publicly available code by Mandel & Agol (2002). In Fig. 6.8, we show light curves with $p = 0.1$, i.e. for the case that the radius of the planet is 1/10 of the star, in the Kepler filter for the same LDC as discussed in Sec. 6.2. Then one can extract that the dwarfs with solar-metallicity exhibit for higher T_{eff} light curves with a more rectangular shaped feature, where the transit center is shallower and the width of the transit is broader than lower T_{eff} . The giant models show similar features with T_{eff} for both [Fe/H]. On the other hand, the metal-poor dwarfs are similarly box-shaped and do not vary much for lower effective temperatures. The limb of the intensity distribution will shape the ingress and egress of the light curve, e.g. when the limb darkening would be a step function ($a_2 \simeq 0$ and $a_k = 0$), then the light curve would be entirely rectangular. A straight linear dropping intensity distribution ($a_2 = 1$ and $a_k = 0$) results in a more elliptical shape with a narrow width, while a curved square root drop ($a_1 = 1$ and $a_k = 0$) would lead to an evenly circular shaped light curve. Therefore, we caution for the use of limb darkening laws that are incapable of rendering the drop-off at the limb, such as the bi- and three-parametric laws, since these will introduce inevitably systematic errors in the theoretical transit light curves. Mandel & Agol (2002) found in a comparison between the quadratic and the four-parameter non-linear power law (with $p = 0.1$) differences by 3%! Furthermore, the depth of the transit light curve depends primarily on the ratio of planet to host p . For larger p the light curves are increasingly deeper at the center, since more stellar light is effectively blocked during the transition due to a larger surface ratio of the planet. The limb darkening is also sensitive to the considered wavelength-regime (see Fig. 6.3). Therefore, the transit light curve will be different depending on the actual considered broad band filter, which samples its specific range in λ . We find in general that the light curve is towards shorter wavelength (ultra-violet) systematically more convex shaped with a deeper center and more slender width, while towards longer wavelength (infra-red) the light curve is more box-shaped with shallower centers and broader width. We note that a multi-band photometry approach states a solution to this issue (see Knutson et al., 2007).

6.4 Comparison with results from 1D models

The ATLAS models are the widest applied 1D atmosphere models for retrieving LDC, since its grid covers the broadest range in stellar parameters leading to seamless coverage. The differences between the 1D and 3D models arise mainly from the differences in the temperature stratification, in particular the temperature gradients.

For the comparison we show in Fig. 6.4 also the limb darkening derived from 1D MLT models from the ATLAS grid (see Sing, 2010). To ensure consistency the four-parameter non-linear laws for 1D models are also shown in the Kepler filter. The 1D dwarf models with solar metallicity exhibit similar increasing curvatures for higher T_{eff} as given by the 3D models, only the 1D models are slightly brighter than the 3D, except for the coolest one (4500 K). In the case of giants the 1D limb darkening is distributed at much lower and also more linear intensities. The limb of the metal-poor 1D models lacks of a similar smooth sharp drop-off that is given in the 3D models, instead they depict a rather discontinuous behavior at the limb, which is doubtful to be correct. For metal-poor models it is known that the enforcement of radiative equilibrium is leading to an overestimation of the temperature stratification in the upper layers due to lack of spectral line absorption (see Asplund et al., 1999b; Collet et al., 2007). The radiation at the limb is emerging from higher layers, therefore, the deviations at the limb are consistent (see Sect. 3.2.1).

The largest deviations are usually found at the limb, since some of the 1D models depict an almost linear run at the edge, while the 3D models exhibit a comparably smooth drop-off at the limb. In Figure 6.10, we show the deviations at the limb, $\Delta I_0/I_1$, between the 1D and 3D limb darkening predictions. The differences increase significantly towards lower metallicity. Therefore, we advise the use of 3D limb darkening coefficients, in particular, for interferometric observations of metal-poor stars.

We display the relative differences in the transit light curve between the 3D and 1D predictions in Fig. 6.9. Similar to the findings of Hayek et al. (2012), we find a characteristic shape in the residuals with two extrema that are usually of opposite sign. One being at the ingress and egress phase, which arises from differences at the limb, and the other one taking place at the disk-center. We found in Sec. 6.2 the 1D

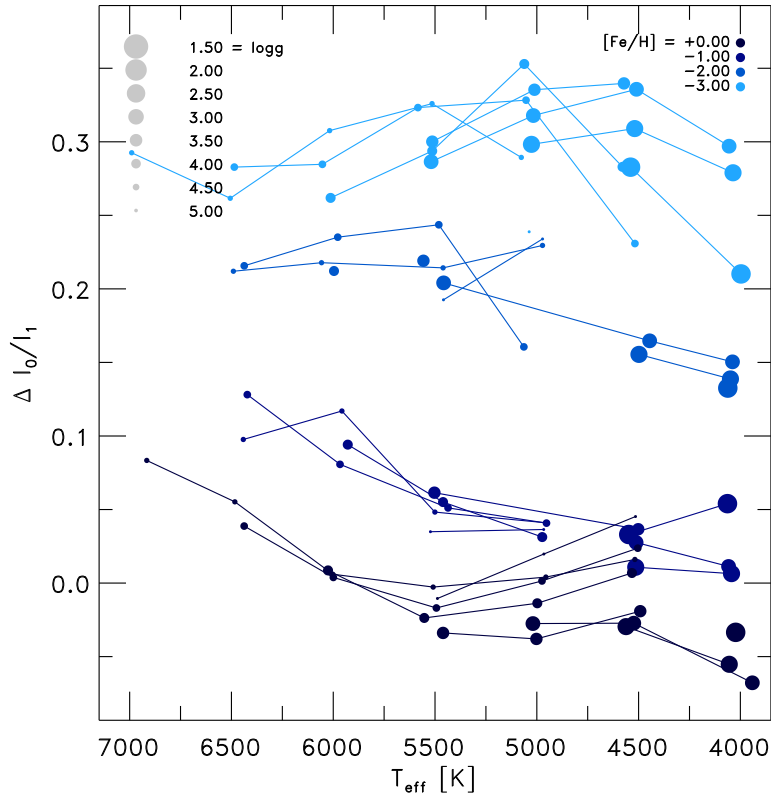


Figure 6.10: Overview of the maximal relative difference in the limb darkening compared between 1D and 3D against T_{eff} with the Kepler filter. The relative deviations are retrieved by $\Delta = 1\text{D} - 3\text{D}$.

models being brighter than the 3D limb darkening, except for the giants at solar-metallicity. The transit light curves for the 1D models are a similarly brighter at the disk-center and dimmer at the transit phase edges for all models, only for the solar-metallicity giants it is the opposite. However, the maximal residuals are relatively small with a global maximum of $\sim 0.04\%$ in the transit light curve.

Chapter 7

STAGGER-grid and 1D models

To account for the convective energy transport Böhm-Vitense (1958) formulated the mixing length theory (MLT), which was initially proposed by Ludwig Prandtl in analogy to the concept of the mean free path in the kinetic gas theory. In the framework of MLT, it is assumed that the heat flux is carried by *convective elements* for a typical distance, before dissolving instantaneously into its surrounding, which is the so-called mixing length, l_m , usually expressed in pressure scale height, $\alpha_{\text{MLT}} = l_m/H_p$. The mixing length is a priori unknown, hence it has to be calibrated with stellar evolutionary calculations by matching the radius, age and luminosity of the Sun with a single depth-independent α_{MLT} , and then applied for all stellar parameters, assuming being constant. Furthermore, MLT is a local and time-independent theory and contains in total four free parameters, and assumes symmetry in the up- and downflows, hence also in the vertical and horizontal direction. The actual formulation of MLT can vary slightly (e.g. see Henyey et al., 1965; Mihalas, 1970).

Many attempts have been made to improve MLT, with one substantial one being the derivation of a non-local mixing length theory (Gough, 1977; Unno et al., 1985; Deng et al., 2006; Grossman et al., 1993). The standard MLT is a local theory, i.e. the convective energy flux is derived from local thermodynamical properties, thereby, non-local effects (e.g. overshooting) of the flow are neglected. Usually, the non-local models are derived from the hydrodynamic equations, which are a set of non-linear moment equations including higher order moments. For their solution, closure approximations are considered (e.g. diffusion approximation, anelastic approximations or introducing a diffusion length). Also, further aspects have been studied: the asymmetry of the flow by a two stream MLT model (Nordlund, 1976), the anisotropy of the eddies (Canuto, 1989), the time-dependence (Xiong et al., 1997) and the depth-dependence of α_{MLT} (Schlatter et al., 1997). The standard MLT accounts only for a single eddy size (being l_m), therefore, Canuto & Mazzitelli (1991, hereafter CMT) extended the standard MLT to a larger spectrum of eddy sizes by including the non-local second order moment (see also Canuto et al., 1996). However, the CMT approach necessitates the depth of the convection zone l_{CZ} as a free parameters. Arnett et al. (2010) found the geometric factor, g_{MLT} , to measure the thickness of the SAR, including a dissipation length l_d .

These approaches are often non-trivial and so far, a sweeping breakthrough has been absent, and despite all the trials of improvements, the standard MLT is still currently widely in use. In 1D atmosphere modeling, the current procedure is to assume for the mixing length parameter α_{MLT} an universal value of 1.5 (see Gustafsson et al., 2008; Castelli & Kurucz, 2004). While for stellar evolutionary models, α_{MLT} is calibrated with solar models that match the age, radius and luminosity of the Sun, and yielding values around $\sim 1.7 - 1.9$ (see Magic et al., 2010). This approach is valid to an extent, however, the single calibrated value is erroneously adopted for all stellar parameters. The actual value of the mixing length is vital, since it sets the convective efficiency and therefore changes the whole structure of the stellar models. Therefore an accurate knowledge of α_{MLT} for different stellar parameter is desirable.

The mixing length can be deduced from multidimensional RHD simulations, where convection emerges from first principles. Over the past decades, the computational power has increased and the steady development of 3D RHD simulations of stellar atmosphere has established their undoubted liability by manifold successful comparisons with observations (Nordlund, 1982; Steffen et al., 1989; Ludwig et al., 1994; Freytag et al., 1996; Stein & Nordlund, 1998; Nordlund & Dravins, 1990; Nordlund et al., 2009). The 3D

RHD models had shown that the basic picture of MLT is incorrect, namely the convective elements were not present, instead highly asymmetric convective motions were found. Nonetheless, the *equivalent* mixing length has been calibrated by Ludwig et al. (1999, hereafter LFS99) based on 2D hydrodynamic models by matching the resulting adiabats with 1D MLT models (see Freytag et al., 1999, for the metal-poor cases). They had shown that α_{MLT} varies significantly with the stellar parameters (from 1.3 to 1.75), and they also studied the impact of a variable α_{MLT} on globular clusters (Freytag & Salaris, 1999). Also, Trampedach (2007) applied a grid of 3D atmosphere models with solar metallicity for the calibration of the mixing length and the so-called mass mixing length (Trampedach & Stein, 2011a).

In this Chapter I discuss the calibration of the mixing length, which I performed with a 1D MLT atmosphere code that employs the identical EOS and opacity (Sect. 7.1), as well as with a 1D stellar envelope code that solves the equations for the stellar structure, however, neglecting the nuclear burning (Sect. 7.2). Furthermore, I elucidate the variation the $T(\tau)$ relations, since these are influencing the calibration of α_{MLT} with the stellar evolutionary models. We derive the vertical correlation length of the vertical velocity (Sect. 7.4) and the mass mixing length (Sect. 7.5) directly from the 3D atmosphere models. Furthermore, we derive the connection of the mass mixing length, which is the inverse gradient of the vertical mass flux, with the mixing length from the hydrodynamic mean field equations.

The mixing length varies clearly with stellar parameters, and the variation tightly correlates with the inverse of the entropy jump. As a highlight I point out the derivation of the mass mixing length from the hydrodynamic mean field equations.

7.1 Mixing Length from 1D atmosphere models

We have developed our own 1D MLT atmosphere code, which uses exactly the same opacities and equation-of-state as the 3D models (see Sect. 2.4). The code uses the MLT formulation by Henyey et al. (1965), similar to the MARCS code (Gustafsson et al., 2008). The turbulent pressure, $p_{\text{turb}} = \beta \rho v_{\text{turb}}^2$, can be included optionally, however, it uses a depth-independent turbulent velocity, v_{turb} , which is the common approach for atmospheric modeling. The resulting temperature stratifications are similar to MARCS (Gustafsson et al., 2008) and ATLAS models (Kurucz, 1979; Castelli & Kurucz, 2004). In Sect. 3.3 we compare the mean (3D) stratifications with our 1D models, and show that below the surface the 1D models are systematically cooler than the (3D) stratifications due to the fixed α_{MLT} with 1.5, in particular for hotter T_{eff} .

Following the method by Ludwig et al. (1999), we calibrated α_{MLT} by matching the asymptotic entropy value of the deep convection zone from the 1D and 3D models (s_{ad} and s_{bot} respectively). We determined s_{ad} as the maximal entropy value in the adiabatic convection zone of the 1D models, i.e. $s_{\text{ad}} = \max s_{\text{cz}}$. On the other hand s_{bot} is an input value for the 3D simulations, and for a given set of $\log g$, $[\text{Fe}/\text{H}]$ and s_{bot} , the resulting radiative cooling and convection lead a to unique T_{eff} . The value of s_{bot} is a fixed boundary condition for 3D simulations, and it depicts the adiabatic entropy value of the incoming upflows at the bottom of the box that are replenishing the outflows. The mean entropy value at the bottom, $\langle s \rangle_{\text{bot}}$, considers the up- and downflows, therefore, it is slightly lower than s_{bot} due to the entropy-deficient downflows ($\langle s \rangle_{\text{bot}} - s_{\text{bot}} \ll 1\%$). However, in our simulations the deeper layers are very close to adiabatic conditions, and the entropy contrast at the bottom is extremely small, therefore, the difference can be neglected.

For the calibration, we computed 1D models with α_{MLT} from 1.0 to 2.5 in steps of 0.1 and determined α_{MLT} by minimizing the difference $\delta s = s_{\text{ad}} - s_{\text{bot}}$ and also the difference in the entropy jumps $\delta s = \Delta s_{\text{1D}} - \Delta s_{\text{3D}}$. We fitted the differences, δs , with a second order polynom to get the exact value of α_{MLT} , since $\delta s(\alpha_{\text{MLT}})$ features a rather smooth variation, and therefore, spared additional iteration steps. The calibration of α_{MLT} is more meaningful, when the EOS are identical, and in particular, the entropy is consistently computed compared to the 3D case. The turbulent pressure, p_{turb} , reduces the gas pressure, thereby, all thermodynamic properties of the 1D model are indirectly affected, in particular, in the SAR, where p_{turb} reaches its maximum. However, we remark that in our calibrations we neglected the turbulent pressure entirely. In Fig. 7.1, we illustrate the calibration of the solar model by illustrating the mean entropy, s , in the convection zone. One can depict, how s converges asymptotically against the adiabatic value of the deep convection zone, s_{bot} . The upflows are essentially adiabatic, i.e. $\langle s \rangle_{\text{up}} \sim s_{\text{bot}}$, until they reach the optical surface and are rather uniform, while the entropy deficient downflows only contribute to the large entropy fluctuations just below the optical surface, which is driving convection (see Stein & Nordlund,

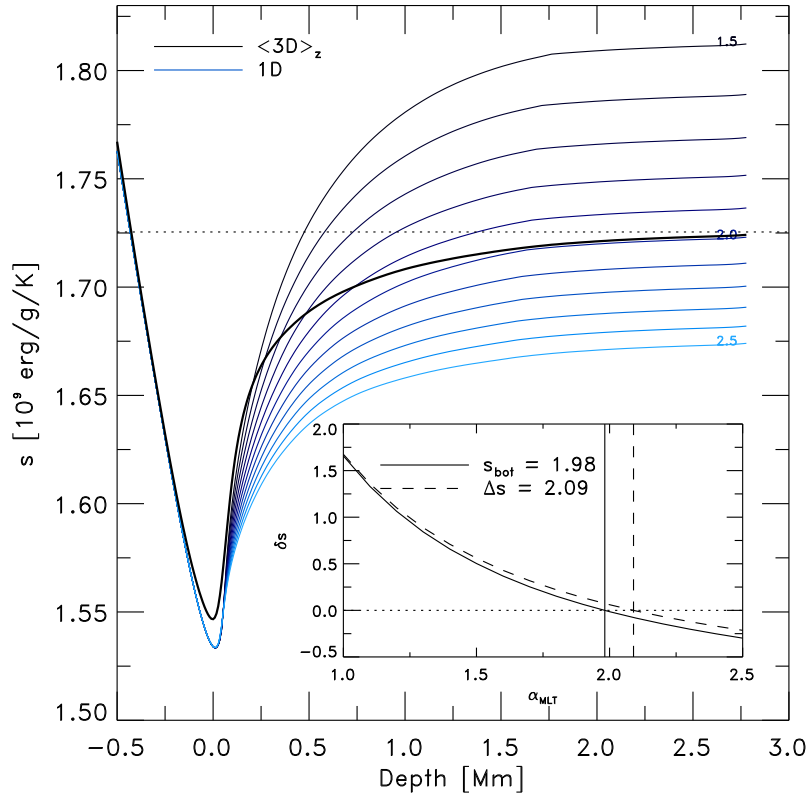


Figure 7.1: Showing the mean $\langle 3D \rangle_z$ entropy (black solid line) vs. the depth and 1D models with varying mixing length $\alpha_{MLT} = 1.5 - 2.5$ (blue lines) of the solar model. The calibration of the mixing length α_{MLT} is illustrated by the small inlay, and the minimal differences between the 1D and 3D models for the constant entropy value of adiabatic convection zone s_{bot} and entropy jump Δs (dashed) yield $\alpha_{MLT} = 1.98$ and 2.09 , respectively.

1998). Furthermore, one can also obtain from Fig. 7.1, how for a higher α_{MLT} the adiabat of the 1D models (s_{ad}) is decreasing in the convection zone, i.e. $\alpha_{MLT} \propto s_{bot}^{-1}$. For the solar simulation, we determined a mixing length of $\alpha_{MLT} = 1.98$ and 2.09 with the adiabatic entropy value and the entropy jump respectively.

7.1.1 Matching the adiabatic entropy value

In Fig. 7.2, we illustrate the overview of the variation of the α_{MLT} values calibrated with s_{bot} for different stellar parameters. The mixing length varies rather systematically, namely, α_{MLT} increases for lower T_{eff} and $[\text{Fe}/\text{H}]$, and higher $\log g$. Some minor deviations towards cooler T_{eff} for metal-poor models can be attributed to the differences in the outer boundary of the 1D models. Cool dwarfs exhibit the largest mixing length values, while hotter models the lower values. A larger α_{MLT} relates to a higher convective efficiency, which implies a smaller entropy jump is necessary to carry the same convective energy flux. Indeed, we find the entropy jump to increase higher T_{eff} , lower $\log g$ and higher $[\text{Fe}/\text{H}]$, and we find that α_{MLT} varies qualitatively inverse to the entropy jump. The mixing length is inversely proportional to the variation of the logarithmic values of the entropy jump, the peak in the entropy contrast and vertical rms-velocity (see Figs. 3.6 and 3.20). This is can be expected based on dimensional considerations, since both the entropy jump and mixing length are setting the convective efficiency.

7.1.2 Matching the entropy jump

We also calibrated the mixing length with 1D MLT atmosphere code by matching the entropy jump Δs . The resulting values are depicted in Fig. 7.3, which are very similar to the above findings in Sect. 7.1.1. Here, the variations with stellar parameters are slightly more systematical, since the entropy jump is a relative value, therefore, the matching is less prone to the outer boundary effects. Furthermore, the α_{MLT} values based on Δs are slightly larger than the values based on s_{bot} (Fig. 7.2) due to the boundary effects in the latter.

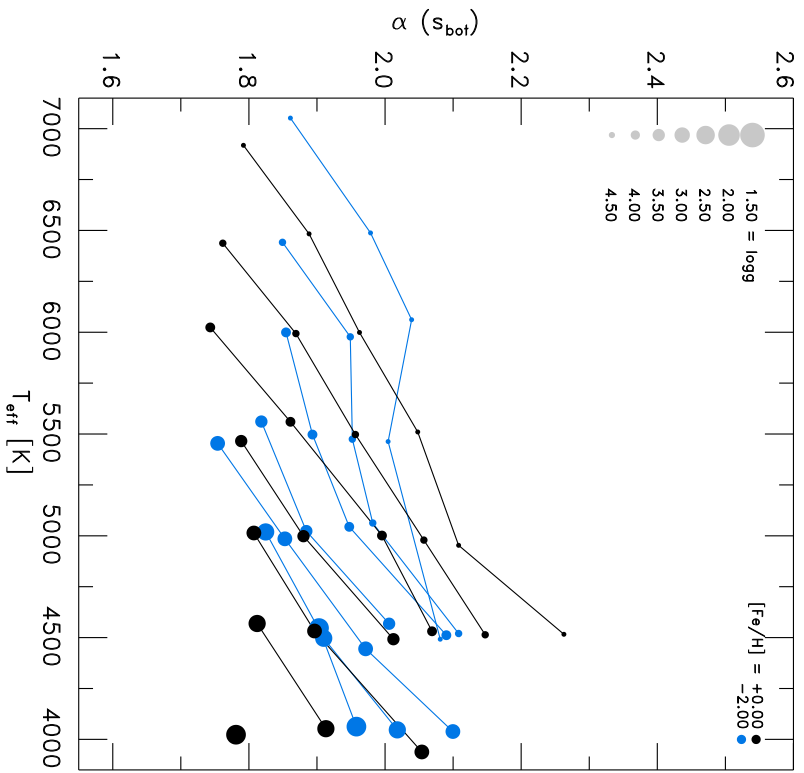


Figure 7.2: Overview of the mixing length α_{MLT} , calibrated with the constant entropy value of adiabatic convection zone s_{bot} , vs. T_{eff} for different stellar parameters.

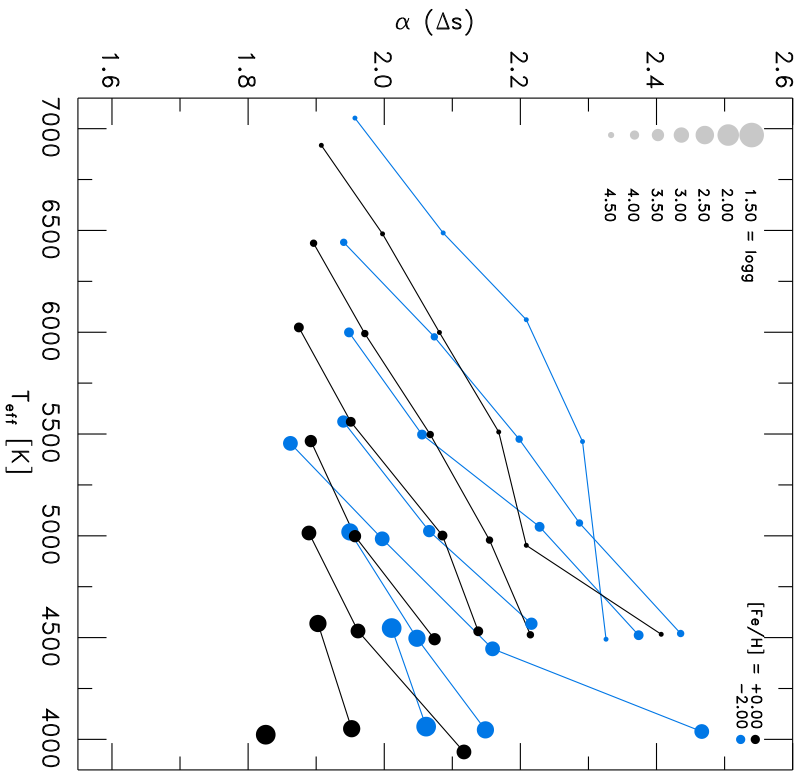


Figure 7.3: Overview of the mixing length α_{MLT} , calibrated with the entropy jump Δs , vs. T_{eff} for different stellar parameters.

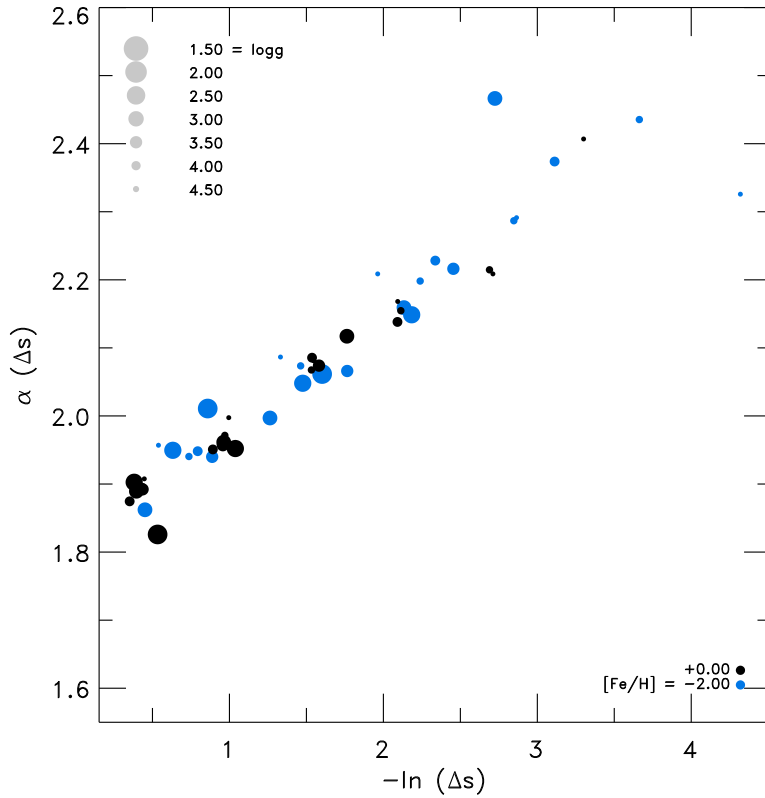


Figure 7.4: The mixing length α_{MLT} , calibrated with the entropy jump, compared with the inverse of the entropy jump.

In Fig. 7.4, we compare the logarithm of the inverse of the entropy jump with the mixing length, and one can see that both correlate very well with each other, while the slight scatter arises probably from the outer boundary conditions in the 1D models. The entropy jump results from the radiative losses at the optical surface, therefore, the correlation of α_{MLT} roots in the interplay of the opacity, radiative cooling rates and vertical velocity of the overturning upflows close the optical surface.

7.1.3 Additional MLT parameters

In the Henyey et al. (1965) formulation of MLT, besides the free mixing length α_{MLT} , there are at least three other free parameters, which are often swept under the rug. These are the scaling factor of the turbulent pressure, β , the energy dissipation by turbulent viscosity, ν , and temperature-distribution of a convective element, y . The default values are usually $\beta = 1/2$, $\nu = 8$ and $y = 3/4\pi^2 = 0.076$, but, the turbulent pressure often is neglected.

The turbulent pressure is given by $p_{\text{turb}} = \beta \rho v_{\text{turb}}^2$, and β has the indirect influence on the T -stratification, gradients and hydrostatic equilibrium by reducing the gas pressure. The parameter ν enters the convective velocity inverse proportionally, $v_{\text{MLT}} \propto \nu^{-1}$ (see Eq. 2.18), and since $v_{\text{MLT}} \propto \alpha_{\text{MLT}}$, an increasing ν would have the same effect as a reduction in α_{MLT} , i.e. $\nu \propto s_{\text{bot}}$. On the other hand, y enters in the (non-linear) convective efficiency factor, Γ , for the superadiabatic excess (see Eq. 2.20), therefore, y is slightly more complex correlated with α_{MLT} , however, this time not inverse to α_{MLT} .

When we consider the variation of the three additional parameters for the solar 1D model, then we notice that the adiabatic entropy value of the deep convection zone is altered significantly (see Fig. 7.5). Furthermore, both of the parameters, ν and y , also change the the entropy jump and the superadiabatic temperature gradient, $\vec{\nabla}_{\text{sad}}$, in particular, the maximum of $\vec{\nabla}_{\text{sad}}$. The inverse variation of y is very similar to that by α_{MLT} , while the y parameter exhibits a non-linear dependence, and converges towards higher values. The increasing turbulent pressure with higher β changes the stratification only slightly, however, interestingly, the location of the maximum of $\vec{\nabla}_{\text{sad}}$ is shifted towards the interior. Another noteworthy

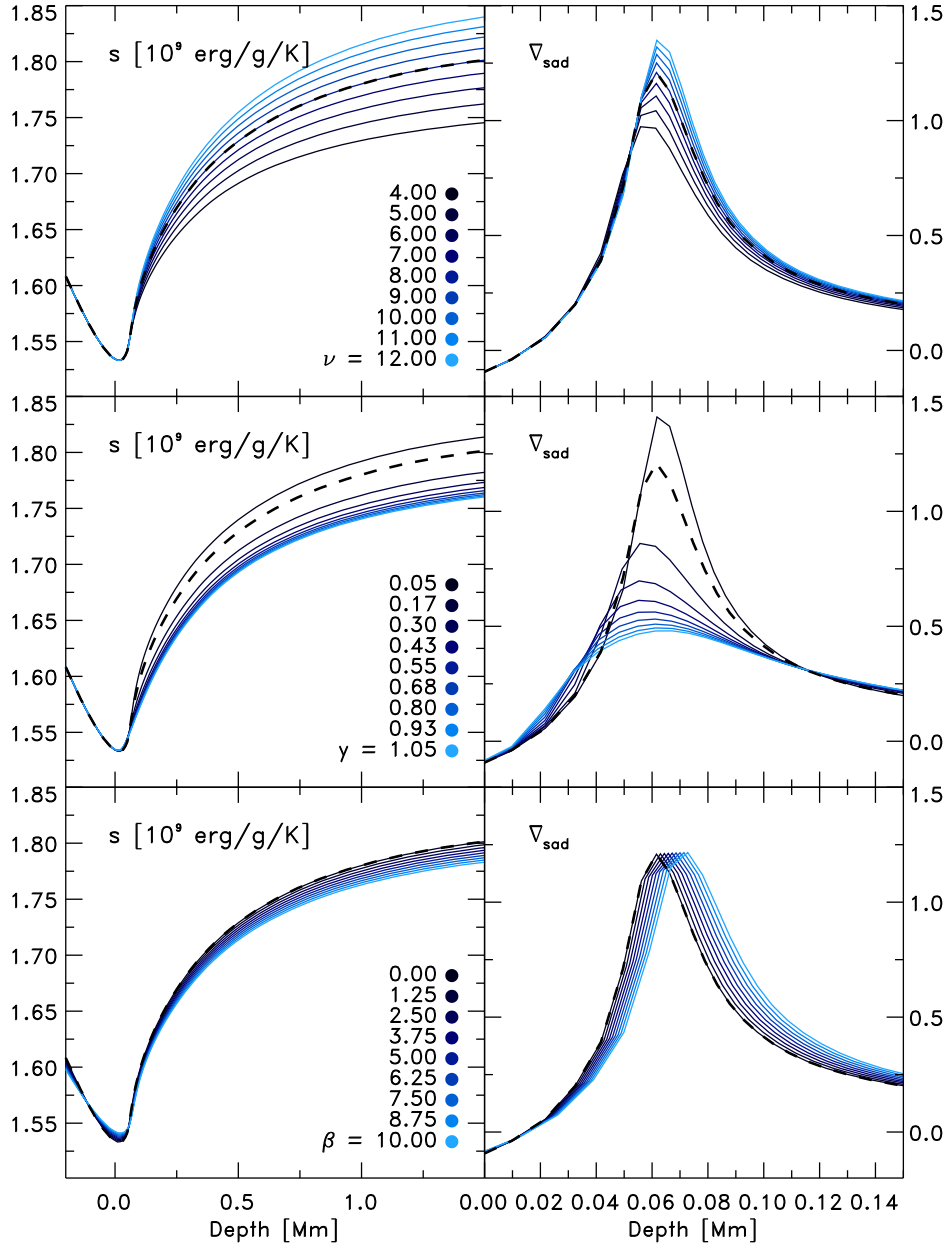


Figure 7.5: The entropy and superadiabatic gradient vs. depth (left and right panel respectively) to illustrate the variation of the additional MLT parameters ν , γ and β (top, middle and bottom panel, respectively), the latter with the depth-independent $\nu_{\text{turb}} = 1$ km/s. In all cases the mixing length is kept fixed with $\alpha_{\text{MLT}} = 1.5$. We included also the standard values with $\beta = 0$, $\nu = 8$ and $\gamma = 0.076$ (dashed line).

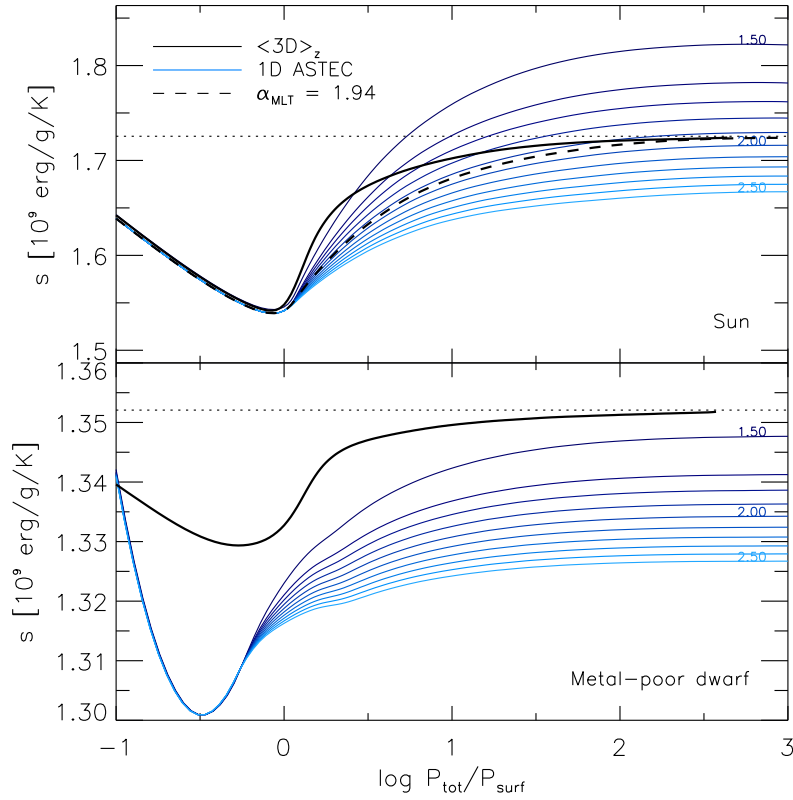


Figure 7.6: The entropy vs. pressure scaled with optical surface pressure for the solar model (top) and the metal-poor dwarf ($T_{\text{eff}} = 4500 \text{ K}$, $\log g = 4.5$, $[\text{Fe}/\text{H}] = -2.0$; bottom panel). The calibration of the mixing length, α_{MLT} , is performed by matching the constant entropy value of adiabatic convection zone, s_{bot} (horizontal dotted line), provided by the $\langle 3D \rangle_z$ (black solid line) with 1D models with varying mixing length $\alpha_{\text{MLT}} = 1.5 - 2.5$ (blue lines). The solar simulation yields $\alpha_{\text{MLT}} = 1.94$ (black dashed line). For the cool metal-poor model a calibration would yield $\alpha_{\text{MLT}} = 1.45$.

aspect, to point out, is the diminishing influence of the MLT parameters towards the optical surface, since the convective flux is gradually dropping to zero. A fine-tuning of β , ν and γ is only useful, when these parameters introduce an independent influence to the mixing length, since otherwise its effects can be summarized in α_{MLT} solely. In the present work we desist from including these additional parameters for the calibration in favor of simplicity and clarity.

7.2 Mixing Length from 1D envelope models

The Arhus STellar Evolutionary Code (ASTEC; Christensen-Dalsgaard, 2008) solves the stellar structure equations (Kippenhahn et al., 2013), and can be operated in the envelope mode, where all time-dependent chemical changes due to nuclear burning and diffusive settling are neglected. In contrast to atmosphere codes, stellar structure codes cover the complete depth of the convection zone, therefore, the adiabatic entropy value of the convective envelope can be retrieved. This code uses the same EOS and chemical composition as the STAGGER-code. The opacities are also the same for $T \lesssim 10^4 \text{ K}$, while for higher T , we use opacities from the Opacity Project (Badnell et al., 2005), and both transit smoothly between each other. In stellar evolutionary codes, like ASTEC, it is custom to include the depth-dependent convective velocity determined by MLT, v_{MLT} , for the evaluation of the turbulent pressure, i. e. $p_{\text{turb}} = \beta \rho v_{\text{MLT}}^2$. We tested the degeneracy of atmospheric stratifications with mass, and we find the differences to be rather small and negligible, even for giant models, where the depth is more extended. For the outer boundary conditions are Eddington gray atmospheres assumed, which is leading to inconsistent α_{MLT} values, in particular, for very cool metal-poor dwarfs models, as we will show. Furthermore, we remark that in this Section we match only s_{bot} .

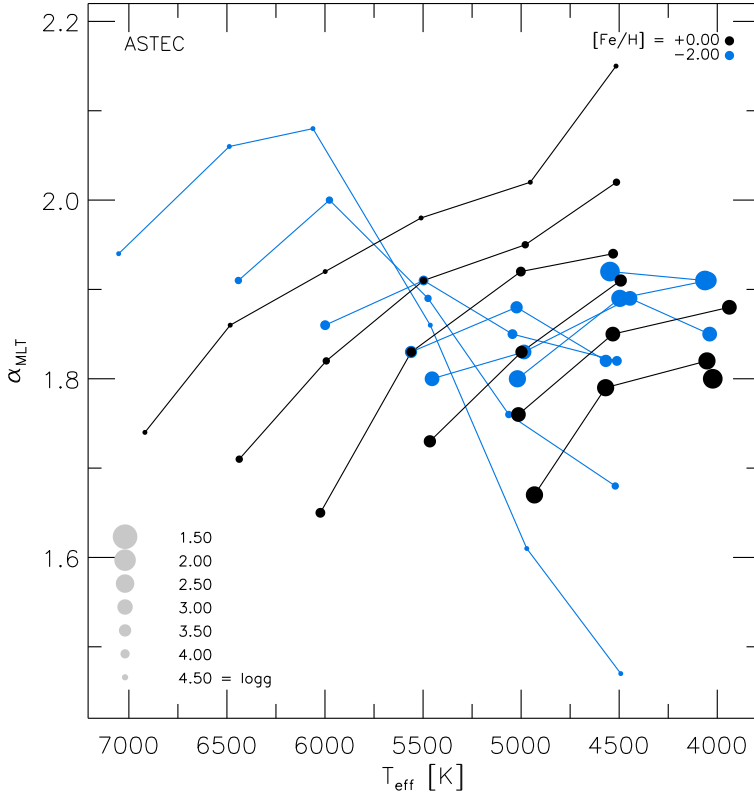


Figure 7.7: Overview of the mixing length α_{MLT} vs. T_{eff} calibrated with the ASTEC code for different stellar parameters.

7.2.1 Matching the adiabatic entropy

In order to illustrate the calibration of α_{MLT} with the ASTEC code, we show the mean stratification of the entropy determined on geometrical height, $\langle s \rangle_z$, for the solar model and a metal-poor dwarf including 1D ASTEC models with different α_{MLT} values in Fig. 7.6. For the solar simulation we yielded a match with $\alpha_{\text{MLT}} = 1.94$, which is rather similar to the value from Sect. 7.1. Moreover, the entropy minimum close to the optical surface is matched closely by the 1D models, while the SAR deviates significantly due to the shortcomings of MLT. In the case of the metal-poor dwarf, s_{bot} is larger than the 1D models with the highest s_{ad} being $\alpha_{\text{MLT}} = 1.5$ (see bottom panel in Fig. 7.6). Therefore, the estimated match for α_{MLT} is leading to a lower value with $\alpha_{\text{MLT}} = 1.48$ for the cooler model. This is in general the case for cooler metal-poor models. The entropy minimum is increasingly deviating between the 1D and 3D models towards cooler T_{eff} , since the outer boundary condition of the 1D models with the Eddington gray atmosphere is increasingly differing from the $T(\tau)$ -relations of the 3D models (see Sec. 7.3). Also, cooler metal-poor models have smaller entropy jumps, therefore, differences in the boundary conditions are increasingly affecting the calibration. When one derives the mixing length with Eddington gray atmospheres, then the resulting mixing length values include the corrections for the differences in the $T(\tau)$ -relations. Ludwig et al. (1999) noted also the same issue with the entropy jump.

In Fig. 7.7 we show an overview of the calibrated mixing length values, and one can obtain that α_{MLT} is systematically distributed with stellar parameters, namely α_{MLT} is decreasing for higher T_{eff} , lower $\log g$ and $[\text{Fe}/\text{H}]$. Towards lower metallicity, in particular, $[\text{Fe}/\text{H}] \leq -2$ the cooler models have lower α_{MLT} than the hotter ones due to the influence of the boundary condition. We have above discussed the increasing influence of the deviations in the entropy jump between 1D and 3D models. The hotter dwarf models with $T_{\text{eff}} \geq 6000$ K and $\log g = 4.5$ exhibit a better match of the entropy jump, in particular, for the metal-poor models. The mismatch starts clearly below 6000 K in effective temperature (see Fig. 7.7). These lower mixing length values for the cooler metal-poor models include the correction for the mismatch of the insufficient $T(\tau)$ -relation with the Eddington gray atmospheres, therefore, these values should be doubted

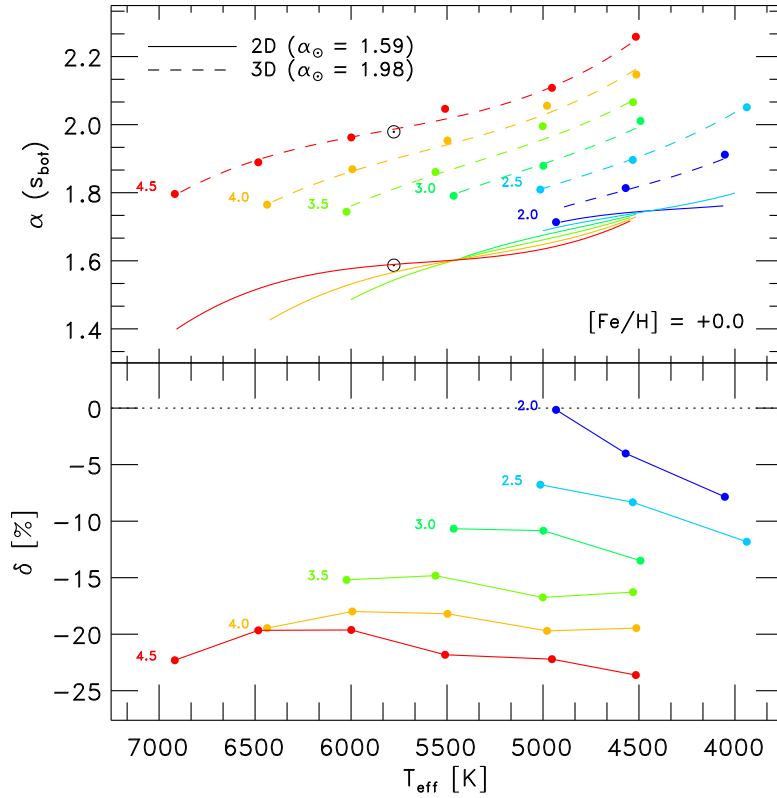


Figure 7.8: Showing α_{MLT} calibrations vs. T_{eff} for 2D and 3D results for comparison (solid and dashed, respectively). The surface gravity is indicated and also color-coded (brighter blue refers to lower $\log g$). Furthermore, the solar values are indicated, and the relative differences are also shown ($\delta = 2\text{D}/3\text{D} - 1$).

to be accurate. Such an influence of the outer boundary might lead to wrong conclusions on the variation of mixing with stellar parameter, therefore, we caution against the indiscriminate derivation of α_{MLT} from 3D RHD simulations or observations with simple boundary conditions (see Sec. 7.2.4).

Finally, it is noteworthy to mention that the solar calibrations of stellar evolutionary calculations lead to similar mixing length values around $\sim 1.7 - 1.9$ (see Magic et al., 2010). Furthermore, we find the vertical correlation length of the vertical velocity and the mass mixing length being also qualitatively similar to α_{MLT} (Sects. 7.4 and 7.5).

7.2.2 Comparison with 2D calibrations

It is worthwhile to compare the differences between the mixing length values we derived with 3D RHD models and the previous results by Ludwig et al. (1999). They employed a grid of 2D RHD atmosphere models and matched the resulting s_{bot} by varying α_{MLT} of a 1D code that uses the same EOS and opacity. We remark that Ludwig et al. (1999) derived $T(\tau)$ -relations from the 2D models, and used them for the 1D models as boundary conditions to render the entropy minimum of the 2D simulations closely. In Sect. 3.1.2 we noticed that s_{bot} resulting from the STAGGER-grid is very similar to values from the 2D grid, while the entropy jump Δs exhibits slight differences.

In Fig. 7.8 we show the calibrated mixing length from both studies in comparison, which are obviously very distinctive. The results of Ludwig et al. (1999) similarly show a clear T_{eff} -dependence, however, the surface gravity implies only very little change in α_{MLT} . The 3D mixing length shows a clear $\log g$ dependence, towards lower surface gravity these are decreasing, while the 2D values are slightly increasing. Their solar mixing length is $\alpha_{\text{MLT}} = 1.59$, which is lower by 0.35 compared to our mixing length value. The dwarf models ($\log g = 4.5$) are in general around 20% lower. Towards giants the difference is diminishing, since the 3D results are smaller. For lower metallicity, the relative differences exhibit qualitatively similar trends (Freytag et al., 1999). In the case of 3D convection simulations, it is known that convection is more efficient in comparison to the 2D case. Therefore, the mixing length values derived from the 3D models

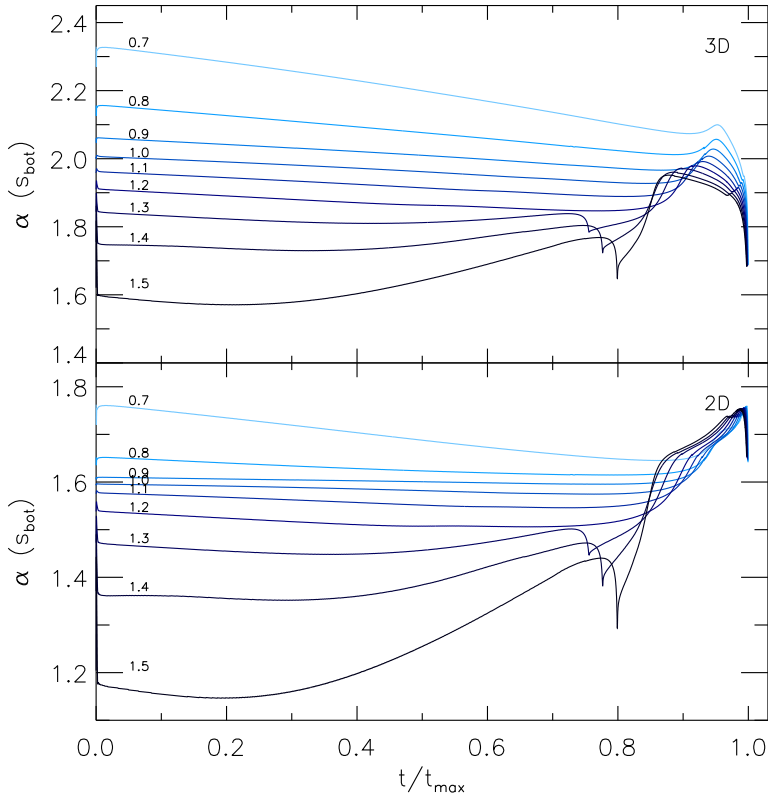


Figure 7.9: The mixing length against the normalized age of stellar evolutionary tracks with the masses from 0.7 to 1.5 M_{\odot} (indicated). The tracks are derived from the 2D and 3D results and all tracks finish at the RGB with $\log g = 1$.

are in general systematically larger.

7.2.3 Impact on stellar evolutionary tracks

When one considers the variation of α_{MLT} along stellar evolutionary tracks¹, then one can notice a clear distinction in α_{MLT} with stellar mass, which is ranging from 1.6 to 2.2 from larger to lower masses, respectively (see Fig. 7.9), which relates to a deviation of $\pm 15\%$ from the solar value. During the main-sequence evolution α_{MLT} varies only little and is almost constant. Larger influence of a variable mixing length takes systematically place during the later evolutionary stages, namely during the TO and the rise along the RGB; α_{MLT} increases first towards values around $\sim 1.9 - 2.0$, then drops sharply down to values of ~ 1.7 . With the 2D mixing length values derived by Ludwig et al. (1999), the stellar tracks are qualitatively similar, however, these are systematically smaller and also the sharp drop is more or less absent. However, the 2D grid spans the RGB only up to $\log g \simeq 2.5$, therefore, the extrapolation above that is dangerous.

7.2.4 Comparison with observations

Observations provide an opportunity to constrain free parameters in theoretical models, like overshooting or mixing length, however, this has to be performed cautiously. Bonaca et al. (2012) calibrated the mixing length α_{MLT} from Kepler-observations of dwarfs and sub-giants (90 stars). They used the frequency of the maximal power, ν_{max} , and the large frequency separation, $\Delta\nu$, together with T_{eff} and $[\text{Fe}/\text{H}]$ from spectroscopic observations to estimate the masses and radii. Then, with a grid of stellar evolutionary tracks that was computed with different α_{MLT} values, they matched the inferred stellar parameters.

Bonaca et al. (2012) found with an average mixing length of 1.60 being in general lower than the solar-calibrated value with 1.69. We compare the functional fit of α_{MLT} with stellar parameter that are inferred

¹We estimated the variation of α_{MLT} based on stellar tracks with a constant mixing length.

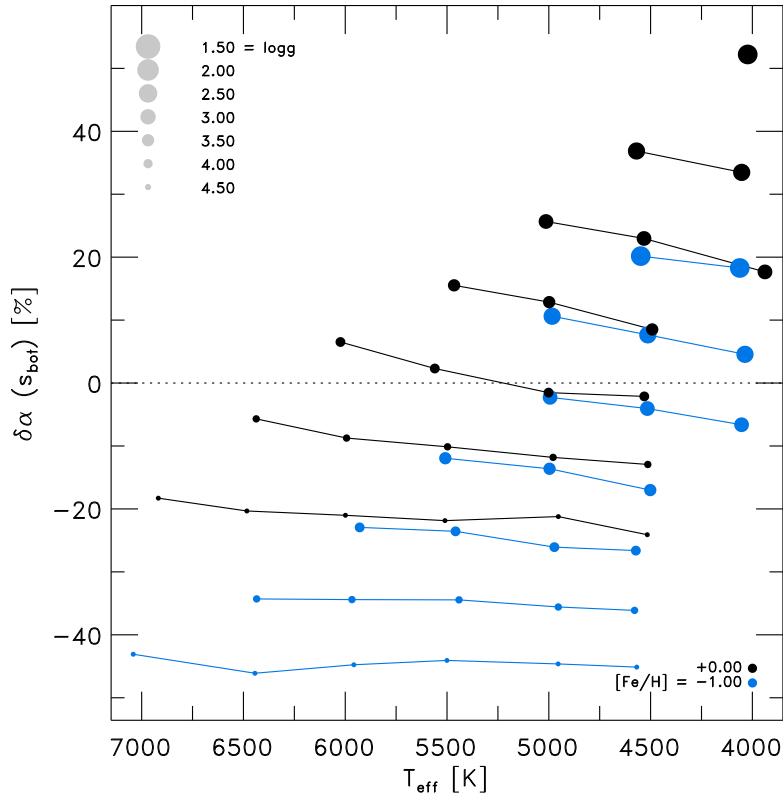


Figure 7.10: Relative difference in the mixing length derived from observations and our 3D RHD models for different stellar parameters.

from observations against our results in Fig. 7.10. We remark that we compare the calibration resulting from the complete data set, since the fit from the dwarf subset deviates completely from our results. Their solar mixing length value is $\alpha_{\text{MLT}} = 1.59$, which is 18% smaller than our result with 1.94. Interestingly, the variation with T_{eff} for a given $\log g$ and $[\text{Fe}/\text{H}]$ is rather similar besides an almost constant offset. For different $\log g$ and $[\text{Fe}/\text{H}]$ we find significant systematical differences (see Fig. 7.10). The values for dwarfs are in general smaller by up to $\sim 20 - 40\%$ depending on the gravity and metallicity, while the giants are greater by the similar amount. Unfortunately, the sample of Bonaca et al. (2012) is in $\log g$ rather small and biased towards dwarfs. Also, their calibration method might carry systematical differences, and the input physics (EOS and opacity) are also different. Therefore, it is difficult to evaluate the actual source for the differences.

7.3 $T(\tau)$ relations

In stellar evolutionary calculations the stellar structure equations are solved with an implicit Henyey-scheme (Henyey et al. 1964) by considering predefined upper boundary conditions, which describe the photospheric transition from optical thick to optical thin regime at the optical surface (see Kippenhahn et al., 2013). The outer boundary conditions are usually expressed in form of $T(\tau)$ -relations that employ the so-called Hopf-function,

$$q(\tau) + \tau = 4/3(T/T_{\text{eff}})^4. \quad (7.1)$$

Then the temperature structure can be retrieved with

$$T = T_{\text{eff}} [3/4(q(\tau) + \tau)]^{1/4}, \quad (7.2)$$

to which we refer as $T(\tau)$ -relations. The most widely used one is the Eddington approximation ($K_\lambda = 1/3J_\lambda$) for a gray (monochrome, i.e. $\tau = \tau_\lambda$) atmosphere, resulting in a linear Hopf-function with $q(\tau = 2/3) =$

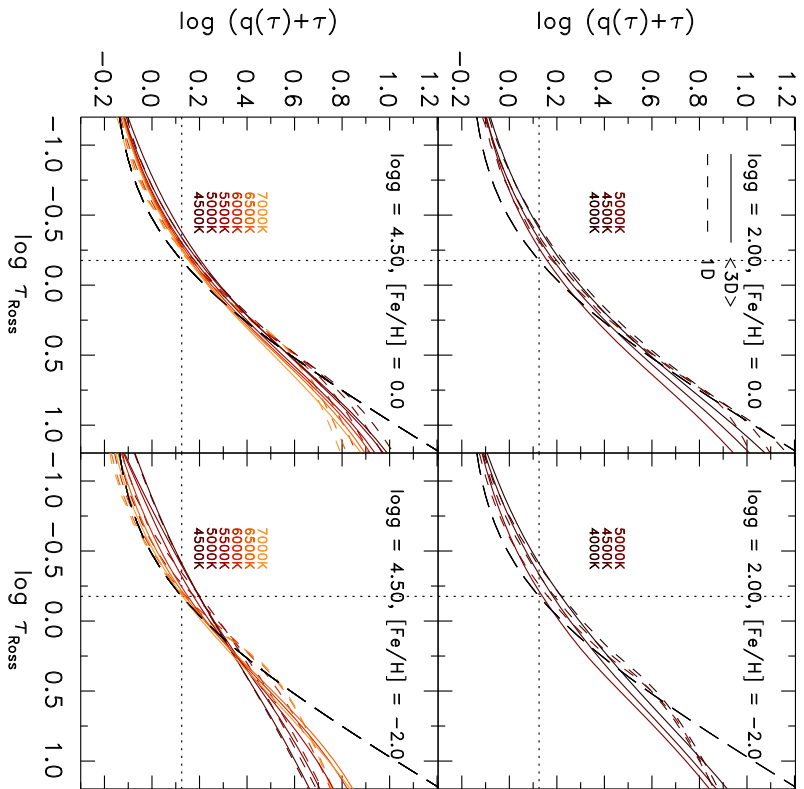


Figure 7.11: Hopf-functions vs. optical depth for different stellar parameters for the averages over layers of constant Rosseland optical depth (solid) and 1D models (dashed lines). The locations for $\tau_{\text{Ross}} = 2/3$ and $q = 2/3$ are indicated (vertical and horizontal dotted lines respectively).

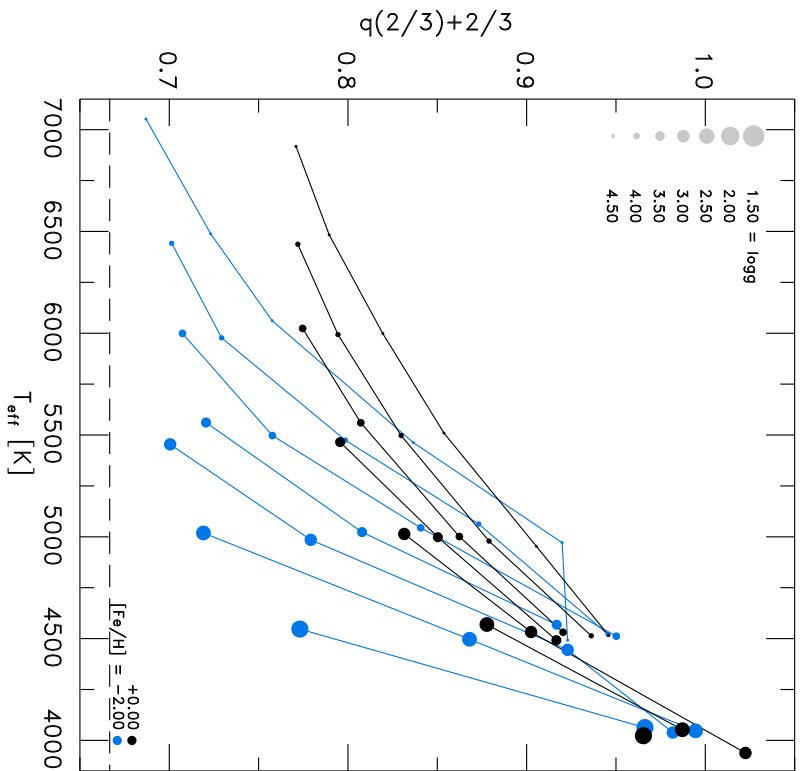


Figure 7.12: Overview of the Hopf-function at $\tau_{\text{Ross}} = 2/3$ vs. T_{eff} for various stellar parameters. Furthermore, we indicated the Eddington approximation (long dashed line).

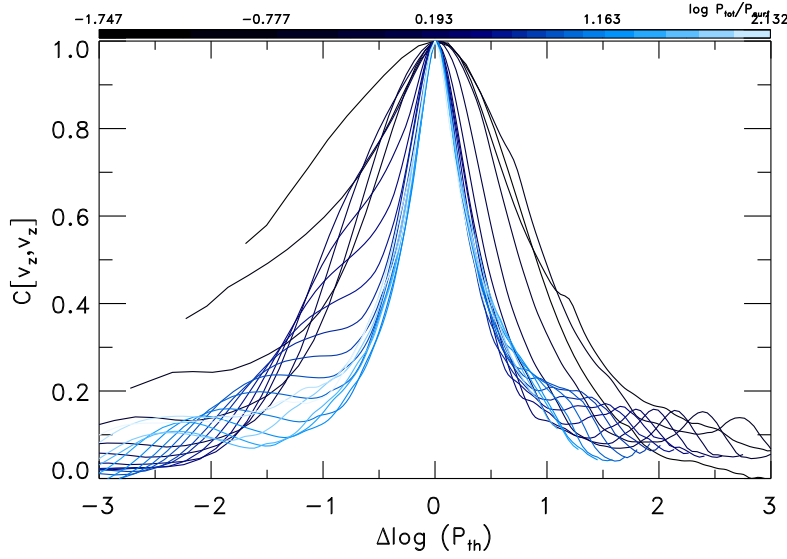


Figure 7.13: Vertical two-point correlation function of the vertical velocity, $C[v_z, v_z]$, vs. difference in thermodynamic pressure, $\Delta \log P_{\text{th}}$, for the solar simulation. The different heights are indicated with a blue color-coding. Note the convergence of the correlation width in the convection zone against an adiabatic value.

$2/3$. Another commonly used one is the semi-empirical $T(\tau)$ -relation by Krishna Swamy (1966), which is derived from solar observations, leading to the fitting formula $q(\tau) = 1.39 - 0.815e^{-2.54\tau} - 0.025e^{-30\tau}$. Both of the latter are usually used for all stellar parameters, with the assumption of being a good approximation, however, is incorrect. Therefore, the inconsiderate use of these outdated $T(\tau)$ -relations will certainly introduce systematical errors, since the outer boundary conditions will influence the stellar structure.

In Fig. 7.11, we show the Hopf-function (Eq. 7.1) from our 3D RHD simulations averaged over layers of constant Rosseland optical depth. Furthermore, we show the Eddington gray atmosphere in comparison, which assumes a constant Hopf-function, however, it is clear that $q(\tau)$ changes with stellar parameters. To depict the variations at $\tau_{\text{Ross}} = 2/3$ with stellar parameters more clearer, we show in Fig. 7.12 the latter. As remarked, the Eddington approximation is not varying with stellar parameter, while the 3D Hopf-functions are doing so. Towards higher T_{eff} , lower $\log g$ and higher $[\text{Fe}/\text{H}]$ the latter is decreasing. Hotter metal-poor dwarfs are close to $2/3$, i.e. these models are very close the Eddington gray approximation, while the cooler models exhibit stronger deviations, in particular, the cool metal-rich giants take a value around 1.

7.4 Velocity correlation length

The physical interpretation of the mixing length is conceptually the mean free path of a convective eddy, over which it can preserve its identity, before it resolves into its environment. In a real stratified hydrodynamic fluid the spatial two-point (auto)correlation function of the vertical velocity can be regarded as the 3D analog of the mixing length α_{MLT} as proposed by Chan & Sofia (1987). The two-point correlation function for the values q_1 and q_2 is given by

$$C[q_1, q_2] = \frac{\langle q_1 q_2 \rangle - \langle q_1 \rangle \langle q_2 \rangle}{\sigma_1 \sigma_2}, \quad (7.3)$$

with σ_i being the the standard deviation of q_i and $\langle \dots \rangle$ depicts the spatial horizontal average.

To derive the vertical correlation function of the convective velocity field, we consider the vertical component of the velocity field, v_z , of a single fixed layer z_0 and derive the correlation functions for all other layers z_i , i.e. $C[v_{z_0}, v_{z_i}]$, which is performed for twenty equidistant layers covering the whole depth scale. In Fig. 7.13 we show the two-point correlation function of the vertical velocity field, $C[v_z, v_z]$, derived for the solar simulation for the individual snapshots and then temporally averaged. For convenience, the correlation function is shown in differences of logarithmic pressure to the considered layer, $\Delta \log P_{\text{th}} = \log P_{\text{th}}(z_0) - \log P_{\text{th}}(z_i)$. Then, the correlation function reaches always unity for $z_i = z_0$ and exhibits a Gaussian-like shape. Furthermore, it is broader above the optical surface ($p_{\text{tot}}/p_{\text{surf}} = 1$), which is due to the rapid decline of the pressure scale height; while below the latter the width seems to converge against

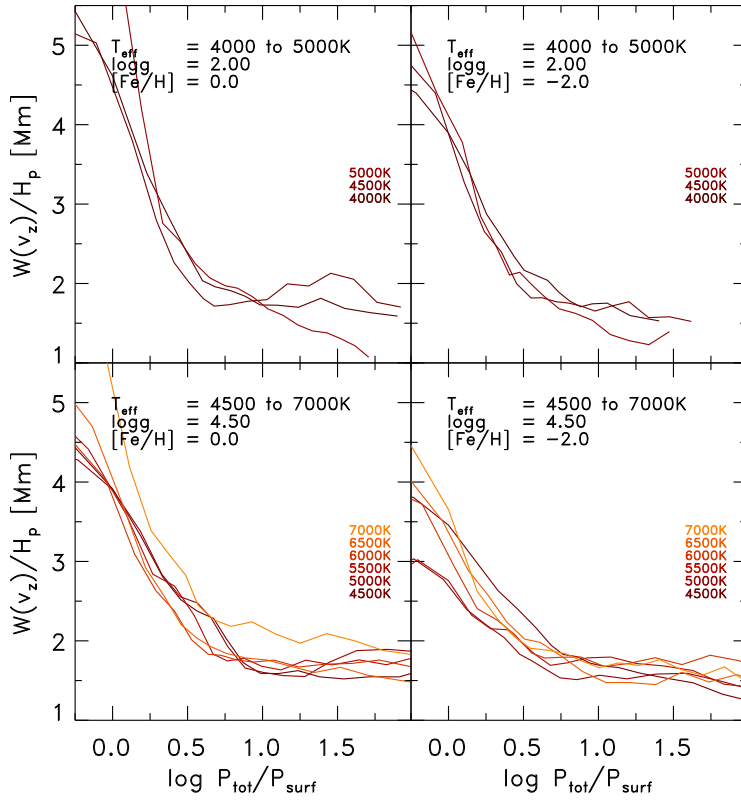


Figure 7.14: Vertical correlation length of the vertical velocity vs. surface normalized pressure for different stellar parameters.

a certain adiabatic value. When one considers the width of the correlation function in geometrical depth, instead of pressure, then it is constant around ~ 0.6 Mm down to 1 Mm and increases then (not shown), which is the same finding as Robinson et al. (2003).

The full-width-half-maximum (FWHM) of the two-point correlation function of the vertical velocity, $W(v_z)$, gives an estimate on the size or length scale of the coherent vertical structures. The characteristic local length scale for the turbulent convective eddies can be determined with $W(v_z)$. With the term vertical correlation length we refer to $W(v_z)$. Similar to the mixing length, it is preferable to scale the correlation length by the pressure scale height, i.e. $W(v_z)/H_p$, since the latter is increasing towards deeper layers. Then, for the solar simulation (see Fig. 7.13) the convergent value for the width is $W(v_z)/H_p = 1.71$. This means that the coherent vertical structures are extending $1.71H_p$ in the convection zone, and is roughly comparable with the mixing length ($\alpha_{\text{MLT}} = 1.94$). For different stellar parameters we find a rather similar convergence of the correlation length of the vertical velocity in the convection zone (see Fig. 7.14). Chan & Sofia (1987, 1989) found also a similar scaling of $C[v_z, v_z]$ with pressure scale height in a 3D simulation for the Sun.

We determined also the mean value of correlation length in the convection zone below $\log p_{\text{tot}}/\log p_{\text{surf}} > 1$ and close to the bottom boundary, the correlation function will increasingly overturn due to missing information in the deeper layers, therefore, we applied a cut for the consideration of a mean correlation length. The resulting values for different stellar parameters are depicted in Fig. 7.15, which are distributed around ~ 1.65 . This is an interesting result, since it confirms the physical motivation for the mixing length α_{MLT} , namely the vertical velocity field, hence the vertical mass flux, correlates along ~ 1.65 pressure scale heights in the convection zone. The correlation length is significant for the transport of convective energy, and the MLT has the underlying assumption,

$$F_{\text{conv}} = C[v_z, \delta T] c_p T' \rho v_z',$$

which states that the convective flux is carried by the fluctuations of T and v_z , scaled by the correlation of the latter.

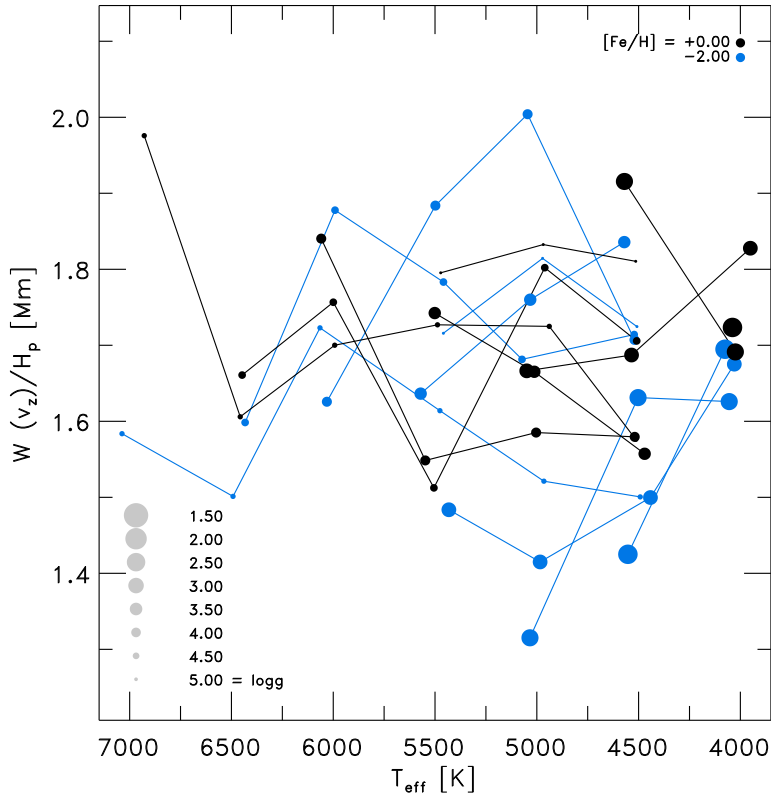


Figure 7.15: Overview of mean vertical correlation length of the vertical velocity in the convection zone for different stellar parameters.

The vertical scaling of the vertical velocity with the pressure scale height is indeed very similar to the horizontal scaling of the granule size with the pressure scale height (see Sect. 3.1.6). The granular cells we find with the temperature excess in Sect. 4.5 show a distinct regular flat cylindrical or pillar-like topology among each other. These findings are connected to the fact that convection operates in a very self-similar way, despite very different physical conditions, and the universal filling factor is here also involved.

Unfortunately, there is no specific systematic variation of the correlation length with stellar parameters in Fig. 7.15, which we found for α_{MLT} and α_{MML} (see Sect. 7.5). The reason for this might be due to poor temporal statistics. Furthermore, we considered the correlation length of other variables, and we find that the horizontal velocity is rather similar, but with slightly lower correlation with ~ 1.4 . Also, we find for the entropy, temperature and pressure values around ~ 1.3 , while for the density it is close to unity.

7.5 Mass mixing length

The temporal and spatial averaged momentum equation for a stationary system yields in the equation for hydrodynamic equilibrium (Eq. 1.8),

$$\partial_z(p_{\text{th}} + \rho v_z^2) = \rho g.$$

This equation states that a given mass stratification (ρg) has to be supported by the joint thermodynamic (p_{th}) and turbulent pressure ($p_{\text{turb}} = \rho v_z^2$) forces, in order to sustain equilibrium. Since the vertical (turbulent) velocity, v_z , appears here, we solve for the latter and get

$$v_z = \sqrt{\frac{g - p_{\text{th}}/\rho \partial_z \ln p_{\text{th}}}{\partial_z \ln \rho + 2 \partial_z \ln v_z}}.$$

Then, similar to the temperature gradient, $\vec{\nabla} = d \ln T / d \ln p_{\text{tot}}$, we introduce the notation for the gradient for a value X , however, instead of the total pressure it is scaled by the thermodynamic pressure scale height,

$$\nabla_X = \partial_z \ln X / \partial_z \ln p_{\text{th}},$$

and we can rewrite the vertical velocity to

$$v_z = \sqrt{\frac{g/\partial_z \ln p_{\text{th}} - p_{\text{th}}/\rho}{\nabla_\rho + 2\nabla_{v_z}}}. \quad (7.4)$$

This analytical exact equation depicts the correlation of the vertical velocity with the gravity and pressure stratification, as well as the gradient of the density and the gradient vertical velocity itself in the hydrodynamic equilibrium. Now, we consider the gradient of the absolute vertical mass flux, $j_z = \rho v_z$, for the up- or downflows with

$$\nabla_{j_z} = d \ln |j_z^{\uparrow\downarrow}| / d \ln p_{\text{th}},$$

which indicates the length, over which the up- or downflow has changed by the e -fold, expressed in pressure scale heights. Furthermore, we define the mass mixing length as the inverse of the gradient of the vertical mass flux,

$$\alpha_{\text{MML}} \equiv \frac{1}{\nabla_{j_z}}, \quad (7.5)$$

and we decompose the gradient of the vertical mass flux into its components and find

$$\alpha_{\text{MML}} = \frac{1}{\nabla_\rho + \nabla_{v_z}},$$

which states that the mass mixing length is the sum of the changes in the density and vertical velocity gradients. Finally, we can now identify the mass mixing length in the denominator of the vertical velocity (Eq. 7.4) and get the following expression

$$v_z = \sqrt{\frac{\alpha_{\text{MML}}}{1 + \alpha_{\text{MML}} \nabla_{v_z}} \left(\frac{g}{\partial_z \ln p_{\text{th}}} - \frac{p_{\text{th}}}{\rho} \right)}. \quad (7.6)$$

This illustrates, why the vertical velocity depends on the mass mixing length, similar to the MLT velocity v_{MLT} that depends on mixing length with $v_{\text{MLT}} \propto \alpha_{\text{MLT}}$ (see Eq. 2.18). The mass mixing length was introduced by Trampedach & Stein (2011b), however, they ignored to explain and motivate further its connection to the mixing length.

To complete the comparison of the mass mixing length with the MLT mixing length, we derive its dependence with the convective energy flux. The mean convective energy flux consists of the fluctuations of the total energy ($\varepsilon_{\text{tot}} = \varepsilon + p_{\text{th}}/\rho + \bar{v}^2/2$), which we depicted with f , and is carried by the mean vertical mass flux, i.e.

$$F_{\text{conv}} = f \rho v_z,$$

where we assume that v_z is the hydrodynamic velocity given in Eq. 7.4. We determine the divergence of the convective energy flux, i.e. $\partial_z F_{\text{c}}$, and solve for the total energy fluctuations

$$f = \frac{1}{\nabla_\rho + \nabla_{v_z}} \frac{\partial_z F_{\text{conv}} / \rho v_z + \partial_z f}{\partial_z \ln p_{\text{th}}}.$$

Then, we can substitute the convective energy losses, $\partial_z F_{\text{conv}}$, with the radiative cooling rate, $-q_{\text{rad}}$, due to conservation of total energy, and we can identify the mass mixing length in the convective energy flux as well with

$$F_{\text{conv}} = -\alpha_{\text{MML}} \frac{(q_{\text{rad}} + \rho v_z \partial_z f)}{\partial_z \ln p_{\text{th}}}. \quad (7.7)$$

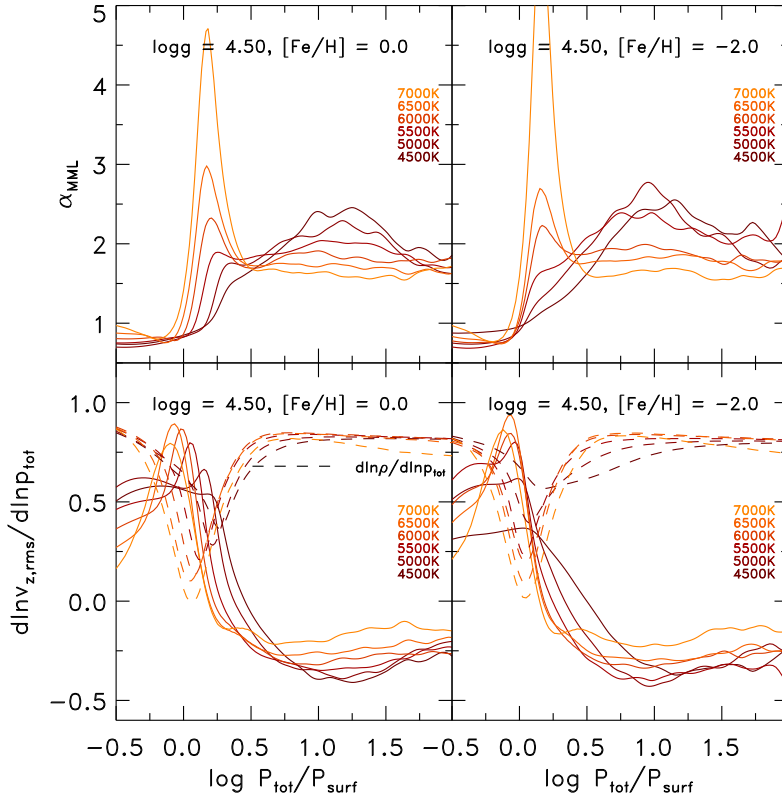


Figure 7.16: The mass mixing length α_{MML} (top) and its components (bottom) for different stellar parameters.

This equation is basically the expression for the conservation of energy. Both of these equations for the velocity and the convective energy flux are just reformulations of the hydrodynamic mean field equations. To close this set of equations one still would need information about the gradient of the velocity and total energy fluctuation, as well as the radiative cooling rates.

In Fig. 7.16, we illustrate the temporal averaged, depth-dependent mass mixing length for different stellar parameters, which we have derived from our 3D RHD simulations. Above the optical surface, α_{MML} exhibits lower values around ~ 0.5 , in the convection zone it has larger values around ~ 2 . For higher T_{eff} , the transition in between increases, while in the convection zone it is flatter. Furthermore, we show also the gradients of the density and vertical velocity in Fig. 7.16, which are the components of α_{MML} . One can depict that the variation of α_{MML} in the convection zone arises only due the different velocity gradients, since the density gradient converges always against its adiabatic value (γ_{ad}^{-1}). The cooling rates are imprinted in the gradients for the density and velocity at the vicinity of the optical surface.

We determined also the mean mass mixing length in the convection zone for $\log p_{\text{tot}}/\log p_{\text{surf}} > 1$ and due to artificial boundary effects, we removed several layers at the bottom. The results are displayed in Fig. 7.17. The mass mixing length depicts qualitatively very similar systematic variations with stellar parameter, as we found for α_{MLT} above. In particular, it decreases for higher T_{eff} and $[\text{Fe}/\text{H}]$, and lower $\log g$, and the range in α_{MML} is qualitatively similar to the α_{MLT} . Furthermore, the inverse variation of α_{MML} is similar to the logarithmic variation of the entropy jump, the peak in the entropy contrast and vertical rms-velocity (see Figs. 3.6 and 3.20). In Fig. 7.18 we compare α_{MML} with the logarithm of the inverse of the entropy jump scaled with $\log(1/\Delta s)/5 + 1.55$, and we find a similar tight correlation between the two, as we have found for the mixing length α_{MLT} above (Sect. 7.1.2). The stronger deviations for the metal-poor giants originate from the fact that these models are slightly shallower, therefore, the match of the mass mixing length is perturbed due to the lower boundary effects on the velocity.

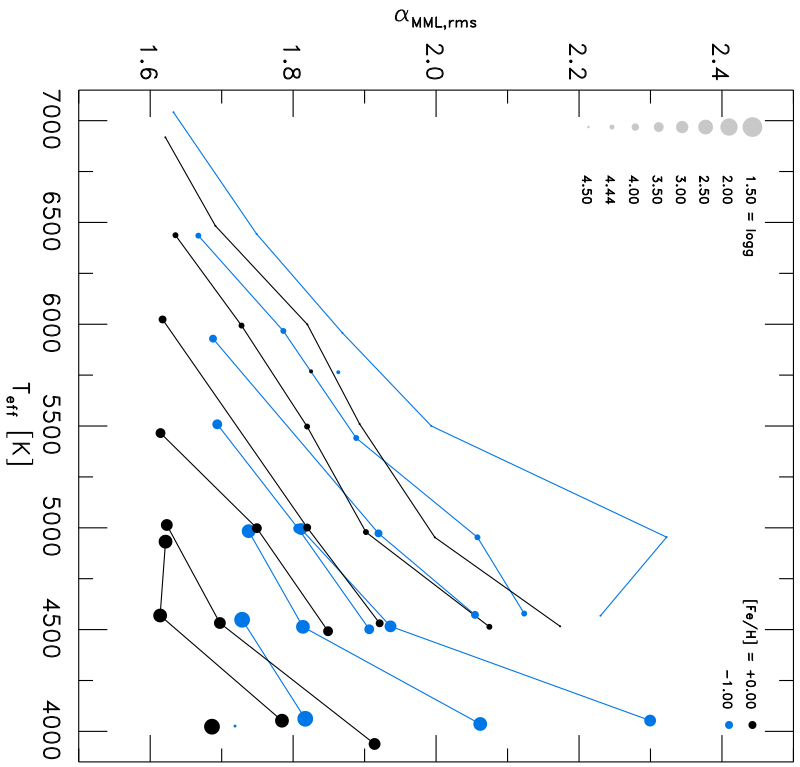


Figure 7.17: Overview of the mass mixing length α_{MML} for different stellar parameters.

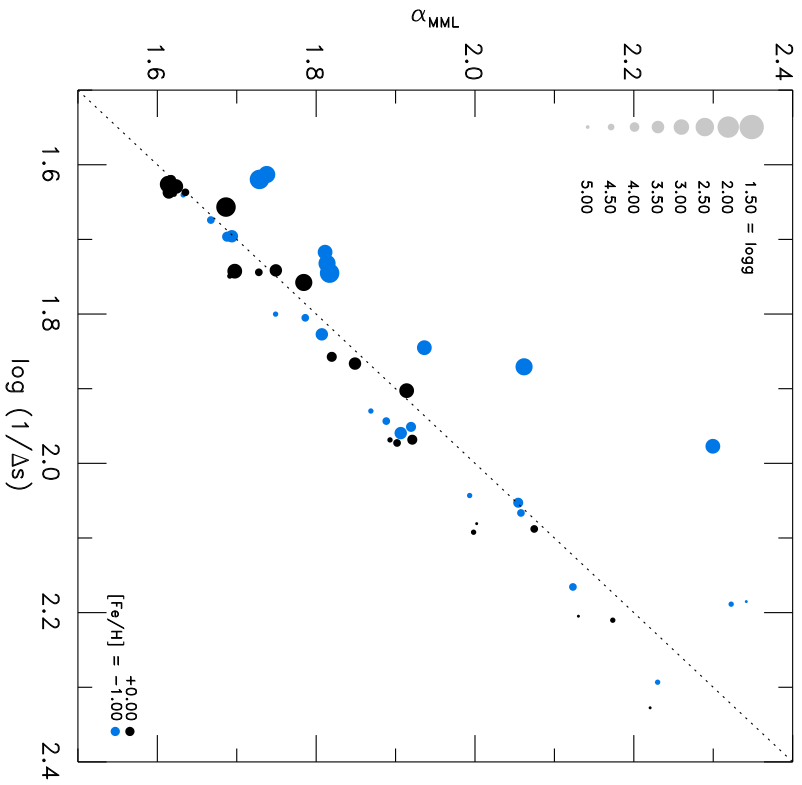


Figure 7.18: Correlation of the mass mixing length α_{MML} with the logarithmic inverse of the entropy jump Δs .

Chapter 8

Conclusions

We presented here a comprehensive grid of realistic, state-of-the-art, three-dimensional (3D), time-dependent, radiative-hydrodynamic (RHD) stellar atmosphere models for late-type stars, covering a substantial portion of stellar parameter space, and provided a detailed description of the approach we followed for the construction of models. With the aid of our realistic 3D RHD simulations, we are able to access and render details of stellar atmospheres and subsurface convection, that are out of reach for 1D models and also inaccessible by observations. We presented and discussed a number of important global physical properties of the simulations as well as the mean stratifications resulting from the relatively large amount of data.

The constant entropy value of the adiabatic convection zone has a profound influence on several aspects and properties of the 3D RHD simulations. In particular, we find systematic correlations among the constant entropy value of the adiabatic convection zone, the entropy jump, and the vertical velocity, which we interpreted as *scaling relations*. In addition, we find that the variation in intensity contrast is enhanced at lower metallicity. Also, we determined that the granule size scales basically with the pressure scale height close to the surface, which can be explained in the picture of what we refer to as Nordlund scaling relation.

We discussed in great detail the depth-dependent temporal and spatial averages of various important physical quantities. In particular, we determined and examined various systematic trends in the variations of the entropy jump, the density, and the vertical velocity with stellar parameters. The latter can be discussed by regarding the changes in the transition of energy transport from convective to radiative at the photosphere. Namely, for different stellar parameters, the coupling between radiation and matter through the radiative transfer necessitates specific physical conditions due to changes in the opacity, which in turn alters the density. These variations in the density on the other hand require adjustments in the entropy jump and the vertical velocity. This can be illustrated under consideration of the total energy flux and conservation of energy. The named important values are coupled with each other, and these also set basically the general physical framework of the stellar atmosphere. The actual particular connections of these correlations have to be studied carefully in more detail, thus possibly leading to an improved understanding of the physical mechanisms operating in subsurface convection, hence stellar atmospheres.

Also, we compared our 3D models and their mean stratifications to 1D models employing the same input physics, thereby revealing important systematic differences between the two kinds of models due to the incomplete treatment of convection by the 1D mixing-length theory (MLT) and the assumption of radiative equilibrium. The latter leads to an overestimation of the temperature stratification in metal-poor stars. While below the optical surface, we find that the temperatures are typically underestimated due to a fixed mixing length ($\alpha_{\text{MLT}} = 1.5$), in particular, for higher T_{eff} and lower $\log g$. Also, we find that MLT fails to render a realistic vertical velocity field. The often neglected turbulent pressure has towards giants a non-negligible contribution on the total pressure, thereby, indicating that the thermal gas pressure is also overestimated significantly. We also quantified the differences with widely used 1D atmosphere models, in particular, ATLAS and MARCS. For a number of important values we provide functional fits with stellar parameters, so that these can be accessed immediately. Thereby, one can easily scale new 3D models based on these informations.

We have investigated the properties of different methods in detail for computing temporal and horizontal average stratifications from 3D RHD STAGGER-grid simulations of stellar surface convection. The choice

of the reference depth is critical, as comparisons of the various $\langle 3D \rangle$ demonstrated. We find in general that the temperature stratifications of the $\langle 3D \rangle_z$ and $\langle 3D \rangle_m$ are hotter close to the continuum forming layers and cooler in the upper layers compared to averages on surfaces of constant optical $\langle 3D \rangle_{\text{Ross}}$ and $\langle 3D \rangle_{500}$, while the density shows differences in the opposite sense. The flux-weighted temperature average and brightness temperature average are distinctively hotter than the plain averages, both close to the optical surface and in the upper atmosphere, since the Planck function and the fourth powers weights the larger temperatures higher. Averages obtained from the logarithmic values lead to lower temperature and density distributions by giving more weight the lower values in the distribution. These characteristics increase with higher T_{eff} , lower $\log g$ and especially with lower $[\text{Fe}/\text{H}]$.

The statistical properties change depending on the reference depth scale, since the transformation to the new depth scale will inevitably imply a remapping of the values from different heights. The translation to layers of constant optical depth will smooth out temperature fluctuations as a byproduct: the temperature is in fact, the main source of spatial corrugation of the surfaces of constant optical depth due to the strong temperature sensitivity of the dominant H^- continuum opacity source. Therefore, the temperature contrast and extrema are distinctively reduced, in particular, in the superadiabatic region. However, this has also the side effect of enhancing both contrast and minimum-maximum range of the density. The concomitant remapping of properties from deeper or higher layers during the transformation to the new reference depth scale will in turn change the average values.

Furthermore, we examined the effects of reversed granulation in the upper layers of metal-poor stars, namely the lowering of temperatures above the granules in metal-poor 3D models compared to classical 1D models. We found that the contribution of radiative reheating due to weak spectral line absorption features relative to cooling due to mechanical expansion in the upper atmospheric layers is reduced towards higher T_{eff} . On the other hand, the temperature in the regions immediately above the intergranular lanes are primarily controlled by mechanical expansion or compression and do not appear to be affected by the reduced metallicity. The two combined effects result in an enhanced contrast in the reversed granulation. This in turn leads to an increase in the corrugation of the surfaces of constant optical depth, which implies that the averages on constant optical depth are sampling values from a very wide range in geometrical height, thereby affecting the statistical properties such as mean value and contrast.

We derived extensive details of stellar granulation by applying the multiple layer tracking algorithm for the detection of granules imprinted in the emergent (bolometric) intensity map, which was originally developed for solar observations. This method works very reliable for different stellar parameters. Then, we determined for the individual detected granules properties: diameter, intensity, temperature, density, velocity and geometry. The granule diameters span a large range, therefore, we advise the use of a logarithmic equidistant histogram, since otherwise, the smaller scales are under-resolved, which leads to the misinterpretation of a large population of small granules. A distinguished dominant granule size can always be determined with the maximum of the area contribution function, which is often very close the maximum of the diameter distribution. Furthermore, we find two distinct fractal dimensions (slopes of the area-perimeter relation) that are divided at the dominant granule size. For smaller granules the fractal dimension is always very close to unity, which points out that these evenly shaped. The larger granules are distinctively larger and closer to 2, depending on primarily on the effective temperature. For lower T_{eff} we find fractal dimension being larger. In the case of the solar simulation, the dual fractal dimension we find is in contradiction to the finding by Bovelet & Wiehr (2001), who finds only a single fractal dimension with the same method from solar observations, and the discrepancy might root in observational constraints. The bifurcation of the fractal dimension above the dominant granule size arises simply due to the fragmentation of granules, which will inevitably entail that the perimeter increases. We studied also the the properties prevailing at the optical surface in our stellar atmosphere simulations. We find that the corrugation of the optical surface increases for higher T_{eff} and lower $\log g$. Also, we revealed the systematic correlation of the intensity, temperature and density with the vertical velocity as a natural consequence of the convective energy transport. For solar simulation, we illustrated the convective cells with the temperature excess, and the complex topology of the turbulent downdrafts in the convection zone with the vorticity, which depicts often transsonic velocities.

The comparison of Fe I and Fe II calculated in full 3D and different $\langle 3D \rangle$ atmosphere models reveals the surprising result that the averages on column mass density $\langle 3D \rangle_m$ typically provide the best representation of the 3D model with respect to the line formation. The commonly preferred averages on layers of constant

optical depth $\langle 3D \rangle_{\text{Ross}}$ or $\langle 3D \rangle_{500}$ in general perform worse. We located the reason for the underperformance in the predictions of 3D RHD by the $\langle 3D \rangle_{\tau}$ models being due to the optical depth, $d\tau_{\lambda} = \rho \kappa_{\lambda} dz$, which contains the additional non-linearity of opacity κ_{λ} , in contrast to the column mass density, $dm = \rho dz$; therefore, the statistical properties, in particular, the mean value, are more prone to distinctive temperature fluctuations present in the superadiabatic region and the upper layers, where the reversed granulation takes place. The differences between the lines calculated with the $\langle 3D \rangle_{\tau}$ models and the full 3D RHD models are significant, in particular, for metal-poor simulations due to the enhanced reversed granulation in the upper layers. We find that the neutral Fe I lines with low excitation potential feature the largest differences between the mean $\langle 3D \rangle$ and full 3D line calculations. The 1D MLT models perform quite well at solar metallicity; however, for metal-poor models the mismatch is evident. Therefore, we caution against using 1D models for metal-poor stars, which will lead to systematic errors in the spectral analysis.

For spectral line formation calculations with $\langle 3D \rangle$ models from the STAGGER-grid, we recommend using averages obtained on layers of constant column mass density, $\langle 3D \rangle_m$, since these provide the closest match to the spectral line strengths obtained with the full 3D RHD models. Furthermore, we advise strongly against using geometrical averages $\langle 3D \rangle_z$ for spectral line formation calculations. For purposes of improving stellar structures and asteroseismology, the $\langle 3D \rangle_z$ models are, however, useful, since these averages alone fulfill the hydrostatic equilibrium, and therefore, comparisons with helioseismological observations are in better agreement. It is obvious that the temporally and spatially averaged models are incapable of substituting the full 3D atmospheric structure. The reduction due to the averaging will unavoidably lead to sacrificing required information. A promising intermediate approach could be the so-called "1.5D" approximation. This approach emulates atmospheric inhomogeneities, which are probed by the traversing radiation, by considering a series of perturbed 1D stratifications for spectral synthesis (e.g., see Ayres et al., 2006). In the spirit of the latter, one could utilize the temporal averaged histograms for an improved spectral line synthesis, since these contain additional information on the statistical distribution of the 3D simulations. A initial proof-of-concept was shown with the minimal approach considering mean averages for the up- and downflows separately. Interestingly, the resulting spectral line profiles exhibit astonishing similarity to the full 3D line profiles, and therefore mark a promising start.

We explored the properties of synthetic spectral lines from neutral and singly ionized iron in late-type stars with the aid of 3D hydrodynamical model atmospheres. We studied the variations with stellar parameters of aspects such as the strength, width, and depth of spectral lines, as well as line asymmetries and wavelength shifts. We related such variations and the morphology of the asymmetries to the structural and thermal properties of the 3D models, with particular focus on velocity and temperature inhomogeneities and their correlation with depth in the stellar atmosphere.

We derived the limb darkening coefficients on the basis of the STAGGER-grid for the various bi-parametric and non-linear limb darkening laws. The non-linear four-parameter power law introduced by Claret (2000) is the only limb darkening law that is sufficiently versatile enough to express the intensity distribution with an excellent accuracy, while all other limb darkening laws are insufficient, in particular, at the limb. Therefore, we recommend the use of the four-parameter functional basis only, in particular for the comparison with high-precision measurements in the hunt of extrasolar planets. We discussed the limb darkening in the Kepler filter for various stellar parameters, and outlined systematical variations that exposed the complex changes of the brightness distribution, in particular with the effective temperature. We compared also our new LDC with predictions from widely used 1D ATLAS models, and the largest differences are given towards the limb. The 1D models are often brighter than 3D predictions, only for giant models with solar-metallicity we find opposite differences. Furthermore, we displayed the systematical (anti-)correlations between the coefficients a_k between half-integer and integer exponents of the four-parameter law. We found the coefficient of linear limb darkening law, u , to scale with the temperature gradient and the Planck function. Theoretical transit light curves indicate similar systematical differences between 1D and 3D as the limb darkening variations implied, which are relatively small. However, as observations indicate (Knutson et al., 2007; Hayek et al., 2012), these can be measured with high-precision observations. Therefore, we advise to use of the new LDC.

We calibrated the mixing length by employing a 1D code for stellar structure and also a 1D code for stellar atmospheres. The calibration was achieved by varying the mixing length and matching the adiabatic entropy value of the deeper convection zone, s_{bot} , or alternatively matching the entropy jump. In both ways we find the mixing length to decrease for higher T_{eff} and $[\text{Fe}/\text{H}]$, and lower $\log g$. However, the calibration

depends on the assumed $T(\tau)$ relation, which influences the thermal stratification as input parameter. In particular, metal-poor 1D models with a fixed $T(\tau)$ relation, such as the Eddington-grey atmosphere, will suffer from the latter, and will result in wrong mixing length values. The 1D atmosphere code manages without the need for any $T(\tau)$ relation, since it solves the radiative transfer by itself, therefore, the resulting calibrations show no mismatches at lower metallicity. We derived also the vertical velocity correlation length, which is interestingly similar to the mixing length with approximately ~ 1.5 of pressure scale height. Furthermore, we derived from the hydrodynamic mean field equations for the first-time a physical motivated connection of the mass mixing length, which is the inverse of the vertical mass flux gradient, with the mixing length. We determined the mass mixing length, and find that it varies qualitatively similar to the mixing length. Finally, in both cases, the mass mixing length and mixing length, we find a strong correlation with the logarithmic inverse of the entropy jump for different stellar parameters.

Appendix A

Functional fits

The resulting amount of data from our numerical simulations is enormous. A convenient way to provide important key values is in form of functional fits, which can be easily utilized elsewhere (e.g., for analytical considerations). In the present paper we have frequently discussed various important global properties that are reduced to scalars. Some of them are global scalar values and some are determined at a specific height from the $\langle 3D \rangle$ stratifications, i.e. temporal and spatial averages on layers of constant Rosseland optical depth. We fitted these scalars with stellar parameters for individual suitable functions, thereby enforcing a smooth rendering. However, we would like to warn against extrapolating these fits outside their range of validity, i.e. outside the confines of our grid. Also, one should consider that possible small irregularities between the grid steps might be neglected, which arise due to non-linear response of the EOS and the opacity. On the other hand, we provide also most of the actual shown values in Table B.1.

We use three different functional bases for our fits and we perform the least-squares minimization with an automated Levenberg-Marquardt method. Instead of the actual stellar parameters, we employ the following transformed coordinates: $x = (T_{\text{eff}} - 5777)/1000$, $y = \log g - 4.44$ and $z = [\text{Fe}/\text{H}]$. Furthermore, we find that in order to accomplish an optimal fit with three independent variables, $f_i(x, y, z)$, simultaneously, the metallicity should be best included implicitly as nested functions in the form of second degree polynomial $\zeta_a(z) = \sum_{i=0}^2 a_i z^i$, each resulting in three independent coefficients a_i . The linear function

$$f_1(x, y, z) = \zeta_a(z) + x\zeta_b(z) + y\zeta_c(z) \quad (\text{A.1})$$

is applied for the following quantities: s_{min} (Fig. 3.1), $\log \rho_{\text{peak}}$ (Fig. 3.20), $\log v_{z,\text{rms}}^{\text{peak}}$ (Fig. 3.20), $\log d_{\text{gran}}$ (Fig. 3.9), $\log \Delta t_{\text{gran}}$ and f_u^{peak} . The resulting coefficients are given in Table A.1. On the other hand, we considered the exponential function

$$f_2(x, y, z) = f_1(x, y, z) + \zeta_d(z) \exp [x\zeta_e(z) + y\zeta_f(z)] \quad (\text{A.2})$$

for s_{bot} , Δs (Figs. 3.1 and 3.20) and $[p_{\text{turb}}/p_{\text{tot}}]_{\text{peak}}$ (Fig. 3.23). For $\vec{\nabla}_{\text{peak}}$ and $\vec{\nabla}_{\text{sad}}^{\text{peak}}$ 3.17 we applied the following function

$$f_3(x, y, z) = f_1(x, y, z) + x^2 \zeta_d(z), \quad (\text{A.3})$$

with coefficients for f_2 and f_3 listed in Table A.2. Finally, we showed in Fig. 3.5 the entropy jump Δs as a function of s_{bot} , which we fitted with

$$f_4(x) = a_0 + a_1 x + a_3 \tanh [a_4 + a_5 x]. \quad (\text{A.4})$$

The resulting coefficients are listed in Table A.3.

Table A.1: The coefficients a_i of the linear function f_1 (Eq. A.1) for s_{\min} [10^{11} erg/g/K], $\log \rho_{\text{peak}}$ [10^{-7} g/cm 3], $\log v_{z,\text{rms}}^{\text{peak}}$ [10km/s], $\log d_{\text{gran}}$ [Mm] and $\log \Delta t_{\text{gran}}$ [10^2 s]. In the last two rows, we listed the root-mean-square and maximal deviation of the fits.

a_i	s_{\min}	$\lg \rho_{\text{peak}}$	$\lg v_{z,\text{rms}}^{\text{peak}}$	$\lg d_{\text{gran}}$	$\lg \Delta t_{\text{gran}}$
a_0	1.5440	0.3968	-0.4626	0.2146	-0.7325
a_1	0.0387	-0.2549	0.0568	0.0666	-0.0054
a_2	0.0046	-0.0344	0.0068	0.0108	-0.0016
b_0	0.0621	-0.4232	0.1988	0.1174	0.0410
b_1	-0.0189	0.1260	-0.0255	0.0187	0.0046
b_2	0.0013	-0.0007	0.0050	0.0033	0.0000
c_0	-0.0898	0.6814	-0.1845	-1.0922	-0.9970
c_1	0.0038	-0.0282	0.0116	-0.0462	-0.0038
c_2	-0.0004	-0.0021	-0.0006	-0.0075	-0.0006
rms Δ	0.0711	20.3286	1.0018	483.4921	47.6416
max Δ	0.1843	138.7171	1.3365	2697.2449	144.2399

Table A.2: The coefficients a_i of the functional bases f_2 and f_3 (Eqs. A.2 and A.3) for s_{bot} [10^{11} erg/g/K], Δs [10^{11} erg/g/K], $[p_{\text{turb}}/p_{\text{tot}}]_{\text{peak}}$, \vec{V}_{peak} and $\vec{V}_{\text{sad}}^{\text{peak}}$. In the last two rows, we listed the root-mean-square and maximal deviation of the fits.

a_i	s_{bot}	Δs	$p_{\text{turb}/\text{tot}}^{\text{peak}}$	\vec{V}_{peak}	$\vec{V}_{\text{sad}}^{\text{peak}}$
a_0	1.5789	-0.0006	0.0321	1.0941	0.8713
a_1	0.0455	0.0043	0.0459	-0.0089	0.0338
a_2	0.0111	0.0064	0.0111	0.0000	0.0076
b_0	0.0784	0.0017	0.0138	0.2498	0.3401
b_1	-0.0183	0.0049	0.0007	-0.0532	-0.0717
b_2	0.0071	0.0060	0.0019	-0.0050	-0.0091
c_0	-0.1076	0.0028	-0.0260	-0.4004	-0.4847
c_1	-0.0028	-0.0029	-0.0087	0.1052	0.0990
c_2	-0.0042	-0.0032	-0.0016	0.0142	0.0155
d_0	0.1602	0.1979	0.1335	-0.0600	-0.0622
d_1	0.0618	0.0675	-0.0257	0.0016	-0.0006
d_2	0.0062	0.0059	-0.0081	-0.0133	-0.0128
e_0	1.2867	1.1479	0.5894	–	–
e_1	-0.0824	-0.0866	0.1141	–	–
e_2	0.0970	0.0788	0.0337	–	–
f_0	-1.2136	-1.0996	-0.5330	–	–
f_1	-0.0338	-0.0316	-0.0864	–	–
f_2	-0.0764	-0.0614	-0.0249	–	–
rms Δ	0.2555	0.2047	0.0758	0.4533	0.5016
max Δ	0.7268	0.6602	0.1841	1.1245	1.2550

Table A.3: The coefficients a_i of the hyperbolic tangent function f_4 (Eq. A.4) for fitting Δs as function of s_{bot} .

T_{eff}	a_0	a_1	a_2	a_3	a_4
4000.0	1.2910	-0.3559	1.0367	-2.6408	1.2059
4500.0	5.1768	-2.1859	4.5280	-1.4475	0.6756
5000.0	7.0730	-3.0946	6.8382	-1.2330	0.5799
5500.0	7.6382	-3.4144	7.5981	-1.1812	0.5636
6000.0	6.8963	-2.9796	6.9907	-1.1769	0.5504
$\log g$	a_0	a_1	a_2	a_3	a_4
1.5	5.3693	-2.0610	5.3770	-1.2576	0.5461
2.0	1.1012	-0.2599	0.9218	-2.8316	1.2958
2.5	1.5805	-0.5023	1.2081	-2.5467	1.1888
3.0	5.2106	-2.1433	4.6691	-1.4254	0.6548
3.5	4.9821	-2.0989	4.2522	-1.5136	0.7111
4.0	8.0957	-3.5548	7.9721	-1.1979	0.5625
4.5	14.1757	-6.3782	17.4802	-0.8936	0.4180

Appendix B

Tables

In Table B.1 we have listed important global properties with the stellar parameters. Due to the lack of space, we show only an excerpt with solar metallicity ($[\text{Fe}/\text{H}] = 0.0$). The complete table is available at CDS <http://cds.u-strasbg.fr>.

In Table B.2, we present the Fe I and Fe II line parameters that are used for the line formation calculations, in the present work. While in Table B.3 we show a subset from the main results we presented in our work retrieved for the solar simulation. The complete list is online available on CDS.

In Table B.4 we listed a subset of the limb darkening coefficients. The full table is available at CDS.

Table B.1: The stellar parameters: effective temperature, surface gravity (Cols. 1 and 2 in [K] and [dex]). The main input variables: the density ρ_{bot} , internal energy per unit mass ϵ_{bot} (Cols. 3 and 4 in [10^{-7}g/cm^3], [10^5erg/g]). We also added the temperature T_{bot} , thermodynamic pressure $p_{\text{th}}^{\text{bot}}$ and entropy values s_{bot} at the bottom (Cols. 5, 6 and 7 in [K], [10^5dyne/cm^2], [10^9erg/g/K]). Furthermore, the jump in entropy Δs , the maximal vertical rms-velocity $v_{z,\text{rms}}^{\text{peak}}$ and intensity contrast ΔI_{rms} values are given (Cols. 8, 9, 10 in [10^9erg/g/K], [km/s], [%]). Finally, we display the horizontal $s_{x,y}$ and vertical box size s_z (Cols. 11 and 12 in [Mm], [Mm]), the mean granule diameter d_{gran} (Col. 13 in [Mm]), the time step Δt and total time t (Cols. 14 and 15 in [10^2s], [10^2s]).

T_{eff}	$\log g$	$\lg \rho_{\text{bot}}$	$\lg \epsilon_{\text{bot}}$	$\lg T_{\text{bot}}$	$\lg p_{\text{th}}^{\text{bot}}$	s_{bot}	Δs	$v_{z,\text{rms}}^{\text{peak}}$	ΔI_{rms}	$\lg s_{x,y}$	$\lg s_z$	$\lg d_{\text{gran}}$	$\lg \Delta t$	$\lg t$
4023	1.50	0.717	1.124	4.272	1.061	2.300	0.602	5.145	18.4	3.820	3.490	3.121	2.176	4.352
4052	2.00	1.125	1.004	4.233	1.368	2.018	0.361	4.167	17.1	3.322	2.971	2.623	1.695	3.871
3938	2.50	1.691	0.908	4.239	1.889	1.775	0.174	3.210	14.4	2.740	2.446	2.041	1.188	3.364
4569	2.00	0.679	1.187	4.342	1.120	2.411	0.723	5.845	18.4	3.380	3.069	2.778	1.740	4.041
4532	2.50	1.357	1.060	4.279	1.669	2.039	0.395	4.391	17.2	2.845	2.517	2.243	1.241	3.282
4492	3.00	1.785	0.955	4.266	2.029	1.808	0.210	3.486	14.5	2.342	1.966	1.643	0.692	2.692
4530	3.50	2.103	0.900	4.269	2.322	1.682	0.126	2.903	12.2	1.778	1.442	1.079	0.188	2.364
4513	4.00	2.419	0.858	4.277	2.625	1.578	0.069	2.367	9.4	1.146	0.895	0.544	-0.319	1.681
4516	4.50	2.721	0.835	4.292	2.927	1.500	0.037	1.937	7.7	0.602	0.399	-0.000	-0.824	1.276
4512	5.00	3.013	0.819	4.308	3.226	1.434	0.021	1.541	6.3	0.146	-0.102	-0.553	-1.301	0.875
4932	2.00	0.042	1.291	4.535	0.700	2.757	1.047	8.331	50.4	3.544	3.127	3.544	1.876	4.052
5013	2.50	0.883	1.202	4.374	1.358	2.376	0.706	5.880	18.0	2.903	2.586	2.204	1.287	3.463
4998	3.00	1.534	1.082	4.308	1.882	2.024	0.399	4.407	16.9	2.362	2.055	1.663	0.765	2.765
5001	3.50	1.960	0.987	4.295	2.243	1.805	0.223	3.608	14.8	1.813	1.496	1.114	0.220	2.317
4978	4.00	2.292	0.919	4.293	2.538	1.661	0.125	2.896	11.7	1.279	0.952	0.580	-0.292	1.749
4953	4.50	2.604	0.877	4.301	2.837	1.560	0.068	2.363	8.8	0.699	0.455	0.000	-0.824	1.217
4963	5.00	2.885	0.854	4.314	3.118	1.485	0.038	1.868	6.8	0.176	-0.048	-0.301	-1.301	0.796
5465	3.00	1.084	1.215	4.403	1.589	2.337	0.685	5.815	17.7	2.447	2.125	1.748	0.819	2.995
5560	3.50	1.663	1.119	4.345	2.062	2.040	0.428	4.598	17.4	1.903	1.572	1.204	0.318	2.415
5497	4.00	2.139	1.010	4.322	2.456	1.791	0.226	3.597	15.3	1.362	1.023	0.663	-0.284	1.892
5510	4.50	2.486	0.947	4.322	2.769	1.649	0.128	2.959	12.1	0.845	0.503	0.146	-0.770	1.230
5480	5.00	2.791	0.905	4.330	3.060	1.547	0.072	2.323	9.0	0.301	0.001	-0.398	-1.301	0.699
5768	4.44	2.367	0.997	4.336	2.688	1.725	0.186	3.293	14.6	0.903	0.601	0.204	-0.678	1.419
6023	3.50	1.130	1.266	4.493	1.737	2.395	0.751	6.183	17.9	1.903	1.703	1.301	0.467	2.564
5993	4.00	1.865	1.122	4.364	2.281	1.991	0.397	4.514	17.9	1.415	1.095	0.716	-0.155	1.942
5998	4.50	2.301	1.026	4.344	2.644	1.771	0.222	3.572	16.1	0.845	0.552	0.146	-0.721	1.279
6437	4.00	1.384	1.263	4.495	1.989	2.315	0.686	5.818	18.3	1.447	1.221	0.748	-0.081	2.016
6483	4.50	2.008	1.134	4.386	2.448	1.969	0.386	4.516	18.7	0.903	0.624	0.204	-0.638	1.403
6918	4.50	1.545	1.283	4.543	2.201	2.292	0.673	5.737	18.6	1.041	0.781	0.342	-0.638	1.362

Table B.2: The Fe I and Fe II line parameters with reference number, ionization degree, wavelength λ , lower excitation potential χ_{exc} , oscillator strength $\log gf$, weighting factor g_u , radiation damping $\log \gamma_{\text{rad}}$, lower level l_l , upper level l_u .

#	id	λ	χ_{exc}	$\log gf$	g_u	$\log \gamma_{\text{rad}}$	l_l	l_u
1	1	4445.4717	0.087	-5.412	1	4.22	s	p
2	1	5247.0503	0.087	-4.961	1	3.63	s	p
3	1	5491.8315	4.186	-2.188	2	8.09	d	p
4	1	5600.2242	4.260	-1.420	2	8.01	p	s
5	1	5661.3457	4.284	-1.756	2	8.00	p	s
6	1	5696.0896	4.548	-1.720	2	8.33	p	d
7	1	5705.4648	4.301	-1.355	2	8.38	p	s
8	1	5778.4531	2.588	-3.440	2	8.21	s	p
9	1	5784.6582	3.396	-2.532	3	8.05	p	s
10	1	5855.0767	4.608	-1.478	2	8.33	p	d
11	1	5956.6943	0.859	-4.552	1	4.00	s	p
12	1	6151.6182	2.176	-3.282	1	8.29	s	p
13	1	6240.6460	2.223	-3.287	3	6.81	s	p
14	1	6311.5003	2.831	-3.141	2	8.20	s	p
15	1	6498.9390	0.958	-4.695	1	4.36	s	p
16	1	6518.3671	2.831	-2.448	2	8.21	s	p
17	1	6574.2285	0.990	-5.010	1	4.22	s	p
18	1	6609.1104	2.559	-2.682	1	7.99	s	p
19	1	6699.1416	4.593	-2.101	2	8.09	s	p
20	1	6739.5220	1.557	-4.794	3	7.24	s	p
21	1	6793.2593	4.076	-2.326	2	7.56	d	p
22	1	6837.0059	4.593	-1.687	2	7.85	s	p
23	1	6854.8228	4.593	-1.926	2	7.81	s	p
24	1	7401.6851	4.186	-1.500	2	8.01	d	p
25	1	7912.8670	0.859	-4.848	1	3.68	s	p
26	1	8293.5146	3.301	-2.203	2	8.20	s	p
27	2	4620.5129	2.828	-3.210	31	8.56	s	p
28	2	5264.8042	3.230	-3.130	31	8.56	s	p
29	2	5414.0717	3.221	-3.580	31	8.56	s	p
30	2	6432.6757	2.891	-3.570	31	8.49	s	p
31	2	6516.0767	2.891	-3.310	31	8.49	s	p
32	2	7222.3923	3.889	-3.260	31	8.56	s	p
33	2	7224.4790	3.889	-3.200	31	8.56	s	p
34	2	7515.8309	3.903	-3.390	31	8.56	s	p
35	2	7711.7205	3.903	-2.500	31	8.56	s	p

Table B.3: Table with main results from synthetic spectral flux profiles: line strength, width, depth, shift, minimum and maximum of bisector for the solar simulation. The line number in the first column is the same as used in Table B.2.

#	W_λ	l_s	l_w	l_d	min	max
1	43.948	-0.374	4.850	0.561	-0.373	-0.248
2	67.517	-0.192	5.381	0.664	-0.276	-0.195
3	13.965	-0.501	4.867	0.145	-0.500	-0.288
4	41.099	-0.420	5.213	0.382	-0.432	-0.241
5	25.989	-0.475	5.040	0.246	-0.473	-0.247
6	18.203	-0.476	5.037	0.172	-0.490	-0.254
7	43.520	-0.420	5.312	0.385	-0.421	-0.242
8	24.787	-0.432	4.757	0.248	-0.431	-0.254
9	30.014	-0.440	4.965	0.282	-0.434	-0.237
10	25.239	-0.483	5.108	0.227	-0.473	-0.249
11	54.501	-0.272	4.997	0.505	-0.303	-0.202
12	51.801	-0.310	5.085	0.453	-0.332	-0.203
13	49.442	-0.315	5.027	0.432	-0.337	-0.204
14	28.465	-0.422	4.802	0.258	-0.412	-0.235
15	45.180	-0.318	4.802	0.399	-0.321	-0.214
16	59.973	-0.286	5.283	0.476	-0.308	-0.191
17	29.505	-0.375	4.595	0.267	-0.371	-0.224
18	63.179	-0.224	5.325	0.487	-0.295	-0.190
19	8.560	-0.481	4.802	0.073	-0.481	-0.237
20	16.198	-0.392	4.541	0.145	-0.403	-0.236
21	14.832	-0.442	4.880	0.122	-0.443	-0.243
22	18.876	-0.473	4.880	0.155	-0.463	-0.226
23	12.255	-0.476	4.807	0.102	-0.474	-0.229
24	44.531	-0.357	5.134	0.317	-0.360	-0.203
25	48.607	-0.280	4.773	0.353	-0.291	-0.187
26	58.154	-0.297	5.216	0.360	-0.306	-0.193
27	56.562	-0.352	5.702	0.584	-0.425	-0.279
28	45.612	-0.372	5.453	0.433	-0.414	-0.259
29	28.478	-0.495	5.210	0.278	-0.487	-0.264
30	42.298	-0.314	5.268	0.341	-0.344	-0.209
31	53.208	-0.247	5.458	0.410	-0.306	-0.205
32	19.331	-0.456	5.141	0.143	-0.470	-0.226
33	21.188	-0.448	5.141	0.156	-0.457	-0.226
34	15.578	-0.488	5.105	0.112	-0.483	-0.224
35	48.518	-0.238	5.437	0.312	-0.304	-0.204

Table B.4: Limb darkening coefficients derived from 3D RHD models in the Kepler filter for different stellar parameters (Cols. 1,2,3). The linear (Col. 4), quadratic (Cols. 5,6), square root (Cols. 7,8) and four-parameter non-linear laws (Cols. 9,10,11,12) are listed.

T_{eff}	$\log g$	[Fe/H]	u	a	b	c	d	a_1	a_2	a_3	a_4
3941	2.50	+0.0	0.7540	0.6785	0.0890	0.6046	0.1951	0.5990	-0.4726	1.0476	-0.3332
4023	1.50	+0.0	0.7684	0.6494	0.1403	0.5441	0.2930	0.8608	-1.0485	1.6560	-0.5755
4038	2.50	-2.0	0.7422	0.5071	0.2772	0.3434	0.5209	0.9583	-0.9036	1.3231	-0.4712
4048	2.00	-2.0	0.7533	0.5602	0.2278	0.4293	0.4233	0.7804	-0.6288	1.1742	-0.4396
4054	2.00	+0.0	0.7478	0.6437	0.1227	0.5483	0.2606	0.8231	-1.0372	1.6583	-0.5805
4061	1.50	-2.0	0.7437	0.5735	0.2006	0.4555	0.3765	0.7604	-0.6899	1.2810	-0.4836
4445	2.50	-2.0	0.7211	0.4438	0.3270	0.2835	0.5718	0.7194	-0.2703	0.7589	-0.3418
4491	3.00	+0.0	0.7249	0.5963	0.1515	0.4995	0.2944	0.7125	-0.7275	1.3470	-0.4986
4498	2.00	-2.0	0.6953	0.4067	0.3403	0.2394	0.5956	0.7239	-0.2435	0.6632	-0.2992
4504	4.00	+0.0	0.7464	0.5897	0.1848	0.4746	0.3552	0.7620	-0.6927	1.2480	-0.4484
4515	5.00	+0.0	0.7427	0.5235	0.2585	0.3809	0.4727	0.6645	-0.1364	0.5109	-0.1660
4518	4.50	+0.0	0.7475	0.5811	0.1962	0.4682	0.3648	0.5975	-0.1796	0.6672	-0.2292
4523	2.50	+0.0	0.7126	0.5668	0.1720	0.4624	0.3270	0.7578	-0.8409	1.4793	-0.5671
4532	3.50	+0.0	0.7350	0.5877	0.1737	0.4776	0.3364	0.7766	-0.8008	1.3862	-0.5061
4561	2.00	+0.0	0.6996	0.4989	0.2366	0.3703	0.4301	0.7433	-0.6130	1.1598	-0.4616
4912	2.00	+0.0	0.6342	0.3729	0.3081	0.2040	0.5620	1.0760	-1.4316	1.9551	-0.7880
4955	4.50	+0.0	0.7063	0.5219	0.2175	0.4122	0.3842	0.6170	-0.3960	1.0439	-0.4496
4965	5.00	+0.0	0.7291	0.5310	0.2337	0.4208	0.4027	0.4763	0.0861	0.5163	-0.2512
4971	5.00	-2.0	0.6677	0.1788	0.5766	-0.1094	1.0153	1.0223	-0.1248	0.0105	-0.0014
4972	4.50	-2.0	0.6886	0.2313	0.5393	-0.0329	0.9426	0.8534	0.2272	-0.2835	0.1041
4974	4.00	+0.0	0.6992	0.5192	0.2123	0.4060	0.3830	0.6923	-0.6002	1.2283	-0.5045
4997	3.50	+0.0	0.6932	0.5118	0.2138	0.4025	0.3798	0.6349	-0.4662	1.1038	-0.4691
5001	3.00	+0.0	0.6744	0.4956	0.2108	0.3903	0.3712	0.6142	-0.4649	1.1166	-0.4850
5019	2.50	+0.0	0.6752	0.4877	0.2210	0.3724	0.3955	0.6738	-0.5504	1.1461	-0.4778
5063	4.00	-2.0	0.6757	0.3013	0.4414	0.0918	0.7628	0.5381	0.7597	-0.7436	0.2794
5457	2.50	-2.0	0.6145	0.2464	0.4341	-0.0011	0.8042	1.2077	-1.0587	1.0038	-0.3082
5458	5.00	-2.0	0.6434	0.1859	0.5394	-0.0762	0.9402	0.6630	0.8211	-1.0901	0.4458
5460	4.50	-2.0	0.6431	0.2014	0.5208	-0.0648	0.9248	0.8651	0.2191	-0.4478	0.2207
5460	3.00	+0.0	0.6294	0.3857	0.2873	0.2516	0.4936	0.4160	0.4190	-0.1084	0.0097
5481	4.00	-2.0	0.6398	0.2278	0.4857	-0.0393	0.8873	1.2188	-0.9165	0.8428	-0.2634
5488	5.00	+0.0	0.6648	0.4376	0.2679	0.3173	0.4539	0.4739	0.0915	0.4573	-0.2538
5493	4.00	+0.0	0.6489	0.4214	0.2683	0.2955	0.4617	0.5413	-0.0765	0.5818	-0.2854
5509	4.50	+0.0	0.6632	0.4384	0.2651	0.3119	0.4590	0.5493	-0.0749	0.5772	-0.2752
5552	3.50	+0.0	0.6321	0.3764	0.3015	0.2358	0.5176	0.5239	0.0998	0.2968	-0.1694
5556	3.00	-2.0	0.6036	0.2157	0.4573	-0.0528	0.8575	1.3578	-1.3509	1.2117	-0.3623
5767	4.44	+0.0	0.6391	0.3926	0.2906	0.2535	0.5037	0.5850	-0.1023	0.5371	-0.2580
5784	4.44	-2.0	0.6210	0.2036	0.4922	-0.0700	0.9028	1.3022	-1.1507	1.0719	-0.3504
5977	4.00	-2.0	0.5986	0.2085	0.4599	-0.0604	0.8608	1.4362	-1.6302	1.5751	-0.5231
5996	3.50	-2.0	0.5915	0.2386	0.4161	-0.0099	0.7856	1.4091	-1.7317	1.7550	-0.5948
5999	4.00	+0.0	0.6117	0.3409	0.3193	0.1872	0.5546	0.5399	0.1729	0.0875	-0.0614
6002	4.50	+0.0	0.6204	0.3557	0.3122	0.2071	0.5400	0.5319	0.1504	0.1629	-0.1009
6025	3.50	+0.0	0.5791	0.2739	0.3599	0.0827	0.6484	0.7083	0.0037	-0.0342	0.0616
6057	4.50	-2.0	0.6032	0.2186	0.4535	-0.0359	0.8349	1.2365	-1.1144	1.0596	-0.3421
6437	4.00	-2.0	0.5686	0.1783	0.4602	-0.0941	0.8658	1.3962	-1.4639	1.2697	-0.3755
6437	4.00	+0.0	0.5718	0.2641	0.3627	0.0758	0.6479	0.8062	-0.3950	0.5247	-0.1973
6483	4.50	+0.0	0.5953	0.2805	0.3712	0.0931	0.6561	0.7390	-0.1722	0.3189	-0.1292
6490	4.50	-2.0	0.5907	0.2356	0.4186	-0.0043	0.7773	1.2572	-1.3322	1.3574	-0.4620
6915	4.50	+0.0	0.5623	0.2066	0.4194	-0.0169	0.7566	0.9738	-0.6262	0.6324	-0.2190

Bibliography

- Abramenko, V., Yurchyshyn, V., Goode, P., & Kilcik, A. 2010, *ApJ*, 725, L101
- Abramenko, V., Yurchyshyn, V., & Goode, P. R. 2012a, 455, 17
- Abramenko, V. I., Yurchyshyn, V. B., Goode, P. R., Kitiashvili, I. N., & Kosovichev, A. G. 2012b, *ApJ*, 756, L27
- Allende Prieto, C., Asplund, M., García López, R. J., & Lambert, D. L. 2002, *ApJ*, 567, 544
- Allende Prieto, C., García López, R. J., Lambert, D. L., & Ruiz Cobo, B. 2000, *ApJ*, 528, 885
- Allende Prieto, C., Lambert, D. L., & Asplund, M. 2001, *ApJ*, 556, L63
- Arnett, D., Meakin, C., & Young, P. A. 2010, *ApJ*, 710, 1619
- Asplund, M. 2005, *ARA&A*, 43, 481
- Asplund, M., Carlsson, M., & Botnen, A. V. 2003, *A&A*, 399, L31
- Asplund, M. & García Pérez, A. E. 2001, *A&A*, 372, 601
- Asplund, M., Grevesse, N., & Sauval, A. J. 2005, 336, 25
- Asplund, M., Grevesse, N., Sauval, A. J., & Scott, P. 2009, *ARA&A*, 47, 481
- Asplund, M., Nordlund, Å., & Trampedach, R. 1999a, 173, 221
- Asplund, M., Nordlund, Å., Trampedach, R., Allende Prieto, C., & Stein, R. F. 2000a, *A&A*, 359, 729
- Asplund, M., Nordlund, Å., Trampedach, R., & Stein, R. F. 1999b, *A&A*, 346, L17
- Asplund, M., Nordlund, Å., Trampedach, R., & Stein, R. F. 2000b, *A&A*, 359, 743
- Atroshchenko, I. N. & Gadun, A. S. 1994, *A&A*, 291, 635
- Ayres, T. R., Plymate, C., & Keller, C. U. 2006, *ApJS*, 165, 618
- Badnell, N. R., Bautista, M. A., Butler, K., et al. 2005, *MNRAS*, 360, 458
- Barklem, P. S., Stempels, H. C., Allende Prieto, C., et al. 2002, *A&A*, 385, 951
- Beeck, B., Cameron, R. H., Reiners, A., & Schüssler, M. 2013, *A&A*, 558, A49
- Beeck, B., Collet, R., Steffen, M., et al. 2012, *A&A*, 539, A121
- Bensby, T., Johnson, J. A., Cohen, J., et al. 2009, *A&A*, 499, 737
- Bergemann, M., Lind, K., Collet, R., Magic, Z., & Asplund, M. 2012, *MNRAS*, 427, 27
- Bigot, L., Kervella, P., Thévenin, F., & Ségransan, D. 2006, *A&A*, 446, 635
- Böhm-Vitense, E. 1958, *ZAp*, 46, 108

- Bonaca, A., Tanner, J. D., Basu, S., et al. 2012, *ApJ*, 755, L12
- Bovelet, B. & Wiehr, E. 2001, *Sol. Phys.*, 201, 13
- Caffau, E., Ludwig, H.-G., Steffen, M., et al. 2008, *A&A*, 488, 1031
- Caffau, E., Ludwig, H.-G., Steffen, M., Freytag, B., & Bonifacio, P. 2011, *Sol. Phys.*, 268, 255
- Canuto, V. M. 1989, *A&A*, 217, 333
- Canuto, V. M., Goldman, I., & Mazzitelli, I. 1996, *ApJ*, 473, 550
- Canuto, V. M. & Mazzitelli, I. 1991, *ApJ*, 370, 295
- Carlsson, M., Stein, R. F., Nordlund, Å., & Scharmer, G. B. 2004, *ApJ*, 610, L137
- Cassisi, S., Salaris, M., Castelli, F., & Pietrinferni, A. 2004, *ApJ*, 616, 498
- Castelli, F., Gratton, R. G., & Kurucz, R. L. 1997, *A&A*, 318, 841
- Castelli, F. & Kurucz, R. L. 2004, *ArXiv Astrophysics e-prints*
- Chan, K. L. & Sofia, S. 1987, *Science*, 235, 465
- Chan, K. L. & Sofia, S. 1989, *ApJ*, 336, 1022
- Charbonneau, D., Brown, T. M., Latham, D. W., & Mayor, M. 2000, *ApJ*, 529, L45
- Cheung, M. C. M., Schüssler, M., & Moreno-Insertis, F. 2007, *A&A*, 461, 1163
- Chiavassa, A., Bigot, L., Kervella, P., et al. 2012, *A&A*, 540, A5
- Chiavassa, A., Collet, R., Casagrande, L., & Asplund, M. 2010, *A&A*, 524, A93
- Chiavassa, A., Freytag, B., Masseron, T., & Plez, B. 2011, *A&A*, 535, A22
- Chiavassa, A., Plez, B., Josselin, E., & Freytag, B. 2009, *A&A*, 506, 1351
- Christensen-Dalsgaard, J. 2008, *Ap&SS*, 316, 13
- Claret, A. 2000, *A&A*, 363, 1081
- Claret, A. 2004, *A&A*, 428, 1001
- Claret, A., Diaz-Cordoves, J., & Gimenez, A. 1995, *A&AS*, 114, 247
- Collet, R., Asplund, M., & Trampedach, R. 2006, 306
- Collet, R., Asplund, M., & Trampedach, R. 2007, *A&A*, 469, 687
- Collet, R., Hayek, W., Asplund, M., et al. 2011, *A&A*, 528, A32
- Collet, R., Nordlund, Å., Asplund, M., Hayek, W., & Trampedach, R. 2009, *Mem. Soc. Astron. Italiana*, 80, 719
- Deng, L., Xiong, D. R., & Chan, K. L. 2006, *ApJ*, 643, 426
- Di Mauro, M. P., Christensen-Dalsgaard, J., Rabello-Soares, M. C., & Basu, S. 2002, *A&A*, 384, 666
- Diaz-Cordoves, J., Claret, A., & Gimenez, A. 1995, *A&AS*, 110, 329
- Edvardsson, B., Andersen, J., Gustafsson, B., et al. 1993, *A&A*, 275, 101
- Feautrier, P. 1964, *Comptes Rendus Academie des Sciences (serie non specifiée)*, 258, 3189

- Frebel, A., Collet, R., Eriksson, K., Christlieb, N., & Aoki, W. 2008, *ApJ*, 684, 588
- Freytag, B., Ludwig, H.-G., & Steffen, M. 1996, *A&A*, 313, 497
- Freytag, B., Ludwig, H.-G., & Steffen, M. 1999, 173, 225
- Freytag, B. & Salaris, M. 1999, *ApJ*, 513, L49
- Freytag, B., Steffen, M., Ludwig, H.-G., et al. 2012, *Journal of Computational Physics*, 231, 919
- Fuhrmann, K., Axer, M., & Gehren, T. 1993, *A&A*, 271, 451
- González Hernández, J. I., Bonifacio, P., Ludwig, H.-G., et al. 2010, *A&A*, 519, A46
- Gough, D. O. 1977, *ApJ*, 214, 196
- Gray, D. F. 2005, *The Observation and Analysis of Stellar Photospheres*
- Gray, D. F. 2009, *ApJ*, 697, 1032
- Grossman, S. A., Narayan, R., & Arnett, D. 1993, *ApJ*, 407, 284
- Grupp, F. 2004, *A&A*, 420, 289
- Gudiksen, B. V., Carlsson, M., Hansteen, V. H., et al. 2011, *A&A*, 531, A154
- Gustafsson, B., Bell, R. A., Eriksson, K., & Nordlund, A. 1975, *A&A*, 42, 407
- Gustafsson, B., Edvardsson, B., Eriksson, K., et al. 2008, *A&A*, 486, 951
- Hauschildt, P. H., Allard, F., & Baron, E. 1999, *ApJ*, 512, 377
- Hayek, W., Asplund, M., Carlsson, M., et al. 2010, *A&A*, 517, A49
- Hayek, W., Asplund, M., Collet, R., & Nordlund, Å. 2011, *A&A*, 529, A158
- Hayek, W., Sing, D., Pont, F., & Asplund, M. 2012, *A&A*, 539, A102
- Henyey, L., Vardya, M. S., & Bodenheimer, P. 1965, *ApJ*, 142, 841
- Hirzberger, J. 2002, *A&A*, 392, 1105
- Hirzberger, J., Vazquez, M., Bonet, J. A., Hanslmeier, A., & Sobotka, M. 1997, *ApJ*, 480, 406
- Holweger, H. & Mueller, E. A. 1974, *Sol. Phys.*, 39, 19
- Johnson, H. R. & Krupp, B. M. 1976, *ApJ*, 206, 201
- Kippenhahn, R., Weigert, A., & Weiss, A. 2013, *Stellar Structure and Evolution*
- Knutson, H. A., Charbonneau, D., Noyes, R. W., Brown, T. M., & Gilliland, R. L. 2007, *ApJ*, 655, 564
- Kritsuk, A. G., Nordlund, Å., Collins, D., et al. 2011, *ApJ*, 737, 13
- Kurucz, R. L. 1979, *ApJS*, 40, 1
- Kurucz, R. L. 1993
- Kučinskas, A., Steffen, M., Ludwig, H.-G., et al. 2013a, *A&A*, 549, A14
- Kučinskas, A., Steffen, M., Ludwig, H.-G., et al. 2013b, *A&A*, 549, A14
- Lind, K., Bergemann, M., & Asplund, M. 2012, *MNRAS*, 427, 50
- Ludwig, H.-G. 2006, *A&A*, 445, 661

- Ludwig, H.-G., Caffau, E., Steffen, M., et al. 2010, 265, 201
- Ludwig, H.-G., Caffau, E., Steffen, M., et al. 2009a, *Mem. Soc. Astron. Italiana*, 80, 711
- Ludwig, H.-G., Freytag, B., & Steffen, M. 1999, *A&A*, 346, 111
- Ludwig, H.-G., Jordan, S., & Steffen, M. 1994, *A&A*, 284, 105
- Ludwig, H.-G. & Kučinskas, A. 2012, *A&A*, 547, A118
- Ludwig, H.-G., Samadi, R., Steffen, M., et al. 2009b, *A&A*, 506, 167
- Magic, Z., Collet, R., Asplund, M., et al. 2013a, *A&A*, 557, A26
- Magic, Z., Collet, R., Hayek, W., & Asplund, M. 2013b, *A&A*, 560, A8
- Magic, Z., Serenelli, A., Weiss, A., & Chaboyer, B. 2010, *ApJ*, 718, 1378
- Maltby, P., Avrett, E. H., Carlsson, M., et al. 1986, *ApJ*, 306, 284
- Mandel, K. & Agol, E. 2002, *ApJ*, 580, L171
- Mandelbrot, B. B. 1977, *The fractal geometry of nature*
- Mayor, M. & Queloz, D. 1995, *Nature*, 378, 355
- Mihalas, D. 1970
- Mihalas, D., Dappen, W., & Hummer, D. G. 1988, *ApJ*, 331, 815
- Muthsam, H. J., Kupka, F., Löw-Baselli, B., et al. 2010, *New A*, 15, 460
- Nahar, S. N. 2004, *Phys. Rev. A*, 69, 042714
- Nissen, P. E., Primas, F., Asplund, M., & Lambert, D. L. 2002, *A&A*, 390, 235
- Nordlund, A. 1976, *A&A*, 50, 23
- Nordlund, A. 1982, *A&A*, 107, 1
- Nordlund, A. & Dravins, D. 1990, *A&A*, 228, 155
- Nordlund, Å. & Stein, R. F. 2001, *ApJ*, 546, 576
- Nordlund, Å., Stein, R. F., & Asplund, M. 2009, *Living Reviews in Solar Physics*, 6, 2
- Pereira, T. M. D., Asplund, M., Collet, R., et al. 2013, *A&A*, 554, A118
- Pereira, T. M. D., Asplund, M., & Kiselman, D. 2009a, *Mem. Soc. Astron. Italiana*, 80, 650
- Pereira, T. M. D., Kiselman, D., & Asplund, M. 2009b, *A&A*, 507, 417
- Piskunov, N. E., Kupka, F., Ryabchikova, T. A., Weiss, W. W., & Jeffery, C. S. 1995, *A&AS*, 112, 525
- Ramírez, I., Allende Prieto, C., Koesterke, L., Lambert, D. L., & Asplund, M. 2009, *A&A*, 501, 1087
- Ramírez, I., Allende Prieto, C., & Lambert, D. L. 2008, *A&A*, 492, 841
- Ramírez, I., Collet, R., Lambert, D. L., Allende Prieto, C., & Asplund, M. 2010, *ApJ*, 725, L223
- Rana, N. C. 1991, *ARA&A*, 29, 129
- Robinson, F. J., Demarque, P., Li, L. H., et al. 2003, *MNRAS*, 340, 923

- Rosenthal, C. S., Christensen-Dalsgaard, J., Nordlund, Å., Stein, R. F., & Trampedach, R. 1999, *A&A*, 351, 689
- Roudier, T. & Muller, R. 1986, *Sol. Phys.*, 107, 11
- Ruiz Cobo, B. & del Toro Iniesta, J. C. 1992, *ApJ*, 398, 375
- Rutten, R. J., de Wijn, A. G., & Sütterlin, P. 2004, *A&A*, 416, 333
- Sbordone, L., Bonifacio, P., Caffau, E., et al. 2010, *A&A*, 522, A26
- Schlattl, H., Weiss, A., & Ludwig, H.-G. 1997, *A&A*, 322, 646
- Schrijver, C. J., Hagenaar, H. J., & Title, A. M. 1997, *ApJ*, 475, 328
- Sing, D. K. 2010, *A&A*, 510, A21
- Skartlien, R. 2000, *ApJ*, 536, 465
- Smalley, B., Gardiner, R. B., Kupka, F., & Bessell, M. S. 2002, *A&A*, 395, 601
- Socas-Navarro, H. 2011, *A&A*, 529, A37
- Southworth, J. 2008, *MNRAS*, 386, 1644
- Steffen, M. 1993, in *Astronomical Society of the Pacific Conference Series*, Vol. 40, IAU Colloq. 137: Inside the Stars, ed. W. W. Weiss & A. Baglin, 300
- Steffen, M. & Holweger, H. 2002, *A&A*, 387, 258
- Steffen, M., Ludwig, H.-G., & Freytag, B. 1995, *A&A*, 300, 473
- Steffen, M., Ludwig, H.-G., & Kruss, A. 1989, *A&A*, 213, 371
- Stein, R. F., Benson, D., Georgobiani, D., & Nordlund, Å. 2006, 624
- Stein, R. F., Georgobiani, D., Schafenberger, W., Nordlund, Å., & Benson, D. 2009, 1094, 764
- Stein, R. F., Lagerfjård, A., Nordlund, Å., & Georgobiani, D. 2011, *Sol. Phys.*, 268, 271
- Stein, R. F. & Nordlund, A. 1998, *ApJ*, 499, 914
- Stein, R. F. & Nordlund, Å. 2001, *ApJ*, 546, 585
- Stempels, H. C., Piskunov, N., & Barklem, P. S. 2001, 223, 878
- Tinsley, B. M. 1979, *ApJ*, 229, 1046
- Trampedach, R. 2001, *Journal of Astronomical Data*, 7, 8
- Trampedach, R. 2007, 948, 141
- Trampedach, R., Asplund, M., Collet, R., Nordlund, Å., & Stein, R. F. 2013, *ArXiv e-prints*
- Trampedach, R. & Stein, R. F. 2011a, *ApJ*, 731, 78
- Trampedach, R. & Stein, R. F. 2011b, *ApJ*, 731, 78
- Trampedach, R., Stein, R. F., Christensen-Dalsgaard, J., & Nordlund, Å. 1999, 173, 233
- Uitenbroek, H. & Criscuoli, S. 2011, *ApJ*, 736, 69
- Unno, W., Kondo, M.-A., & Xiong, D.-R. 1985, *PASJ*, 37, 235
- van Hamme, W. 1993, *AJ*, 106, 2096

- Vernazza, J. E., Avrett, E. H., & Loeser, R. 1976, *ApJS*, 30, 1
- Vögler, A., Shelyag, S., Schüssler, M., et al. 2005, *A&A*, 429, 335
- Weiss, A. & Schlattl, H. 2008, *Ap&SS*, 316, 99
- Williamson, J. H. 1980, *Journal of Computational Physics*, 35, 48
- Xiong, D. R., Cheng, Q. L., & Deng, L. 1997, *ApJS*, 108, 529

Acknowledgment

I want to thank my (co)supervisor Achim Weiss, for giving me the opportunity to perform an internship and subsequently my Diploma thesis work at the Max Planck Institute for Astrophysics, which was the initiation of my scientific endeavors in stellar astrophysics. Also, I want to express my highest gratitude towards my (main)supervisor for my PhD thesis, Martin Asplund, for giving me the freedom to bloom and develop myself with his excellent, inspiring mentorship and guidance. Furthermore, I want to thank Remo Collet for helping me getting acquainted with the `STAGGER`-code and his support throughout several projects, and hosting me in Canberra, Australia. I want to thank also Aake Nordlund for his helpful discussions. Finally, I would like to thank my collaborators Wolfgang Hayek, Regner Trampedach and Andrea Chiavassa for their contribution for the individuals projects they were involved with.

This PhD thesis is dedicated to my mother, Alгаа Magic, who early on inspired my interest for physics. I am very thankful for the unrestrained support by my father, sister and brother.

Curriculum vitae

Zazralt Magic

Personal information

Born 17. December 1981
Male, Single, German Citizen
Ulan Bator, Mongolia

University education

2010 - 2014	Max Planck Institute for Astrophysics PhD in Astrophysics	Garching, Germany
2006 - 2010	Ludwig-Maximilians-Universität Diploma in Physics	Munich, Germany
2004 - 2006	Ludwig-Maximilians-Universität Preliminary Diploma in Physics	Munich, Germany

School education

2002 - 2004	Upper Vocational School Abitur (University-entrance Diploma)	Munich, Germany
1999 - 2002	Apprenticeship at HypoVereinsbank AG Graduation as a bank clerk	Munich, Germany
1995 - 1999	Maria-Probst Secondary High School Mittlere Reife (General Certificate of Secondary Education)	Munich, Germany